Ultrafast Dynamics of Transition Metal Complexes

The University Of Sheffield.

George Adam Farrow

A thesis submitted to the University of Sheffield in partial fulfilment of the requirements for the degree of Doctor of Philosophy

Department of Chemistry

University of Sheffield

September 2019

Abstract

Natural photosynthetic systems have utilized electron transfer in the process of converting sunlight into chemical energy for millions of years. With research motivation driven by the need to move away from the usage of fossil fuels, investigations into artificial systems capable of replicating such processes are becoming more frequent.

Transition metal (TM) complexes possessing charge-separate excited-states are ideal candidates for the exploration of the underlying mechanisms of electron transfer. Via systematic alteration of ligands, the properties of TM complexes can be carefully tuned.

The primary goal of this thesis is to examine the ultrafast emission of Pt(II) square planar complexes as a means of interrogation of the process of intersystem crossing, the 'forbidden' transition between singlet and triplet excited states. This phenomenon is essential in the generation of long-lived charge-separated states capable of undertaking further electron transfer steps. Evidence for the rapid formation of these types of triplet states is ubiquitous in TM complexes in the literature, however, many fundamental questions regarding the mechanism and the dependence on the rates of such process on molecular structure, remain unanswered.

Utilizing 'Fluorescence Upconversion Spectroscopy', the ultrafast emission of two related families of platinum(II) trans-acetylides, was recorded. For both families, singlet emission was found to persist much longer than the lifetimes of ISC quoted in the literature. For one family, a series of three symmetrical 'Donor-Bridge-Donor' with varying lengths of 'linkers' within the bridge, no obvious dependence of ISC on linker length was found.

Additionally, ultrafast two-dimensional infrared spectroscopy was used to investigate the vibrational couplings in the ground-state of related platinum(II) diimine complexes. Vibrational energy transport was found to occur via at least two mechanisms, with interactions between modes > 10 Å apart observed.

The research presented within demonstrates the ability of various ultrafast spectroscopic techniques in the unravelling of the early-time dynamics of transition metal complexes.

Acknowledgements

First and foremost, I would like to thank my supervisor, *Professor Julia Weinstein* for giving me such an incredible opportunity to undertake a project within her research group. Julia's inexhaustible enthusiasm has been a source of inspiration throughout the entirety of my PhD. I am ever so grateful for her unwavering support, without which, the completion of this doctorate degree would not have been possible.

I have been extremely fortunate to learn all things FLUPS under the supervision of *Professor Niko Ernsting*. I have thoroughly enjoyed all time spent working together, in both Sheffield and Humboldt. Professor Niko has been an invaluable source of wisdom, for which I am very thankful.

The ultrafast emission measurements wouldn't have been possible without the expert guidance of *Dr Dimitri Chekulaev*. I am grateful for all of Dimitri's hard work in ensuring the best possible conditions for the performance of our experiments.

Throughout my PhD, I was blessed to be involved in numerous experimental visits to the Central Laser Facility, Research Complex at Harwell, Rutherford Appleton Laboratories. I am very grateful that I was given the opportunity to work on the various, cutting-edge, laser techniques under the supervision of some of the best laser scientists in the world; *Dr Igor Sazanovich*, *Dr Greg Greetham*, *Dr Paul Donaldson* and *Professor Michael Towrie.*

I am thankful to all of my colleagues in the Weinstein group, past and present. In particular, I am thankful for; my reliable assistant *Alex Auty*, for providing a pair of hands whenever called upon and countless stimulating discussions, *Dr Ed Greenough*, for introducing me to ultrafast laser spectroscopy and support throughout the first half of my PhD, *Dr Andy Sadler*, for guidance in all things synthesis and the making of my molecules, and *Dr Theo Keane*, for numerous insightful discussions in the interpretation of spectroscopic data.

Thanks to all those I've shared the office with over the years; Saeed, Milan, Marina, Steven, Liam, Mike, Sam, Martin and Guanzhi.

I would like to thank my family and friends. Dad, Lauren, Grandma and Grandad, Uncle Kev, Auntie Jo, Joshua, Josh, Aaron and Jack, words cannot express how much your unfaltering support means to me. To my brother, my best mate, Joe, I simply could not have done this without you. I would like to thank my girlfriend Saphron, for tireless support in the final stages.

And last, but certainly not least, I would like to thank my Mum. My biggest inspiration, I am so grateful for everything you have done for me. This thesis is dedicated to you.

Abbreviations

2DIR	Two-Dimensional Infrared
A	Acceptor
bpy	2,2'-Bipyridyl
CCD	Charge Coupled Device
cm	Centimetre
CSS	Charge separated state
CT	Charge Transfer
DAS	Decay Associated Spectra
DFT	Density Functional Theory
EAS	Evolution Associated Spectra
ES	Excited State
ET	Electron Transfer
eV	Electron Volt
FC	Franck-Condon
fs	Femtosecond
FT	Fourier Transform
FWHM	Full Width Half Maximum
GS	Ground State
HOMO	Highest Occupied Molecular Orbital
IC	Internal Conversion
IR	Infrared
IRF	Instrumental Response Function
ISC	Intersystem Crossing
IVR	Intramolecular Vibrational Redistribution
Laser	Light Amplification by Stimulated Emission of Radiation
LUMO	Lowest Unoccupied Molecular Orbital
MLCT	Metal-to-Ligand Charge Transfer
MMLLCT	Mixed Metal-Ligand-to-Ligand Charge Transfer
NAP	1,8-Napthalimide
nm	Nanometre
ns	Nanosecond
OD	Optical Density
ps	Picosecond
PTZ	Phenothiazine
TA	Transient Absorption
TOPAS	Travelling-Wave Optical Parametric Amplifier of Superfluorescence
TRIR	Time-Resolved Infrared
UV	Ultra-violet
Vis	Visible
VR	Vibrational Relaxation
W	Watt
λ	Wavelength
τ	lifetime

Table of Contents

1 Introduction

1.1 Motivation

Undeniably, the first Industrial Revolution (1760 – 1840) had a huge impact on humanity, leading to drastic increases in life expectancy,[1] improvements in health care and bountiful technological advancements. Nevertheless, it certainly came at a cost, namely the health of the planet. Massive upscaling of production and industrialisation inevitably led to a gigantic surge in the demand for energy, this resulting in an exponential-like growth in the consumption of fossil fuels, see **Figure 1.1**, from around 1850 onwards.[2,3]

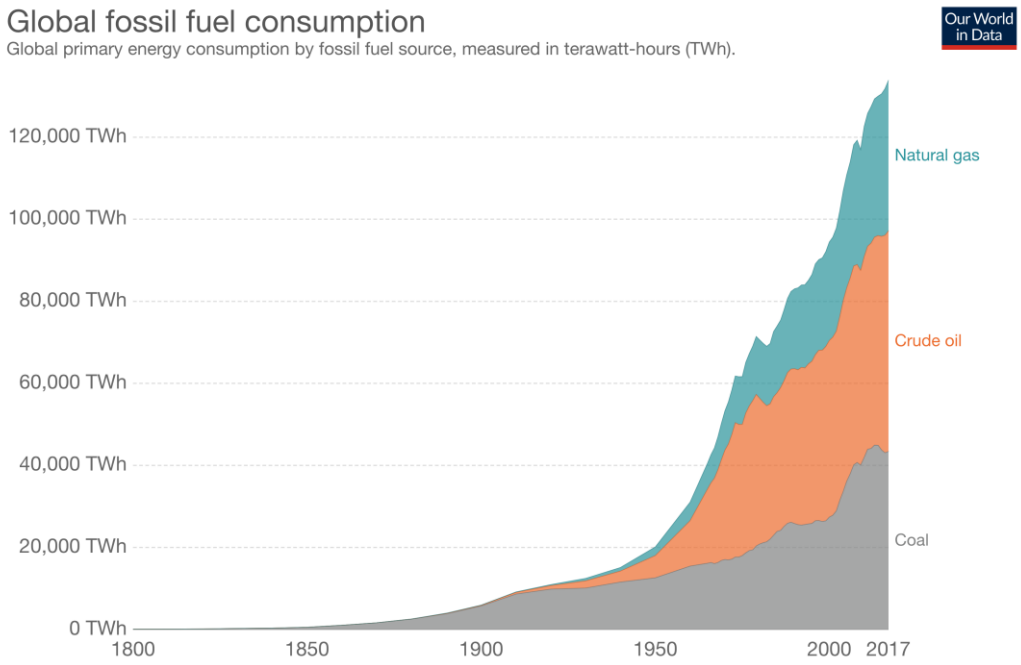

Figure 1.1 Global primary energy consumption by fossil fuel source, measured in terawatt-hours (TWh), between the year 1800 and 2017. Source: Vaclav Smil. Energy Transitions: Global and National Perspective & BP Statistical Review of World Energy.

With the burning of vast amounts of fossil fuels comes the release of vast amounts of CO_2, and with this the consequent rise in global temperatures, i.e. global warming. Since 1880, the average global temperature has risen by around 0.8 °C.[4] This problem persists, with projections estimating a further increase in temperature of between 1.0 and 3.7 °C in the 21st Century.[5]

In 2018, the global total primary energy demand was 14,301 Mtoe (million tons of oil equivalent) or 166,321 TWh,[6] a 2.3 % increase on the previous year. In 2018, Coal, Oil and

Gas combined accounted for 80 % of energy supply.[6] Worryingly, growth in energy demand is somewhat self-perpetuating, with almost 20 % of the increase in global energy demand attributable to change in weather conditions. Drops in average winter temperatures driving a demand for heating, and perhaps more significantly, record high temperatures in summer months increasing demand for cooling. Changing weather conditions undoubtedly having some dependence on the increase in atmospheric CO_2, a result of fossil fuel burning.

Anthropogenic climate change is harmful to the planet in a great number of ways. Occurrences of extreme weather events such as wildfires, hurricanes, flooding and droughts continually rise.[7] Not only can these events be devastating from a personal point of view but they are also very costly fiscally.[8] Certain habitats may cease to exist altogether, while others may expand in size, with threatened and endangered species most susceptible to these changes.[9] In order to mitigate these disastrous changes, a move away from our huge fossil fuel consumption must take place. Additionally, the finite nature of fossil fuels means there simply is no other option, for the long-term sustainability of our species, an alternative simply has to be found.

The use of renewable energy resources is not a modern phenomenon. In the Mediterranean, around 5,500 years ago, sail ships relied on the energy of the wind.[10] Windmills were used in India around 2,500 years ago.[11] Greek civilisations used solar energy; Archimedes wrote a book on the use of 'burning mirrors', used for igniting fires.[12] The issue is the magnitude to which energy is required, our species simply outgrew these simplistic approaches to the harnessing of these energy sources. Renewable energy resources refer to energy resources, which are naturally replenished on a human timescale.[13] These include: wind, wave, tidal, geothermal and solar energy. Although there has been a global push in the direction of their use, in 2018, renewables still only provided just 15 % of global energy.[6] On the scale on which energy is consumed, in the recent past at least, fossil fuels have had by far the largest price-performance ratio. In order to facilitate a switch towards renewable energy resources, adequate technological progress is needed.

Not only is solar the most abundant of these energy sources but as chemists, this is perhaps where the largest research contribution can be made. Solar energy capture and conversion will be explored further below.

1.2 Solar Energy - Artificial Photosynthesis

The solar radiation incident upon Earth provides an enormous amount of energy. With an average of approximately 1.08×10^{17} W reaching the Earth's surface,[14] this is equivalent to an energy of 388,800,000 TWh in a single hour of irradiation, i.e. more than 2000 times the annual global energy consumption. Covering just 0.16% of the surface of the Earth with solar energy conversion systems with an efficiency of 10% could provide 2×10^{13} W of power or 72,000 TWh with an hours' worth of energy capture and conversion.[15] However, this does rely on an efficient method of capturing the solar energy. This is where we focus our attention.

Photosynthesis, the process by which solar radiation is used in the synthesis of energy-rich molecules, has been exploited by natural systems for billions of years. There is evidence to suggest that photosynthetic organisms may have existed more than 3.4 Ga ago.[16] It is estimated that the average rate of energy storage by all of the photosynthetic organisms on Earth combined is about 1×10^{15} W.[17]

Natural photosynthesis involves the splitting of water using the energy of sunlight, and the consequential reduction of carbon dioxide. The process leads to the production of energy-rich sugars and other organic molecules, and the release of molecular oxygen into the atmosphere. Effectively, the organic molecules are used as a means of storing solar energy within chemical bonds. A schematic diagram of natural photosynthesis is shown in **Figure 1.2**. Although the mechanistic details may differ from one organism to another, the key steps are universal and are as follows.[18]

I. Absorption of light via a chromophore leading to an initial charge-transfer, excited state (ES).
II. Electron/hole migration to system periphery creating a long-distance, charge-separated state.
III. Independent redox reactions at each site.

The synthesis of artificial systems, capable of mimicking natural photosynthetic processes is very attractive as a means of generating clean, renewable energy. The concept is not particularly new, having been discussed for more than a hundred years.[19] An artificial system will follow all of the steps present in nature, however fine-tuning of the components and the individual steps may lead to much greater efficiencies of energy conversion.

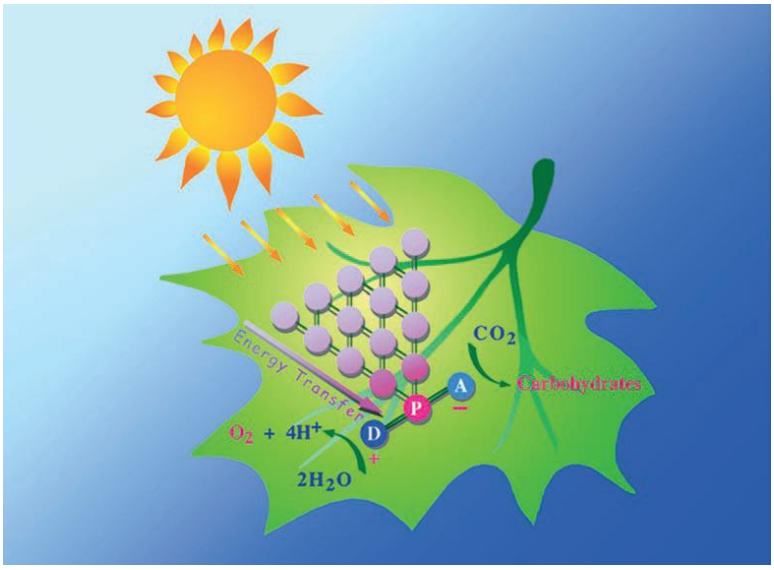

Figure 1.2 A schematic of natural photosynthesis. The absorption of light and energy transfer to a pigment (P), the consequential separation of charge between the donor (D) and acceptor (A) groups, and reactions at both a reductive and oxidative catalyst forming both oxygen and carbohydrates.[15]

In practice, a system will have the following basic structure; A chromophore (C), capable of absorbing solar radiation, electron donor (D) and electron acceptor (A) substituents attached to the chromophore in such a way that gives fast, efficient electron transfer in the desired direction and both a reduction and oxidation catalyst at the system periphery, capable of performing desired reactions. A simple model is shown in **Figure 1.3**.

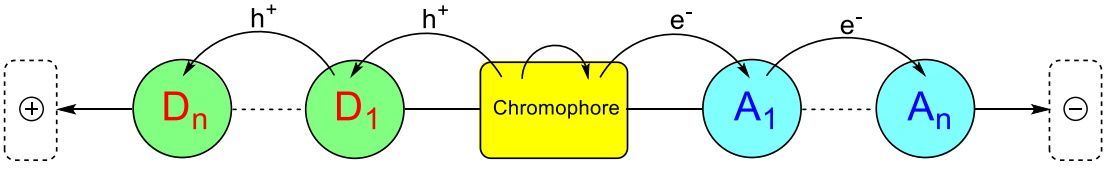

Figure 1.3 A schematic of artificial photosynthesis. **I.** The absorption of light and separation of charge in a chromophore. **II.** Cascade electron transfer across the system; from donors (D), across the chromophore, to the acceptors (A). **III.** Accumulation of positive/negative charge at the catalytic sites.

The utilisation of solar radiation via photosynthesis relies on photo-induced charge transfer (CT), a mechanism that results in the formation of energy-rich, charge-separated states. It is also vital that the charge-separated state lives long enough for the catalytic reactions to occur; recombination of the charge (back electron transfer) should be relatively slow.

1.3 Transition Metal Complexes as Chromophores

In recent years, transition metal (TM) complexes have been subject to extensive scientific investigation due to their unique photophysical properties. Strong absorption of visible light and long-lived charge-transfer (CT) states make these complexes very attractive candidates for use as chromophores in artificial photosynthetic systems.[17,18,20,21] The molecular structure of $[Ru(bpy)3]^{2+}$, perhaps the complex subject to the most thorough photophysical investigation, is shown in **Figure 1.4**.

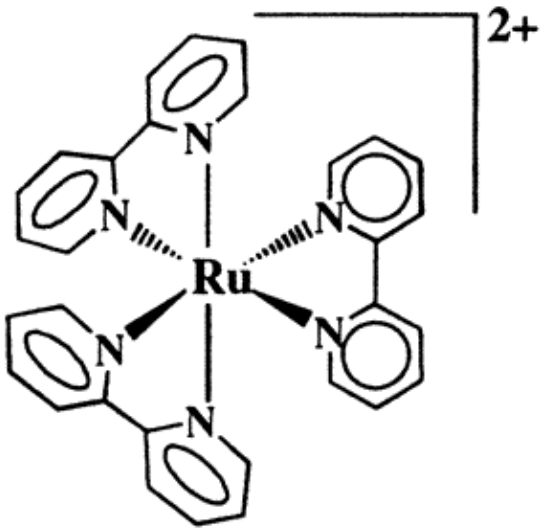

Figure 1.4 Molecular structure of the series of $[Ru(bpy)3]^{2+}$. The archetypal transition metal complex, subject to extensive photophysical investigation. Figure taken directly from source.[22]

TM complexes are also of much interest in other applications, including biological imaging and molecular devices.[23–26] Unlike with organic molecules, the properties of these complexes are also highly tuneable via alteration of the ligands, essential in the engineering of new systems.

The suitability of a complex for a specific application will depend upon:

1. The nature and energy of the electronics states accessible from the ground state.

2. The rates and efficiencies of the various relaxation processes that occur upon photoexcitation.

Types of electronic excited states and the pathways of relaxation are discussed below.

1.3.1 Electronic Excited States

The constituent components of a transition metal complex will determine the nature of the frontier molecular orbitals, which in turn will determine the types of excited states accessible as well as how they interact with another. With transition metal complexes there are 3 types of electronic transitions of particular importance: *d-d* transitions, charge-transfer (CT) transitions and π-π^* transitions. In order to be able to tune the metal complexes and obtain desirable properties, an understanding of these different types of transitions is essential.

d-d transitions

When a complex or system contains a transition metal, *d-d* transitions may occur. *d-d* transitions are also known as metal-centred or ligand-field (LF) transitions. Such a transition occurs when an electron moves from one metal d orbital to another.

Any transition metal, in a vacuum, will possess 5 *d*-orbitals, all of the same energy (5 degenerate energy levels). Each of these orbitals has a different orientation around the metal centre; there is a different distribution of electron density for an electron in each of the 5 orbitals. The addition of coordinating ligands to a metal centre leads to the raising in energy of the 5 orbitals by different amounts, the levels are 'split'. Repulsive interactions between lone pairs of electrons situated on the ligands and the *d*-electrons are responsible for the increase in energy. Crystal Field Theoryprovides a description for the splitting of the *d*-orbitals. Ligands are considered as being bound to the metal through electrostatic interactions only, with no metal-ligand covalent bond character. The ligands are modelled as point charges, which combined, produce a static electric field. Interactions with the electric field are responsible for splitting of the *d*-orbitals. The degree of splitting is dependent on the nature of the metal and the oxidation state of the metal. The splitting is also dependent on the nature of the ligands and their arrangement around the metal ion.

Different ligands will split the energy of the orbitals by different amounts. Ligands are arranged in a 'spectrochemical series', the order of the ligands indicating their relative 'field strength'. Ligands which cause a large splitting of the orbitals are denoted 'strong field' ligands and ligands which cause a small splitting are denoted 'weak field' ligands.

The energy gaps between the various *d*-orbitals often correspond to the energy of light in the UV/visible region. The transitions are spin allowed. However, as the transitions occur within the set of *d* orbitals; there is no change in orbital angular momentum and the transitions are therefore forbidden by the Laporte selection rule. Geometric distortions during molecular vibrations mean that the transitions may become transiently allowed; therefore, *d-d* transitions are seen but typically have very low extinction coefficients (~10^2 M^{-1} cm^{-1}).

π-π^* transitions

The acceptor ligands typically used in the chromophores are based upon planar, conjugated π systems of poly-pyridines. The ligands will have occupied π, bonding molecular orbital delocalised across the entire system. The absorption of light may promote electrons from π, bonding orbitals to unoccupied π^*, anti-bonding orbitals. The energy gap between the orbitals often corresponds to the UV/Visible region. The π-π^* energy gap is dependent on the size of the conjugated system; with larger, extended ligands having smaller gaps, and hence absorbing light of lower energy/longer wavelength. π-π^* transitions are fully allowed, there is also very good spatial overlap between the orbitals involved in a transition; this leads to very highly intense absorption. Extinction coefficients for π-π^* transitions are typically in the range of 10^4 – 10^5 M^{-1} cm^{-1}. For example, the π-π^* transition of $[Ru(bpy)_3]^{2+}$ at 287 nm, has an extinction coefficient of 85,300 M^{-1} cm^{-1} (in water).[27]

Charge-Transfer (CT) transitions

Electronic transitions occur between the frontier molecular orbitals. The distribution of an electron within a molecule will differ depending on the molecular orbital in which it is situated. CT transitions occur when the two orbitals involved in a transition have considerable electron density localised on different parts of the molecule; i.e. absorption of light leads to a considerable shift in electron density within the molecule. In the types of metal complexes of interest in this project, there are a few different types of CT transitions commonly seen. The naming of the transitions is dependent on the localisation of the two orbitals involved in the transition. Transitions include:

I. Metal to ligand charge-transfer (MLCT).

II. Ligand to ligand charge-transfer (LL'CT).

III. Mixed metal/ligand to ligand charge-transfer (MMLL'CT).

CT transitions are allowed and are therefore give intense absorption. In general, there will be less overlap between the orbitals involved in a transition relative to π-π^* transitions and the absorbance is therefore not as intense. Extinction coefficients are typically in the range of $10^3 - 10^4$ M^{-1} cm^{-1}. For example, the transition of $[Ru(bpy)_3]^{2+}$ at 452 nm, which is assigned as an MLCT, has an extinction coefficient of 14,600 M^{-1} cm^{-1} (in water).[27]

1.3.2 Excited-State Processes and Kasha's Rule

The absorption of a photon leads to the population of higher energy states (ES). Once in the ES, various processes may occur. An example of accessible states and processes are summarised in a Jablonski diagram, shown in **Figure 1.5**.

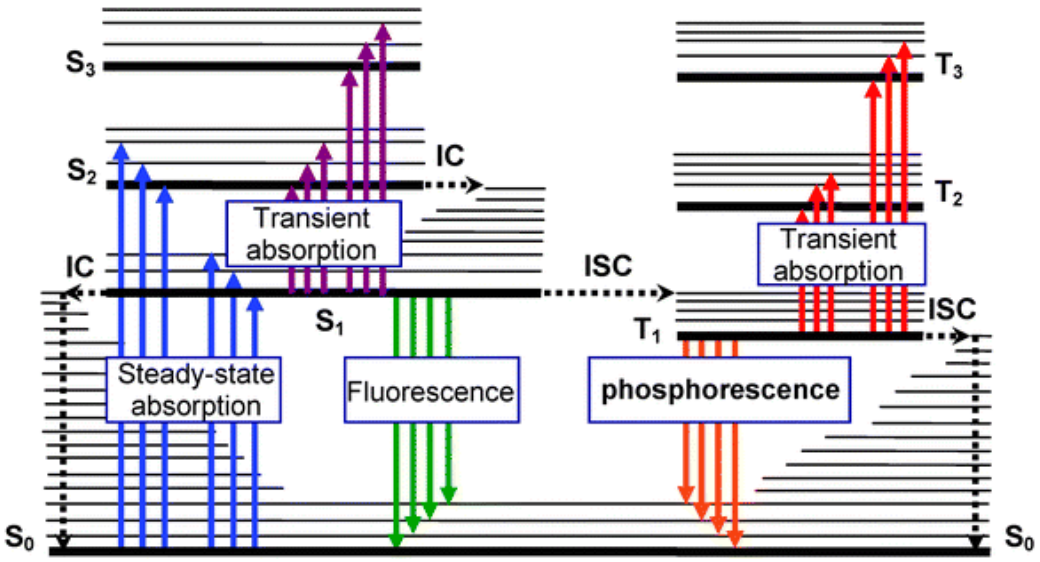

Figure 1.5 Jablonski diagram – the diagram is illustrative of the different types of electronic states accessible upon light absorption and their relative energies. The types of transitions that may occur between the states are also shown; Steady-state absorption, transient absorption, internal conversion (IC) and inter-system crossing (ISC).

Steady-state absorption (absorption from the ground state) occurs from the lowest energy singlet state, S_0. Selection rules state that there may not be a change of electron spin in transition; initial photon absorption only populates other, higher energy, singlet

states. The transitions may also involve vibrational and rotational excitation. Vibrational levels of each electronic state are also shown in the diagram.

Population of the excited state is energetically unfavourable relative to the ground state, and naturally, will eventually decay. There are numerous ways in which a molecule may lose the excess energy; these can be separated into three categories.

I. Radiative decay processes.
II. Non-radiative decay processes.
III. Photochemical reactions.

Radiative decay may either be in the form of fluorescence or phosphorescence. Both processes involve the emission of a photon and decay to lower energy states. Fluorescence occurs without a change in spin multiplicity, e.g. S_n to S_m; it is spin-allowed and is therefore a fast process. Phosphorescence involves a change in spin multiplicity, e.g. S to T; it is spin-forbidden and is therefore a relatively slow process.

Non-radiative decay processes include internal conversion (IC), an isoenergetic transition between two states of the same multiplicity, intersystem crossing (ISC), an isoenergetic transition between two states of different multiplicity, i.e. a spin flip. All ISC is reversible , that is, there is equal probability of the reverse transition (typically T to S) occurring as the initial crossing. However, the triplet state (state of higher multiplicity) will typically be lower in energy and therefore offers more routes to the population of a thermodynamically more stable, lower energy, state via the dissipation of vibrational energy and descent into the energy well. The net outcome of ISC between two states will depend on the competition between the forward and reverse transitions, and therefore also the influence of the routes to further energy dissipation from the lower in energy of the two states involved in the ISC step.

Additionally, molecules with excess energy will undergo intramolecular vibrational redistribution (IVR), this is a process by which vibrational energy is rearranged within a molecule, typically, high-energy modes transfer energy to lower-energy modes within the molecule. The rate of non-radiative decay is dependent on the size of the energy gap between the upper and lower states. For charge-transfer excited states, the rate of non-

radiative decay is found to increase exponentially with decreasing energy gap, this is the so-called 'energy gap law'.[28]

With the Jablonski diagram shown here, Kasha's rule is obeyed, that is that 'the emitting state of a given multiplicity is the lowest excited level of that multiplicity, i.e. within a multiplicity, emission will only occur once a 'relaxed' state is reached, that is, all other decay processes precede the emission.[29]

Simply put, it is assumed that IVR precedes IC, which in turn, precedes ISC (i.e. $k_{IVR}>>k_{IC}>>k_{ISC}$). However, with transition metal complexes, this is not always the case. Selection rules for electronic transitions state that a process involving a change in spin is forbidden, i.e. should not occur to any appreciable extent. However, ISC has been observed to occur on ultrafast time-scales (less than picosecond timescale) in numerous TM complexes. The presence of the heavy metal means that there is strong spin-orbit coupling. This often leads to fast ISC and therefore, once excited, there is fast relaxation into the lowest energy triplet state, T_1.

The generation of a triplet metal-to-ligand charge-transfer state (^{3}MLCT) is integral to the function of the TM complex in many applications; efficient population of such a state relies directly upon efficient ISC. ISC in transition metal complexes is discussed further below.

1.4 Intersystem Crossing in Transition Metal Complexes

Ultrafast intersystem crossing, typically from a singlet to triplet electronic state, is an essential step in the formation of a long-lived charge-separated state. The primary concern of the work here is not an in-depth understanding of the theory behind, or mechanism behind ultrafast ISC, but an understanding of how the spin-changes manifest spectroscopically and how the rates of such processes depend on chemical structure. A brief overview of the underlying theory is presented here, followed by a review of relevant spectroscopic investigations into ISC of TM complexes.

1.4.1 ISC in TM Complexes – Principles

Presented here is a brief introduction to the underlying principles of transitions between electronic states, with a particular focus on transitions between states of different spin, i.e. intersystem crossing. The material is adapted from the books 'Modern Molecular Photochemistry' by Nicholas J. Turro and 'Principles of Molecular Photochemistry' by Nicholas J. Turro, V. Ramamurthy and J. C. Scaiano.[30,31]

Classical Dynamics: Transitions Between States

A combination of Newtonian *ideas* and the energy-motion conservation *laws* are employed in the development of a qualitative and quantitative understanding of the transition between electronic states. This 'classical theory' of electronic transitions is based upon the following two Newtonian principles:

1. Understanding dynamic processes relies on the identification of interactions (forces, energies, or work) involved in the changing of the motion of the particles of a system.
2. Deviations from original motions occur because of interactions and these will occur reciprocally, i.e., to each action there is an equal and opposite reaction.

Additionally, to these two principles, two *laws* apply in the analysis of the dynamics of any classical system:

1. *The Law of Conservation of Energy.* In any isolated system energy may only be transformed from one kind or another, it cannot be created or destroyed.

2. *The Law of Conservation of Momentum.* In any isolated system, momentum may be transformed from one kind to another but cannot be created or destroyed. (Angular momentum may be transformed into linear momentum and vice versa, but the sum of angular and linear momentum must be conserved.

Based upon these laws / principles, the procedure for analysing the transitions between electronic states takes the following form:

1. The energetic and structural differences between the initial and final states are identified.
2. Any implied momentum differences between the two states are identified.
3. Forces which may convert the initial structure into that of the final are identified.

Upon successful completion of these 3 steps, a possible mechanism for the conversion of one state to another has been identified. In order to be a plausible one, the mechanism must obey both the conversation of both energy and momentum.

If either law is violated, the transition is strictly forbidden. With regards to the conservation of energy, an external energy source / sink may be introduced to satisfy this requirement.

With regards to the conservation of momentum, an additional, initially ignored term, be it either internal or external must be added in order to ensure total momentum remains constant.

It is worth noting, 'forbidden' and 'allowed', in the context of electronic transitions, are simply relative terms. That is, a 'forbidden' transition is typically slower than an 'allowed' transition, it doesn't mean it will not occur to any degree at all.

Quantum Dynamics: The Golden Rule for Transitions Between States

The 'Golden Rule', **equation 1.1**, is an expression for the rate of processes in terms of quantum dynamics: '*the rate of transitions between two states is proportional to the square of the matrix element corresponding to the first order perturbation coupling the Zero Order states.*

$$k(obs) = \frac{2\pi}{h}\rho\langle H'\rangle^2$$

equation 1.1

Where ρ is the 'density' of final states capable of coupling to the initial state, and $\langle H' \rangle$ represents the matrix element for the perturbation coupling the initial and final states.

The rate of transitions between two states is dependent upon the magnitude of the perturbation (force) which changes the position / motion of the particles of initial state, 'reshaping' this state so as to make it 'look' like the final state.

Spin-Orbit Coupling

Transitions between states of different spin multiplicity are forbidden by so-called 'spin-selection' rules. However, this rule only holds where spin and orbital functions can be rigorously separated. 'Spin-orbit coupling' leads to departures from this approximation. The movement of electrons around a nucleus generates a magnetic field. This magnetic field interacts with electrons due to their spin, i.e. there is, spin-orbit coupling.

Conventional spin labelling of states doesn't strictly hold, and states will have mixed spin character, transitions between states of 'different spin' may occur, this perturbation, is what gives rise to spin transitions: the most important perturbation, in the act of making the initial singlet state 'look like' the triplet state is the coupling of the electron spin motion to the electron orbital motion. An additional term for perturbation may be added to **equation 1.1** and it may be rewritten in the form of **equation 1.2**.

$$k(obs) = \underbrace{\left[\frac{k^0_{max}\langle\psi_1|P_{vib}|\psi_2\rangle^2}{\Delta E^2_{12}}\right]}_{Vibrational\ coupling} \times \underbrace{\left[\frac{\langle\psi_1|P_{SO}|\psi_2\rangle^2}{\Delta E^2_{12}}\right]}_{\substack{Spin-orbital \\ coupling}} \times \underbrace{\left[\langle\chi_1|\chi_2\rangle^2\right]}_{\substack{Vibrational\ overlap \\ Franck-Condon\ factors}}$$

equation 1.2

The 'Spin-orbital coupling' term of **equation 1.2** is larger with increased SOC, and the rate of ISC will be larger. Spin-orbit coupling scales with the atomic number, to the power of four, of the involved atoms see **equation 1.3**. Where Z is atomic number.

$$SOC \propto Z^4$$

equation 1.3

Complexes involving transition metals can exhibit very large spin-orbit coupling, this is known as the 'heavy-atom effect'.

The heavy-atom effect is clearly illustrated with a series of substituted Naphthalenes. The rates of ISC, and fluorescence and phosphorescence quantum yields, for this series, are

given in **Table 1.1**. The substitution of a hydrogen with the halides Cl, Br and I, shows significant effect on the rate of ISC. As larger, heavier atoms are introduced, the rate of ISC, and consequently the phosphorescence quantum yield, increases. The fluorescence quantum yield shows the inverse effect, as faster ISC leads to a decrease in singlet state lifetime and the subsequent reduction of fluorescence.

Table 1.1 Rate of ISC, and quantum yields of fluorescence and phosphorescence, for a series of substituted naphthalene molecules. Data are for rigid solutions at 77 K. Table adapted from source.[31]

Molecule	k_{ISC} / s^{-1} (S to T)	Φ_F	Φ_P
Naphthalene	10^6	0.55	0.05
1-Fluornaphthalene	10^6	0.84	0.06
1-Chloronaphthalene	10^8	0.06	0.54
1-Bromonaphthalene	10^9	0.002	0.55
1-Iodonaphthalene	10^{10}	0.000	0.70

Intersystem Crossing: Vibrational Factors & The Energy Gap Law

Non-radiative transitions between states, including ISC, rely on the overlap of molecular orbitals (wavefunction overlap). In order for a transition between states to occur, there must be both electronic and nuclear geometric rearrangement. Molecular vibrations effectively result in the exploration of the potential energy surfaces and may provide pathways for the crossing between states. For two states of similar nuclear geometry, the degree of overlap of the two electronic wavefunctions will be inversely proportional to the energy gap between the two states. This is summarised in the 'Energy Gap Law', see **equation 1.4**, where ΔE is the energy gap. The rate of non-radiative transitions increases as the energy gap between the initial and final state decreases.

$$k_{nr} \propto \exp\left(\frac{-\Delta E^2}{A}\right)$$

equation 1.4

1.4.2 Literature Review – ISC in TM Complexes

Transition metal complexes capable of photoinduced charge-transfer find application in a variety of roles. Examples including; ruthenium-based systems for solar cell photosensitization,[32,33] iridium complexes for two-photon photodynamic therapy,[34]

platinum complexes in organic light-emitting diodes,[35] and rhenium probes for protein relaxation dynamics.[36] The formation of triplet metal-to-ligand charge-transfer (^{3}MLCT) states is crucial in all of these applications. In order to effectively tailor these systems, first an understanding of the relationship between molecular structure and photophysical behaviour is required, i.e. how does each of the complexes arrive at the desired ^{3}MLCT after photoexcitation? How long does the state take to form? What is the mechanism of formation? Are there detrimental pathways competing with the formation? Additionally, transition metal complexes of this nature are of interest from a purely fundamental point of view, exhibiting phenomena in apparent opposition to classical ideas regarding photophysical processes and 'laws'.

This section is a review of the literature on intersystem crossing, the conversion of singlet to triplet electronic states in particular, in transition metal complexes. The untangling of the early time dynamics of the initially populated Franck-Condon excited-state, presents a particularly difficult task. Such states are typically extremely short-lived with multiple ultrafast decay processes occurring in tandem, contrary to a traditional cascade model where vibrational relaxation, internal conversion and intersystem crossing occur sequentially. ISC is often rapid in such systems, with lifetimes in the region of tens of femtoseconds to picoseconds reported in the literature. Additionally, the various states present may be very similar, almost identical in some cases, spectroscopically. In particular, with regards to transient absorption signatures. Time-resolved fluorescence spectroscopy is perhaps better suited to the task of distinguishing singlets and triplets. Typically, the singlet electronic state will be much more emissive than the corresponding triplet, with a larger oscillator strength for emission, due to the Laporte Rule. The singlets and triplets are also likely to be well separated spectrally, with the triplet state being lower in energy than the corresponding singlet state.

A brief review of ISC in transition metal complexes is presented here. An in-depth discussion of all reporting's would be impractical, so an emphasis is placed upon a select number of studies. It is worth noting that a comprehensive review of the ultrafast intersystem crossing in transition metal complexes, documenting the majority of cases, was published in 2015.[37] Within the last 15 years or so, there have been numerous reported observations of ISC in complexes containing Cr,[38,39] Fe,[40–46] Cu,[47,48] Zn,[49] Ni,[50] Ru,[51,52] Re,[53] Os,[54] Pt,[35,50,63,64,55–62] Pd,[50] and Mo.[65] ISC occurs over a large range of

timescales, from <30 femtoseconds,[40] to 100's of picoseconds. Contrary to the 'heavy atom effect', the rates of ISC for TM complexes, do not seem to be well correlated with strength of spin-orbit coupling (SOC). The literature suggests there may be dependence of ISC rates upon, metal-ligand bond stretching frequency,[53] ligand size,[55] and in some cases even solvent.[57] In the majority of the studies the technique of choice is time-resolved emission spectroscopy by upconversion method, with supplementary use of transient absorption spectroscopy.

Symmetrical Platinum Acetylide Complexes with Varied Bridge Lengths

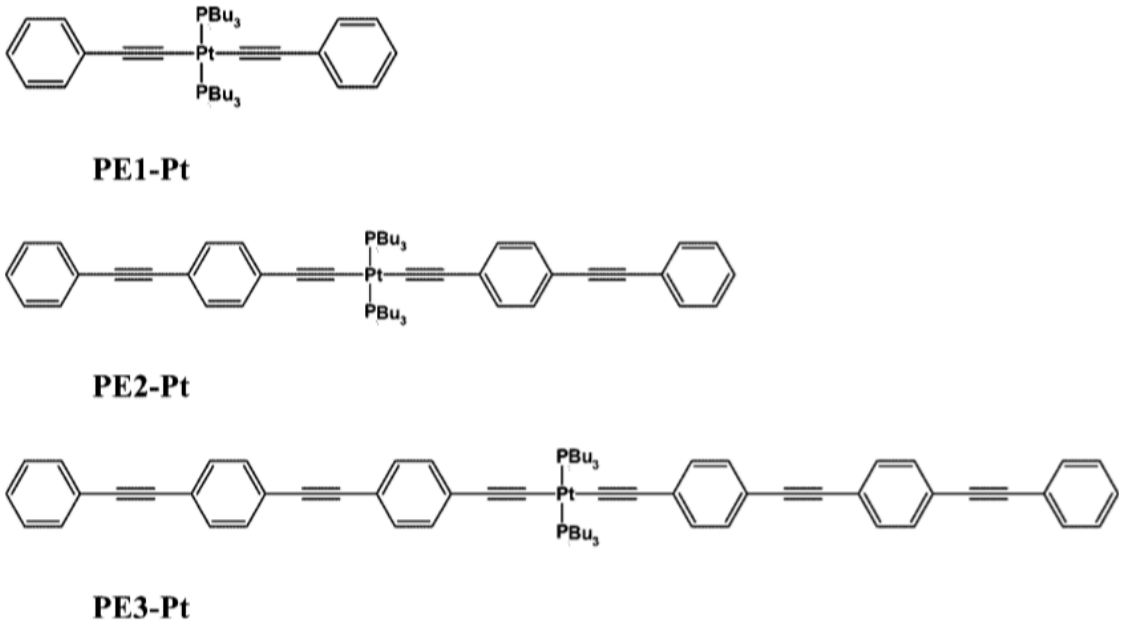

Figure 1.6 Molecular structures of the three symmetrical platinum acetylide complexes, PE1-Pt, PE2-Pt and PE3-Pt. Figure taken directly from source.[55]

In 2008, Ramakrishna et al., reported on a series of three symmetric platinum acetylide complexes, where there was the apparent observation of ISC occurring on a sub 100 fs timescale.[55] In the investigation of the photophysics of these complexes transient absorption and monochromatic fluorescence upconversion were utilised. This study is somewhat of an outlier, with the absence of broadband fluorescence measurements, and for this reason is presented first.

The molecular structures of the three complexes are shown in **Figure 1.6**.

In the transient absorption measurements, each of the three complexes PE1-Pt, PE2-Pt and PE3-Pt, were pumped at their absorption maxima (340, 365 and 380 nm respectively),

and probed in the region of about 400 – 800 nm. The IRF, obtained by fitting of solvent response, was given as around 130 fs. The solutions were stirred during the experiments, and no photodegradation was observed.

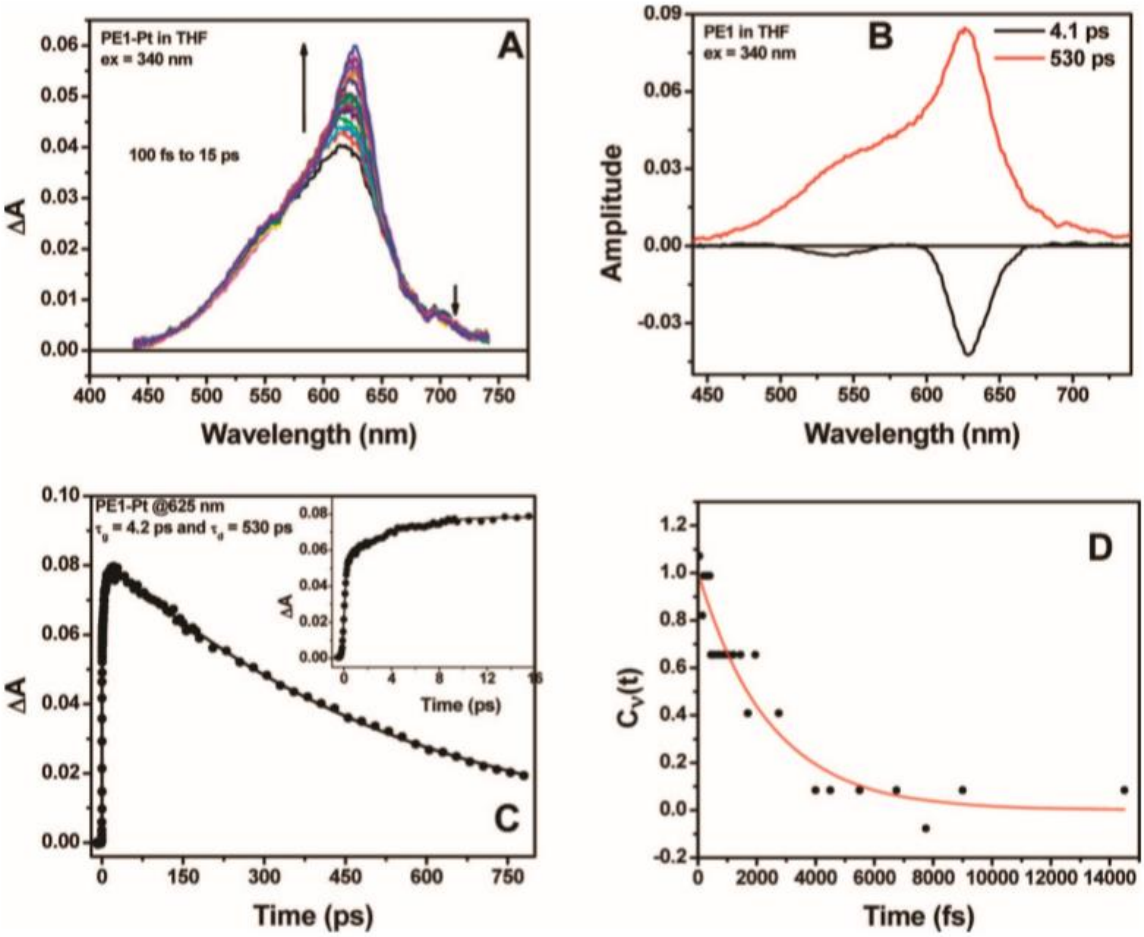

Figure 1.7 (**A**) TA spectra between 100 fs and 15 ps for PE1-Pt, in THF, upon excitation at 340 nm. (**B**) DAS, obtained via global analysis, for the dataset presented in **A**. (**C**) Kinetic traces of the ESA at 625 nm, inset shows expansion of the first 16 ps, showing growth of the signal with a lifetime of 4.2 ps. (**D**) Plot of spectral function of the absorption maxima obtained from the ESA spectra of plot **A**. Figure taken directly from source.[55]

Both spectrally and dynamically the TA data are all very similar for the 3 complexes; spectra and kinetics of PE1-Pt alone are shown for illustrative purposes, see **Figure 1.7**. For all 3 complexes, a single, broad transient signal was observed in the TA spectra. In all cases, this broad absorption grows in with the IRF and exhibits dynamics on the order of a few ps (1.95 – 9.9 ps). These early time dynamics result in minor spectral shifting and shape change, with very little change in the overall magnitude of absorption. The long-lived absorption feature decays mono-exponentially and is assigned as absorption of the lowest energy triplet state in each case, with lifetimes on the order of nanoseconds. It is

suggested that the early time dynamics could be due to either ISC or relaxation of the triplet state.

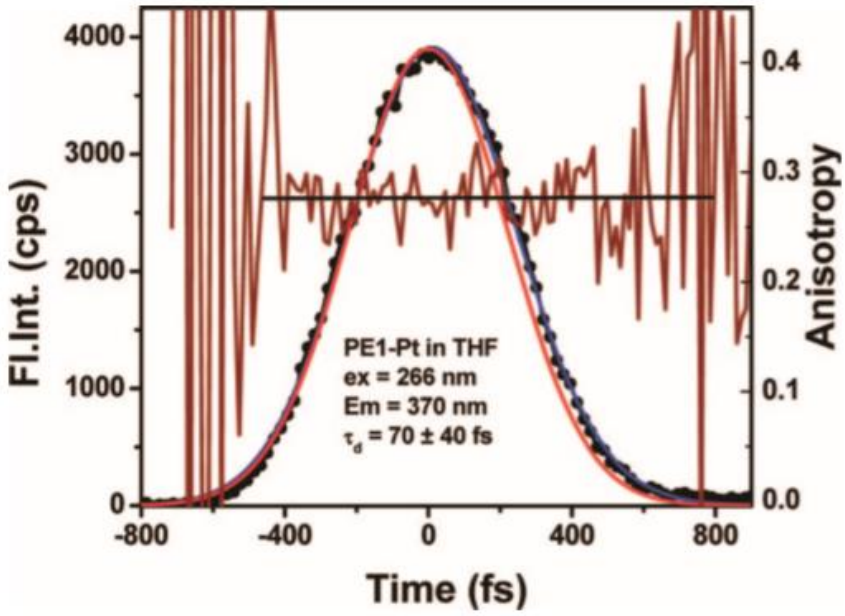

Figure 1.8 A kinetic trace of the emission of PE1-Pt, in THF, at 370 nm, upon excitation with 266 nm. Corresponding anisotropy trace and IRF of the setup are also shown. Figure taken directly from source.[55]

In addition to the TA measurements, monochromatic fluorescence upconversion measurements were also performed, with the hope of aiding in the assignment of the early time (1.95 – 9.9 ps) dynamics. In the fluorescence upconversion experiments, 266 nm pulses were used for sample excitation. Pump pulses were set to magic angle, with respect to the detected fluorescence, using a Berek compensator. Horizontally polarized fluorescence was collected and upconverted in a BBO crystal with gate beams at 800 nm. A monochromator and photomultiplier tube were used to record monochromatic emission, at a few select wavelengths, as a function of time. The IRF for this experiment was determined to be around 350 fs, this value obtained from the fitting of the rise of fluorescence from several dye molecules. A kinetic trace of the emission of PE1-Pt, in THF, at 370 nm is shown in **Figure 1.8**.

For PE1-Pt and PE2-Pt, sub-picosecond decay of the emission at 370 and 420 nm, respectively (70 and 480 fs, respectively) was observed. For PE3-Pt, decay of the emission, at 420 nm, occurred with a 2.1 ps lifetime. 'ISC' lifetimes, along with triplet relaxation lifetimes, are summarised in **Table 1.2**. In the case of PE1-Pt, this lifetime is much shorter than the IRF; around a fifth of the fwhm, 350 fs. In all cases, this lifetime is assigned as

being that of decay of the singlet emission and therefore, the lifetime for ISC. The fast dynamics observed in the TA spectra subsequently being assigned as relaxation of the triplet state formed upon ISC. Time-resolved emission decay was also measured at 350 and 380 nm, in both cases, yielding the same lifetimes of decay.

With ISC, we expect a concomitant, significant decrease in oscillator strength as the highly emissive singlet state is replaced a weakly emitting triplet state. With these monochromatic measurements, it is impossible to determine overall emission intensity of a band, i.e. oscillator strength. If the emission band of the three complexes, probed in the time-resolved emission studies were to shift significantly at early times (sub-picosecond), this could also give the result of rapid decay at the 'probed' fluorescence wavelengths. I.e. these results could also be explained in terms of the emission band shifting rapidly, with these lifetimes (70 fs, 480 fs and 2.1 ps), to lower energy perhaps, with little overall change in emission intensity and therefore oscillator strength. For this set of complexes, broadband fluorescence upconversion measurements would be very useful in the confirmation of the ISC assignment. The broadband measurements would allow for the monitoring of the overall change in emission intensity as a function of time.

Table 1.2 Excited state deactivation observed for platinum acetylide complexes, from time-resolved measurements. Table taken directly from source.[55]

molecule	intersystem crossing (τ_{isc})[a]	minor fluorescence decay[a]	relaxation (τ_{th})[b]
PE1-Pt	70 ± 40 fs (100%)	N/A	4.1 ps
PE2-Pt	480 ± 130 fs (93.5%)	8.0 ± 0.7 ps(6.5%)	4.8 ps
PE3-Pt	2.1 ± 0.15 ps (96.7%)	21 ± 2.0 ps(3.3%)	9.5 ps

[a] From fluorescence upconversion. [b] From transient absorption.

Symmetrical Platinum Acetylide Complexes with Varied Substituents

The effect of functional group substitution on ISC rates was extensively studied with a series of symmetric platinum(II) acetylide complexes by Haley et al.[66] The series of complexes shared common molecular structure, 'Pt-Fl-R', displayed in **Figure 1.9**, each

member of the series featuring a different functional group 'R', spanning a large range of electron withdrawing / donating abilities. Recordings of fluorescence, phosphorescence and ultrafast transient absorption spectra allowed for the determination of ISC rates. Additionally, DFT and TDDFT calculations were used in order to develop an enhanced understanding of the photophysical processes.

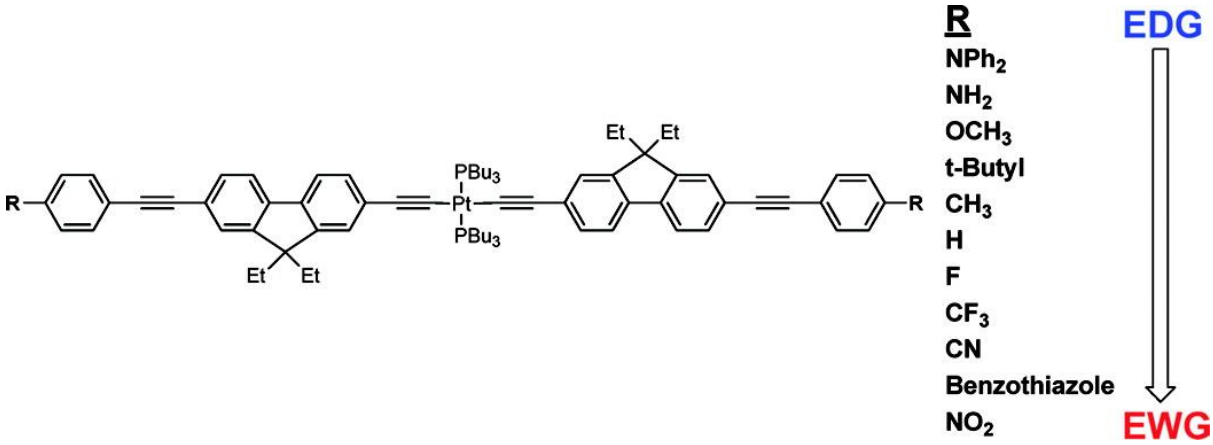

Figure 1.9 General molecular structure of the series of 'Pt-Fl-**R'** complexes. Substituents '**R**' are also listed, ordered with respect to their respective electron donating / withdrawing abilities. Figure taken directly from source.[66]

ISC rates were found to be strongly dependent upon substituent 'R'. **Table 1.3** shows the lifetimes for the vibrational relaxation of, and intersystem crossing from the singlet state populated upon excitation, values obtained from ultrafast transient absorption.

Table 1.3 Absorption maxima ($S_1 - S_{n,max}$), Vibrational relaxation lifetime (τ_{s1}) and Intersystem crossing lifetime (τ_{s2}), for the series of complexes 'Pt-Fl-R'. Values obtained from ultrafast transient absorption and emission measurements. Table adapted from source.[66]

R	$S_1 - S_{n,max}$ (nm)	τ_{S1}(air) (ps)	τ_{S2}(air) (ps)
NH_2	611	0.8 ± 0.3	20.9 ± 18.9
OCH_3	575	2.2 ± 1.8	42.5 ± 19.4
NPh_2	670	0.7 ± 0.3	23.4 ± 9.2
t-Butyl	575	0.8 ± 0.4	25.3 ± 19.3
CH_3	575	0.8 ± 0.5	28.5 ± 22.0
H	575	0.5 ± 0.1	48.5 ± 17.7
F	570	1.2 ± 0.7	30.3 ± 22.3
Bt	645	3.0 ± 2.3	34.4 ± 12.7
CF_3	567	0.8 ± 0.4	12.1 ± 8.5
CN	578	1.0 ± 0.6	17.1 ± 3.7
NO_2	578	1.2 ± 1.2	109 ± 53

A Binuclear Platinum Complex in Various Solvents

In 2010, van der Veen et al,[57] reported on the ultrafast vibrational – electronic relaxation of another platinum complex, the binuclear, $[Pt_2(P_2O_5H_2)_4]^{4-}$ ('PtPOP'), in various solvents. The chemical structure and a simplified potential energy curve scheme are shown in **Figure 1.10**.

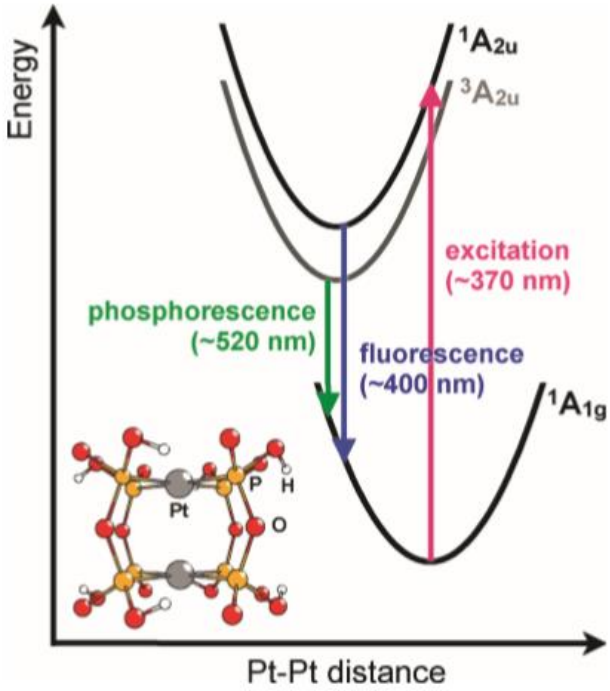

Figure 1.10 Simplified potential energy scheme of the ground state ($^1A_{1g}$) and the lowest-excited states ($^{1/3}A_{2u}$) of PtPOP. Molecular structure of PtPOP is shown bottom left. Figure taken directly from source.[57]

Femtosecond broadband fluorescence upconversion and transient absorption spectroscopy were used in this study. For the transient absorption measurements PtPOP, in various solvents, was excited with ~100 fs, 370 nm laser pulses. With the initial population of the singlet excited state '$^1A_{2u}$'. 315 – 525 nm pulses were used to probe the excited state. **Figure 1.11** shows a representative 2D map of TA data, this particular map is of PtPOP in ethylene glycol.

The TA spectra show excited-state absorption (ESA) bands centred around 335 ('EAS_1') and 460 nm ('ESA_2'). Stimulated emission (SE) from the state $^1A_{2u}$ is seen around 400 nm. The SE band decays with a lifetime of 30.3 ps, while the both ESA red-shift on this same timescale. The decay of the $^1A_{2u}$ SE, leads to this time constant being assigned as the lifetime of ISC between the $^1A_{2u}$ and $^3A_{2u}$ states. The time constants for decay of the SE and therefore ISC, in various solvents are given in **Table 1.4**. Very surprisingly, the rate of

ISC in this complex is found to be strongly dependent on solvent. The rate is almost three times as fast in DMF than it is in ethylene glycol.

For the fluorescence measurements, PtPOP, in various solvents, was excited with ~120 fs, 380 nm laser pulses. Emission between 400 and 440 nm was collected and upconverted, with an IRF of around 190 fs.

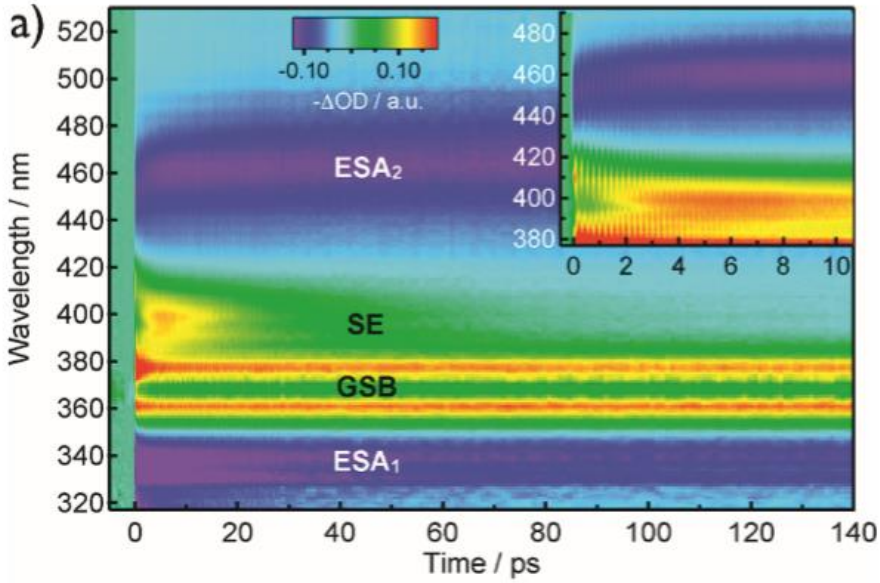

Figure 1.11 A 2D map of the transient absorption spectra of PtPOP in ethylene glycol, excited with a ~ 100 fs laser pulse at 370 nm. The inset shows an expansion of the initial 10 ps. Figure taken directly from source.[57]

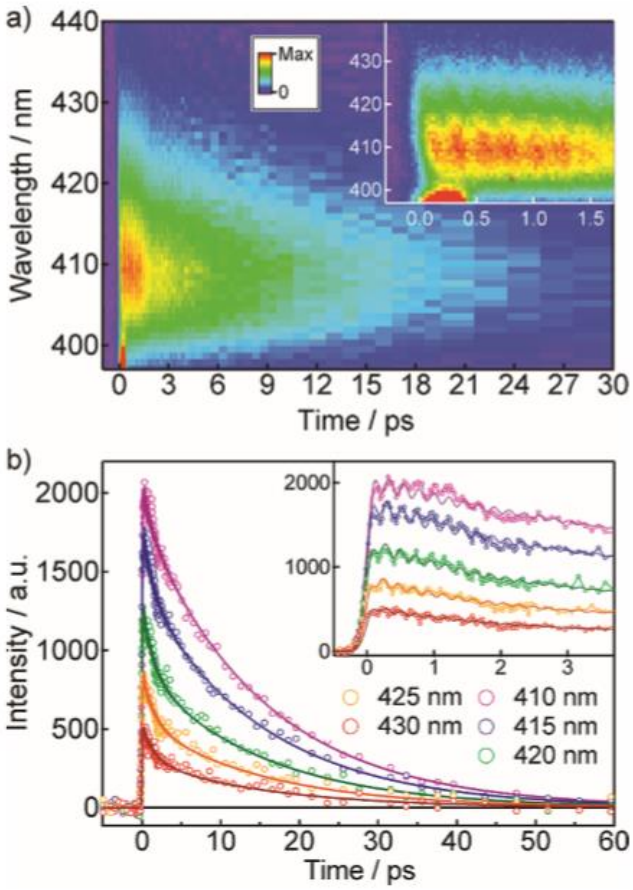

Figure 1.12 (a) A 2D map of the time-resolved emission spectra of PtPOP in water, with excitation at 380 nm (~120 fs). (b) Kinetic traces, at select wavelength (see legend), with fits from global analysis shown as solid lines overlaid on data points. The inset shows an expansion of the initial 3.7 ps time window. Figure taken directly from source.[57]

A 2D map of the time-resolved emission of PtPOP in water, along with kinetic traces at select wavelengths are shown in **Figure 1.12**. A single emission band is observed centred around 400 nm, assigned as emission from the $^1A_{2u}$ state. Oscillations in time can be seen in both insets (inset of 2D map and kinetic traces). These oscillations are attributed to vibrational coherences in the $^1A_{2u}$ state. At all wavelengths sampled, the signal shows bi-exponential decay on the timescale of a few picosecond, attributed to vibrational relaxation. This is followed by mono-exponential decay of the band, attributed to ISC to the $^3A_{2u}$ state. The time constants for ISC, obtained via global analysis of the time-resolved emission data are shown in **Table 1.4**. The values are in good agreement with those obtained via TA spectroscopy.

Further spectroscopic investigations into ISC in PtPOP were made a few years after the initial measurements, were the rate of ISC in MeCN was determined. ISC was found to occur much faster than in the other solvents previously used, see **Table 1.4**. The drastically

increased rate was attributed to the involvement of additional intermediate electronic states, made accessible by the effect of solvent-solute interaction on the energy of said state.

Table 1.4 Comparison of ISC time constants (standard deviations in parentheses) for PtPOP in four different solvents. Constants obtained from the analysis of FLUPS (380 nm excitation) and TA (370 nm excitation). Table adapted from source.[57]

Solvent	τ_{ISC} **/ ps FLUPS**	τ_{ISC} **/ ps TA**
Ethylene glycol		30.3(0.2)
=Ethanol	28.9(0.4)	25.6(0.2)
Water	15.4(0.3)	13.7(0.2)
DMF		11.0(0.1)
MeCN	0.7-0.9	

Iron Polypyridine - $[Fe(bpy)_3]^{2+}$

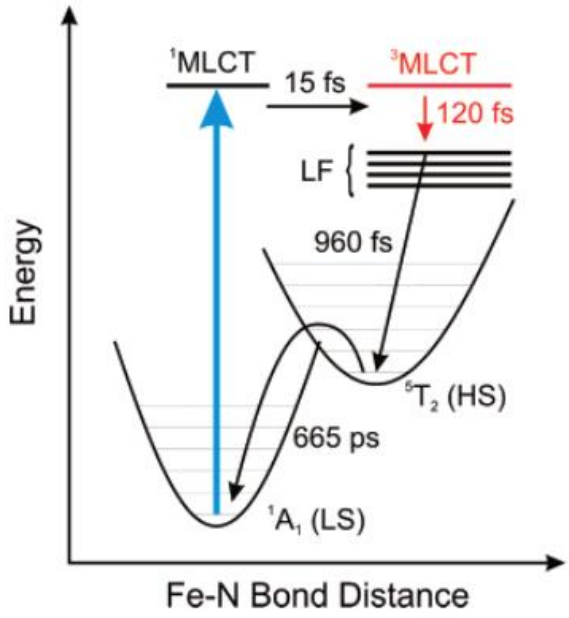

Figure 1.13 The electronic energy levels involved in the photophysical cycle of $[Fe(bpy)_3]^{2+}$ in water, upon excitation at 400 nm (at room temperature). Lifetimes presented in this figure are those obtained in this study. The Fe-N coordinate is only relevant to the ground state ($^1A_1$) and the high-spin state, ($^5T_2$). Figure taken directly from source.[40]

Ultrafast photophysical studies of group 8 polypyridine complexes provide an excellent example of the erratic trends seen in TM complex ISC rates. Iron Polypyridine - $[Fe(bpy)_3]^{2+}$, is discussed here, whilst very similar complexes of Ru and Os, are discussed in the following subsections. Based upon SOC constants of the metal ion alone, a progressive increase in ISC rates going down the group may be expected. However, the studies presented here show this not to be true.

Iron (II)-tris-(bipyridine), $[Fe(bpy)_3]^{2+}$, and its derivatives have been studied extensively, with interest stemming from the low-spin (LS) to high-spin (HS) transition of the *d*-orbitals, which can be induced via temperature/light and reversed via an increase in pressure. This phenomenon shows great potential for use in magnetic data storage and other applications.[67] Iron is a first row transition metal with a SOC constant of 0.05 eV. $[Fe(bpy)_3]^{2+}$ exhibits a strong, broad absorption band in the visible region (λ_{max} = 523 nm), corresponding to a ^{1}MLCT state. The route to optical population of the HS state (quintet state, $^5T_2$) involves excitation into the ^{1}MLCT state, followed by ISC to the ^{3}MLCT state, in turn, followed by ISC into the $^5T_2$ state (see **Figure 1.13**).

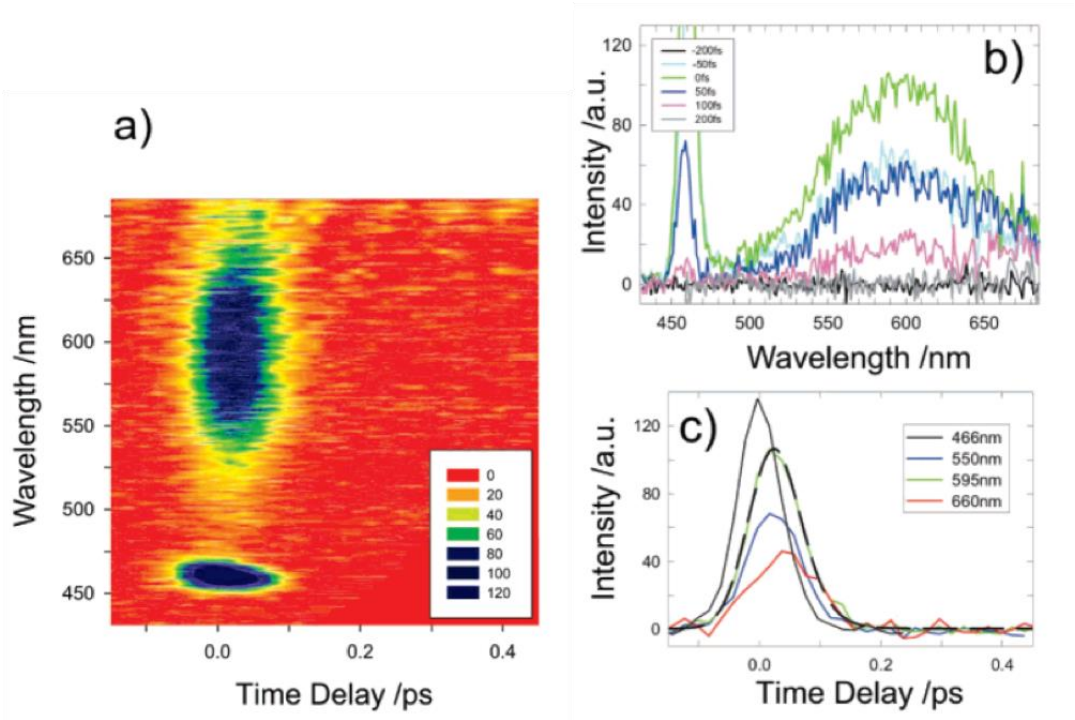

Figure 1.14 (a) A 2D map of the time-resolved emission spectra of $[Fe(bpy)_3]^{2+}$ in water, upon excitation at 400 nm. The signal centred around 460 nm is the Raman line of water. (b) Emission spectra at select time delays (see legend). (c) Kinetic traces at select wavelengths, the 595 nm trace (green) has its fit function overlaid (black). Figure taken directly from source.[40]

A 2D map of the time-resolved emission of aqueous $[Fe(bpy)_3]^{2+}$, upon excitation at 400 nm, alongside spectra at select time delays and kinetic traces at select spectral positions are shown in **Figure 1.14**. Broad emission in the region of 500 – 650 nm, centred at 600 nm, is seen at t = 0 fs. This signal rises and decays with the instrument response function (approximately 120 fs). The band undergoes no change in spectral shape during its decay. Fitting of the kinetic traces at, 466, 550 and 595 nm (see **Figure 1.14 (c)**), with an exponential decay component convoluted with the instrumental response function gives a decay time constant of 20 ± 5 fs. This is assigned as the lifetime of the decay from the ^{1}MLCT state, and therefore the lifetime for ISC between the ^{1}MLCT and ^{3}MLCT states.

A second, weak emission band is seen at $\lambda \geq 650$ nm from around 100 fs onwards (see trace 100 fs of **Figure 1.14 (b)**). This band is assigned as 3MLCT phosphorescence. This band decays with a lifetime of 120 fs, this is attributed to the ISC between the ^{3}MLCT and $^5T_2$ states.

Ruthenium Polypyridine - $[Ru(bpy)_3]^{2+}$

Ruthenium (II)-tris-(bipyridine), $[Ru(bpy)_3]^{2+}$, and its derivatives are perhaps the most widely studied transition metal complexes in terms of their photochemistry and photophysics. $[Ru(bpy)_3]^{2+}$ has a strong absorption band in the visible (λ_{max} = 453 nm, ε = 14,650 $M^{-1}cm^{-1}$ in water) and emits in the red (λ_{max} = 620 nm).[68] The absorption in this region is attributed to the ^{1}MLCT transition, while the emission in the red is attributed to phosphorescence from the ^{3}MLCT state. ISC between these two states is found to occur with near-unity quantum efficiency.[69] Initial ultrafast studies of this complex, performed in the late 1990s, employing femtosecond TA experiments demonstrated that the ^{3}MLCT state in this complex was formed within ∼300 fs of excitation into the ^{1}MLCT state, i.e. a time constant for ISC of <100 fs.[70,71] The experiments involved excitation at 400 nm, this corresponding to an excess in energy of ∼8500 cm^{-1} in relation to a vibrationally cold ^{3}MLCT state, the mechanism for the dissipation of this energy within ∼300 fs still remained unclear. Femtosecond, single wavelength fluorescence upconversion studies,[22] as well as picosecond broadband fluorescence upconversion studies were later performed in an attempt to unravel these early-time dynamics, however, in the former study, emission from the ^{3}MLCT state could not be observed and the latter, with a time resolution of ∼3 ps could not resolve the fast dynamics.[72] Most recently, a broadband fluorescence upconversion setup, capable of monitoring emission in the 440 – 690 nm range, with a time resolution ∼110 fs has been used to study the ES dynamics of $[Ru(bpy)_3]^{2+}$.[51]

A 2D map of the time-resolved emission of aqueous $[Ru(bpy)_3]^{2+}$, alongside spectra at select time delays, are shown in **Figure 1.15**. An intense emission band, centred at 18,500 cm^{-1}, grows in with the instrument response function. This band decays rapidly, within tens of femtoseconds, revealing a weaker emission band centred at 16,300 cm^{-1}. The initial intense band is assigned as emission from the ^{1}MLCT state. Fitting of the decay of this band leads to the assignment of an ISC rate of with a lifetime of < 30 fs.

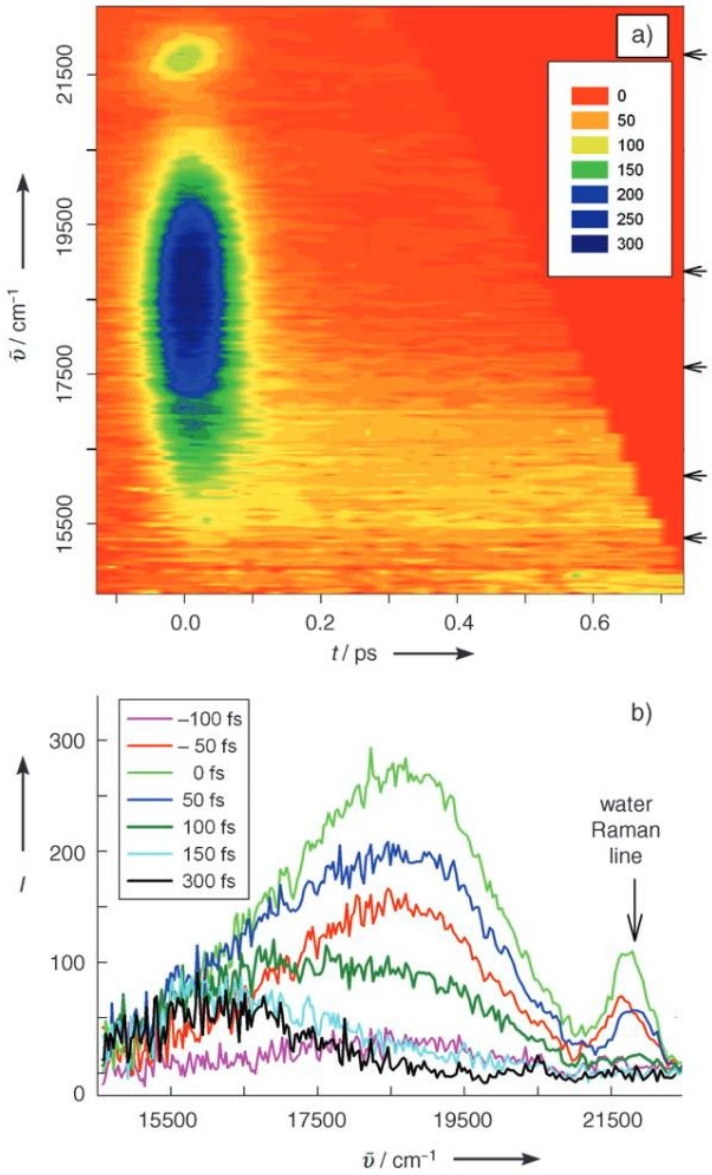

Figure 1.15 (a) A 2D map of the time-resolved emission spectra of $[Ru(bpy)_3]^{2+}$ in water, upon excitation at 400 nm. The signal centred around 460 nm is the Raman line of water. (b) Emission spectra of $[Ru(bpy)_3]^{2+}$ in water, upon excitation at 400 nm, at select time delays (see legend). Figure taken directly from source.

Osmium-Polypyridine Complexes

As mentioned above, the absorption maxima of ruthenium polypyridine complexes lie in the green region. For applications based upon solar energy harvesting, it would be favorable to extend absorption down towards the red region where solar light is more intense. Osmium polypyridine complexes exhibit broader absorption spectra relative to related ruthenium complexes and are therefore of interest in these applications.[73] Based upon the increase in SOC from ruthenium (0.1 eV) to osmium (0.37 eV), an enhancement

in ISC rates could be expected in polypyridine complexes of the latter. This however, upon investigation of ISC in these complexes, was found to not be the case.

In 2013, ISC rates for two closely related Os-polypyridine, $Os(dmbp)_3$ (**Os1**) and $Os(bpy)_2(dpp)$ (**Os2**), were reported upon, by Bräm et al.[54] The study used femtosecond broadband fluorescence upconversion in the determination of the ISC rates. For both complexes, ISC was deemed to occur in sub-100 fs. Molecular structures, alongside absorption and emission spectra, for the two complexes are shown in **Figure 1.16**.

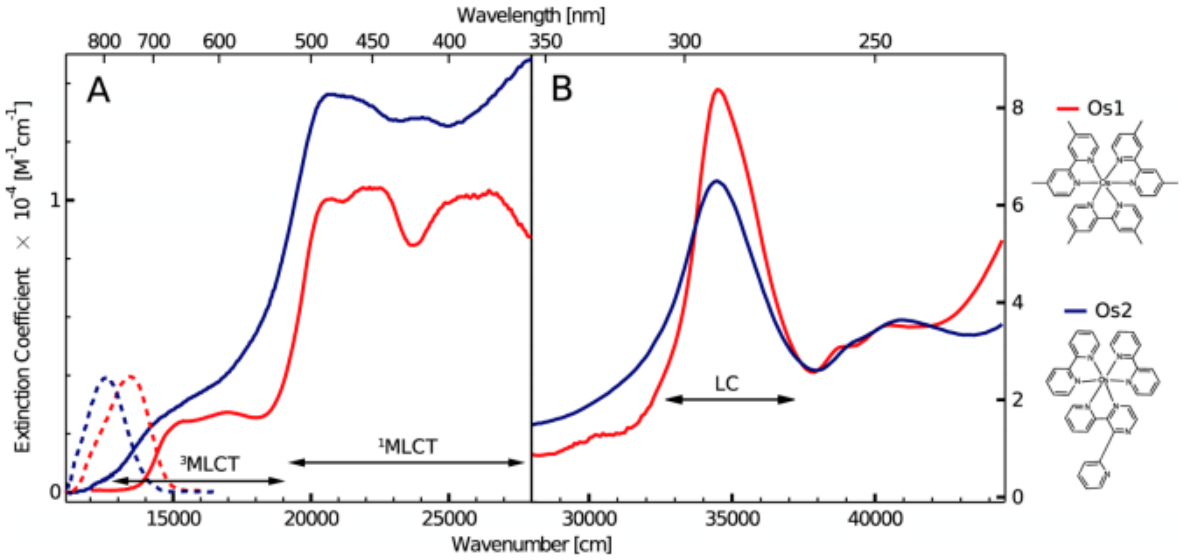

Figure 1.16 Extinction coefficients are shown as solid lines, steady-state emission, upon 480 nm excitation, are shown as dashed lines, for **Os1** (red) and **Os2** (blue), in ethanol solutions. Band assignments are indicated by the black arrows. The molecular structures for both complexes are shown to the right. Figure taken directly from source.[54]

Both complexes exhibit multiple absorption bands spanning 200 – 800 nm. Bands in the region of 300 – 500 nm are assigned as ^{1}MLCT transitions for both complexes, while the weaker bands in the region of 500 – 800 nm are assigned as ^{3}MLCT transitions. Although weaker than the ^{1}MLCT transitions, the relative integrated intensity of the ^{3}MLCT transitions, with respect to that of the corresponding singlet states are much larger than in $[Ru(bpy)_3]^{2+}$ or $[Fe(bpy)_3]^{2+}$ complexes, this is attributed to a stronger mixed singlet – triplet character of the triplet state as a consequence of the larger SOC of osmium.

The steady-state emission spectra of both complexes are shown as dashed lines in **Figure 1.16**. Single, broad structureless bands are exhibited for both complexes. With emission maxima at 740 and 795 nm for **Os1** and **Os2** in ethanol, respectively. In both cases, this emission is assigned as phosphorescence from the lowest-energy ^{3}MLCT state.

Time-resolved emission spectra, at select time delays, for **Os1** and **Os2** are shown in **Figure 1.17**.

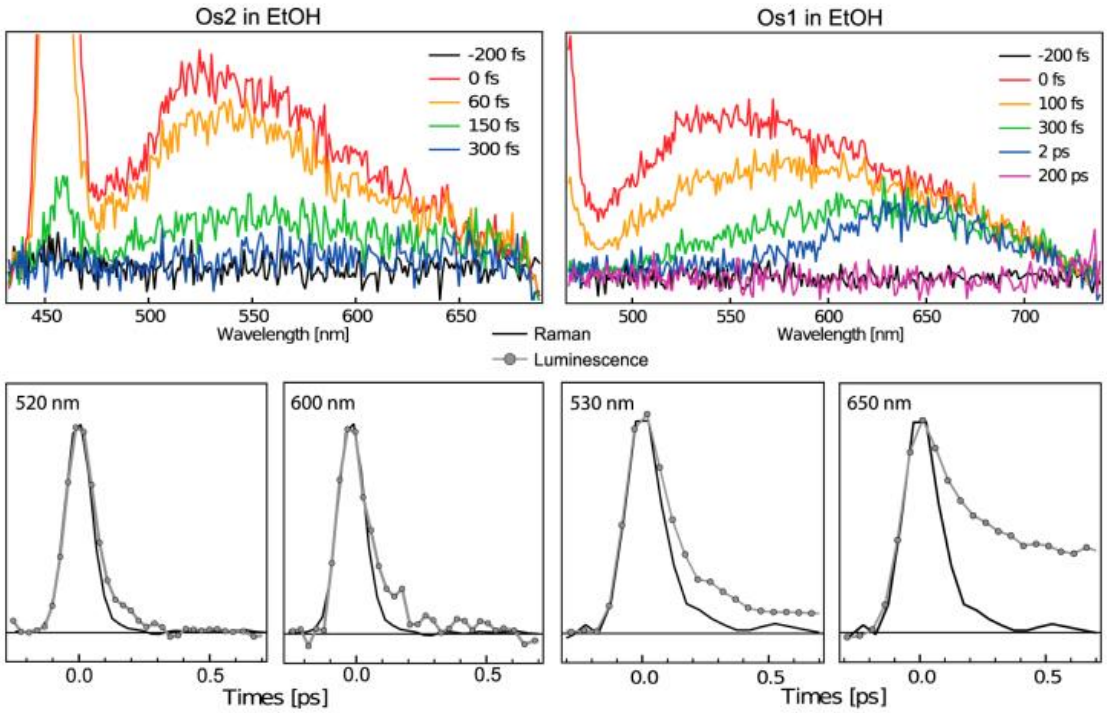

Figure 1.17 Top panels: time-resolved emission spectra of **Os2** (left) and **Os1** (right), in ethanol solutions. Recorded at time delays between -200 and 300 fs, with additional points at 2 and 200 ps for **Os1**, see legend for labels. Bottom panels: kinetics traces at select spectral positions, for better comparison of kinetic behaviour, kinetic trace for the Raman line at 453 nm is shown in each case. Figure taken directly from source.[54]

At the earliest times recorded, growing in with the IRF, both complexes show a broad emission band centred at 530 – 550 nm. The early time emission is mirror symmetric with respect to the lowest-energy singlet absorption band is attributed to singlet fluorescence. In each case, this emission decays bi-exponentially with time constants of <50 fs and 150 fs for **Os2**, and 100 fs and 1.5 ps for **Os1.** In both complexes, around 90% of the signal at 530 – 550 nm decays within approximately 100 fs. The <50 fs and 100 fs time constants are assigned as ISC between the ^{1}MLCT and ^{3}MLCT states, for **Os2** and **Os1** respectively. In addition to the short-lived ^{1}MLCT fluorescence, **Os1** exhibits a second emission band, centred at around 650 nm. This band decays mono-exponentially with a time constant of 50 ps. This is attributed to emission of an intermediate triplet state, not the lowest-energy triplet state observed in the steady-state emission, which decays with a lifetime of 25 ns. The differing rates of ISC in these two very structurally similar complexes are further evidence that the magnitude of SOC constant of the metal centre alone, is not sufficient

in explaining ISC rates. The lack of an intermediate emissive triplet state and faster ISC rate in Os2 are rationalised as being a result of the higher density of states present within the MLCT manifold.[54]

Rhenium Carbonyl – Bipyridine Complexes

A strong dependence of ISC rates on ligand substitution was clearly demonstrated in a study performed on a series of rhenium complexes.[53] The complexes were of general formula $[Re(L)(CO)_3(bpy)]^n$ (L = Cl, Br, I, n = 0; L = 4-Et-pyridine, n = 1+). The SOC constant of rhenium is 0.335 eV, larger than that of Fe (0.05 eV) and Ru (0.1 eV), and comparable to that of Os (0.37 eV). The presence of the halide ligand in each complex, may also be expected to enhance SOC, with increasing effect upon going down the group (Cl, Br then I). However, ISC was found to occur on timescales of 85 – 150 fs, significantly slower than observed in similar complexes of Fe and Ru. **Figure 1.18** shows the general molecular structure of the series of $[Re(L)(CO)_3(bpy)]^n$ complexes where L = Cl, Br, I, n = 0; L = 4-Et-pyridine, n = 1+

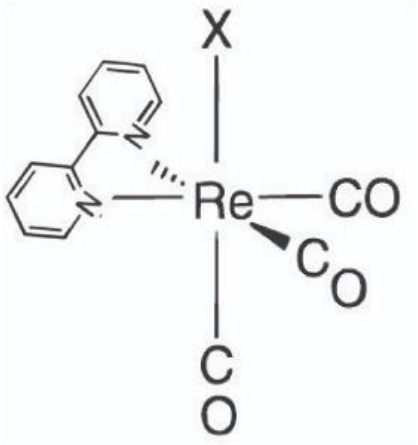

Figure 1.18 General molecular structure of the series of $[Re(L)(CO)_3(bpy)]^n$ complexes where L = Cl, Br, I, n = 0; L = 4-Et-pyridine, n = 1+. Figure taken directly from source.[53]

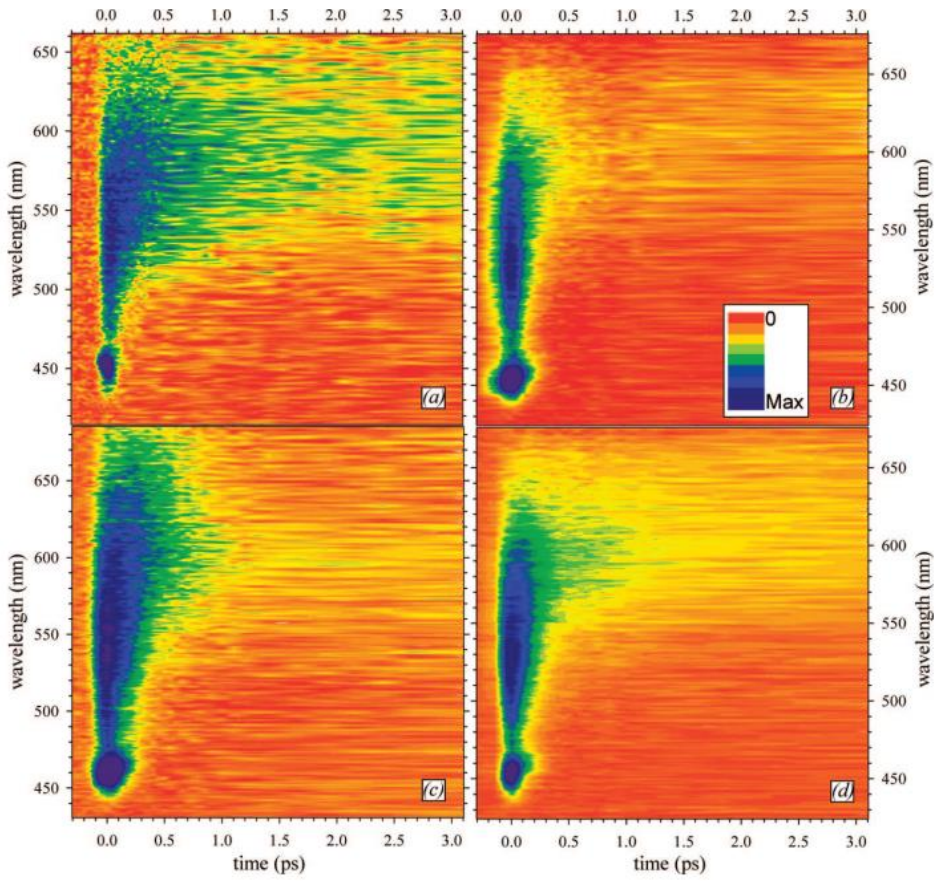

Figure 1.19 2D maps of the time-resolved emission spectra of $[Re(L)(CO)_3(bpy)]^n$ in CH_3CN, upon excitation at 400 nm. (a): L = Etpy; (b): L = Cl; (c): L = Br; (d): L = I. Intensity represented by colour, see inset of (b). The peak seen in all maps at 457 nm, is due to Raman scattering by the solvent. Figure taken directly from source.[53]

Femtosecond broadband fluorescence upconversion was the primary tool used in the determination of the ISC rates. 2D maps of the time-resolved emission for the four complexes are shown in **Figure 1.19**.

Measured rates of ISC scale inversely with the spin – orbit coupling constant of the varied ligand but show good correlation with the vibrational periods of the Re – L stretching mode. These results allude to the importance particular vibrational modes can have in the mediation of ultrafast ISC.

1.4.3 Summary of ISC Rates in TM Complexes

Table 1.5 summarises the ISC lifetimes for the complexes discussed above, with the addition of ISC lifetimes for complexes not reviewed here. Spin-orbit coupling constants for the central metal atom are also given. The complexes are arranged, in ascending order, with respect to the spin-orbit coupling constant. With the complexes presented, it is apparent that the rate of ISC does not scale with the spin-orbit coupling (SOC) constant alone. Trends, however, are observed. For the $[ReX(CO)_3bpy]^+$ series, ISC is seen to scale with the inverse of the period of the Re-L bond stretching vibration, indicating the importance of vibrational coupling w.r.t. ISC. Most relevant to the work presented in chapters 3 and 4, of this thesis, are the two platinum(II) acetylide series. Interestingly, these platinum complexes exhibit some of the slowest ISC rates, whilst also having the highest SOC constants of all the metals discussed. Clearly, the relationship between ISC and molecular is a complex one.

Table 1.5 Table of ISC lifetimes and spin-orbit coupling constants (eV), alongside literature references, for the TM complexes discussed above. Additional data for TM complexes not discussed in review are also added.

Complex	ISC lifetime	Spin-Orbit coupling constant (eV)	Reference
$Cr(acac)_3$	<100 fs	0.027	ef[38,39]
$[Fe(bpy)_3]^{2+}$ (^{1}MLCT to ^{3}MLCT)	≤30 fs	0.050	Ref[40]
$[Fe(bpy)_3]^{2+}$ (^{3}MLCT to ^{5}T)	~130 fs	0.050	Ref[41,42]
$[Fe(tren(py)_3)]^{2+}$ (^{1}MLCT to ^{5}T)	~190 fs	0.050	Ref[43]
$[Fe(phen)_3]^{2+}$ (^{3}MLCT to ^{5}T)	~220 fs	0.050	Ref[45]
Fe-porphyrins	~150 fs	0.050	Ref[74]
$Mo_2(O_2C$-9-anthracene)	~10 ps	0.07	Ref[65]
$[Cu(dmphen)_2]$ (S_1 to T_1)	7.4 ps	0.1	Ref[47]
$[Ru(bpy)_3]^{2+}$	≤30 fs	0.1	Ref[51]
RuN719	≤30 fs	0.1	Ref[52]
RuN3	≤45 fs	0.1	Ref[52]
ZnTPP	4 – 160 ps	0.150	Ref[49]
Pd(thpy)2 (S_1 to T_1)	~800 ps	0.173	Ref[75]
$ReX(CO)_3bpy]^+$		0.335	Ref[53]
x = Cl	85 fs	0.355	Ref[53]
x = Br	130 fs	0.355	Ref[53]
x = I	150 fs	0.355	Ref[53]
x = etpy	130 fs	0.355	Ref[53]
PEn-Pt (see Table 1.2)	~70 – 2100 fs	0.583	Ref[55]
Pt-Fl-R (see Table 1.3)	12.1 – 109 ps	0.583	Ref[66]
$[Pt(^tbut_3$-trpy)PMI(PF_6)	~170 – 300 fs	0.583	Ref[76]
$Pt(thpy)_2$	~50 fs	0.583	Ref[77]
$Pt(Br)_6$	<150 fs	0.583	Ref[58]
Pt_2POP (solvent dependent, see Table 1.4)	~0.8 – 30 ps	0.583	Ref[57]

1.5 Experimental techniques

The primary aim of the research presented in this thesis is to develop an understanding of the ultrafast processes proceeding the excitation of molecules, in solution, into higher energy excited states of some form or another. This enhanced understanding, in theory, allows for better design, attaining more useful, better 'fit for purpose' chemicals. Electromagnetic spectroscopy, the study of the interaction of light with matter, is the method of choice in the observation and characterisation of these ultrafast happenings. The use of various portions the electromagnetic spectrum, from ultraviolet to the infrared, allows the probing of a vast array of states and transitions within the molecules of interest. Ultrashort laser pulses, down to < 100 fs, allow for the temporal resolution of these processes which occur over extremely short periods of time.

1.5.1 Building the Foundation: Steady-State Spectroscopy & Other 'Slow' Techniques

Interpretation of the results of the various ultrafast spectroscopic techniques would be virtually impossible without some prior knowledge of the systems electronic and vibrational energy levels. 'Steady-state' spectroscopic techniques allow for the interrogation of the energy levels, and transitions, accessible from the ground-state, i.e. the system at equilibrium. Firstly, a brief review of some of the basic laws of principles surrounding these spectroscopic techniques is presented.

The Beer-Lambert Law

Essential to the interpretation of the results of absorption techniques in general, is an understanding of the Beer-Lambert law. The Beer-Lambert law describes the process of absorbance, that is, the attenuation of radiation by a medium. Two forms of the Beer-Lambert law are presented here, see **equation 1.5** and **equation 1.6**.

$$-\ln\frac{I}{I_0} = \sigma l N$$

equation 1.5

$$A = -\log\frac{I}{I_0} = \varepsilon l c$$

equation 1.6

Here, I is the intensity of light after transmittance by a medium, I_0 is the initial intensity of light, σ is the absorption cross-section area, l is the total path length of the sample, N is the density of absorptive species, A is absorbance (also known as optical density (OD)), ε is the molar extinction coefficient and c is the concentration of absorptive species.

Spectrometers allow for the measurement of I and I_0 and hence calculation of A. If the concentration of sample, c, is known, then the molar extinction coefficient, ε, may also be calculated (it is assumed path length, l, is also known). Conversely, if the absorbance of a sample of known ε is measured, the concentration of said sample may be calculated.

Steady-State UV-Vis Absorption and Emission Spectroscopy

Steady-state UV-Vis absorption spectroscopy yields information on the electronic energy levels accessible from the ground-state as well as the ground-state itself. The absorption of a photon, by definition, leads to the population of a Franck-Condon (FC) state, thus these are the states probed with such a technique.

The lowest-energy electronic excited-states typically lie 1.5 – 6 eV above the ground-state (this corresponds to around 830 – 200 nm). UV-Vis absorption spectroscopy entails measuring the degree of attenuation of light as a function of spectral position, typically in the region of 200 – 800 nm.

The spectral position, and thus transition energy, of an absorption band allows for some information to be inferred. Additionally, the oscillator strength of a transition may aid assignment. π-π^* transitions centred on organic ligand fragments typically occur in the spectral region of 200 – 350 nm with high oscillator strengths.

MLCT transitions are typically lower in energy than π-π^* transitions and lie in the visible region, around 350 – 800 nm. MLCT absorption are often broad, typically composed of multiple electronic transitions, between different metal d-orbitals and ligand-centred π^* orbitals.

Steady-state emission spectroscopy can be used to probe radiative excited-states. Steady-state emission spectroscopy is effectively an integral over all time. Steady-state emission spectroscopy is ‘slow’ relative to molecular relaxation, typically the spectra will be dominated by the lowest-energy emissive state, and information on the earliest

populated emissive states is effectively averaged out. Emission bands are usually red-shifted relative to that of the corresponding absorption band, this ‘stokes shift’ can provide information on the relaxation, both intramolecular and w.r.t the solvent, of the molecule after population of FC excited-states.

Steady-State Infrared Absorption Spectroscopy

The vibrational energy levels of any given electronic state are typically separated by 0.01 – 0.45 eV, this corresponds to transitions in the mid-IR region. Steady-state infrared absorption spectroscopy is usually performed using the interferometric Fourier-Transform IR (FTIR) method. As if with UV-Vis absorption above, the spectral position and oscillator strengths of IR absorption bands allow for the inference of information pertaining to the vibrational transitions and therefore the types of bonds present within a system. The transition energy and therefore spectral position will be dependent upon the strength of bond probed. For an IR transition to be allowed, a change in dipole moment must occur upon transition, i.e. fully symmetric bond stretches are IR inactive.

1.5.2 Ultrafast Spectroscopy: Pump-probe techniques

Perhaps the most important tools in the study of molecular, ES dynamics are pump-probe spectroscopic techniques. In general, a pump-probe technique will utilise a sequence of two or more pulses of laser radiation. A 'pump' pulse will excite a specific molecular transition. A 'probe' pulse will then examine the resultant spectroscopic changes. Pump-probe data is typically presented as difference spectra, that is, spectra are recorded with and without the 'pump' pulse, and the difference is calculated. By probing the system at multiple different time delays between the pump and probe, kinetic information is obtained. A simplified pump-probe scheme is shown in **Figure 1.20**.

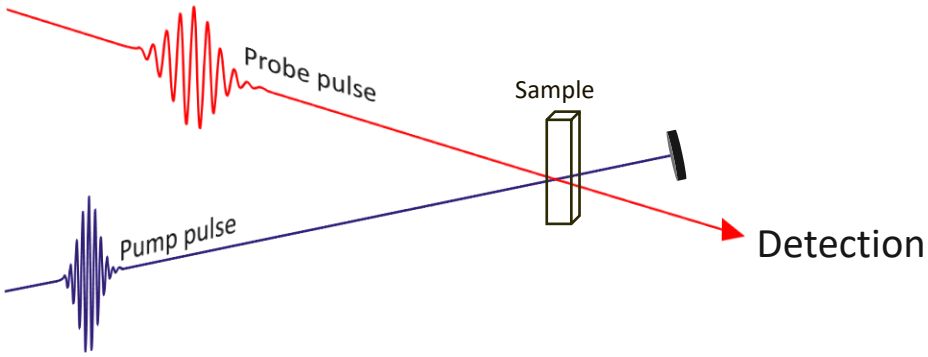

Figure 1.20 A simple schematic of pump-probe spectroscopy. The pump and probe pulses pass through a cuvette containing a sample, the pulses are spatially overlapped when incident upon the sample. The pump pulse is blocked after exciting the sample. The probe pulse is directed towards the detection equipment.

The use of laser radiation in pump-probe spectroscopy offers many advantages over conventional light sources. These include:

- Narrow spectral width, allowing selective pumping of specific transitions.
- Narrow temporal width, allowing observation of processes occurring on very short timescales, i.e. vibrational relaxation and vibrational energy transport.
- Highly tuneable spectral position, giving access to a wide range of molecular transitions.

The temporal width of the laser source is of particular importance. The time-scales accessible by a technique are determined by the instrument response function (IRF), the IRF is a convolution of the temporal width of the pump and probe pulses. Here TA, TRIR and 2DIR are discussed. Time-resolved emission by method of upconversion is discussed in more detail in the next chapter.

Time-Resolved UV-Vis Absorption ('Transient Absorption, TA') Spectroscopy

Perhaps the most widely used pump-probe technique, transient absorption spectroscopy, involves the excitation of a population of molecules, within a sample, into electronic excited-states via a narrowband, temporally short, UV-Vis pump pulse, and the probing of the subsequentially populated states, at some time delay τ, via a broadband, temporally short, UV-Vis probe. Measurement of the total absorption of the sample, both with and without excitation, allows for the calculation of a difference absorption spectrum, effectively the spectrum of the sample in the excited state minus the spectrum of the sample in the ground. The difference absorption, i.e. the change in absorption is denoted ΔA.

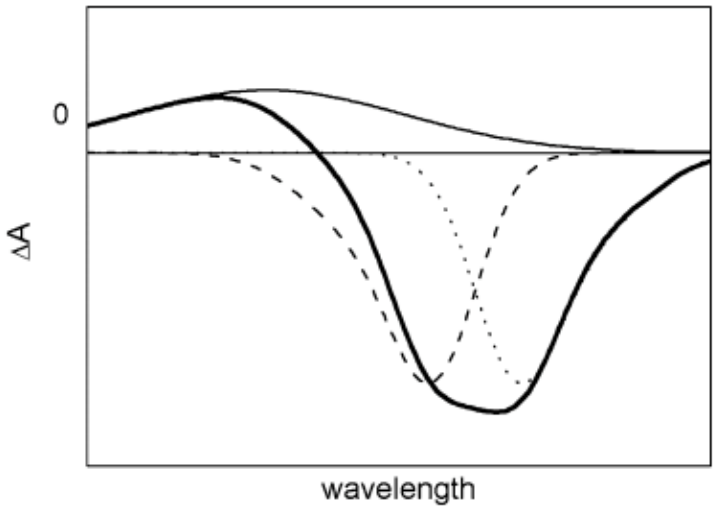

Figure 1.21 The various contributions to a ΔA spectrum: ground-state bleach (dashed line), stimulated emission (dotted line), excited state absorption (thin black line) and the sum of all the contributions (thick black line). Taken from reference.[72]

Difference absorption spectra will typically be comprised of 3 types of signals:

1. Depletion of ground-state population upon photoexcitation leads to less ground-state absorption with the pump than without the pump. A negative signal is observed where the ground-state absorbs, a so-called ground-state bleach (GSB) see **Figure 1.21** (dashed line).
2. The probe pulse will induce stimulated emission (SE) from the excited-state, where the transition is optically allowed, this results in an increase in intensity of light, at

emission wavelengths, at the detector, this is equivalent to a loss of absorption and results in a negative signal in the ΔA spectrum, see **Figure 1.21** (dotted line).

3. The generation of a population of excited-state molecules upon photoexcitation leads to excited-state absorption (ESA), see **Figure 1.21** (thin solid line).

The electronic transitions available to each electronic excited-state will be unique; each excited-state, will have unique ESA. The measurement of ΔA, and therefore ESA, as a function of time allows for the monitoring of the excited-state evolution. The change in absorbance, from a particular excited-state, is proportional to the change in concentration of said state, this relationship is given by Beer-Lambert law, see **equation 1.5** and **equation 1.6** above**.** Additionally, the recovery of the ground-state absorption, provides dynamic information, revealing the fate of excited molecules.

Decomposition of the ΔA into components corresponding to each of the excited-states populated on the route from excitation back to ground state allows for a better understanding of the excited-state dynamics. The method by which entire spectra are decomposed into spectral and kinetic components is known as global analysis. Global analysis is used in the interpretation of numerous time-resolved spectroscopic techniques and is discussed below.

Time-Resolved Infrared Absorption ('TRIR') Spectroscopy

A closely related technique to that of TA spectroscopy, time-resolved infrared absorption spectroscopy, is used to monitor excited-state dynamics upon photoexcitation by the probing of changes in IR-active vibrational transitions as a function of time. As with TA, a narrowband, temporally short, UV-Vis pump pulse is used to excite a population of a sample into the excited-state. A broadband, temporally short, IR probe is used to probe vibrational transitions of the excited states populated. As with TA, measurements with and without the pump pulse are made, and ΔA is calculated. The recording of ΔA as a function of time, that is, by altering the delay time τ between the pump and probe pulses, kinetic information is obtained. TRIR is complementary to TA and can provide additional structural information not obtainable by TA alone. The strength of molecular bonds and therefore the energy of vibrational transitions is highly dependent on the distribution of

electron density within a molecule. Therefore, TRIR may allow for a better understanding of types of electronic excited states populated.

Ultrafast Two-Dimensional Infrared ('2DIR') Spectroscopy

Each electronic state of a molecule will have its own unique equilibrium geometry (i.e. the lowest energy structural conformation), as the absorption of light occurs on the timescale of ~10^{-15} s, which is effectively instantaneous relative to the timescale of structural changes, the electronic excitation is likely to form an excited species far from its equilibrium geometry. As a result, the electronic excitation will typically be accompanied by vibrational excitation of various modes associated with the geometric distortions between the two involved electronic states. This simultaneous excitation of both electronic and vibrational state is termed a 'vibronic' transition. This phenomenon is summarised in the Franck-Condon principle.

The population of higher vibrational levels is energetically unfavourable, and the dissipation of the excess energy will begin immediately after excitation. The initially excited, high-frequency, vibrational modes will begin to relax, redistributing the energy amongst the low-frequency modes in the spatial vicinity, this process is termed intramolecular vibrational redistribution (IVR). In the solution phase, these transitions will be mediated by the solvent molecules, accounting for energy differences between modes and allow relaxation on the timescale of 10^{-14} to 10^{-10} s. Following the IVR will be the process of 'vibrational cooling' where any excess vibrational energy is transferred to the 'solvent bath', i.e. the energy is dissipated as heat. IVR and vibrational cooling are collectively known as vibrational relaxation (VR). Both IC and ISC processes will also result in the population vibrational excited states and are therefore also followed by VR.

IVR and vibrational cooling also occur in the electronic GS. The excitation of a specific vibrational mode via the absorption of infrared light will trigger the VR processes.

Vibrational energy transport within molecules may be essential in meditating transitions between electronic states and may also have significant effects on the rates and pathways of electron transfer.[78,79] Understanding the relationship between molecular structure and vibrational couplings within metal complexes may allow for better design, optimising the rates of electron transfer.

Before examining the VR processes in the ES, it is beneficial to develop an understanding of the vibrational couplings and dynamics present in the GS. Two-dimensional infrared (2DIR) spectroscopy is the ideal tool for studying for such processes, allowing the

excitation of various specific modes within a molecular system, and the probing of the consequential VR.

Two-dimensional infrared spectroscopy utilises a spectrally narrow (narrowband) infrared pulse to pump specific vibrational modes, followed by a spectrally broad (broadband) infrared pulse to probe the response of multiple vibrational modes within the system. Scanning the narrowband pump pulse across all of the vibrational modes of interest allows the generation of a 2D map. An example 2DIR map is shown in **Figure 1.22**, taken from literature.[80]

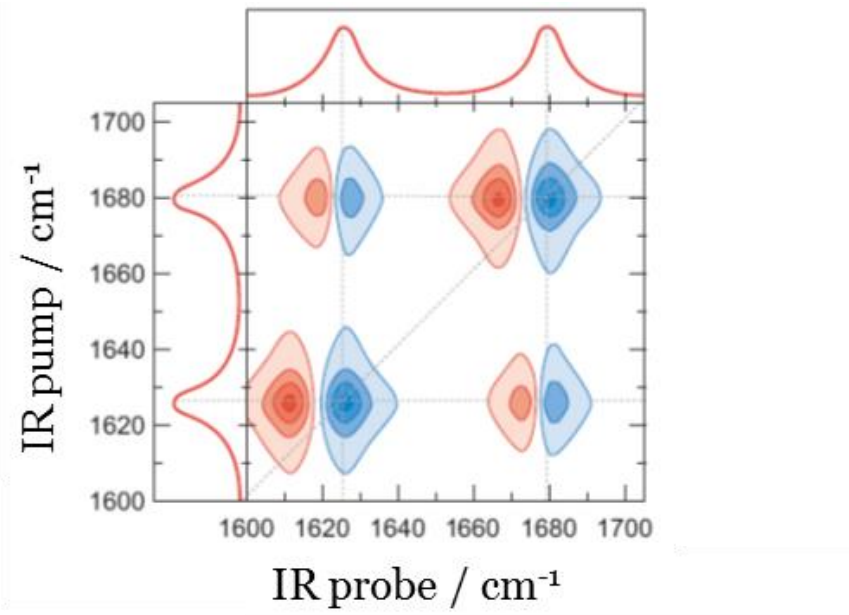

Figure 1.22 A 2DIR map of $Rh(acac)(CO)_2$. Negative signals, corresponding to GS bleach and stimulated emission, are shown in blue. Positive signals, corresponding to ES absorption, are shown in red. Spectrum taken from literature.[80]

The signals along the diagonal line show the response of a mode to the pumping of that same mode, known as the 'self-response'. The signals off of the diagonal line show the response of a mode, to the pumping of another mode in the system, known as 'crosspeaks'. As described above in the introduction to pump-probe spectroscopy, spectra are recorded with and without the pump pulse. In the case of 2DIR, the 'pump-off' spectra, should effectively be identical to a steady-state FTIR spectrum, i.e. the bleaches we see in 2DIR maps (the blue features) should correspond to bands in the FTIR. The positive, transient, signals we see in the 2DIR map are the signals observed as a response to the pump pulse. The self-response bleach signals are due to the loss of population of the $v = 0$ vibrational state upon excitation. The self-response transient signals are due to

the increase in population of the $v = 1$ vibrational state upon excitation. The vibrational anharmonicity is responsible for differing spectral positions of bleaches and transients, i.e. the $v = 1 \leftarrow 0$ transition is a larger energy transition than the $v = 2 \leftarrow 1$ transition and therefore appears at higher energy (higher wavenumber).

The crosspeaks appear in 2DIR spectra due to the interactions between different vibrational modes within the molecule, i.e. the probed vibrational mode is disturbed by the excitation of the pumped mode. There are multiple mechanisms by which different modes may interact. Two mechanisms relevant to the molecules of interest here are shown in **Figure 1.23**.

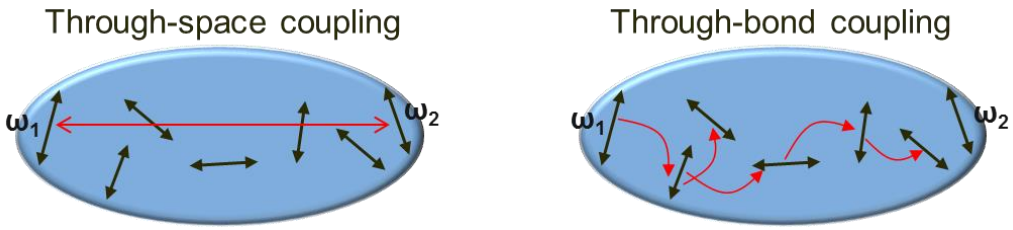

Figure 1.23 Two mechanisms for the coupling of two different vibrational modes. The left-hand side diagram shows a through-space coupling, which is a dipole-dipole interaction. The right-hand side diagram shows a through-bond interaction, where intramolecular vibrational energy redistribution from one mode towards another, results in the mechanical disturbance of the second mode.

Through-space coupling is the interaction of one dipole in a molecule with another dipole in the molecule, i.e. two bonds. The excitation of a mode will result in an oscillating dipole, different in nature to that of the GS. This change in one mode will result in the disturbance of any modes coupled to this in a dipole-dipole fashion. With through-space coupling energy transfer occurs between the two modes, the $v = 1 \leftarrow 0$ transition is populated and a transient signal arising from the $v = 2 \leftarrow 1$ transition appears at lower energy. Through-space interactions are effectively instantaneous, i.e. the crosspeak response dynamics will be identical to the self-response dynamics.

Through-bond coupling arises from intramolecular vibrational energy redistribution. Through-bond coupling is also known as 'low-frequency-assisted' coupling. Energy is transferred from the initially populated vibrational mode to low-frequency modes in the spatial vicinity, and then propagates via other low-frequency modes across the molecule.

If vibrational energy reaches a probed high-frequency mode, a mechanical disturbance will be felt and a crosspeak will be seen.

Recording 2D spectra at multiple time delays allows the determination of rates of vibrational energy transport. The analysis of 2DIR spectra are discussed in several publications.[78,81–83]

1.5.3 Determination of Kinetic Parameters and Global Analysis

The lifetime of an excited-state species, τ, is defined as the time taken for the concentration of the species to decrease to $1/e$ of that of its starting value. The lifetime, τ, is dependent upon the rates of decay of all processes leading to the loss of concentration of the species. The rate of all radiative decay processes is denoted k_r, while the rate of all the non-radiative decay processes is denoted k_{nr}. The relationship between τ, k_r and k_{nr} is given by **equation 1.7**.

$$\tau = \frac{1}{k_r + k_{nr}}$$

equation 1.7

Time-resolved spectroscopic techniques such as TA, TRIR, 2DIR and FLUPS allow for the determination of excited-state lifetimes. The change in probe intensity (or change in emission intensity with FLUPS), will typically show exponential behaviour, as a function of time. Kinetic traces, formed of the intensity, at a select wavelength, vs. time, can be fit with an exponential decay function, see **equation 1.8**. Where I_t is the intensity at time t, I_0 is the initial intensity and τ is the excited state lifetime.

$$I_t = I_0 \cdot \exp(\frac{-t}{\tau})$$

equation 1.8

$$I_t = I_1 \cdot \exp\left(\frac{-t}{\tau 1}\right) + I_2 \cdot \exp(\frac{-t}{\tau 2})$$

equation 1.9

Typically, the decay in intensity at a given wavelength will be multiexponential in nature. In such cases kinetic traces may be fit with a function composed of multiple exponential functions. **Equation 1.9** shows the form of the function for a bi-exponential decay.

The dynamics of a system may be assessed by fitting the intensity as a function of time for a given spectral position, λ_1. However, the dynamics observed at λ_1 may be different to that of another spectral position, λ_2 for example. If multiple excited-states are populated, where said states exhibit different decay dynamics and give rise to spectroscopic signatures in different spectral regions, the simultaneous fitting of all time-resolved data with a discrete set of spectral and kinetic parameters may be preferred. Such a fitting method is termed global analysis. Global analysis assumes a finite number of distinct spectroscopic states are populated upon excitation and that the spectroscopic signature of each of the states are independent of one another, i.e, the signal measured for a mixture of excited states resembles the sum of the spectroscopic signals of the individual states. The results of global analysis are spectral components corresponding to specific states / processes present within the spectroscopic data, along with kinetic parameters describing the evolution of the spectral component as a function of time. A detailed description of global analysis, and closely related target analysis, can be found in the references.[84]

1.6 Research Aims

The aims of the work presented in this work are the following:

1. To probe the photophysics of metal complexes relevant to solar energy conversion, using various ultrafast laser spectroscopy techniques.
2. To measure ultrafast, broadband emission of platinum complexes using fluorescence upconversion spectroscopy.
3. To investigate the effect of systematic changes in molecular structure on rates of intersystem in two closely related series of platinum complexes.
4. With the use of 2DIR spectroscopy, track the redistribution of vibrational energy (IVR) in donor-bridge-acceptor complexes, studying the effect of linker substitution on rates of IVR.

The chapters within this thesis are stand alone and can be read independently of one another. The work presented in Appendix B – 'Ultrafast Transient Absorption of a C_{60} Fullerene [3]Rotaxane Shuttle' is part of a collaboration, and has been published.[85]

1.7 References

1 Office for National Statistics, How has life expectancy changed over time?, https://www.ons.gov.uk/peoplepopulationandcommunity/birthsdeathsandmarriages/lifeexpectancies/articles/howhaslifeexpectancychangedovertime/2015-09-09, (accessed 21 June 2019).

2 V. Smil, *Energy Transitions : Global and National Perspectives*, Praeger, 2nd edn., 2016.

3 BP, *BP Statistical Review of World Energy*, 2019.

4 NASA Goddard Institute for Space Studies, GISS Surface Temperature Analysis (GISTEMP), version 4., https://data.giss.nasa.gov/gistemp/, (accessed 21 June 2019).

5 T. R. Anderson, E. Hawkins and P. D. Jones, *Endeavour*, 2016, **40**, 178–187.

6 International Energy Agency, *Global Energy & CO2 Status Report 2018*, 2019.

7 CarbonBrief, Mapped: How climate change affects extreme weather around the world.

8 S. Chu and A. Majumdar, *Nature*, 2012, **488**, 294–303.

9 J. Wilkening, , DOI:10.1002/wsb.944.

10 W. H. Stahl, C. Singer, E. J. Holmyard and A. R. Hall, *Class. Wkly.*, 1955, **49**, 26.

11 B. Sorensen, *A history of renewable energy technology*, 1991.

12 A. B. Meinel and M. P. Meinel, *Applied solar energy : an introduction*, Addison-Wesley Pub. Co, 1976.

13 O. Ellabban, H. Abu-Rub and F. Blaabjerg, *Renew. Sustain. Energy Rev.*, 2014, **39**, 748–764.

14 M. Thirugnanasambandam, S. Iniyan and R. Goic, *Renew. Sustain. Energy Rev.*, 2010, **14**, 312–322.

15 N. Armaroli and V. Balzani, *Angew. Chem. Int. Ed. Engl.*, 2007, **46**, 52–66.

16 M. M. Tice and D. R. Lowe, *Nature*, 2004, **431**, 549–552.

17 J. Barber, *Chem. Soc. Rev.*, 2009, **38**, 185–196.

18 S. Archer and J. A. Weinstein, *Coord. Chem. Rev.*, 2012, **256**, 2530–2561.

19 G. Ciamician, *Science (80-.).*, 1912, **36**, 385.

20 N. S. Lewis and D. G. Nocera, *Proc. Natl. Acad. Sci. U. S. A.*, 2006, **103**, 15729–35.

21 J. H. Alstrum-Acevedo, M. K. Brennaman and T. J. Meyer, *Inorg. Chem.*, 2005, **44**, 6802–27.

22 A. C. Bhasikuttan, M. Suzuki, S. Nakashima and T. Okada, *J. Am. Chem. Soc.*, 2002, **124**, 8398–8405.

23 V. Balzani, G. Bergamini, F. Marchioni and P. Ceroni, *Coord. Chem. Rev.*, 2006, **250**, 1254–1266.

24 K. Kalyanasundaram, *Coord. Chem. Rev.*, 1998, **177**, 347–414.

25 J. N. Demas and B. A. DeGraff, *Coord. Chem. Rev.*, 2001, **211**, 317–351.

26 E. Baggaley, J. A. Weinstein and J. A. G. Williams, *Coord. Chem. Rev.*, 2012, **256**, 1762–1785.

27 K. Kalyanasundaram, *Coord. Chem. Rev.*, 1982, **46**, 159–244.

28 J. V. Caspar, E. M. Kober, B. P. Sullivan and T. J. Meyer, *J. Am. Chem. Soc.*, 1982, **104**, 630–632.

29 M. Kasha, *Discuss. Faraday Soc.*, 1950, **9**, 14–19.

30 N. J. Turro, *Modern Molecular Photochemsitry*, University Science Books, 1978.

31 N. J. Turro, V. Ramamurthy and J. C. Scaiano, *Principles of Molecular Photochemistry*, University Science Books, 2009.

32 A. Hagfeldt and M. Grätzel, *Acc. Chem. Res.*, 2000, **33**, 269–277.

33 M. Grätzel, *Nature*, 2001, **414**, 338–344.

34 L. K. McKenzie, I. V. Sazanovich, E. Baggaley, M. Bonneau, V. Guerchais, J. A. G. Williams, J. A. Weinstein and H. E. Bryant, *Chem. - A Eur. J.*, 2017, **23**, 234–238.

35 C. Cebrián and M. Mauro, *Beilstein J. Org. Chem.*, 2018, **14**, 1459–1481.

36 A. M. Blanco-Rodríguez, M. Busby, C. Grădinaru, B. R. Crane, A. J. Di Bilio, P. Matousek, M. Towrie, B. S. Leigh, J. H. Richards, J. Antonín Vlček and H. B. Gray, *J. Am. Chem. Soc.*, 2006, **128**, 4365–4370.

37 M. Chergui, *Acc. Chem. Res.*, 2015, **48**, 801–8.

38 J. N. Schrauben, K. L. Dillman, W. F. Beck and J. K. Mccusker, *Chem. Sci.*, 2010, **1**, 405–410.

39 E. A. Juban, A. L. Smeigh, J. E. Monat and J. K. Mccusker, *Coord. Chem. Rev.*, 2006, **250**, 1783–1791.

40 W. Gawelda, A. Cannizzo, V.-T. Pham, F. van Mourik, C. Bressler and M. Chergui, *J. Am. Chem. Soc.*, 2007, **129**, 8199–8206.

41 C. Consani, M. Prémont-Schwarz, A. Elnahhas, C. Bressler, F. van Mourik, A. Cannizzo and M. Chergui, *Angew. Chem. Int. Ed. Engl.*, 2009, **48**, 7184–7.

42 C. Bressler, C. Milne, V.-T. Pham, A. Elnahhas, R. M. van der Veen, W. Gawelda, S. Johnson, P. Beaud, D. Grolimund, M. Kaiser, C. N. Borca, G. Ingold, R. Abela and M. Chergui, *Science*, 2009, **323**, 489–92.

43 A. L. Smeigh, M. Creelman, R. A. Mathies and J. K. McCusker, *J. Am. Chem. Soc.*, 2008, **130**, 14105–14107.

44 O. S. Wenger, *Coord. Chem. Rev.*, 2009, **253**, 1439–1457.

45 J. Tribollet, G. Galle, G. Jonusauskas, D. Deldicque, M. Tondusson, J. F. Letard and E. Freysz, *Chem. Phys. Lett.*, 2011, **513**, 42–47.

46 A. Lapini, P. Foggi, L. Bussotti, R. Righini and A. Dei, *Inorganica Chim. Acta*, 2008, **361**, 3937–3943.

47 M. Iwamura, H. Watanabe, K. Ishii, S. Takeuchi and T. Tahara, *J. Am. Chem. Soc.*, 2011, **133**, 7728–7736.

48 S. Garakyaraghi, E. O. Danilov, C. E. McCusker and F. N. Castellano, *J. Phys. Chem. A*, 2015, **119**, 3181–93.

49 M. T. Colvin, A. L. Smeigh, E. M. Giacobbe, S. M. M. Conron, A. B. Ricks and M. R. Wasielewski, *J. Phys. Chem. A*, 2011, **115**, 7538–7549.

50 F. Frei, A. Rondi, D. Espa, M. L. Mercuri, L. Pilia, A. Serpe, A. Odeh, F. Van Mourik, M. Chergui, T. Feurer, P. Deplano, A. Vlček and A. Cannizzo, *Dalton Trans.*, 2014, **43**, 17666–17676.

51 A. Cannizzo, F. van Mourik, W. Gawelda, G. Zgrablic, C. Bressler and M. Chergui, *Angew. Chem. Int. Ed. Engl.*, 2006, **45**, 3174–6.

52 O. Bräm, F. Messina, A. M. El-Zohry, A. Cannizzo and M. Chergui, *Chem. Phys.*, 2012, **393**, 51–57.

53 A. Cannizzo, A. M. Blanco-Rodríguez, A. El Nahhas, J. Šebera, S. Záliš, A. Vlček and M. Chergui, *J. Am. Chem. Soc.*, 2008, **130**, 8967–8974.

54 O. Bräm, F. Messina, E. Baranoff, A. Cannizzo, M. K. Nazeeruddin and M. Chergui, *J. Phys. Chem. C*, 2013, **117**, 15958–15966.

55 G. Ramakrishna, T. Goodson, J. E. Rogers-Haley, T. M. Cooper, D. G. McLean and A. Urbas, *J. Phys. Chem. C*, 2009, **113**, 1060–1066.

56 R. Monni, G. Capano, G. Auböck, H. B. Gray, A. Vl Cek, I. Tavernelli and M. Chergui,

Proc. Natl. Acad. Sci. U. S. A., 2018, **115**, E6396–E6403.

57 R. M. van der Veen, A. Cannizzo, F. van Mourik, A. Vlček and M. Chergui, *J. Am. Chem. Soc.*, 2011, **133**, 305–315.

58 I. L. Zheldakov, M. N. Ryazantsev and A. N. Tarnovsky, *J. Phys. Chem. Lett.*, 2011, **2**, 1540–1545.

59 S. E. Brown-Xu, M. S. J. Kelley, K. A. Fransted, A. Chakraborty, G. C. Schatz, F. N. Castellano and L. X. Chen, *J. Phys. Chem. A*, 2016, **120**, 543–50.

60 A. Chakraborty, J. E. Yarnell, R. D. Sommer, S. Roy and F. N. Castellano, *Inorg. Chem.*, 2018, **57**, 1298–1310.

61 C. E. Mccusker, A. Chakraborty and F. N. Castellano, *J. Phys. Chem. A*, 2014, **118**, 10391–10399.

62 ‡ Evgeny O. Danilov, † Irina E. Pomestchenko, † Solen Kinayyigit, § Pier L. Gentili, ‖, ⊥ Muriel Hissler, ‖ and Raymond Ziessel and † Felix N. Castellano*, .

63 V. Prusakova, C. E. Mccusker and F. N. Castellano, *Inorg. Chem.*, 2012, **51**, 8589–8598.

64 J. E. Yarnell, I. Davydenko, P. V Dorovatovskii, V. N. Khrustalev, T. V Timofeeva, F. N. Castellano, S. R. Marder, C. Risko and S. Barlow, *J. Phys. Chem. C*, 2018, **122**, 13848–13862.

65 G. T. Burdzinski, R. Ramnauth, M. H. Chisholm and T. L. Gustafson, *J. Am. Chem. Soc.*, 2006, **128**, 6776–7.

66 J. E. Haley, D. M. Krein, J. L. Monahan, A. R. Burke, D. G. McLean, J. E. Slagle, A. Fratini and T. M. Cooper, *J. Phys. Chem. A*, 2011, **115**, 265–273.

67 Y. Garcia, J. Moscovici, A. Michalowicz, V. Ksenofontov, G. Levchenko, G. Bravic, D. Chasseau and P. Gütlich, *Chemistry*, 2002, **8**, 4992-5000on th.

68 F. E. Lytle and D. M. Hercules, *J. Am. Chem. Soc.*, 1969, **91**, 253–257.

69 G. A. Crosby and J. N. Demas, *J. Am. Chem. Soc.*, 1971, **93**, 2841–2847.

70 A. A. T. Yeh, C. C. V. C. Shank and J. J. K. McCusker, *Science (80-.).*, 2000, **289**, 935–938.

71 N. H. Damrauer, *Science (80-.).*, 1997, **275**, 54–57.

72 W. R. Browne, C. G. Coates, C. Brady, P. Matousek, M. Towrie, S. W. Botchway, A. W. Parker, J. G. Vos and J. J. McGarvey, *J. Am. Chem. Soc.*, 2003, **125**, 1706–1707.

73 B. Maubert, N. D. McClenaghan, M. T. Indelli and S. Campagna, *J. Phys. Chem. A*,

2003, **107**, 447–455.

74 P. M. Champion, F. Rosca, D. Ionascu, W. Cao and X. Ye, *Faraday Discuss.*, 2004, **127**, 123.

75 H. Yersin, *Transition Metal and Rare Earth Compounds*, Springer Berlin Heidelberg, Berlin, Heidelberg, 2004, vol. 241.

76 J. E. Yarnell, A. Chakraborty, M. Myahkostupov, K. M. Wright and F. N. Castellano, *Dalt. Trans.*, 2018, **47**, 15071–15081.

77 H. Yersin and K. L. Bray, *Transition Metal and Rare Earth Compounds: Excited States, Transitions, Interactions II*, Springer, 2001.

78 J. Bredenbeck, J. Helbing, C. Kolano and P. Hamm, *ChemPhysChem*, 2007, **8**, 1747–1756.

79 * Kenneth G. Spears, and Xiaoning Wen and R. Zhang, , DOI:10.1021/JP960444A.

80 P. Hamm, J. Helbing and J. Bredenbeck, *Annu. Rev. Phys. Chem.*, 2008, **59**, 291–317.

81 P. Hamm and M. Zanni, *Concepts and Methods of 2D Infrared Spectroscopy*, Cambridge University Press, 2011.

82 N. T. Hunt, *Chem. Soc. Rev.*, 2009, **38**, 1837–1848.

83 I. V Rubtsov and R. M. Hochstrasser, *J. Phys. Chem. B*, 2002, **106**, 9165–9171.

84 I. H. M. van Stokkum, D. S. Larsen and R. van Grondelle, *Biochim. Biophys. Acta - Bioenerg.*, 2004, **1657**, 82–104.

85 T. A. Barendt, I. Rašović, M. A. Lebedeva, G. A. Farrow, A. Auty, D. Chekulaev, I. V. Sazanovich, J. A. Weinstein, K. Porfyrakis and P. D. Beer, *J. Am. Chem. Soc.*, 2018, **140**, 1924–1936.

2 Fluorescence Upconversion Spectroscopy (FLUPS)

The centrepiece of the research, narrated in this thesis, was fluorescence upconversion spectroscopy. The method of choice for the time-resolved fluorescence measurements. The technique allows for broadband detection of fluorescence with time-resolution on the order of 100's of femtoseconds. In essence fluorescence, initiated with ultrashort laser excitation, is directed onto a crystal where it is 'upconverted' with a second, ultrashort laser pulse, the 'gate' pulse. The gate pulse is the means of obtaining time-resolution, acting as an ultrafast shutter, not dissimilar to the probe in the pump-probe techniques described in Chapter 1 - Introduction. Spatial separation, followed by detection, of the ultrashort 'slices' of fluorescence gives (in theory) background-free time-resolved fluorescence spectra.

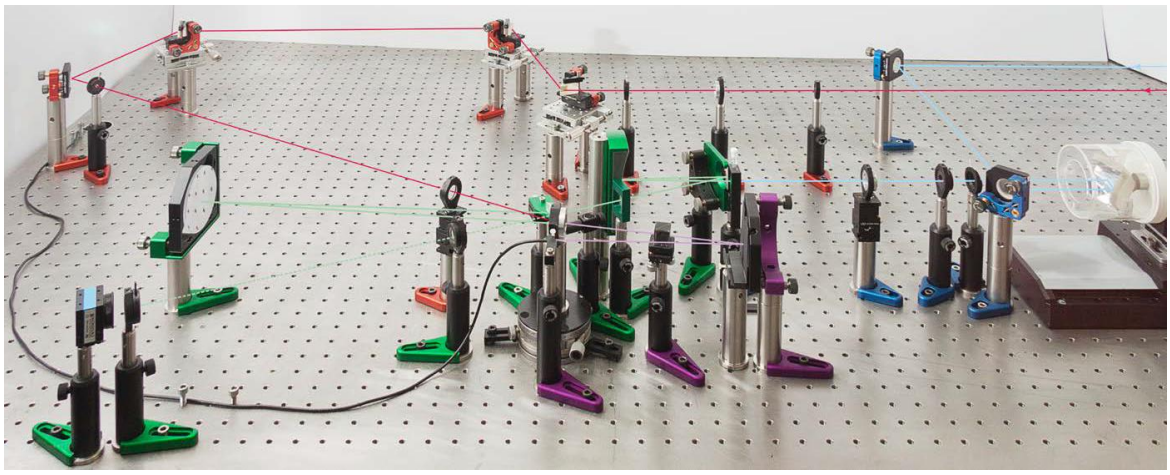

Figure 2.1 A photograph of the Fluorescence Upconversion Spectrometer (FLUPS) used at The Lord Porter Ultrafast Laser Spectroscopy Laboratory, University of Sheffield.

2.1 Brief History

In the pursuit of measurement of fluorescence spectra numerous different methods have been developed and implemented, including; time-correlated single photon counting (TCSPC), streak camera spectroscopy and optical Kerr gating spectroscopy.[1] The various techniques differ primarily in their source of excitation, method of time-gating and choice of photodetection apparatus. The results of these differences manifest themselves most notably in the achievable temporal resolution and measurable spectral range, with each finding itself better suited to application in some field or another.

Fluorescence upconversion is a time-resolved emission technique utilising upconversion as the mechanism of gating. Upconversion is a variant of sum-frequency generation.[2] The first measurements of time-resolved fluorescence, using this method, were reported in 1975 by Mahr and Hirsch.[3] These ground-breaking experiments used ammonium dihydrogen phosphate (ADP) as the nonlinear optical medium, in the upconversion of, firstly, the green light of an argon-ion laser, followed by the green-yellow luminescence of Rhodamine 6G, achieving time-resolution of around 20 ps. The time resolution is almost wholly dependent on the temporal width of the laser pulses used, as laser technology advances, so does the achievable time-resolution. A time resolution of around 40 fs has been achieved using a cavity-dumped Ti:sapphire laser. Since conception, FLUPS has been used to study a wide range of phenomena, such as fluorophore solvation dynamics,[4–6] photoinduced electron transfer porphyrins,[7] ultrafast isomerization,[8,9] protein solvation,[10] and most relevant to our research, the ultrafast dynamics of transition metal complexes. [11–16]

2.2 Basic Principles

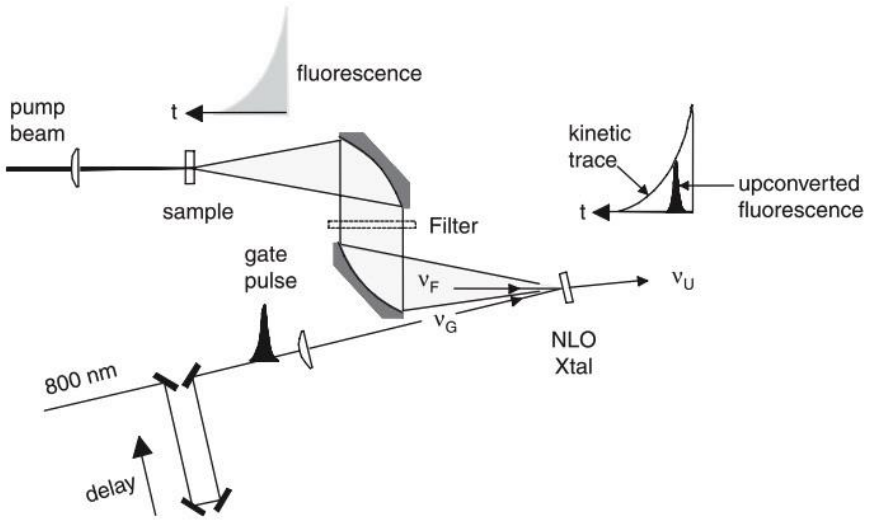

Figure 2.2 Scheme of a typical fluorescence upconversion setup. NLO Xtal represents the nonlinear optical crystal. In this scheme the gate pulse is composed of 800 nm light. Taken from reference.[1]

Figure 2.2 shows a simple schematic of the key components of a fluorescence upconversion setup. A solution of a chromophore is irradiated with a temporally short pulse of light, with a population of the sample being excited from the ground state into higher-energy electronic states. Any subsequent emission, at frequency ν_F, is collected and then focussed upon a nonlinear optical (NLO) crystal; the medium for upconversion. At some time, t, after sample excitation, temporally short gate pulses, at frequency ν_G, are mixed with the emission at the NLO crystal. With an appropriate crystal orientation, the sum frequency generation emission and gate will take place, producing upconverted light at frequency, ν_U, see **equation 2.1**.

$$\nu_U = \nu_F + \nu_G$$

equation 2.1

The gate pulse acts as a temporal shutter, only allowing emission to 'pass through' the crystal while gate light is present. The intensity of the upconverted light generated is directly proportional to the intensity of the emission in the given time window. The temporal profile of the upconverted light is dictated by the temporal profile of the gate pulses. Altering the time delay between excitation and gating allows the emission to be probed as a function of time, obtaining kinetic information. Detection apparatus is

arranged such as to exclusively capture the 'pulses' of upconverted light, both spatially and spectrally, resulting in nearly background free recording of fluorescence. This is a major advantage of this technique over the Optical Kerr gating method. The spectral information acquired in the detection of the upconverted signal and prior knowledge of the spectral profile of the gate pulse allow us to deduce the spectral profile of the original emission.

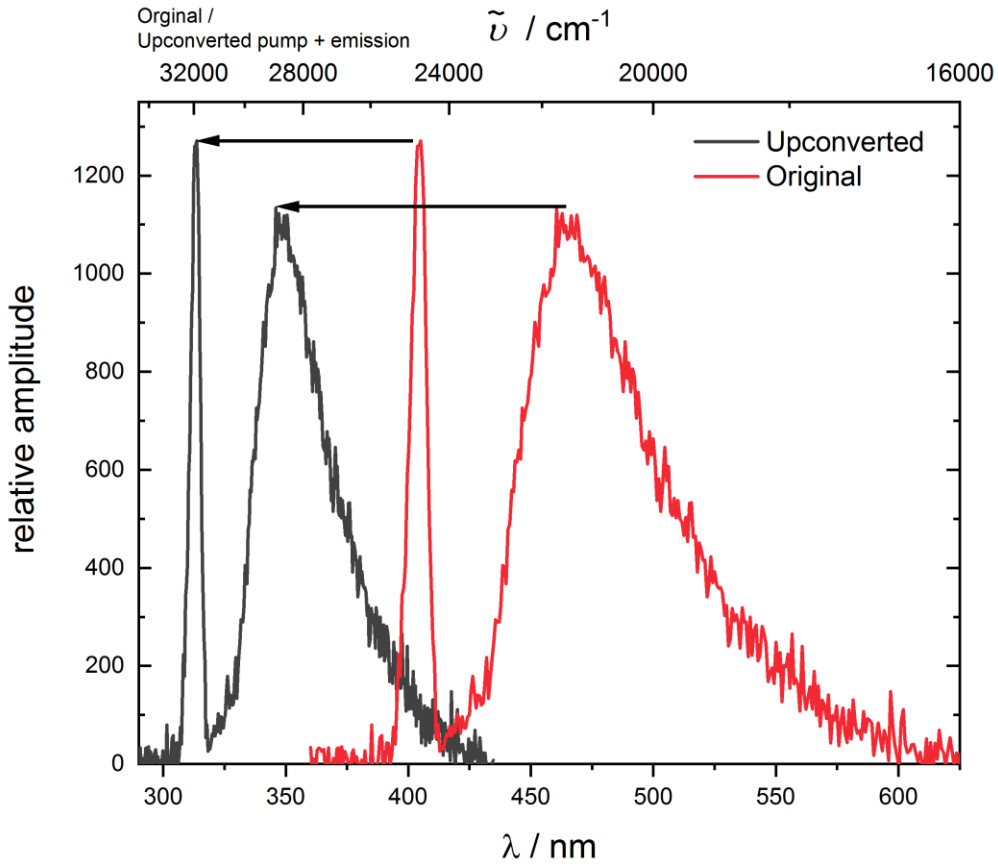

Figure 2.3 This figure illustrates the process of the upconversion of an emission spectrum. The original emission (red line), centred around 460 nm is upconverted to give an upconverted spectrum centred at around 350 nm. A signal at 400 nm, due to scattered pump light is observed. The pump light will also be upconverted, this signal appears at around 308 nm.

The upconversion of an emission spectrum is illustrated in **Figure 2.3**. The entire photon distribution of the 'original' emission spectrum (red line) is simultaneously upconverted to that of the 'upconverted' spectrum (black line). Residual pump light is seen as a narrow band at 400 nm. Upconverted 400 nm light is seen as a narrow band at around 308 nm. The wavenumber / energy of the gate pulse can be calculated from the difference in

spectral position of the scattered 400 nm pump and that of the upconverted 400 nm pump, the 'cross correlation'. Once the wavenumber of the gate pulse is known, the upconverted photon distribution may be 'converted' back to that of the original. This figure is purely illustrative, in reality the range of the spectrograph is approx. 300 to 500 nm, meaning only the blue edge of the original emission would be detectable. Additionally, the spatial arrangement of the setup is such that only upconverted emission is intentionally directed onto the spectrograph for detection.

2.3 Sum Frequency Generation and Phase Matching

As stated above, Fluorescence Upconversion spectroscopy (FLUPS) utilises the process of sum frequency generation in a non-linear crystal as the means of time-gating emission spectra. The use of sum frequency generation as the means of time-gating means FLUPS benefits from good separation of generated signal and the two input beams (sample emission and gate beams) in terms of both spectral and spatial separation. This is the major advantage of FLUPS, over other methods.

Sum frequency generation is a process where two input beams generate another beam with the sum of the frequencies of the two input beams, see **equation 2.2** (**equation 2.2** is a general form of **equation 2.1**).

$$\nu_3 = \nu_1 + \nu_2$$

equation 2.2

The process of sum frequency generation relies upon, and will take place within, a crystal exhibiting '$\chi^{(2)}$ nonlinearity'. Crystal materials absent of inversion symmetry may possess such a property.

In order for efficient sum frequency generation to occur, there should be 'phase matching' of the two interacting input waves and the generated signal wave. Essentially, phase matching means a proper phase relationship between waves is maintained along the direction of propagation. The magnitude of a wave vector is denoted k, see **equation 2.3.**

$$k = \frac{2\pi}{\lambda}$$

equation 2.3

In order to maximise phase matching, wave vector mismatch, $\Delta\vec{k}$, should be minimized, see **equation 2.4**.

$$\Delta\vec{k} = \vec{k}_{eU} - \{\vec{k}_{oF} + \vec{k}_{eG}\}$$

equation 2.4

The nonlinear crystals used for upconversion are birefringent. That is, the refractive index of the crystal is dependent upon the polarization and propagation of light. Vertically polarized emission, which is ordinary relative to the crystal optical axis, is upconverted with horizontally polarized gate pulses, which are extraordinary relative to the crystal optical axis. The output of the sum frequency generation will also be extraordinary, rotation of the crystal will influence the refractive index of both gate and upconverted beams but not the emission. $\vec{k}$, **equation 2.4**, is dependent upon the refractive index, thus rotation of the crystal can be used to adjust $\vec{k}_{eU}$ and $\vec{k}_{eG}$ and minimise $\Delta\vec{k}$. In practice, the system is engineered such that $\Delta\vec{k}$ will be minimised for a broad emission range and the 1340 nm gate pulses, at a single crystal angle. For details see references.[1,17,18]

2.4 Specifics of the Setup @ The Lord Porter Ultrafast Laser Spectroscopy Laboratory, The University of Sheffield

A concise description of the experimental setup can be found in Chapter 7 – Experimental. This section is more in the form of a user's guide, with the specifics of the working of the system at Sheffield discussed, as well as the introduction of relevant principles / theory where deemed applicable.

2.4.1 Laser System

The fluorescence upconversion spectrometer at Sheffield used a common source for the generation of both the pump and gate pulses. The two pulse trains were therefore intrinsically synchronised. The relative timing of the two pulse trains was controlled solely by manipulation of their relative path lengths, with the use of a motorised delay stage.

A Ti:Sapphire oscillator (Mai Tai, Spectra-Physics) provided 800 nm seed pulses (25 fs fwhm, 84 MHz) which were passed through a Ti:Sapphire regenerative amplifier (Spitfire ACE PA-40, Spectra-Physics). The regenerative amplifier performed two bouts of amplification of the seed pulses. The lasing medium (crystal) in both stages of amplification was pumped by a Nd:YLF laser (Empower, Spectra-Physics). The output of the regenerative amplifier was high-energy, ultrashort, 800 nm laser pulses at a repetition rate of 10 kHz ($1.2\ mJ, 40\ fs$ fwhm, $10\ kHz$). The 800 nm pulses were partitioned with the use of beam-splitters. A portion of the pulse was used to generate the 400 nm pump pulses ($40\ fs$ fwhm, $10\ kHz$, ~$0.3\ \mu J$) by frequency doubling in a in a β-barium borate crystal within a commercially available doubler/tripler (TimePlate, Photop Technologies). ~1340 nm gate pulses ($80\ fs$ fwhm, $10\ kHz$, $80\ \mu J$) were the signal pulses generated by a traveling-wave optical parametric amplifier of superfluorescence (TOPAS prime, Light Conversion) pumped by a second portion of the $800\ nm$ ($40\ fs\ fwhm$, $10\ kHz$, $0.5\ mJ$) output of Ti:Sapphire regenerative amplifier.

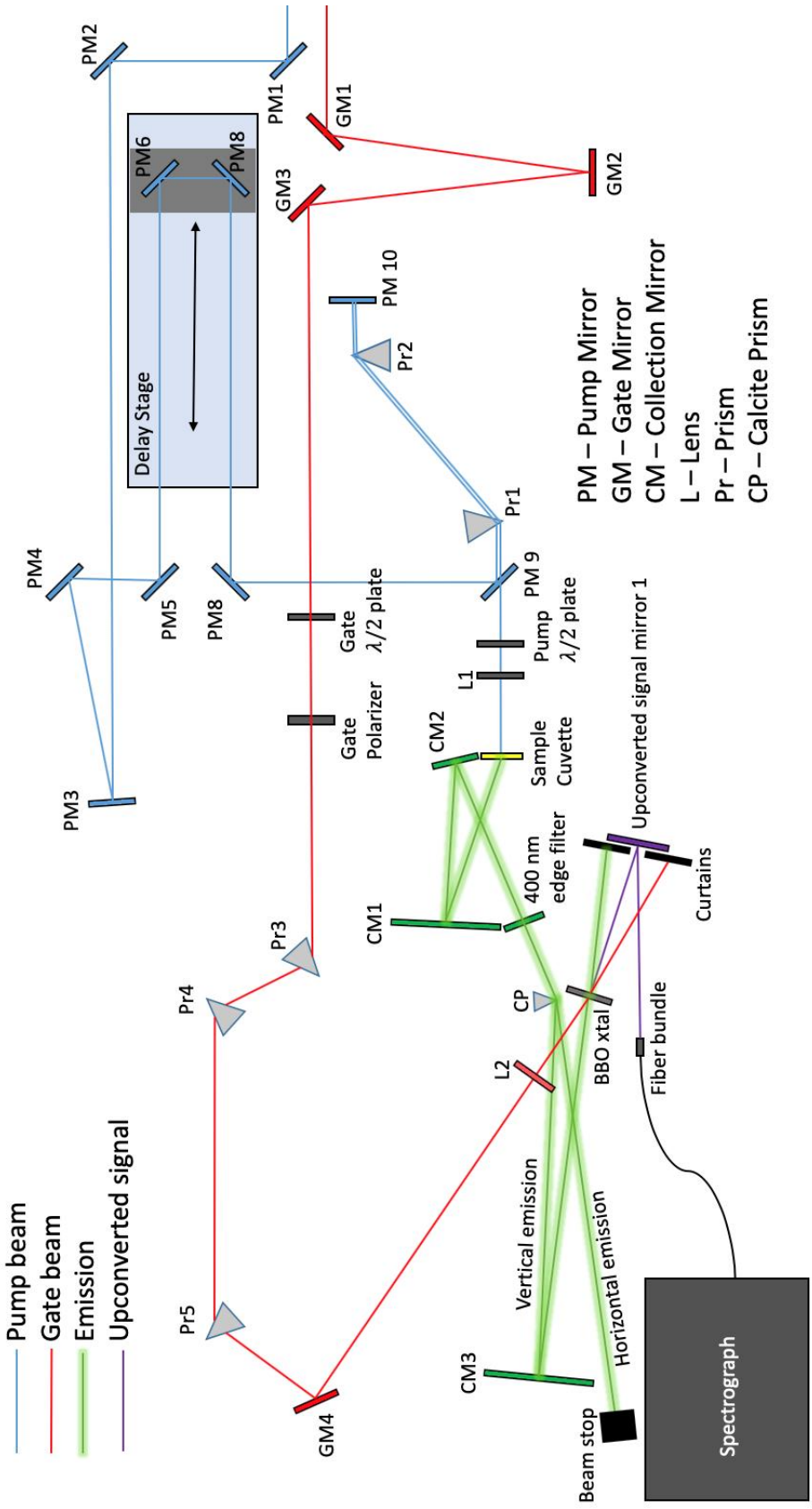

Figure 2.4 A schematic diagram of the optical setup of the fluorescence upconversion spectrometer (FLUPS), at The Lord Porter Ultrafast Laser Spectroscopy Laboratory, University of Sheffield. The scheme includes only the optics on the FLUPS table itself, the beams are prepared prior to 'PM1' and 'GM1', the first two mirrors on the FLUPS table. Generation of the two beams, pump and gate, is described above and in the Experimental.

2.4.2 Optical Arrangement

Figure 2.4 shows the arrangement of optics on the FLUPS table; the optics responsible for the manipulation (polarization, power) and guidance of the beams, to both, pump the sample and temporally gate any resultant emission. The different beam lines are differentiated by colour, see key. The spectrograph is a homemade spectrometer, utilising a diffraction grating, and attached CCD camera.

2.4.3 Pump Beam - Optical Arrangement, Routing and Alignment

Frequency Doubling

The 400 nm beam is generated by frequency doubling of the 800 nm laser output. This is done within the 'TimePlate' by sum frequency generation in a BBO crystal, see **Figure 2.5**. The efficiency, and therefore output power, of the generation is dependent on crystal angle. Power can be optimised by rotation of the crystal whilst measuring the beam power (**Figure 2.5 A**). The 400 nm is centred upon an iris directly after ejection from the TimePlate (**Figure 2.5 B**). The pulse beam is then split into several fractions via an arrangement of beam splitters (**Figure 2.5 C**), before being directed into each of the experimental rooms (for FLUPS, **Figure 2.5 D**).

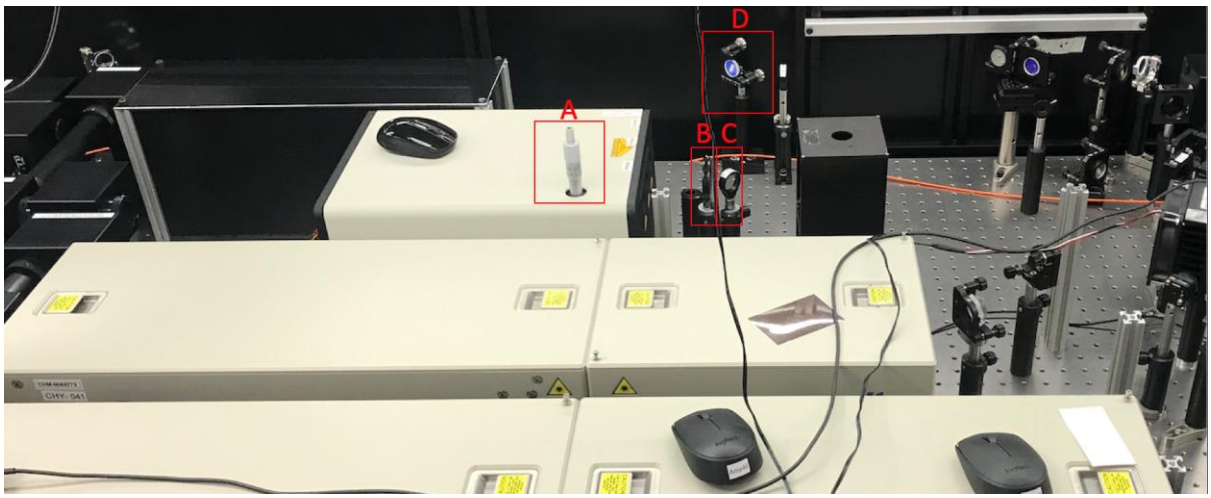

Figure 2.5 Photograph of the apparatus used for the generation of the 400 nm by frequency doubling of the 800 nm laser output. **A** shows a screw for adjusting the angle of a BBO crystal. **B** is the iris for the alignment of the 400 nm output before it is split for the various experiments. **C** is a beam splitter to separate the 400 nm into a pathway to FLUPS, and to TA/TRIR. **D** is the first mirror for alignment of the FLUPS fraction of 400 nm light.

Delay Stage Alignment

Once on the FLUPS table, the 400 nm beam is guided to the sample cuvette, via an array of mirrors, lens, prisms and filters. PM1-PM5 (**Figure 2.6**and **Figure 2.7**) are used to guide the 400 nm beam onto the delay stage. The delay stage is comprised of a motorized, computer-controlled translation stage, and two mounted mirrors (PM6 & PM7, **Figure 2.7**).

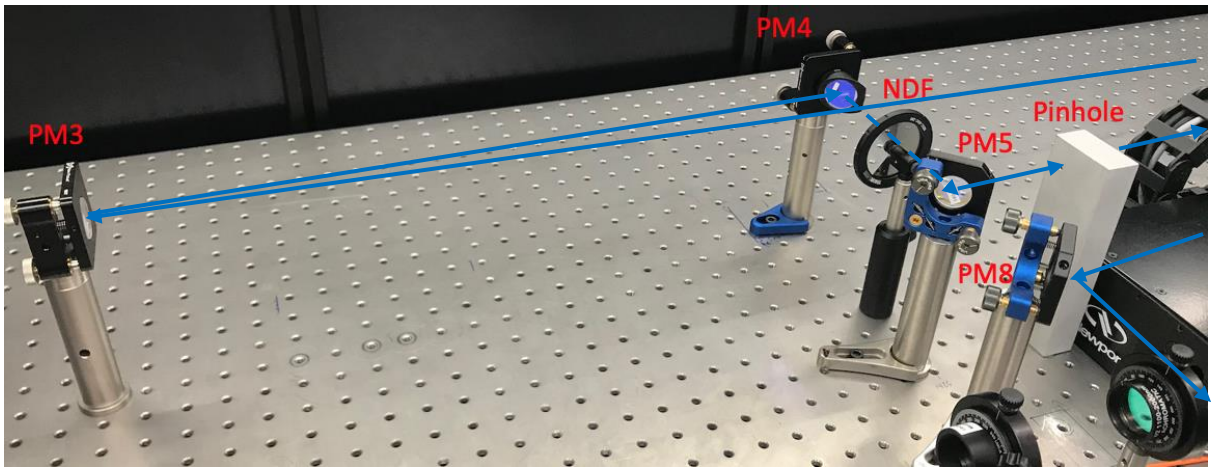

Figure 2.6 Figure shows the delay stage and the optics that guide the 400 nm pulse to and from the stage. **NDF** is a neutral density filter. The **Pinhole** is a moveable pinhole for alignment of beams to and from the delay stage.

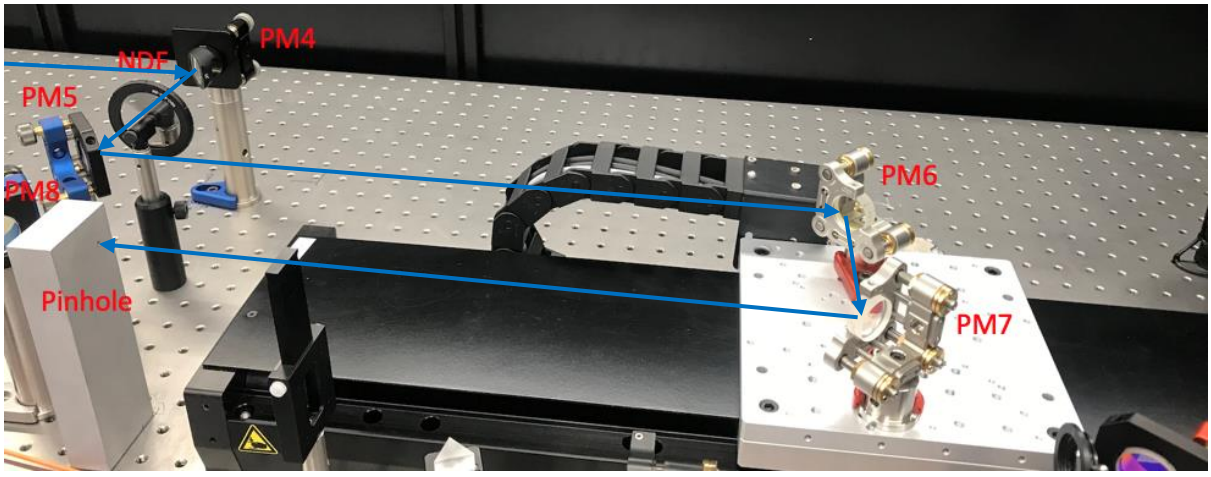

Figure 2.7 Figure shows the delay stage and the optics that guide the 400 nm pulse to and from the stage.

If the delay stage itself is aligned, that is, if the mirrors PM6 and PM7 are set such that an incoming beam, parallel to the stage, exits parallel to the stage, PM6 and PM7 do not need to be adjusted. In this case, mirrors PM3 and PM4 are used to align the beam onto the stage. The following procedure should be used:

1. PM3 (**Figure 2.6**) is used to the centre to the beam onto the pinhole, placed in the position shown in **Figure 2.6**.
2. PM4 is then used to centre the beam onto the pinhole, placed in the position shown in **Figure 2.7**.
3. Repeat step 1 and 2 until the beam is centred upon the pinhole in both positions without adjustment of either mirror.

In order to assess if the delay stage is aligned (if PM6 and PM7 are set correctly), firstly, the above procedure should be performed. Then, whilst the pinhole is the second position as seen in **Figure 2.7** the stage should be moved to either end of its range. If the stage is aligned, the beam will be centred upon the pinhole whilst at both ends of its range. The following procedure can be used if translation of the beam at the pinhole is observed.

1. The mirrors PM6 and PM7 should be sent to the back of the stage (most negative time on the software), i.e. furthest available position from the pinhole. PM7 should be used to centre the beam upon the pinhole.
2. The mirrors should be sent to front of the stage (most positive time on the software), i.e. closest available position from the pinhole. PM6 should then be used to centre the beam upon the pinhole once more.
3. Steps 1 and 2 should be repeated until there is no apparent movement of the beam, at the pinhole, upon translation of the delay stage.

Once the delay stage is aligned, the pump beam is centred upon the iris of **Figure 2.8** using PM8 (**Figure 2.6** and **Figure 2.7**)

Pump Compression

Upon generation within the TimePlate, the 400 nm pump pulses are approximately 40 fs in temporal width. In the delivery of the pump beam to the sample cuvette, the pulses will be subject to numerous interactions with optics (mirrors, lenses, filters, etc.) which will result in group-velocity dispersion and an increase in pulse temporal length. For optimal experimental time-resolution, pulse compression is necessary to account for this dispersion and provide pump pulses of shortest possible temporal width. A pair of prisms, which are 'double passed', are used to introduce negative dispersion, cancelling out the effect of any dispersion in the system, see **Figure 2.8**. PM9 passes the pump beam through

Pr1, to Pr2, to PM10, back through Pr2, then Pr1. PM10 is set such that the return leg is slightly elevated, and the beam passes above PM9 on the second leg, exiting the compressor. Negative dispersion in a pair of prisms is well described in the literature.[19] In practice, a thorough assessment of all the dispersion inducing interactions in the system is not required, the compressor may be adjusted in order to achievefor the narrowest, temportal, cross-correlation of pump and gate pulses. The two handles for the control of the compressor are the distance (L) between the apex of the two prisms, and the amount of material traversed by the pump beam. In practice, the adjustment of the amount of material traversed is more straight forward than the adjustment of L. Therefore, L is fixed once a reasonable degree of compression is obtained and the 'Pump Compressor Screw' is used to adjust the position of Pr2 relative to the beam path and hence the amount of prism traversed by the pump beam.

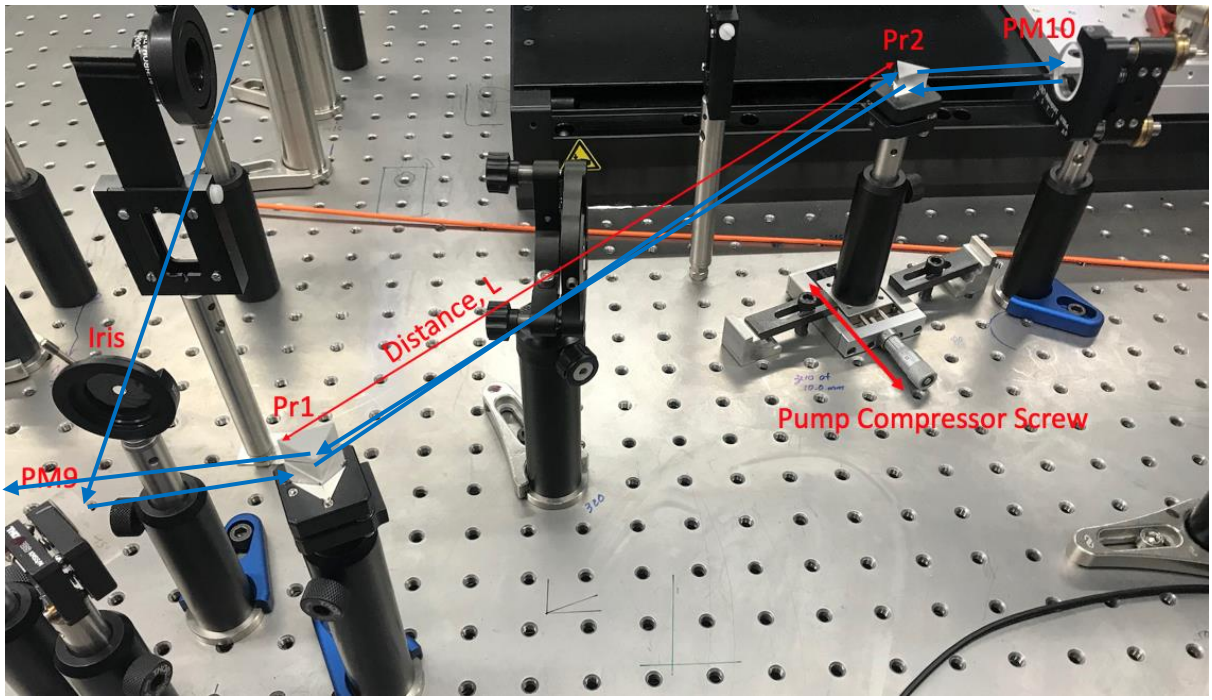

Figure 2.8 A double pass two prism compressor, for the compression of the 400 nm pump pulse. The distance between the two prisms, L, and the amount of material traversed ('Pump Compressor Screw') is adjusted in order to add appropriate amount of negative dispersion, determined by minimising temporal width of cross-correlation.

Adjustment of Pump Polarization

With the fluorescence upconversion spectrometer a calcite prism (**Figure 2.4, CP**) is used to separate emission into two beams of vertical and horizontal polarization respectively. The horizontally polarized emission is discarded with the use of a beam stop. The vertically polarized emission is directed onto the BBO crystal for upconversion. For the majority of

time-resolved emission measurements, the sample is pumped at magic angle with respect to vertical polarization, in order to account for the effects of molecular rotation. In order to set the pump to magic angle (~54.7°), vertical polarization of the pump must first be determined. The calcite prism can be used to set the pump to vertical polarization. The sample cuvette is removed, and the pump beam is directed onto pinhole just before the calcite prism, the prism is translated perpendicular to the beam path until whole beam enters the prism. A power meter is placed in the path of the right-hand side of the two beams exiting the calcite prism (vertically polarized). The pump $\lambda/2$ plate is rotated until a maximum reading on the power meter is achieved. A polarizer is placed in the pump beam path, just after the $\lambda/2$ plate, and rotated until maximum is read on the power meter once more. The polarizer is now set to the vertical. For magic angle, the polarizer should now be rotated by ~54.7° in either direction. The power of the beam should be maximised, after passing through the polarizer, by rotation of the $\lambda/2$ plate (this should be approximately 27.4°, or half of 54.7°).

Alignment onto Sample Cuvette Holder

The optics for the collection of sample emission are optimised for emission radiating from a specific point within the sample cuvette. A 'dummy cuvette', featuring a pinhole in the position for optimal excitation is used to align the pump beam, see **Figure 2.9**.

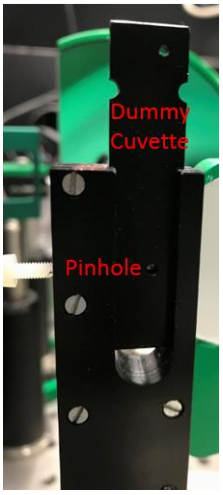

Figure 2.9 Dummy cuvette with pinhole for the alignment of the pump beam onto sample cuvette.

L1, see **Figure 2.4** and **Figure 2.10**, is a lens used for the focussing of the pump beam onto the sample cuvette / through the pinhole of the dummy cuvette (**Figure 2.9** and **Figure 2.10**). Adjustment of the lens position, by use of the two screws allows for the alignment

of the pump beam through the pinhole. An alignment card should be held behind the pinhole, while the two screws are carefully adjusted for maximum brightness of pump on the card.

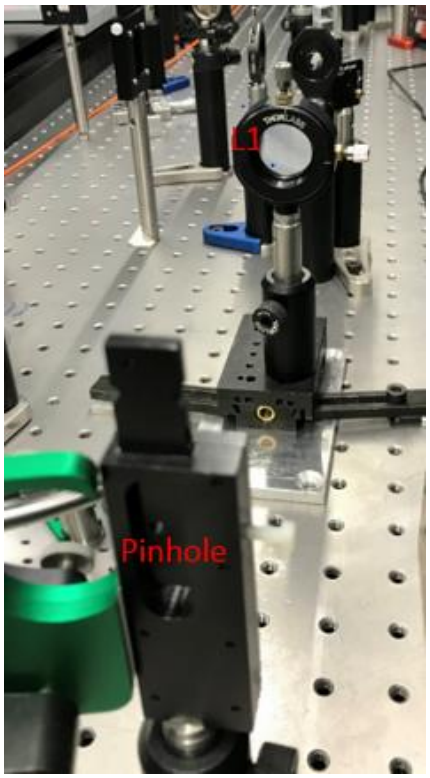

Figure 2.10 The dummy cuvette with pinhole, along with, L1, the lens used for the focusing of the pump beam onto the sample cuvette / dummy cuvette.

2.4.4 Gate Beam - Optical Arrangement, Routing and Alignment

Generation and Frequency Doubling for Alignment

The gate beam, which is typically set to ~1340 nm is generated in the TOPAS. For details of generation of the 1340 nm from the 800 nm laser output, the user should refer to the TOPAS user manual itself.

Figure 2.11 Photo shows the exit face of TOPAS. **A** is the BBO crystal used for frequency doubling of the gate, for alignment purposes. **B** is the first mirror for gate beam delivery to flups room. **C** is the second mirror for the delivery of the gate beam to the flups room. The iris is used for the adjustment of the first mirror, **B**.

1340 nm is invisible to the naked eye, in order to aid in the alignment of the gate beam, a BBO crystal (**Figure 2.11 A**) is used to generate frequency doubled gate (670 nm) which is red. The red beam can be used to align the gate beam up to the first prism for gate compression, Pr3, where due to the different wavelength, it will be subject to a different degree of diffraction and consequently misaligned.

Mirror **B** is used to guide the doubled gate beam onto the centre of the iris of **Figure 2.11**, via Mirror **C**, which itself is used to direct the beam on to the centre of the 'Iris 2' of **Figure 2.12**. Mirror **A** of **Figure 2.12**, is used to direct the doubled beam onto the first iris within the flups room itself.

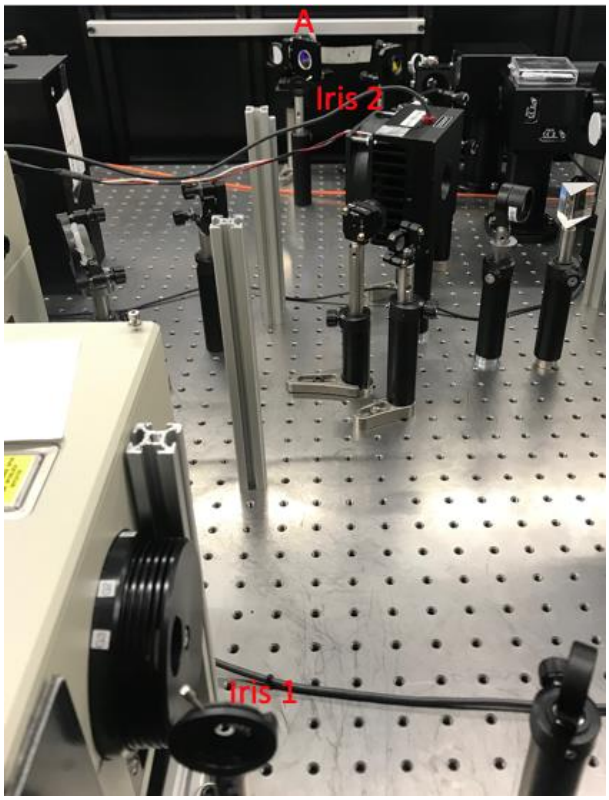

Figure 2.12 Photo shows two irises and a mirror used for the delivery of gate beam, from the output of the TOPAS to the FLUPS experimental room.

Once aligned onto the FLUPS experimental table, GM1, GM2, and GM3 (**Figure 2.4**) are used to guide the gate beam onto the apex of Pr3 (**Figure 2.4** and **Figure 2.13**), the first prism of a three prism compressor. Once the beam is aligned onto Pr3, the BBO crystal for gate doubling must be removed, for reasons stated above.

Adjustment of Gate Polarization

A $\lambda/2$ plate and polarizer pair are situated in the beam path between GM3 and Pr3. The primary role of this pair of optics is to set the polarization of the gate beam, however, they can also be used to attenuate the gate pulse, this can be useful whilst optimizing signal, this will be discussed later.

The experimental setup is designed such that only horizontally polarized gate is used for upconversion in the BBO crystal, for optimal signal generation, the gate beam polarization should be set to horizontal. The refraction of the gate beam in the three prisms of the compressor is polarization dependent, any light which isn't horizontally polarized will not follow the beam path through all three prisms, this can be used to determine horizontal

and set the $\lambda/2$ plate and polarizer pair. The following procedure can be used to set the gate polarization:

1. A power meter is placed in the path of the gate beam between Pr4 and Pr5.
2. The gate $\lambda/2$ plate is rotated until maximum power is read on the power meter.
3. The gate polarizer is rotated until, once again, maximum power is read on the power meter.
4. The polarizer should now be fixed (the polarizer is set to horizontal, and when power is maximised through the polarizer, by rotation of the $\lambda/2$ plate, the $\lambda/2$ plate will also be correctly set).
5. The $\lambda/2$ plate can be used to adjust the power of the horizontally polarized gate beam after the polarizer.

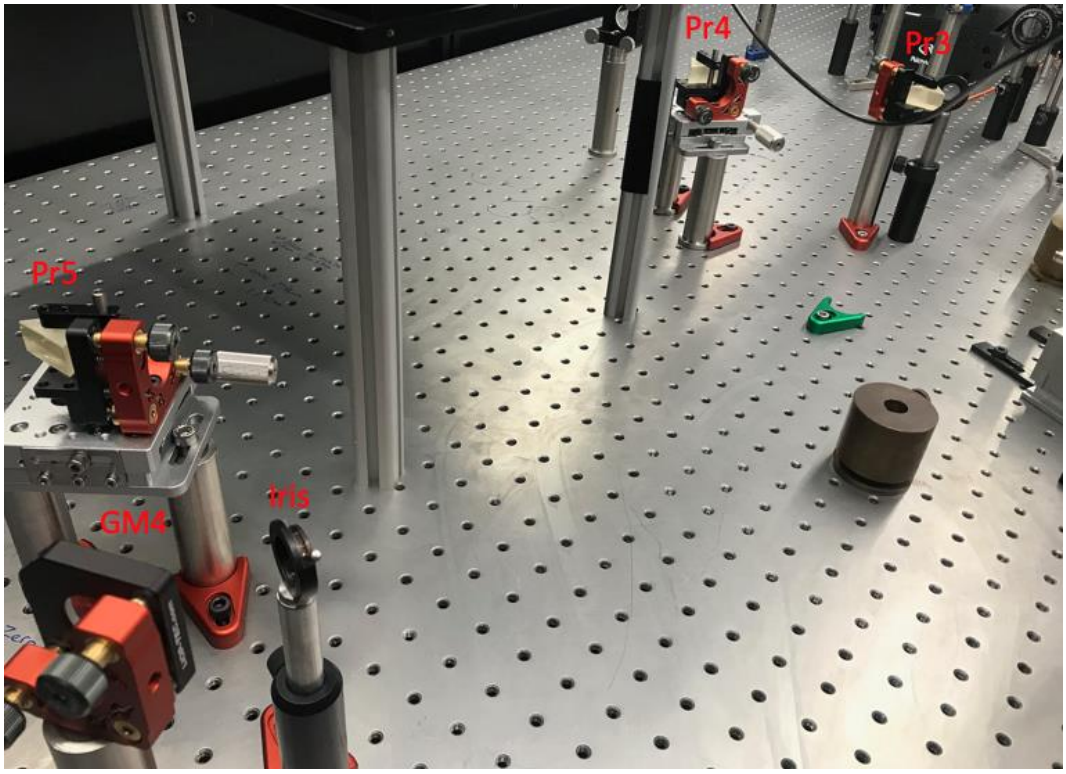

Figure 2.13 A three prism compressor, for the compression and tilting of the 1340 nm gate pulse. The total amount of material traversed is adjusted, by translation of the prisms perpendicular to the gate beam, in order to add appropriate amount of negative dispersion, determined by minimising temporal width of cross-correlation.

Gate Compression and Tilting

The three prisms Pr3, Pr4 and Pr5 are used for the compression of the gate pulses. They are arranged as the first three prisms would be, in a more conventional four prism

compressor, with the fourth prism simply absent here. The removal of the final prism means that in the addition to the compression of the gate pulses, a 'tilt' is added to the pulses wave front. The fourth prism would collimate the spectrally dispersed beam outputted from Pr5, the absence of this fourth prism means that the beam incident upon the BBO crystal retains spectral dispersion, and temporal difference the two edges of the beam effectively produces an angled wave front. By manipulation of both the temporal delay between the two edges of the wave front (compression) and the distance between the two edges, i.e. the spot size (focussing), the angle of the wave front can be adjusted. In order to achieve optimal time resolution, the angle of the wave front should match that of the crystal.

The compression is altered by adjustment of the positions of the prisms Pr3, Pr4, and Pr5 relative to the gate beam path, effectively adjusting the amount of material traversed by the beams. Prisms should be adjusted one at a time, whilst monitoring the temporal width of the cross-correlation. If a minimum in temporal width is reached, there is no need for adjustment of the other prisms.

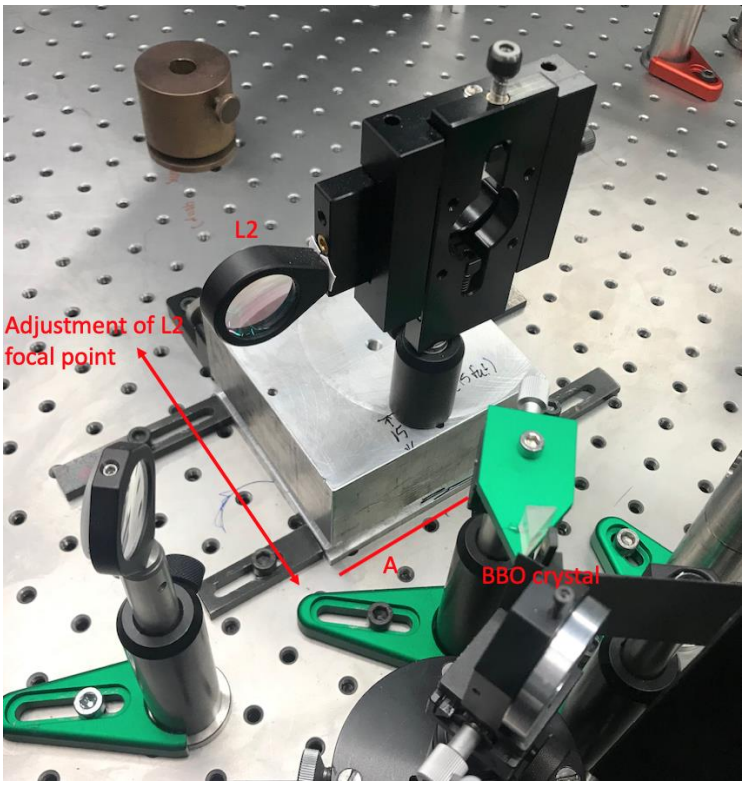

Figure 2.14 L2, the lens for the focussing of the gate beam onto the BBO crystal. The lens is translated parallel to the beam propagation for adjustment of the focal point, tilt of the gate and hence time-resolution are dependent upon lens position. The lens should not be brought forward past the line marked 'A', if beam is focused too tightly onto crystal, crystal may be damaged.

Once the compression is optimised, the position of the lens which focuses the gate beam onto the BBO, L2, can be adjusted (see **Figure 2.14**). The position should be adjusted for minimal fwhm of cross-correlation of pump and gate beams.

2.4.5 Upconversion – Cross-Correlation and Emission Optimization

Cross-Correlation Optimization

Once the pump and gate beams are aligned and their polarizations are correctly set, a cross-correlation of the two beams can be generated and subsequently optimized. The 'cross-correlation' of the pump and gate, is simply the sum frequency of the two beams.

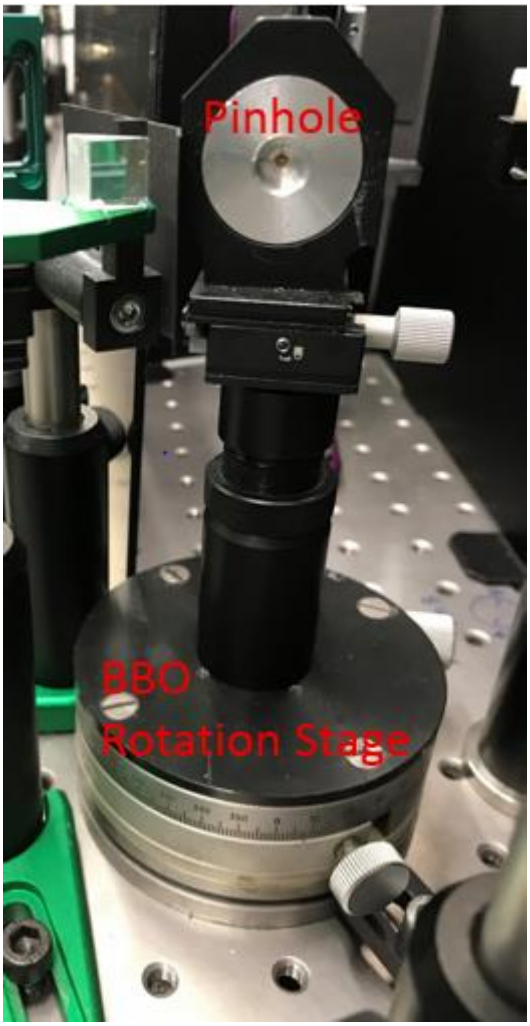

Figure 2.15 A rotation stage, mounted with the holder for the BBO crystal. In this photograph a pinhole is in place of the BBO crystal. The pinhole is used for ensuring spatial overlap of gate beam and emission / pump beam.

The following procedure can be used for the location and optimization of the cross-correlation.

1. The gate beam should be centred upon the pinhole, of **Figure 2.15**, by adjustment of **GM4** (**Figure 2.4**), maximising the power read on a power meter, positioned behind the pinhole.
2. The pump beam should be centred upon the pinhole, of **Figure 2.15**, by adjustment of **CM4** (**Figure 2.4**), maximising the power read on a power meter, positioned behind the pinhole.
3. The pinhole holder should be removed and replaced with a holder mounted with a BBO crystal, see **Figure 2.16**.
4. The rotation stage, on which the BBO crystal is held, should be set to approximately 42°, see **Figure 2.17**.
5. Holding an alignment card in the path of the gate beam, behind the BBO crystal. The red light seen, should be minimized in intensity by rotation of the BBO holder (**Figure 2.16 D**), in the plane of the holder.
6. At this point, the two beams should be spatially overlapped, with the optimal angle for upconversion set. The only remaining parameter for adjustment is the temporal overlap of the two beams. This is done by the translational of the delay stage (**Figure 2.4**). The peak in overlap of the two pulses is denoted 'time zero'. The position on the delay stage corresponding to time zero is denoted the 'time zero position'. An estimate of the time zero position of the stage can be calculated by measuring the path lengths of the two beams and adjusting the stage position such that the two path lengths are equal. The time zero position will remain effectively constant from one experimental day to the next. In order to find the cross-correlation, the stage should be moved to the time zero position last recorded.
7. Once at the 'rough' time zero position, the stage can be scanned for optimal temporal overlap. A card should be placed in front of the mirror in **Figure 2.18**. The pump beam will be seen on the left hand side, the gate beam will be seen on the right hand side (tripled gate, red). The stage should be slowly scanned about the rough time zero position, a blue spot will be seen to 'come and go' as the temporal overlap of cross-correlation is passed over, positioned spatially, in between the pump and gate spots.

8. Once the cross-correlation has been located, spatial overlap, temporal overlap and crystal angle can be optimized. L2 of **Figure 2.14** should be adjusted (X & Y), for maximum brightness of the cross-correlation signal.
9. The angle of the rotation stage, on which the BBO crystal is mounted, should be adjusted for maximum brightness of the cross-correlation signal.
10. Finally, the delay stage position should be adjusted for maximum brightness of the cross-correlation signal.

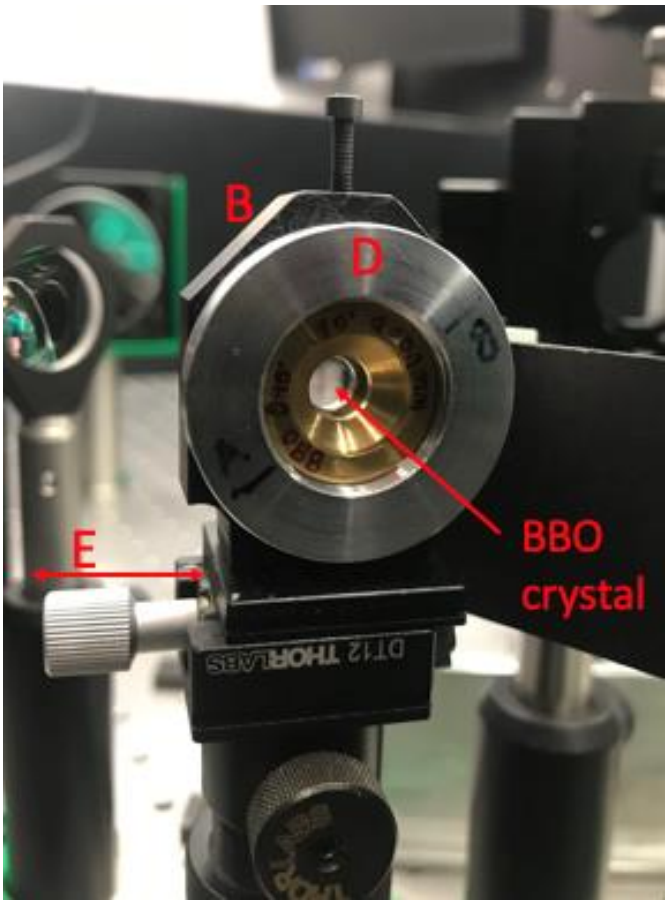

Figure 2.16 Mounted BBO crystal, in a holder, fixed upon a rotation stage. **B:** The holder for the BBO crystal in mounted ring. **D:** BBO holder and mounted BBO crystal. **E:** Screw for tranlation of the BBO crystal (arrow marks plane of translation).

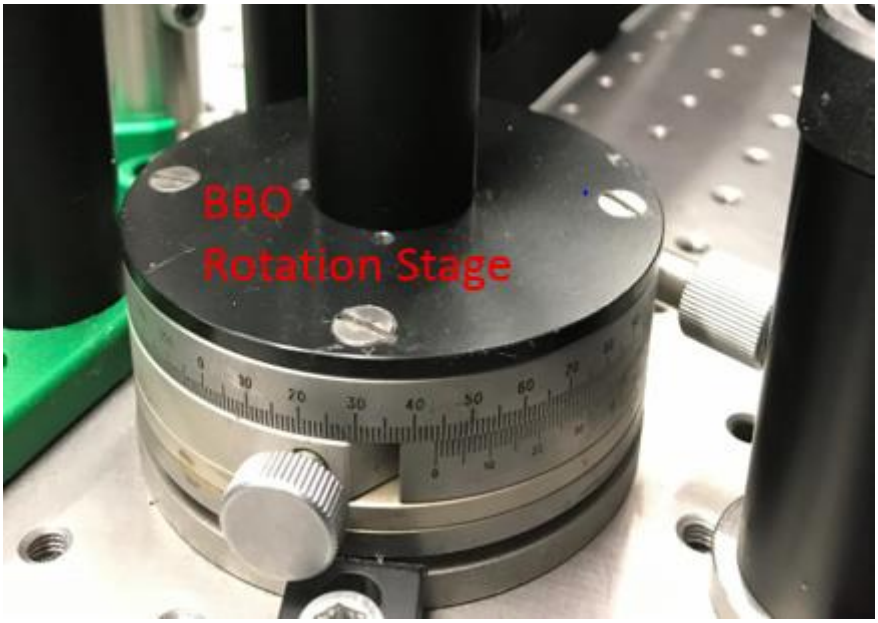

Figure 2.17 The rotation stage on which the BBO crystal is mounted.

Once the cross-correlation has been optimized by eye, it can then be directed onto the spectrograph. The mirror shown in **Figure 2.18**, 'Upconverted signal mirror 1', is used to align the upconverted signal onto the fiber bundle, attached to the spectrograph. The 'curtains' positioned around the face of the mirror are used to minimise the scatter of residual pump, original emission (non-upconverted) and gate beam onto the fiber.

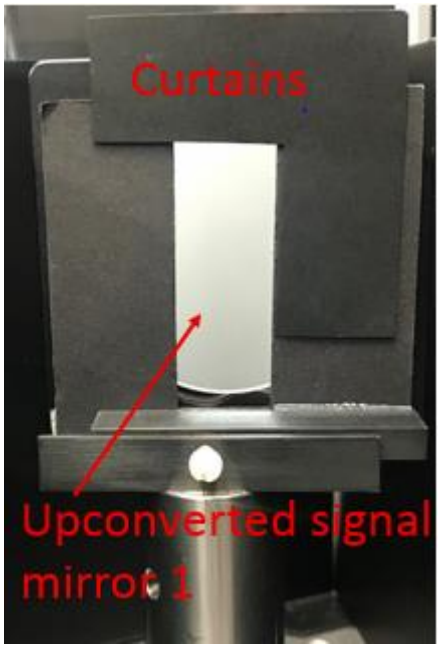

Figure 2.18 Mirror for the collection of the upconverted signal and delivery of the signal to the optic fiber bundle for detection. The curtains are used to mask residual 400 nm pump light and any gate related background signal.

Emission Upconversion Optimization

Once the cross-correlation intensity has been optimized and the signal has been aligned onto the detector, one is now ready to look for upconverted signal from an emissive sample. Emission will be much weaker than the 400 nm pump, therefore, upconverted emission signal will also be much weaker in intensity than the cross-correlation.

The setting of the parameters adjusted above, for the optimization of the cross-correlation, acts as benchmark in the search for upconverted emission signal. The spatial overlap should not need adjustment, however, the crystal angle and temporal overlap will need tweaking.

The angle of BBO crystal needed for efficient upconversion is dependent of the wavelength of the two input beams. The emission will occur at longer wavelength relative to that of the 400 nm pump. Typically, for optimal emission signal, the angle of the BBO crystal will need to be increased by approximately 3 – 4° (from 42 to 45°).

When the pinhole is replaced by the sample cuvette, the pump beam / emission will be retarded. In order to regain temporal overlap, the delay stage will need minor adjustment, the stage will be brought forward until signal is seen.

Once emission signal is observed, optimization, via adjustment of the parameters discussed in points 8 – 10 in the procedure above can be performed once again.

2.5 Data Processing and Analysis

2.5.1 Pump and Gate Assignment

As previously described, both the pump and gate beams are generated from the 800 nm output of a Ti:Sapphire oscillator. The 400 nm pump pulses are generated by frequency doubling of the 800 nm. Scattered pump light, detected with the FLUPS spectrograph allows for an accurate assessment of the pump beam, in situ, at the time of each experiment. The measurement of a raw spectrum, without background removal, allows for the spectral assignment of both the pump and gate pulses. **Figure 2.19** shows an example background recording. Residual pump light, scattered onto the detector, can be seen at 400 nm, this signal allows for accurate assignment of the pump wavelength.

The relatively intense band observed at approximately 450 nm is the product of frequency tripling of the gate in the BBO crystal. The position of this band can be used to assign the gate wavelength, which is 1350 nm, in this case.

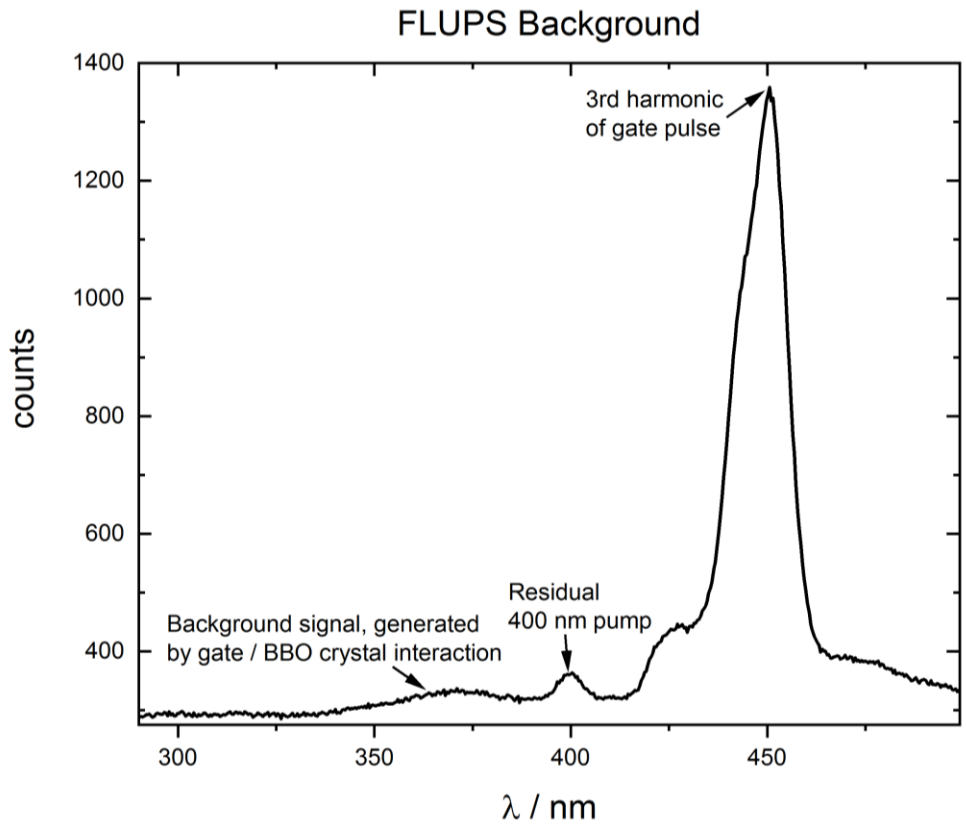

Figure 2.19 The spectrum shows an example of a background recorded prior to an experiment. There are 3 major contributions to the spectrum. The third harmonic of the gate pulse, generated in the BBO crystal, is seen at around 450 nm. Residual pump light, scattered onto the spectrograph, is seen at 400 nm. A broad signal, due to interactions of the gate and BBO crystal, is seen centred around 370 nm.

Additionally, the cross-correlation of pump and gate (sum frequency generation of pump and gate) is often observed in recordings of sample emission, see band at approx. 310 nm in **Figure 2.3**. The spectral position of this signal can also be used to assign the wavelength of the gate beam, once the pump beam has been assigned as above. **Equation 2.5** gives the wavenumber of the cross-correlation (XC), ν_{XC}, which is the sum of the wavenumbers of the pump, ν_{pump}, and the gate, ν_{gate}. **Equation 2.5** is rearranged to give **equation 2.6**. ν_{gate} can be calculated from the recorded position of the cross-correlation and the pump beam respectively. **Equation 2.7** is used to calculate the wavelength of the gate, λ_{gate}.

$$\nu_{XC} = \nu_{pump} + \nu_{gate}$$

equation 2.5

$$\nu_{gate} = \nu_{XC} - \nu_{pump}$$

equation 2.6

$$\lambda_{gate} = \frac{1}{\nu_{gate}}$$

equation 2.7

2.5.2 Cosmic Ray Removal

High-energy cosmic rays, will often hit the detector whilst emission spectra are recorded. The cosmic rays lead to ‘spikes’ superimposed upon the emission spectra. 2 such spikes can be seen in the spectra of **Figure 2.20**.

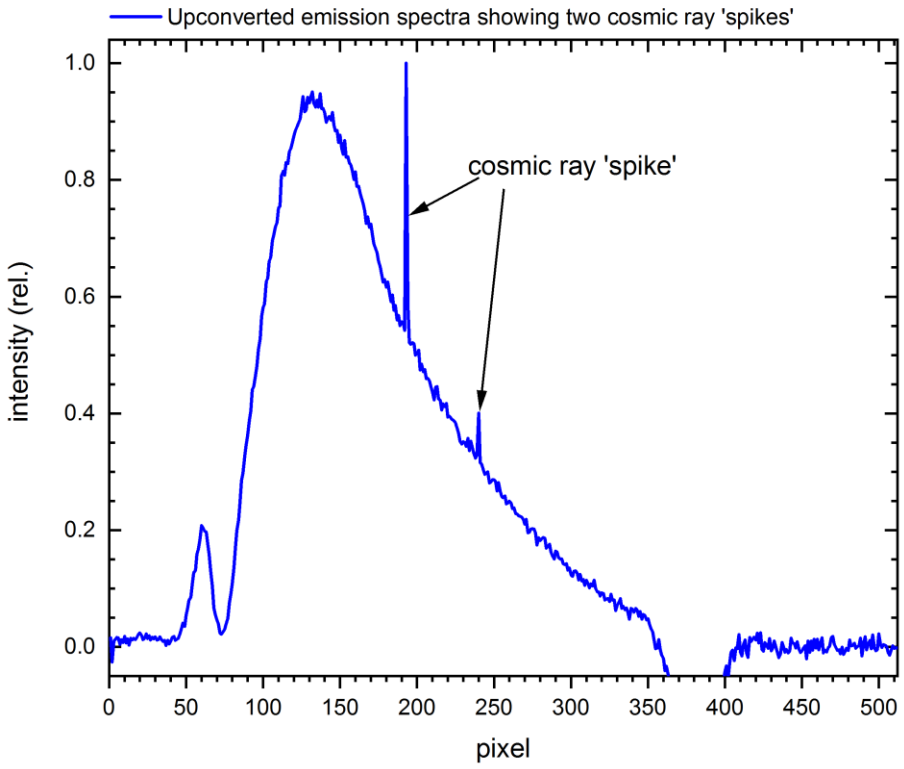

Figure 2.20 Example spectra of upconverted emission, with 2 cosmic ray ‘spikes’ seen.

These spikes should be removed before analysis of the data is performed. For all spectra presented in this thesis, spikes were removed manually, by visual inspection of spectra. Once located, the spikes are accounted for by replacing the measured intensity with the average value of the neighbouring pixels.

2.5.3 Photometric Correction

When fluorescence from a sample is upconverted and detected, at some chosen time delay, a 'technical' count-distribution as a function of pixel is recorded. This spectrum will not have the same spectral shape as that of the true emission. The emission is subject to several incidences of spectral biasing in the process of collection and detection. In order to correct for these wavelength dependent inefficiencies, one must produce a 'photometric correction function', which, once multiplied with the technical recording gives a true spectral representation of the emission, at the chosen time delay.

The most influential process in this spectral biasing is the process of the upconversion of the fluorescence in the crystal. Additionally, the collection optics, optical fiber and spectrograph will impart some spectral biasing.

In practice, the procedure is relatively simple. All of the above components, contributing to the photometric inaccuracy, are accounted for by a single correction function. The function is strongly dependent on the orientation of the BBO crystal, and as such it is not a 'static' function. For each day of experimental measurement, a photometric correction function is produced by the following method. For an in-depth description of the procedure see references.[17,18]

The stationary fluorescence spectra of four dyes in methanol solutions were measured on a fluorimeter, which itself had been calibrated with a secondary lamp. The dyes were chosen as to cover the entire spectral range of the FLUPS spectrometer. The dyes chosen were, 2,5-Bis(5-*tert*-butyl-benzoxazol-2-yl)thiophene (BBOT), Coumarin 6H (C6H), Coumarin 153 (C153) and 4-(Dicyanomethylene)-2-methyl-6-(4-dimethylaminostyryl)-4*H*-pyran (DCM). The dye spectra were taken in the form of photon distributions $\boldsymbol{f_i}^{\boldsymbol{F}}(\tilde{\boldsymbol{\nu}}_{\boldsymbol{F}})$ over wavenumbers. The spectra were fitted with one or more lognormal functions, see **equation 2.8**. The spectrum, photon distribution over wavenumbers, of each dye is obtained by the summing of the lognormal functions, see **equation 2.9**.

$$\mathbf{log\,norm}(\tilde{\boldsymbol{\nu}}_{\boldsymbol{F}}) = \boldsymbol{h}\,\mathbf{exp}\left\{-\ln 2\left(\frac{\ln[1+2\boldsymbol{\gamma}(\tilde{\boldsymbol{\nu}}_{\boldsymbol{F}}-\tilde{\boldsymbol{\nu}}_{\mathbf{0}})/\boldsymbol{\Delta}]}{\boldsymbol{\gamma}}\right)^2\right\}$$

equation 2.8

$$f_i^{(F)}(\tilde{\nu}_F) = \sum \log \mathrm{norm}(\tilde{\nu}_F)$$

equation 2.9

Optimal values for each of the parameters: peak wavenumber $\tilde{\nu}_0$ [cm^{-1}], width Δ [cm^{-1}], asymmetry γ [-] and amplitude h [-] are given in **Table 2.1**.

Table 2.1 Lognormal parameters (see equation 3.1) for the photon distributions over wavenumbers, $f^{(F)}(\tilde{\nu}_F)$, of the four reference dyes (BBOT, C6H, C153 and DCM), in methanol.

Dye	$\tilde{\nu}_0$ / cm^{-1}	Δ / cm^{-1}	γ	h
BBOT	24457	952	0.0303	0.4153
	23859	2216	0.001	0.1797
	22975	1517	0.0564	0.8736
	21532	1599	-0.3423	0.6292
	19826	1989	-0.567	0.1546
	18600	9937	-0.7929	0.0158
C6H	23300	886	0.00001	0.0255
	21000	774	0.087	0.0203
	20717	2950	-0.308	0.9774
	15500	3186	0.00001	0.0499
C153	20481	1601	-0.218	0.0724
	18519	2947	-0.402	0.9913
	16537	2884	-0.781	0.0904
DCM	15829	2388	-0.056	1

The reconstructed spectra of the four complexes, from the lognormal functions, are shown in **Figure 2.21**.

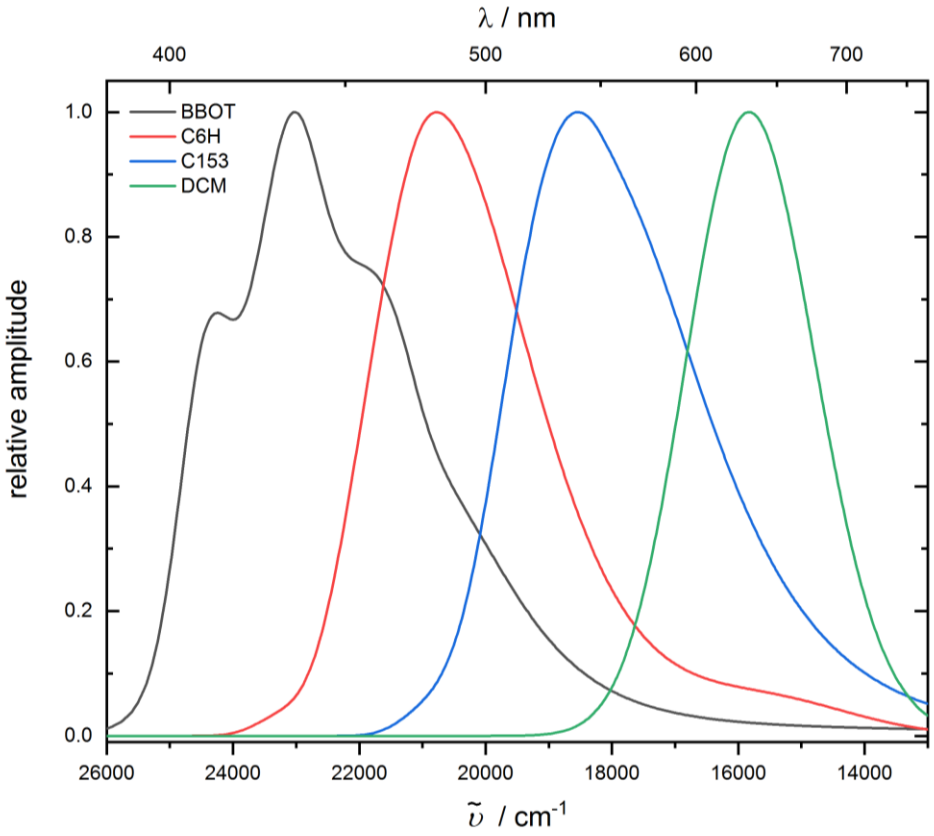

Figure 2.21 Photon distributions over wavenumbers for BBOT (black), C6H (red), C153 (blue) and DCM (green), in methanol solutions. Distributions are reconstructed from fits of stationary fluorescence measurements, with one or more lognormal functions.

It is worth noting here, that although four reference dyes are needed in order to cover the entire spectral range of the FLUPS spectrometer, for particular experiments (or sets of experiments), only one or more of the dyes may be needed to cover the 'useful' spectral range. Useful spectral range here meaning the region of the spectrograph where sample emission is seen. As such, for each day, a different combination of the dyes may be selected for the photometric correction procedure. Here, a set of measurements from the three dyes, BBOT, C6H and C153 will be used in the continued illustration of this correction procedure.

Transient fluorescence spectra of each of the three reference dyes, in methanol solutions, were upconverted with the FLUPS spectrometer. In order to minimise the effect of self-absorption (inner-filter effect) the optical density at 400 nm (pump wavelength) was adjusted to around 0.3. The pump polarization was set to magic angle w.r.t the gate beam.

The power of the pump is set to around 0.5 mW (0.5 μJ per pulse). The time delay was set to 250 ps. At this time, all relaxation (vibrational and solvation) is assumed to have occurred, the spectral shape, to good approximation, is identical to that of the stationary fluorescence. For each dye, *i*, around 60 spectra, with 1 second integration time, are recorded. The average of these gives the corresponding spectrum, $s_i^{(U)}(\lambda_U)$, as upconverted-photon distributions over wavelength, shown in **Figure 2.22**.

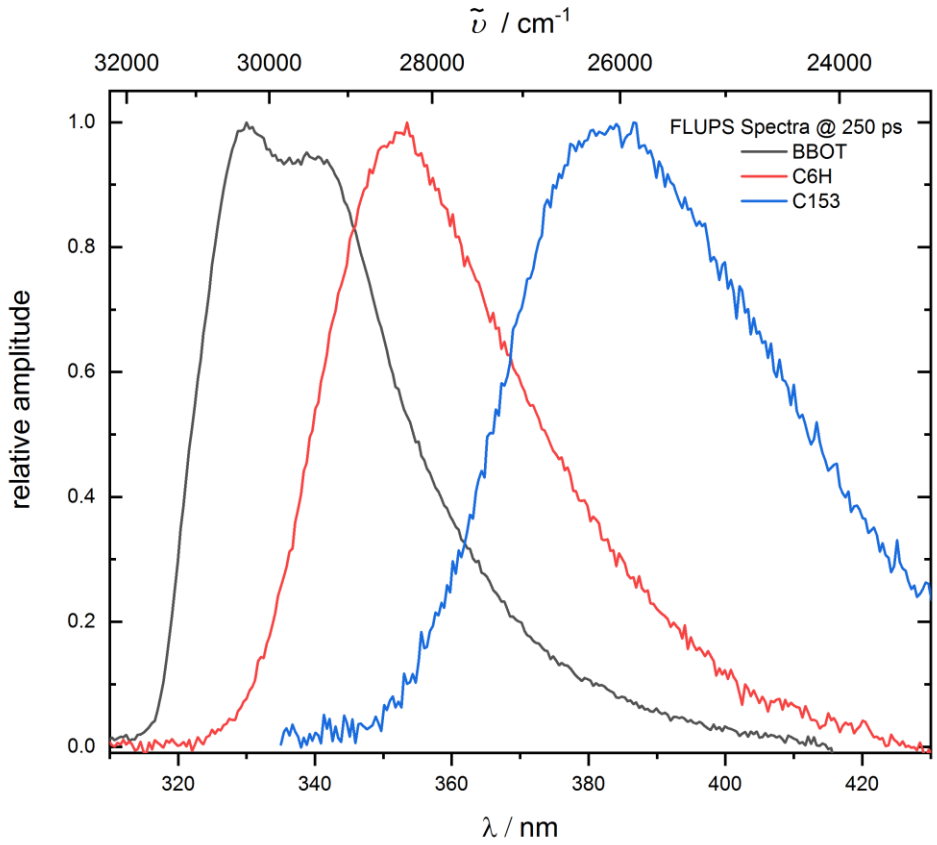

Figure 2.22 Experimental upconverted photon-count distributions, $s_i^{(U)}(\lambda_U)$, over wavelength measured with the FLUPS spectrometer, for BBOT (black), C6H (red) and C153 (blue), in methanol solutions.

In order to use the reference spectra and experimental FLUPS spectra in generation of a correction function, they must first be in the same form, i.e. both as either distributions of photons over wavenumber or upconverted photons over wavelength. Here, the reference spectra, $f_i^{(F)}(\tilde{\nu}_F)$, are converted into distributions over wavelength and then upconverted *in silico* $f_i^{(U)}(\lambda_U)$, see **equation 2.10** and **equation 2.11.**

$$f^{(F)}(\lambda_F) = f_i^{(F)}(\tilde{\nu}_F) \cdot {\lambda_F}^{-2}$$

equation 2.10

$$f_i^{(U)}(\lambda_U) = f_i^{(F)}(\lambda_F) \cdot {\lambda_F}^2 \cdot {\lambda_U}^{-2}$$

equation 2.11

Normalization, by division of peak values, of $f_i^{(U)}(\lambda_U)$ and $s_i^{(U)}(\lambda_U)$ gives $f_{i,norm}{}^{(U)}(\lambda_U)$ and $s_{i,norm}{}^{(U)}(\lambda_U)$ respectively. Both sets of normalized spectra are shown alongside each other in **Figure 2.23**. For each of the three dyes, *i*, a partial correction function is given by division of the normalized reference spectra by normalised experimental spectra, see **equation 2.12.**

$$CF_i = f_{i,norm}{}^{(U)}(\lambda_U) / s_{i,norm}{}^{(U)}(\lambda_U)$$

equation 2.12

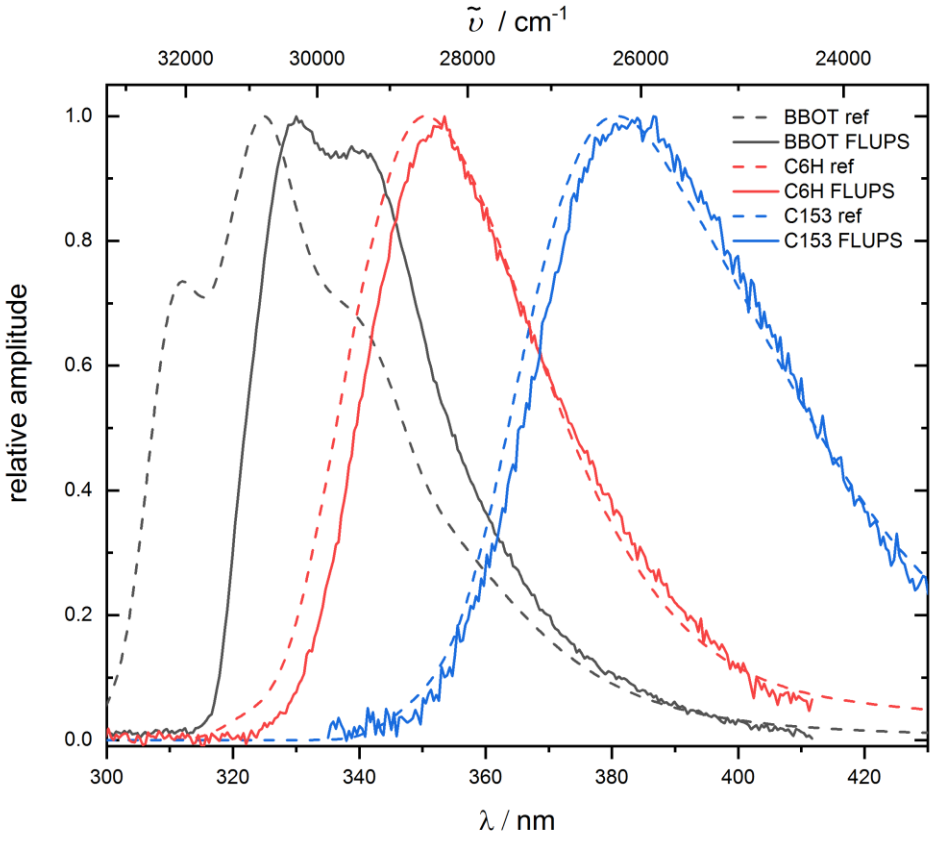

Figure 2.23 Experimental upconverted photon-count distributions, $s_{i,norm}{}^{(U)}(\lambda_U)$, over wavelength measured with the FLUPS spectrometer, for BBOT (black), C6H (red) and C153 (blue), in methanol solutions, shown as solid lines. Corresponding reference spectra in form of upconverted photon distributions over wavelength, $f_{i,norm}{}^{(U)}(\lambda_U)$ are shown as dashed traces alongside measured spectra.

The resultant correction functions, (CF_i), for BBOT, C6H and C153, for this particular experimental setup, are shown in **Figure 2.24**.

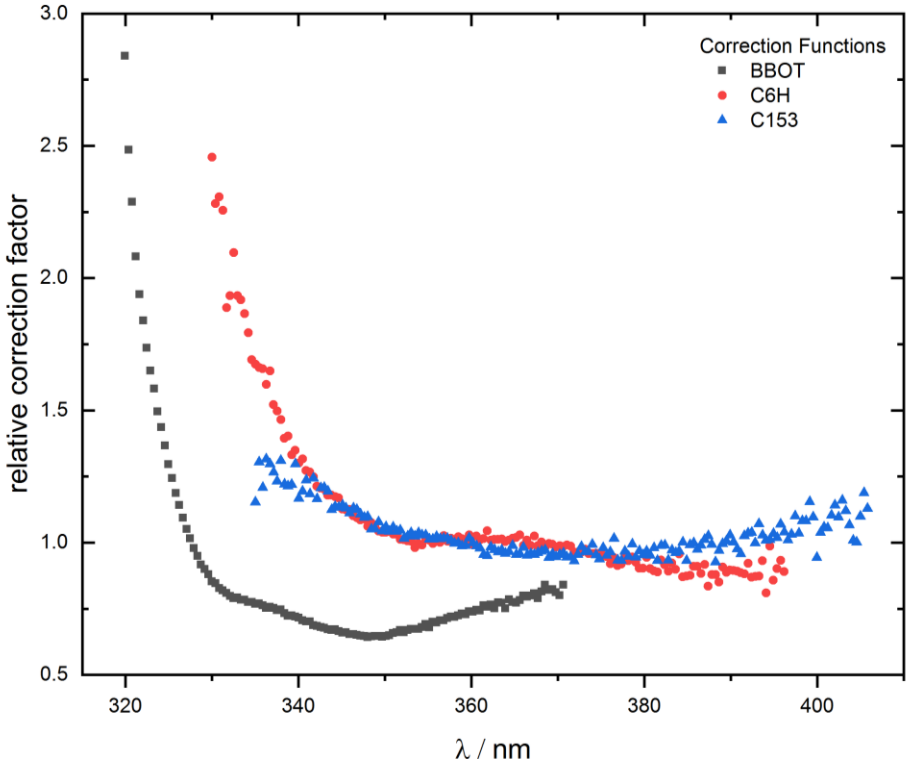

Figure 2.24 Partial photometric correction curves (CF_i) for BBOT (black), C6H (red) and C153 (blue). Obtained by division of ${f_{i,norm}}^{(U)}(\lambda_U)$ with ${s_{i,norm}}^{(U)}(\lambda_U)$.

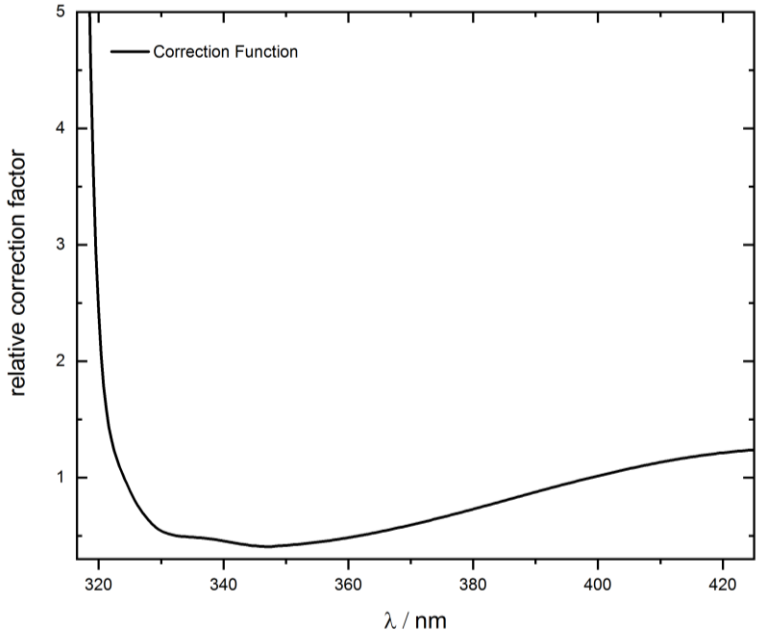

Figure 2.25 Final photometric correction function obtained by fitting a polynomial through the three partial functions, shown in **Figure 2.24**, after scaling using the regions of overlap.

In order to fit a photometric correction function covering the entire useful spectral region, the three partial functions, CF_i, are scaled using the regions of overlap so that they lay upon one another. A single polynomial is used to fit the combined data. The resultant fit is the final correction function, $CF(\lambda_U)$, see **Figure 2.25**. Photometric correction of the initially recorded, 'technical' spectra is simply performed by multiplication of $CF(\lambda_U)$ with each time-gated spectrum, see **equation 2.13.** 'Original' spectra (technical) and corresponding corrected spectra are shown together in **Figure 2.26**.

$$SCorr_s^{(U)}(\lambda_U) = CF(\lambda_U) \cdot S_s^{(U)}(\lambda_U)$$

equation 2.13

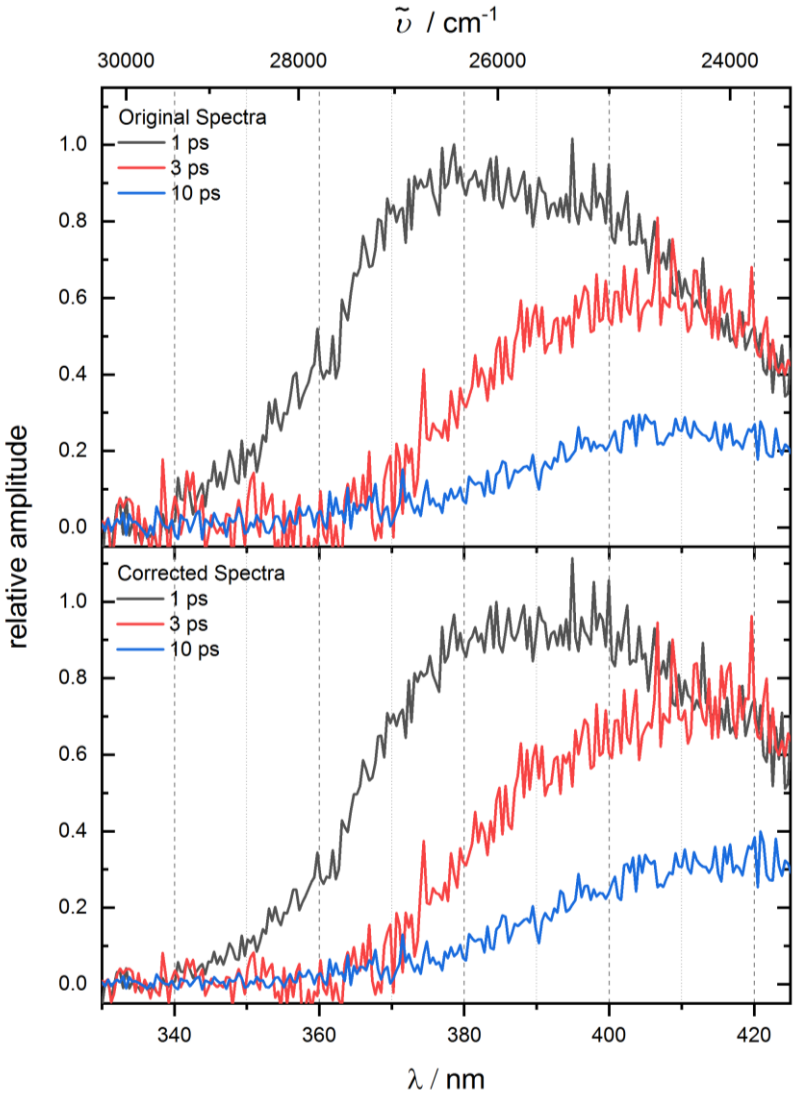

Figure 2.26 Time-resolved emission spectra of a platinum-acetylide complex in DCM. Top panel shows data without photometric correction. Bottom panel shows the same spectra, multiplied with the correction function. Grid lines are shown to aid comparison between spectra.

2.5.4 Group-Velocity Dispersion Correction

For the measurements presented in this thesis, sample solutions were held in 1 mm path length fused-silica cuvettes. 400 nm pump pulses are used to excite the sample and initiate emission. Before being registered on the CCD camera, an emitted photon from a molecule within the sample must pass through any solvent upstream of itself, the exit-face fused-silica window (1 mm) of the cuvette, some amount of calcite prism (used for separation of horizontal and vertical polarization), the collection optics, the BBO crystal (upconversion medium) and finally the fiber optic cable. In the passing through of all these media, the emission will subject to group velocity dispersion (GVD). GVD is the phenomenon that the group velocity of light in a transparent medium depends on the optical frequency or wavelength, see **equation 2.14**.[20] That is, the time taken for a photon to travel from source to detector, through all the media, will depend on wavelength. 'Time-zero' is wavelength dependent, longer wavelength photons will be delayed relative to shorter wavelengths. The resultant temporal delay between different wavelengths is known as chirp. The chirp can be estimated with **equation 2.15.**

$$\mathrm{GVD}(\omega_0) \equiv \frac{\delta}{\delta\omega}\left(\frac{1}{v_g(\omega)}\right)_{\omega=\omega_0}$$

equation 2.14

$$\mathrm{chirp} = (\mathrm{material\ thickness}) \times \mathrm{GVD}(\omega_0) \times (\mathrm{bandwidth})$$

equation 2.15

Similar to the photometric correction described above, a correction procedure is implemented, accounting for all of the GVD components with a single correction function. The objective of this procedure is to obtain a 'zero-time offset' value for each pixel, corresponding to the difference in time between an assigned reference time and the genuine zero-time for pixel in question. The zero-time offset will be used to correct the set of time-delays for each pixel, removing any effects of GVD. A 2D map of un-corrected time-resolved emission is shown in **Figure 2.27**, a curve of time-zero is shown overlaid on the spectra. A fit of this 'curve' is required in order to correct for GVD.

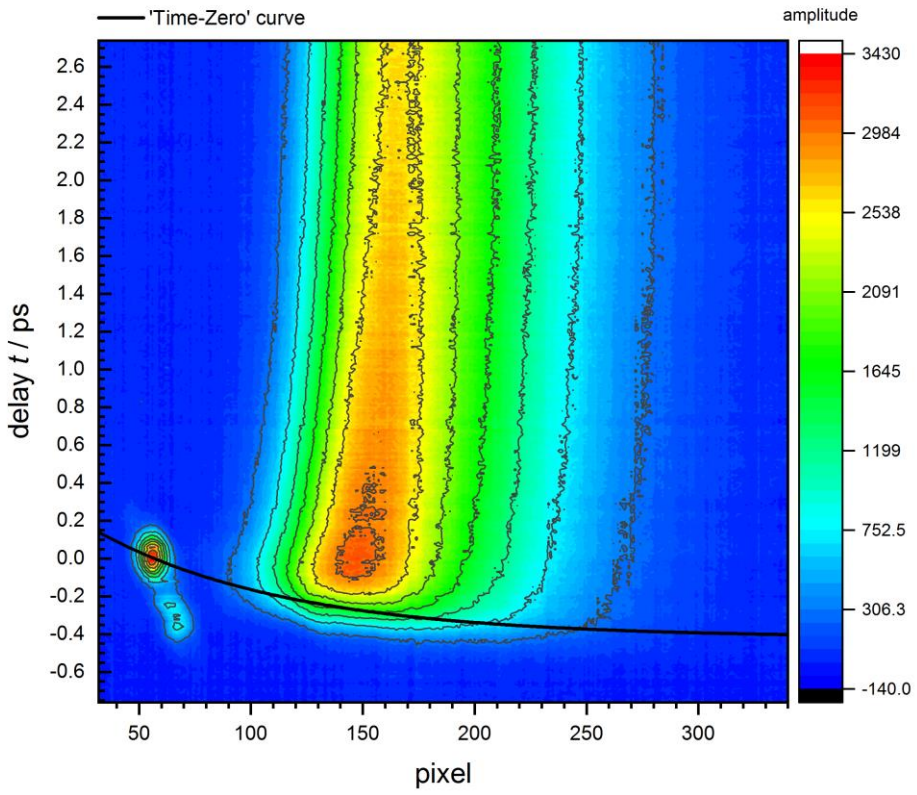

Figure 2.27 A 2D map of un-corrected time-resolved emission of NAP-Pt-Cl in DCM at room temperature. A 'Time-Zero' curve is shown (black line), illustrating the location of the genuine time-zero for each pixel.

The GVD correction is dependent on the precise setup used for each measurement, an important factor is the solvent. As such, the correction is repeated whenever experimental parameters and/or solvent is changed. In order to assess the time-zero offset of each pixel, signal, with a flat rise-response must be recorded: time-resolved emission spectra of the dye, coumarin 153 (C153) in solution, are recorded between -1 and 3 ps in 10 fs steps. This dye was chosen as there are no 'fast' dynamics, which would skew the apparent position of time-zero. It is also important that when performing the measurements, linear steps between time-delays are made, this is crucial when performing interpolation, explained later on. The peak of the cross-correlation of pump and gate (see **Figure 2.27**, around pixel 55, 0 ps) is set to 0 ps, i.e. the time-delay vector is shifted so as to put this point at 0 ps. This point also forms the first point in the time-zero curve.

Kinetic traces, across the C153 emission band, are plotted, around 20 traces across the entire band. The traces are fitted with an IRF function convoluted with an exponential decay function. By definition, the centre (peak) of the IRF function is the time-zero of the trace. By this method, a collection of pixel / time-zero value pairs is obtained. A fit of these values gives a time-zero offset curve, a GVD correction curve, see **Figure 2.27**.

Once the fit is obtained, all experiments performed with the same experimental setup / same solvent, can be corrected. For the sake of the illustration of the procedure below, an example set of pixel / time-zero offset values is provided in **Table 2.2**.

Table 2.2 Example time-zero offset values given pixels, obtained from fit of GVD curve. Values given in picoseconds.

pixel	time-zero offset / ps
1	1.23
2	1.05
3	0.98
4	0.87
5	0.79
6	0.72
7	0.68
8	0.63
9	0.59
...	...
p final	0.27

The fit of the GVD gives a time-zero offset value for every pixel. Subtraction of this value, for each pixel, from the set of time delays for the experiment results in an array of time delays, each pixel having its own unique set of time delays, see **Table 2.3**.

At this point, all GVD has been corrected for, however, the resultant data is somewhat difficult to handle, with no columns of data, there will be no shared x values, i.e. we are unable to plot spectra, only kinetic traces. In order to regain a manageable dataset, we must interpolate to a shared time delay set. A weighted average of the neighbouring values around the new time delays is used to generate a new set of data, with columns of spectra once more. At this point, it is crucial to have small, linear spacing between the time delays. **Figure 2.28** shows an example 2D map of time-resolved emission after correction, the same emission spectra as in **Figure 2.27**.

Table 2.3 Table shows the original time delay values (top row) and then the corrected time delay values for each pixel, upon subtraction of the time-zero offset value for each pixel (see ***Table 2.2***) from the original time delay values.

		time delay / ps							
		-1.00	**-0.20**	**-0.19**	**-0.18**	**-0.17**	**-0.16**	**...**	**3.00**
Pixel	**1**	-2.23	-1.43	-1.42	-1.41	-1.40	-1.39	...	1.77
	2	-2.05	-1.25	-1.24	-1.23	-1.22	-1.21	...	1.95
	3	-1.98	-1.18	-1.17	-1.16	-1.15	-1.14	...	2.02
	4	-1.87	-1.07	-1.06	-1.05	-1.04	-1.03	...	2.13
	5	-1.79	-0.99	-0.98	-0.97	-0.96	-0.95	...	2.21
	6	-1.72	-0.92	-0.91	-0.90	-0.89	-0.88	...	2.28
	7	-1.68	-0.88	-0.87	-0.86	-0.85	-0.84	...	2.32
	8	-1.63	-0.83	-0.82	-0.81	-0.80	-0.79	...	2.37
	9	-1.59	-0.79	-0.78	-0.77	-0.76	-0.75	...	2.41
	...	...	...	...	...	...	...	...	...
	p final	-1.27	-0.47	-0.46	-0.45	-0.44	-0.43	...	2.73

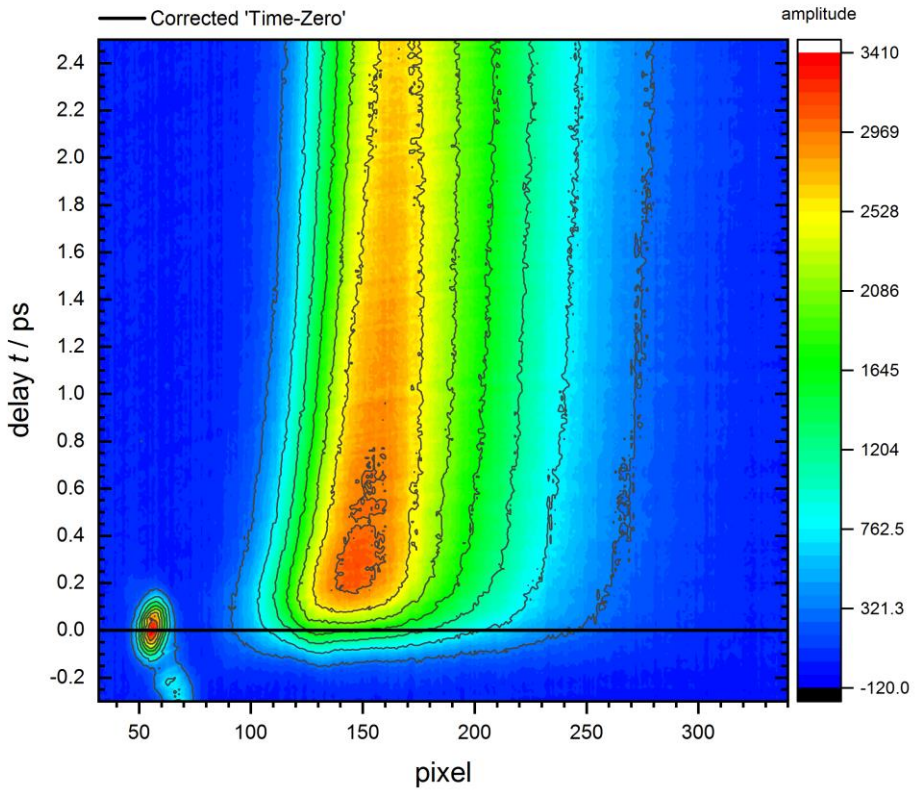

Figure 2.28 A 2D map of corrected time-resolved emission of NAP-Pt-Cl in DCM at room temperature. A corrected 'Time-Zero' line is shown (black line), illustrating the location of the time-zero for each pixel once the correction has been applied.

2.5.6 Distribution Over Wavenumber to Stimulated Emission

In order to make comparisons between the time-resolved emission measurements (FLUPS) and the stimulated-emission bands observed in the TA spectra, the two types of spectra must firstly be of the same form, i.e. they must be presented as the same types of distributions.

Stimulated emission recorded within TA measurements are of the form of a ratio, and therefore can be correctly presented as either SE(wavenumber) or SE(wavelength) with no manipulation required.

The emission spectra recorded with FLUPS have a fundamentally different character, they are of the type of distribution of a number of, F_i, of photons over wavelength.

SE(wvnE)/wvnE is equivalent to $(dFi_E)/dwvnE)/wvnE^3$, where wvnE is the wavenumber of emission. This means that SE(wvnF) is equivalent to $(dFi_E)/dwvnE)/wvnE^2$.

FLUPS data are converted to this form, allowing the comparison of SE from TA with FLUPS spectra. For details of procedure see references.[18]

2.5.7 Data Analysis

Once all the correction procedures, described above, have been undertaken, the data isfit for analysis. Single point fitting and global analysis, described in chapter 1 – Introduction can be performed in order to extract spectral and kinetic information.

2.6 References

1 H. Lemmetyinen, N. V. Tkachenko, B. Valeur, J. Hotta, M. Ameloot, N. P. Ernsting, T. Gustavsson and N. Boens, *Pure Appl. Chem.*, 2014, **86**, 1969–1998.

2 J. Shah, *IEEE J. Quantum Electron.*, 1988, **24**, 276–288.

3 H. Mahr and M. D. Hirsch, *Opt. Commun.*, 1975, **13**, 96–99.

4 W. Jarzeba, G. C. Walker, A. E. Johnson and P. F. Barbara, *Chem. Phys.*, 1991, **152**, 57–68.

5 T. Gustavsson, G. Baldacchino, J.-C. Mialocq and S. Pommeret, *Chem. Phys. Lett.*, 1995, **236**, 587–594.

6 M. G. and and H. Zhang, *Chem. Rev.*, 2004, **104**, 1929–1954.

7 N. Mataga, H. Chosrowjan, Y. Shibata, N. Yoshida, A. Osuka, T. Kikuzawa and T. Okada, *J. Am. Chem. Soc.*, 2001, **123**, 12422–12423.

8 M. Du and G. R. Fleming, *Biophys. Chem.*, 1993, **48**, 101–111.

9 H. Chosrowjan, N. Mataga, Y. Shibata, S. Tachibanaki, H. Kandori, Y. Shichida, T. Okada and T. Kouyama, *J. Am. Chem. Soc.*, 1998, **120**, 9706–9707.

10 P. Abbyad, X. Shi, W. Childs, T. B. McAnaney, B. E. Cohen and S. G. Boxer, *J. Phys. Chem. B*, 2007, **111**, 8269–8276.

11 A. Cannizzo, F. van Mourik, W. Gawelda, G. Zgrablic, C. Bressler and M. Chergui, *Angew. Chemie Int. Ed.*, 2006, **45**, 3174–3176.

12 R. M. van der Veen, A. Cannizzo, F. van Mourik, A. Vlček and M. Chergui, *J. Am. Chem. Soc.*, 2011, **133**, 305–315.

13 L. De Cola, *Coord. Chem. Rev.*, 1998, **177**, 301–346.

14 O. Bräm, F. Messina, A. M. El-Zohry, A. Cannizzo and M. Chergui, *Chem. Phys.*, 2012, **393**, 51–57.

15 W. Gawelda, A. Cannizzo, V.-T. Pham, F. van Mourik, C. Bressler and M. Chergui, *J. Am. Chem. Soc.*, 2007, **129**, 8199–8206.

16 M. Chergui, *Dalt. Trans.*, 2012, **41**, 13022.

17 X.-X. Zhang, C. Würth, L. Zhao, U. Resch-Genger, N. P. Ernsting and M. Sajadi, *Rev. Sci. Instrum.*, 2011, **82**, 063108.

18 M. Gerecke, G. Bierhance, M. Gutmann, N. P. Ernsting and A. Rosspeintner, *Rev. Sci. Instrum.*, 2016, **87**, 053115.

19 R. L. Fork, O. E. Martinez and J. P. Gordon, *Opt. Lett.*, 1984, **9**, 150–152.

3 Ultrafast Emission and Intersystem Crossing in Asymmetric Platinum(II) 'Donor-Bridge-Acceptor' Complexes

3.1 Introduction

As mentioned in the introduction (Chapter 1), Donor-Bridge-Acceptor (D-B-A) compounds are wide-spread models for studying light harvesting, the development of new artificial photosynthetic assemblies, and improving our understanding of the factors governing electron- and energy- transfer in photoinduced reactions.[1–4] D-B-A systems based on transition metal complexes (whereby a metal ion may take part in either some or all parts of the assembly) are studied extensively, with several motives. Transition metal complexes show strong absorption in the visible region, often due to a charge-transfer transition, such as metal-to-ligand charge transfer, which generates an electron-hole pair upon excitation; their redox potentials can be tuned in a broad range by the changing of the central atom and/or ligands' and in a LEGO-style approach, various assemblies of metal complexes are relatively easily constructed. Square-planar d8 Pt(II) complexes are particularly attractive in this regard due to the relative ease of synthesis, lack of chirality (often an issue with d6 octahedral complexes), and directionality of electron transfer. As part of previous research into photoinduced electron transfer in our group, the ultrafast photoinduced excited state dynamics of linear asymmetric Pt(II) donor-bridge-acceptor complexes were extensively studied. Molecular structures are shown in **Figure 3.1 (top)**. A combination of transient infrared and transient absorption spectroscopies, using 50 fs, 400 nm excitation, were employed. Excitation was found to lead to the population of a manifold of ^{3}MLCT states, proceeded by a cascade of charge and energy transfer events. Branching from the initially populated CT manifold led to the population of a NAP – centred triplet state and a triplet charge-separated state (^{3}CSS), with involvement of the PTZ donor.[5]

These complexes have also exhibited an unusual behaviour which had not been previously noted for liquid-phase photochemistry: transient IR-excitation of the bridge-localised vibrations in the course of electron transfer lead to changes in the relative population of the product states. This effect was termed 'IR-control'. Experiments performed on the NAP-Pt-PTZ complex showed such remarkable behaviour. Specifically, introduction of an IR-pump at around 2000 cm-1 to excite Pt/acetylide bridge vibrations after the 400-nm

excitation which initiated electron transfer from the bridge to the acceptor, allowed for the manipulation of the branching ratio to the final two states, the full ^{3}CSS and the NAP-centred triplet state.[6]

A summary of the dynamics of NAP-Pt-PTZ is shown in **Figure 3.1 (bottom)**.

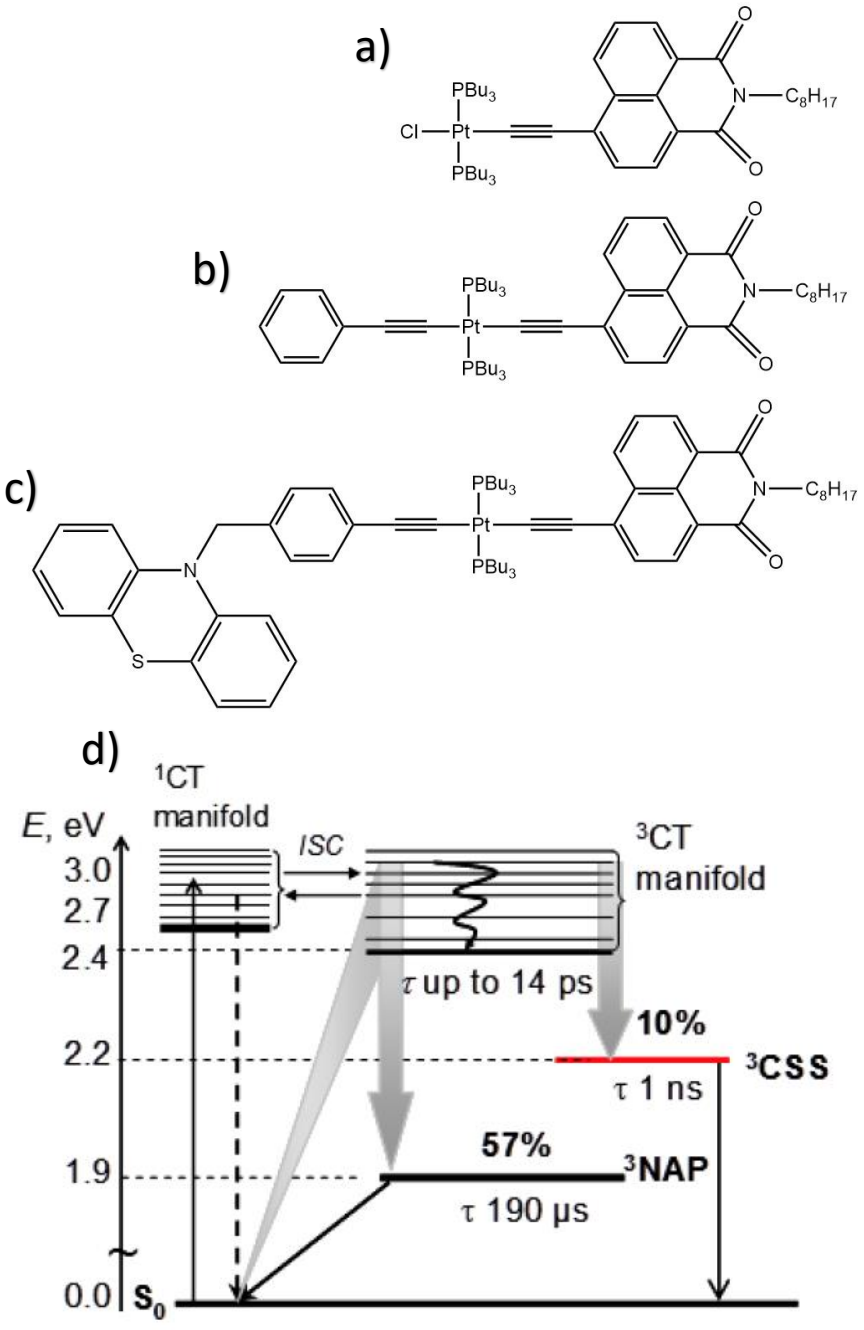

Figure 3.1 From top to bottom, chemical structures for NAP-Pt-Cl (**a**), NAP-Pt-Ph (**b**) and NAP-Pt-PTZ (**c**), discussed in the context of IR-control. (**d**) A summary of the electronic states and processes for NAP-Pt-PTZ, in dichloromethane, upon 400 nm excitation. The energy assignments are derived from a combination of absorption, emission and cyclic-voltammetry data.

The excited state dynamics of the two model complexes, NAP-Pt-Cl which only contained the acceptor and "half" of the bridge, and NAP-Pt-Ph which did not contain the PTZ-donor, were also studied. Transient absorption data for the three complexes are shown in **Figure 3.2**.

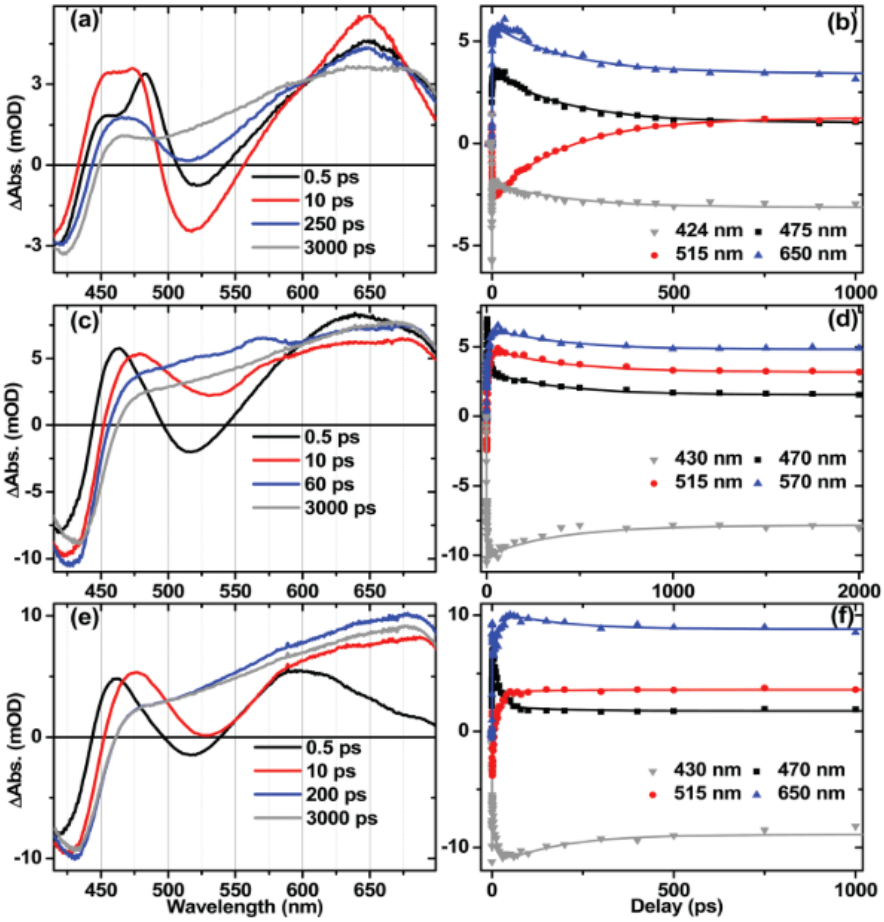

Figure 3.2 Transient absorption spectra, at select time delays, alongside kinetic traces at select spectral positions, for NAP-Pt-Cl (a, b), NAP-Pt-Ph (c, d), and NAP-Pt-PTZ (e, f). All are as solutions in dichloromethane, with 400 nm excitation.[6]

In the transient absorption spectra of all complexes, stimulated emission (SE), persisting for 10's of picoseconds is observed. The SE is assigned as stemming from the MLCT manifold, and by definition, at least, these will be singlet states, as the ground state has singlet character. Global analysis reveals lifetimes for the SE between 13 and 212 ps. This seems somewhat self-contradictory, with ISC assumed to occur within the IRF, yet SE showing lifetimes several orders of magnitude larger than the IRF. The reasons for the initial assumption of the ISC in these complexes being on the order of hundreds of fs or

less, have been outlined in Chapter 1 - Introduction. Briefly, it has been presumed that due to large spin-orbit coupling constant of the Pt(II) centre, and due to direct involvement of Pt in most of the electronic states and electronic transitions that lead from the initial excitation to the final charge-separated state, the ISC will be extremely efficient. Another argument to support the ultrafast ISC was that ^{3}NAP absorption features have been observed in both electronic transient absorption spectra, and TRIR, within the instrument response of each of the methods. Yet, there is also SE present in the transient absorption spectra.

There was thus a contradiction between the necessity of entering the triplet manifold (to account for observation of the state assigned to ^{3}NAP) and the necessity to stay in the singlet manifold for approximately 200 ps (Cl-complex), 20 ps (Ph-complex) and 15 ps (PTZ-complex).

In order to explain these data, one may consider that the idea of step-wise, sequential, processes breaks down on the ultrafast time-scale, and especially in TM complexes. One of the reasons being that transition metal complexes in general possess a manifold of close-lying excited states of different origin (e.g., ligand-centred, CT, others) and that the energy differences between “pure” singlet states and “pure” triplet states may be quite small. For example, in the case of NAP-Pt-Cl, excitation with 400 nm pulse would lie above the energy levels of the “thermalized” S1 – S3 states, and above T1 – T4.

Overall, this implies that within the ~100 fs laser pulse, it is possible to populate a manifold of spin-orbit states, whereby the notion of pure spin-states is no longer valid. If the systems were to go through a discrete change in spin, we would expect to be able to distinguish the different spin-states via time-resolved emission, with drastic decreases in intensity of emission as states of singlet character transition into triplet states, and thus loss of strong fluorescence (to the singlet ground state) and a gain of weak phosphoresce. If, as speculated, there is a dense pool of states with mixed singlet – triplet character, it may not be possible to distinguish discrete states spectroscopically. There would be a gradual red-shift to lower energy emission as the system dissipates excess excitation energy, with vibrational relaxation, ISC and IC all occurring in tandem. As a function of time, the system may maintain a relatively constant mix of singlet – triplet character,

manifesting in no significant changes in oscillator strength of the ensemble as a whole and no drastic changes in emission intensity.

The SE, in all cases, is heavily overlapped with excited-state absorption band. Femtosecond time-resolved emission spectroscopy is the ideal tool for the study of such a signal, removing the additional absorption bands and perhaps allowing for the resolution of the early time dynamics, hidden with TA and TRIR spectroscopies.

Additionally, from a fundamental viewpoint, this series of complexes makes an ideal study for the dependence of ISC on the extension of ligand conjugation, if ISC is to be observed.

3.1.1 Chapter Aims

The work presented in this chapter aims to achieve the following.

1. Produce the most accurate possible account of the ultrafast emission of a family of three asymmetric platinum donor-bridge-acceptor complexes.
2. Investigate the process of intersystem crossing within these three complexes, distinguishing between the emission from singlet and triplet states, and therefore tracking the evolution of spin in the systems as a function of time.
3. If different spin-states are distinguishable in these systems, the effects of the differences in molecular structures between the three complexes will be investigated.

3.2 Results

3.2.1 NAP-Pt-PTZ and Constituent Building Blocks Chemical Structures

The chemical structures of NAP-Pt-PTZ and the two building blocks, NAP-Pt-Ph and NAP-Pt-Cl are shown in **Figure 3.1 (top)**. All of the complexes feature the same central unit, comprised of a square planar platinum centre and two trans 'PBu_3' groups. They all also share the same acetylide-NAP acceptor unit. NAP-Pt-Cl features a chloride in place of a donor unit. NAP-Pt-Ph features a Ph-acetylide unit.

3.2.2 UV-Vis Absorption Spectroscopy

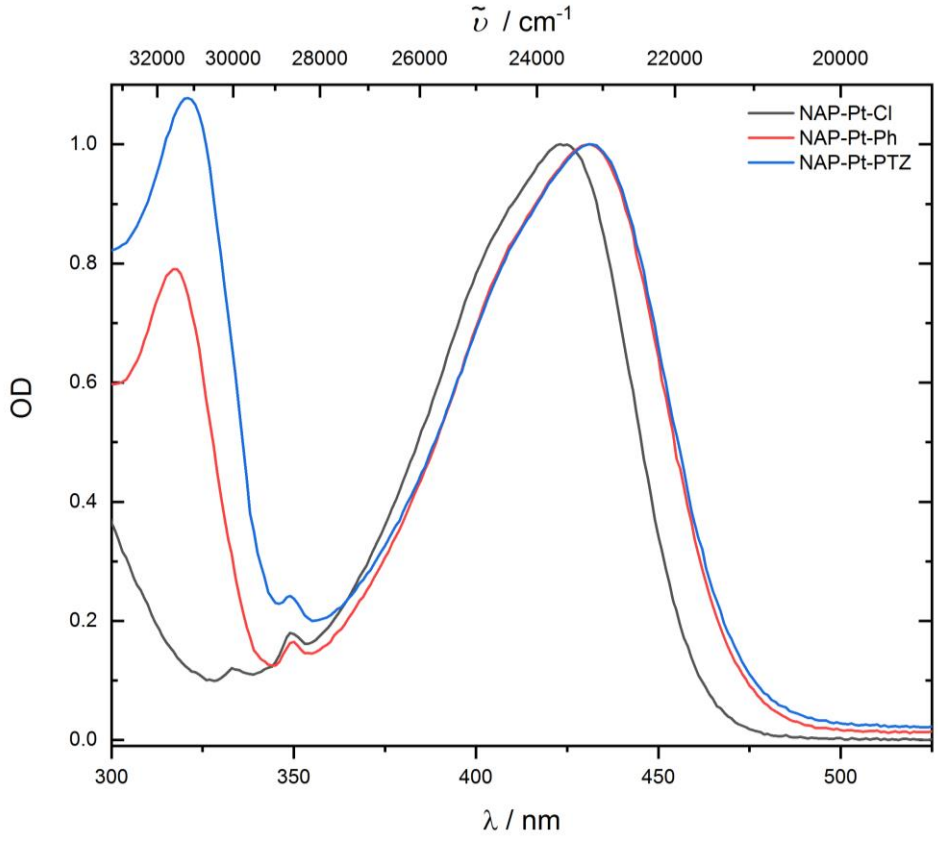

Figure 3.3 UV-Vis absorption spectra for NAP-Pt-Cl (solid black line), NAP-Pt-Ph (solid red line) and NAP-Pt-PTZ (solid blue line) in dichloromethane (CH_2Cl_2) at room temperature.

The steady-state absorption spectra of the three compounds, in CH_2Cl_2 are shown in **Figure 3.3**. In all compounds the region of 240 to 350 nm exhibits bands arising from intraligand π-π^* transitions. Spectra of both NAP-Pt-Ph (red) and NAP-Pt-PTZ (blue) feature a transition which is centred at around 320 nm. This is not present for NAP-Pt-Cl (black dashed line) and is therefore assigned as a phenyl/PTZ centred transition. The lowest energy transition in NAP-Pt-Cl, centred at 424 nm, is assigned as a metal-to-ligand

charge transfer (MLCT) transition from the Pt/acetylide centre to the NAP ligand. The breadth of this band (centred at 424 nm) indicates that it is comprised of several charge-transfer transitions; indeed, previous studies including DFT suggest that it is an envelope of MLCT transitions. Similar absorption bands are present in the absorption spectra of both NAP-Pt-Ph and NAP-Pt-PTZ, almost identical to one another, however, slightly red-shifted relative to NAP-Pt-Cl, centred at 430 nm.

3.2.3 Ultrafast Time-Resolved Emission Spectroscopy (Fluorescence Upconversion)

Time-resolved emission studies where performed using a fluorescence upconversion spectrometer. Excitation of the sample with 400 nm, ca. 70 fs pulses, leads to emission across visible spectrum. This emission signal is upconverted (sum-frequency) with ~100 fs near-infrared “gate pulses” (1340 nm), and the resulting emission spectrum is recorded on a multiplex detector. Photometric correction for set-up sensitivity across the wavelength range of interest (300 – 430 nm) and time-zero dispersion (group-velocity dispersion) are performed, see Experimental Section and references for details.[7,8] In this way, a spectrum as distribution of emission photons over wavenumbers for a range of delay times between pump and gate pulses, are obtained. The details of the procedure are discussed in Chapter 2 – ‘Fluorescence Upconversion Spectroscopy (FLUPS)’.

Transient absorption spectra for the compounds discussed here have been reported previously.[9] For ease of comparison between the time-resolved emission data presented here and the stimulated emission observed in the transient absorption spectra, the data here are presented in the form of stimulated emission distributions. Optical densities at excitation wavelengths, in the pathlengths used, were approximately 0.3.

NAP-Pt-Cl

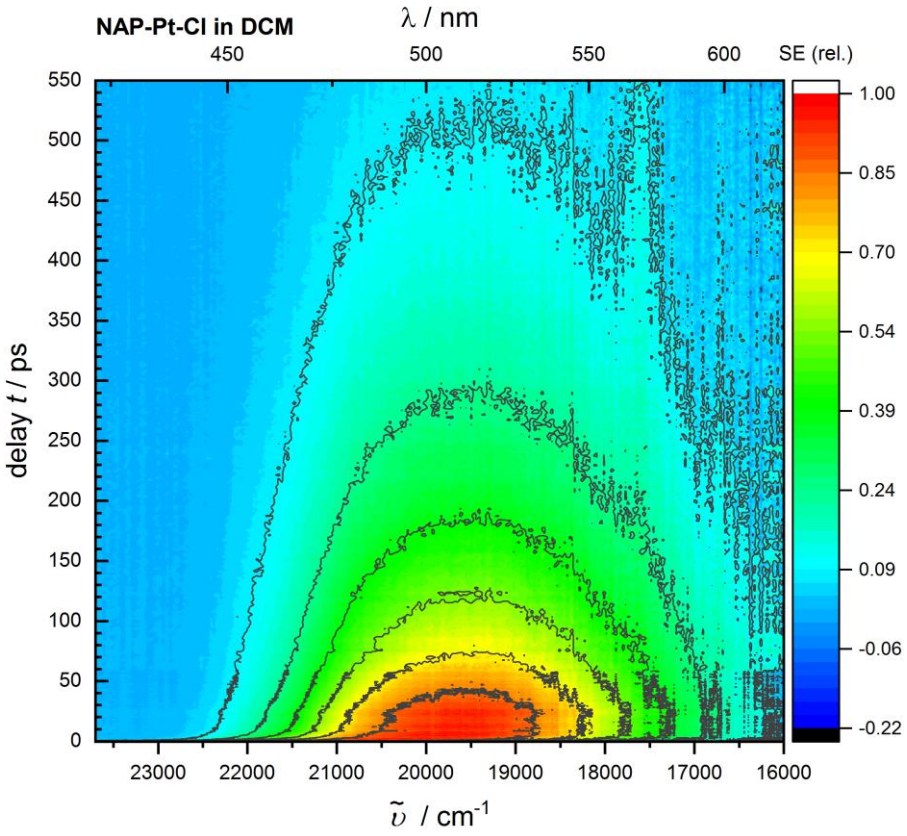

Figure 3.4 A 2D map of time-resolved emission spectra of NAP-Pt-Cl in dichloromethane upon 400 nm excitation, obtained by fluorescence upconversion. The optical density at the pump wavelength was approximately 0.3. Photometric- and time-zero dispersion- corrections have been applied to the raw data.

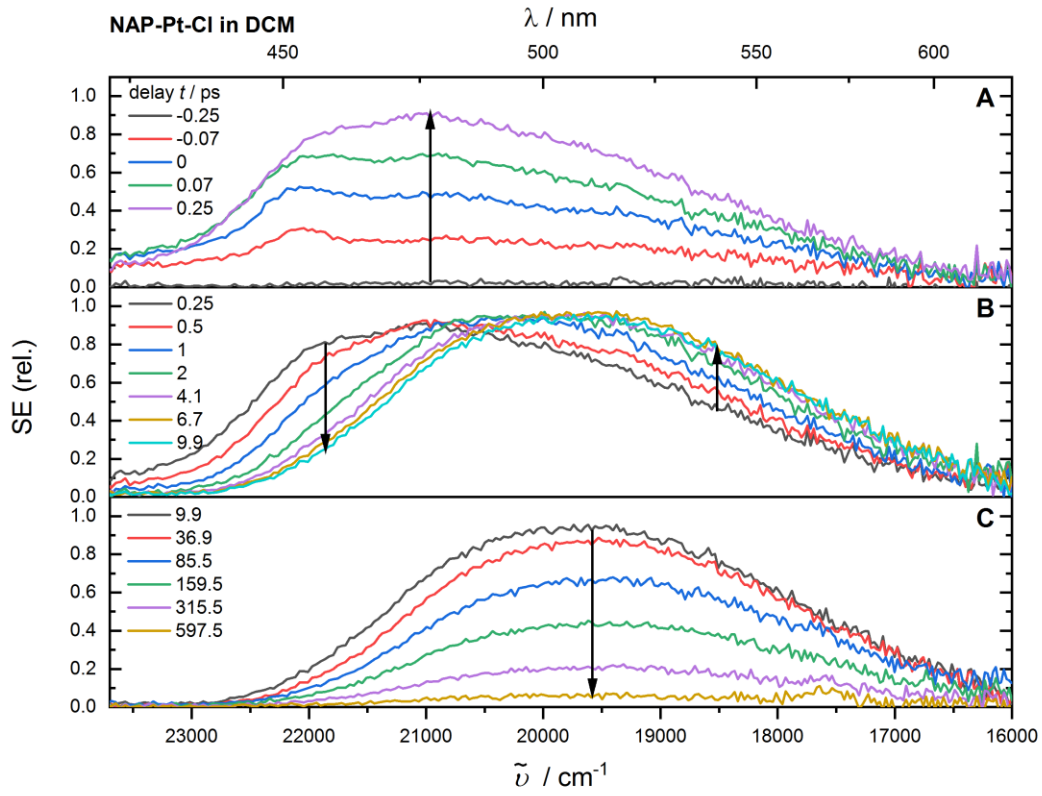

Figure 3.5 Time-resolved emission spectra of NAP-Pt-Cl in dichloromethane upon 400 nm excitation, obtained by fluorescence upconversion. The optical density at the pump wavelength was approximately 0.3. Three distinct temporal ranges are shown in each of the panels, A (-250 – 250 fs), B (250 fs – 9.9 ps) and C (9.9 ps – 597.5 ps). Arrows indicate the characteristic evolutionary feature within each range. Photometric- and time-zero dispersion- corrections have been applied to the raw data.

Figure 3.4 and **Figure 3.5** show time-resolved emission spectra of NAP-Pt-Cl, in a dichloromethane (CH_2Cl_2) solution, upon ~70 fs, 400 nm excitation. The spectra were obtained by fluorescence upconversion as outlined above. Three distinct temporal regions, each showing clear changes in the spectral shape were identified, and are shown in each of the panels **A**, **B** and **C**. Excitation with 400 nm (25,000 cm^{-1}) light leads to population of the singlet metal-to-ligand charge transfer state, ^{1}MLCT (absorption maximum at 424 nm or 23,585 cm^{-1}), with excess vibrational energy of 1415 cm^{-1} (0.175 eV). Panel **A** shows the rise of a broad emission band, covering the region of 16,000 to 24,000 cm^{-1}, with a maximum at about 21,000 cm^{-1}. Within experimental error the intensity rises uniformly across all wavenumbers, within the instrument response. This immediate emission band is 4000 cm^{-1} lower in energy than the 25,000 cm^{-1} (400 nm) excitation, with the excess energy dissipated within the instrument response. Initially, as

seen for example in the spectrum at 0.25 ps, the emission appears to be composed of multiple bands, with a weak shoulder at about 19,000 cm^{-1}.

A relatively sharp band, overlaid with the emission, observed at about 22,000 cm^{-1}, is assigned to the Raman scattering of the 25,000 cm^{-1} (400 nm) excitation pulse associated with the 3000 cm^{-1} Raman-active transition of dichloromethane. This band rises and decays with the IRF, confirming the origin of the signal.

Within the first 10 picoseconds, considerable spectral change is observed (Panel **B**). The emission spectrum shifts towards lower energy, to a maximum at about 19,500 cm^{-1} by ca. 10 ps. After 10 ps, no further shift of the band position is observed. Concomitantly with the spectral shift, the emission spectrum becomes narrower and undergoes significant change in spectral shape. The spectrum at 9.9 ps, unlike that of 0.25 ps, exhibits no obvious shoulder and displays a shape more typical of a single emission band. These 'early time' dynamics could be signatures of vibrational relaxation. Within the first 10 ps, very little change in emission intensity is observed, the area under the spectra remains almost constant as a function of time.

Panel **C** shows the exponential decay of the quasi-stationary emission band on a ~200 ps time scale. At 597.5 ps, the longest time delay measured, very weak emission signal persists.

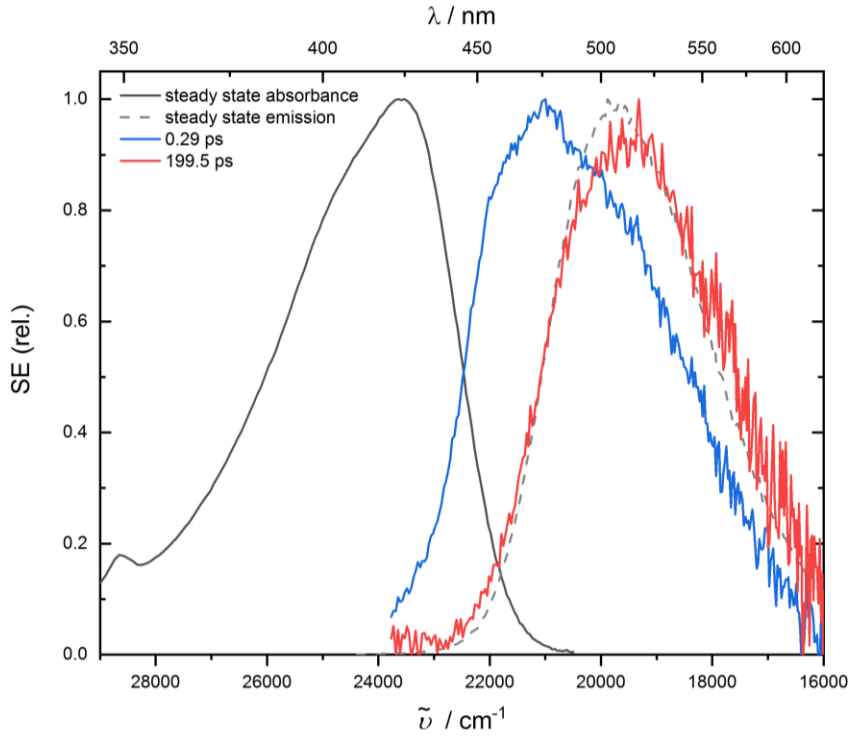

Figure 3.6 Steady-state absorption (black solid trace) and steady-state emission (grey dashed trace) spectra for NAP-Pt-Cl, in dichloromethane. Shown alongside these are time-resolved emission spectra, at 0.29 ps (blue trace) and 199.5 ps (red trace).

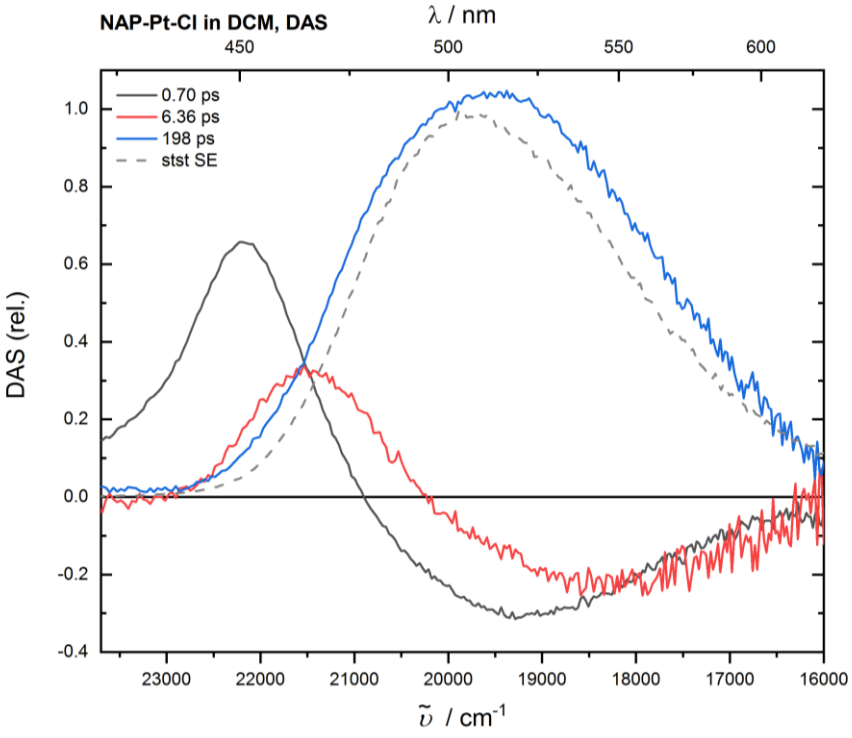

Figure 3.7 Decay-Associated Spectra (DAS) of the emission spectra of NAP-Pt-Cl (shown in **Figure 3.5**), obtained via global analysis using three exponential time functions. The corresponding time constants are given as insets. The steady-state (stst) emission spectrum of NAP-Pt-Cl, converted to the form of stimulated-emission (SE), is also shown (grey dashed trace, stst SE).

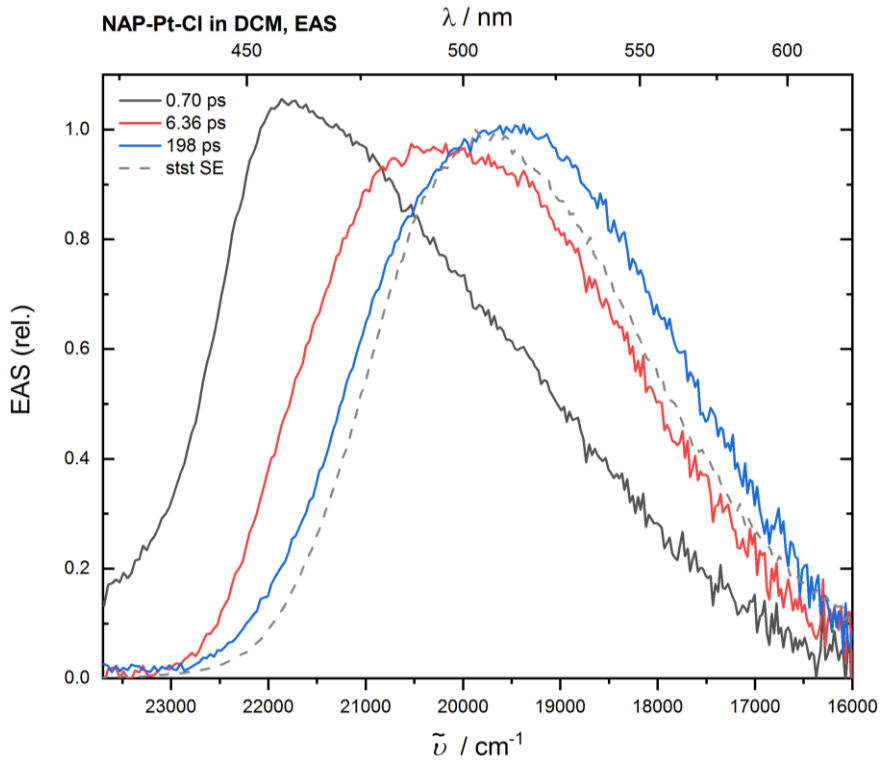

Figure 3.8 Evolution-Associated Spectra (EAS) of the emission spectra of NAP-Pt-Cl (shown in **Figure 3.5**), obtained via global analysis using three exponential time functions. The corresponding time constants are given as insets. The steady-state (stst) emission spectrum of NAP-Pt-Cl, converted to the form of stimulated-emission (SE), is also shown (grey dashed trace, stst SE).

Global analysis has been performed in order to extract spectral and dynamic information. Initially a parallel kinetic model with three exponential time functions was used to fit the data, i.e., it is assumed that the initial population of states decays along 3 parallel pathways to the ground state. The resultant Decay-Associated Spectra (DAS) are shown in **Figure 3.7**, with the corresponding kinetic parameters shown in the inset. The decomposition of the spectra into the DAS gives an estimate of the number of observable processes / states involved in the dynamics. The 0.91 and 7.7 ps DAS components (black and red line, respectively) describe the initial red-shift and narrowing, illustrated in panel **B** of **Figure 3.5**. The spectrum of this component matches the steady-state emission spectrum of the complex (displayed in **Figure 3.6**, dashed grey line) and is therefore assigned as emission from a charge transfer state. The DAS obtained suggest the emission observed arises from a single electronic state. The spectra of the 198 ps component can be considered as that of the thermally-equilibrated electronic state, with the 0.91 and 7.7 ps components describing the relaxation from the initially populated, hot, state. The

temporal components needed to describe the evolution of the data are relatively distinct, i.e. each of different orders of magnitude. As this is the case, both parallel and sequential models yield identical time-constants. With these types of systems, a sequential model for the excited state decay is typically more applicable.

In summary, the model implies excitation from 0 (ground-state) to A (represented by EAS1), followed by transition to B (EAS2) then C(EAS3), and ultimately return back to 0 (ground-state), 0->A->B->C->0.

The Evolution-Associated Spectra (EAS) obtained with a sequential model represent emission from the various states populated after excitation are shown in **Figure 3.8**.

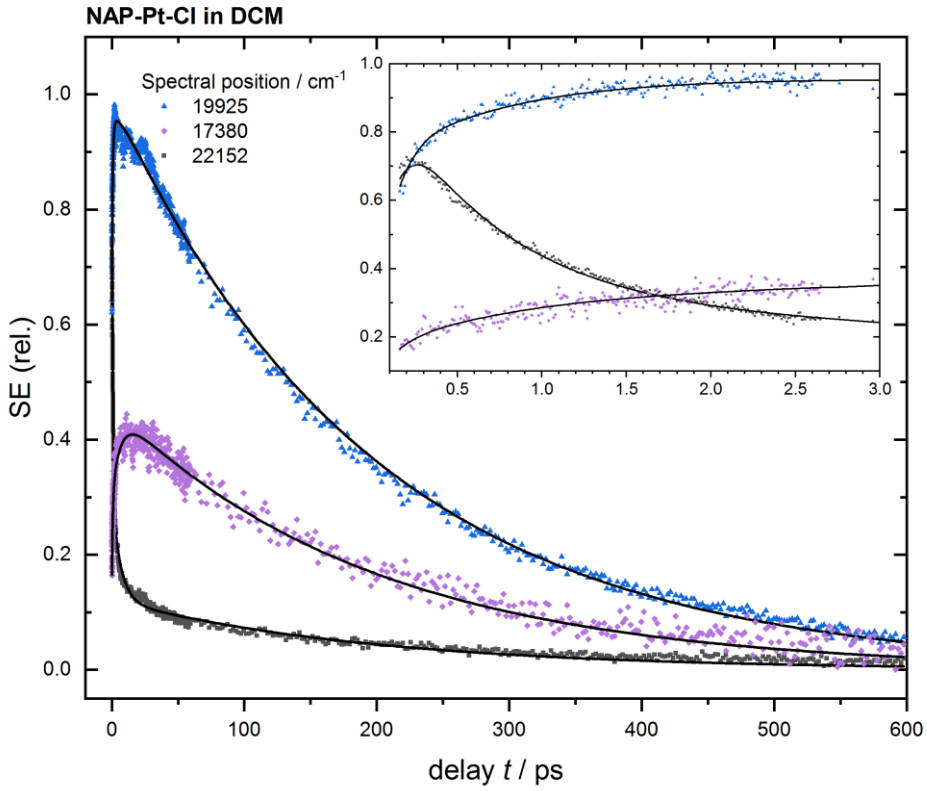

Figure 3.9 Kinetic traces showing the dynamics of the emission of NAP-Pt-Cl, at select spectral positions. Solid lines represent best fits obtained via global analysis using three exponential time functions in a sequential model. Inset shows an expansion of the first 3 ps.

Kinetic traces at select spectral positions, alongside the fits obtained with global analysis are shown in **Figure 3.9**. For NAP-Pt-Cl, three exponential time components were the

minimum number required in order to achieve a satisfactory ft of the data, without a systematic deviation of the residual vs. signal.

NAP-Pt-Ph

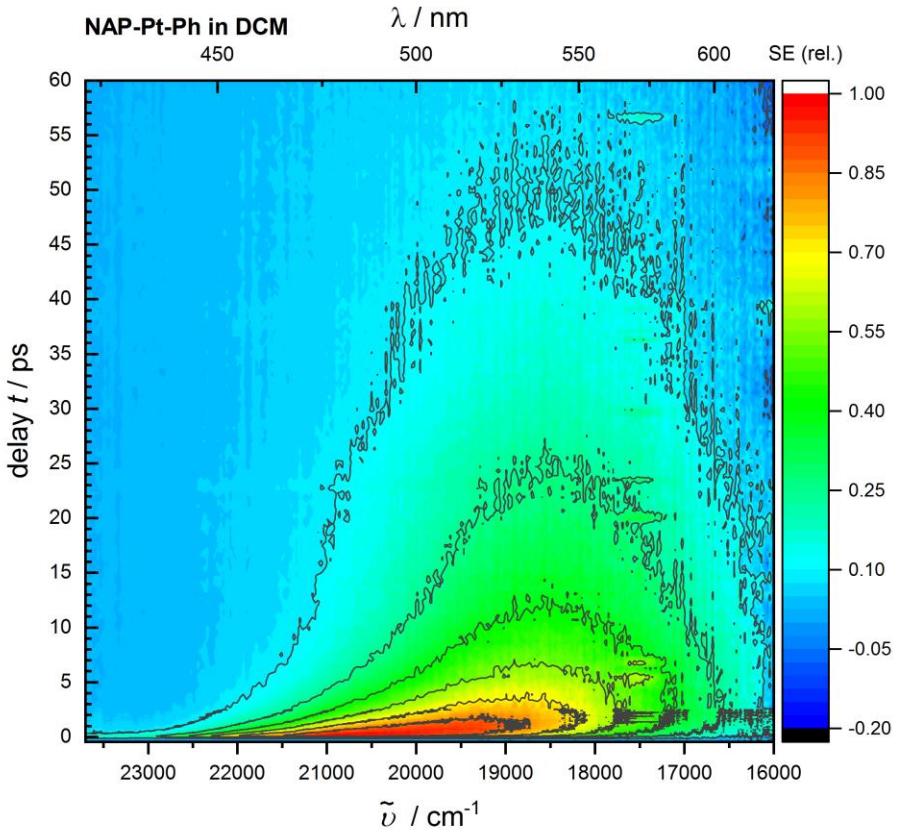

Figure 3.10 A 2D map of time-resolved emission spectra of NAP-Pt-Ph in dichloromethane upon 400 nm excitation, obtained by fluorescence upconversion. The optical density at the pump wavelength was approximately 0.3. Photometric- and time-zero dispersion- corrections have been applied to the raw data.

Figure 3.10 and **Figure 3.11** show time-resolved emission spectra of NAP-Pt-Ph, in a dichloromethane (CH_2Cl_2) solution, upon ~70 fs, 400 nm excitation. Similarly, to the NAP-Pt-Cl data described above, three distinct temporal regions associated with spectral changes are identified (panels A-C, Figure 10), albeit with the faster dynamics observed. Excitation with 400 nm (25,000 cm^{-1}) light leads to population of the singlet mixed-metal-ligand-to-ligand charge transfer state, ^{1}MMLL'CT (absorption maximum at around 430 nm or 23,256 cm^{-1}), with excess vibrational energy of 1474 cm^{-1} (0.175 eV). Panel **A** shows the rise of a broad emission band, covering the region of 16,000 to 24,000, with a maximum at about 20,600 cm^{-1}. Within experimental error the intensity rises uniformly across all wavenumbers, within the instrument response. This immediate emission band is 4,400 cm^{-1} lower in energy than the 25,000 cm^{-1} (400 nm) excitation, with the excess energy dissipated within the instrument response. Initially, as seen for example in the spectrum

at 0.25 ps, the emission appears to be composed of multiple bands, with a weak shoulder at about 19,000 cm^{-1}.

As with the NAP-Pt-Cl spectra (**Figure 3.5**), a relatively sharp band at about 22,000 cm^{-1}, rises and decays with the IRF, and is assigned to a Raman-active vibration of the solvent.

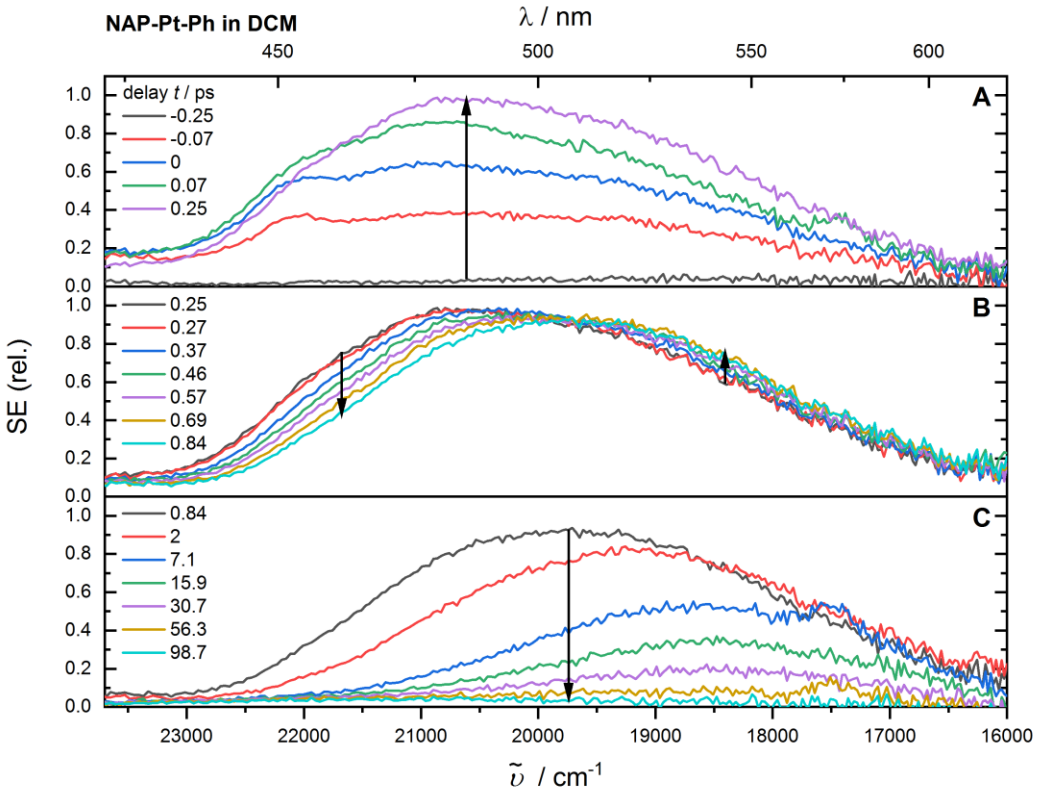

Figure 3.11 Time-resolved emission spectra of NAP-Pt-Ph in dichloromethane upon 400 nm excitation, obtained by fluorescence upconversion. The optical density at the pump wavelength was approximately 0.3. Three distinct temporal ranges are shown in each of the panels, A, B and C. Arrows indicate the characteristic evolutionary feature within each range. Photometric- and time-zero dispersion- corrections have been applied to the raw data.

Within the first 10 picoseconds, considerable spectral change is observed. As is illustrated in Panel **B** and **C**, the emission band shifts towards lower energy, from 20600 cm^{-1} to a maximum at about 18,600 cm^{-1} which is complete by approx. 7 ps Concomitant with the shift in the emission spectrum position, a significant narrowing and change in spectral shape are observed. The spectrum at 7.1 ps, unlike that of 0.25 ps, exhibits no obvious shoulder and displays a shape more typical of a single emission band, with FWHM of 3744 cm^{-1}. These 'early time' dynamics could be signatures of vibrational relaxation. Unlike with

NAP-Pt-Cl, in the first 7.1 ps, a loss of around 50% in integrated emission intensity is observed.

Panel **C** shows the exponential decay of the quasi-stationary emission band on a ~20 ps time scale. By 98.7 ps, almost no detectable emission signal remains.

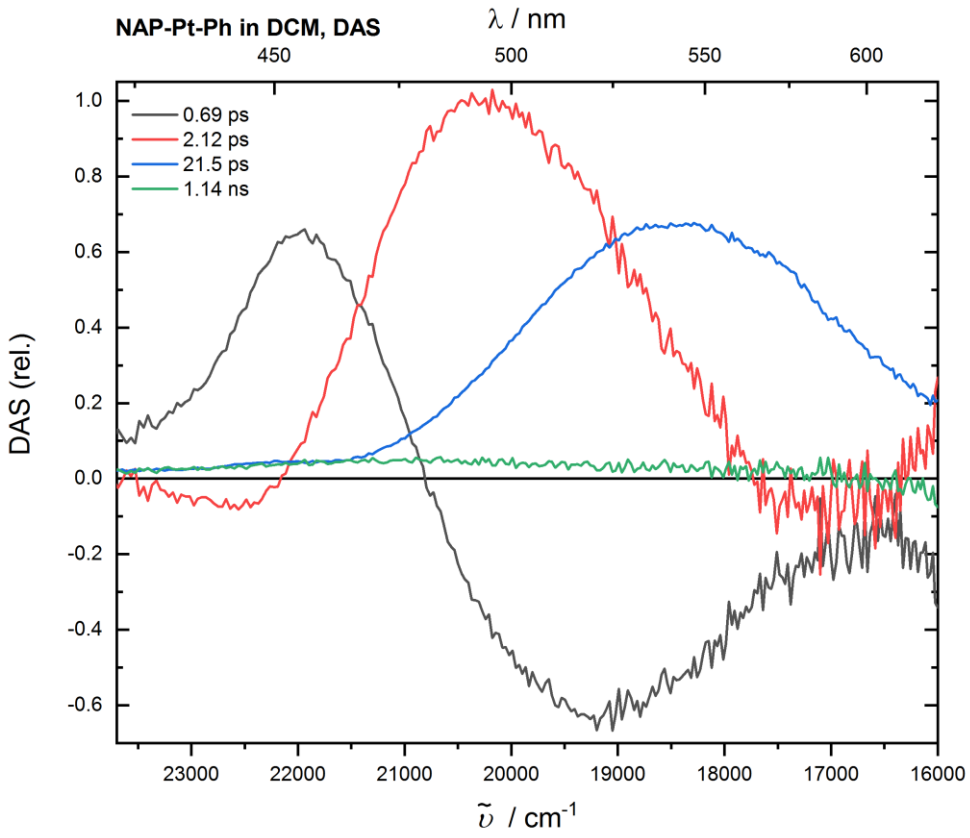

Figure 3.12 Decay-Associated Spectra (DAS) of the emission spectra of NAP-Pt-Ph (shown in **Figure 3.11**), obtained via global analysis using three exponential time functions. The corresponding time constants are given as insets.

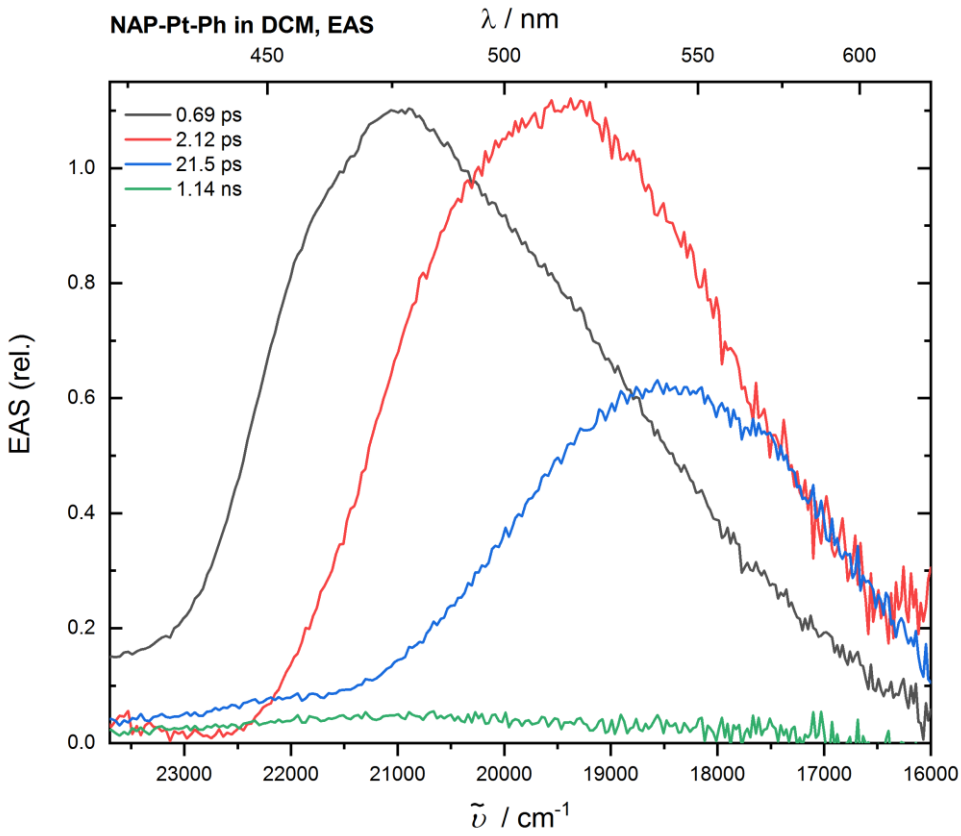

Figure 3.13 Evolution-Associated Spectra (EAS) of the emission spectra of NAP-Pt-Ph (shown in **Figure 3.11**), obtained via global analysis using three exponential time functions. The corresponding time constants are given as insets.

A similar global analysis procedure, as above, was performed on this data set, in order to extract spectral and dynamic information. Initially a parallel model with four exponential time functions was used to fit the data. The resultant Decay-Associated Spectra (DAS) are shown in **Figure 3.12**, with the corresponding kinetic parameters shown in the inset. The 0.69 and 2.12 ps DAS components (black and red line, respectively) describe the initial red-shift and narrowing, illustrated in panel **B** and **C** of **Figure 3.11**. The 21.2 ps component describes the decay of band, illustrated in panel **C** of **Figure 3.11**. This component is a good match with the steady-state emission spectrum of the complex and is therefore assigned as emission from a charge transfer state. The DAS obtained suggest the emission observed arises from a single electronic state. The spectra of the 21.2 ps component can be considered as that of the thermally-equilibrated electronic state, with the 0.69 and 2.12 ps components describing the relaxation from the initially populated, hot, state. The temporal components required to describe the evolution of the data differ by at least one

order of magnitude, therefore both parallel and sequential models fit the data with identical time constants. We note that for NAP-Pt-Ph, a forth, long-lived component (1.14 ns, green trace) is required in order to fit the data satisfactorily, which has been noted in previous studies of the same compound (in different experiments, and from independently synthesised samples); sthe amplitude of this component is very small in comparison to the first three components, additionally it at least an order of magnitude longer-lived relative to the first three components. The minor amplitude and long-life mean it effectively has no involvement in the early time dynamics, upon which we are focused, and it will therefore not be discussed further

Following excitation of NAP-Pt-Ph in DCM solution with a 400 nm, ~70 fs laser pulse, excitation from 0 (ground-state) to A (represented by EAS1), is followed by transition to B (EAS2) then C (EAS3), and ultimately return back to 0 (ground-state). The final component, EAS4, is potentially emission from a photodissociation product.

The Evolution-Associated Spectra for emission of NAP-Pt-Ph obtained with a sequential model represent emission from the various states populated after excitation, are shown in **Figure 3.13**.

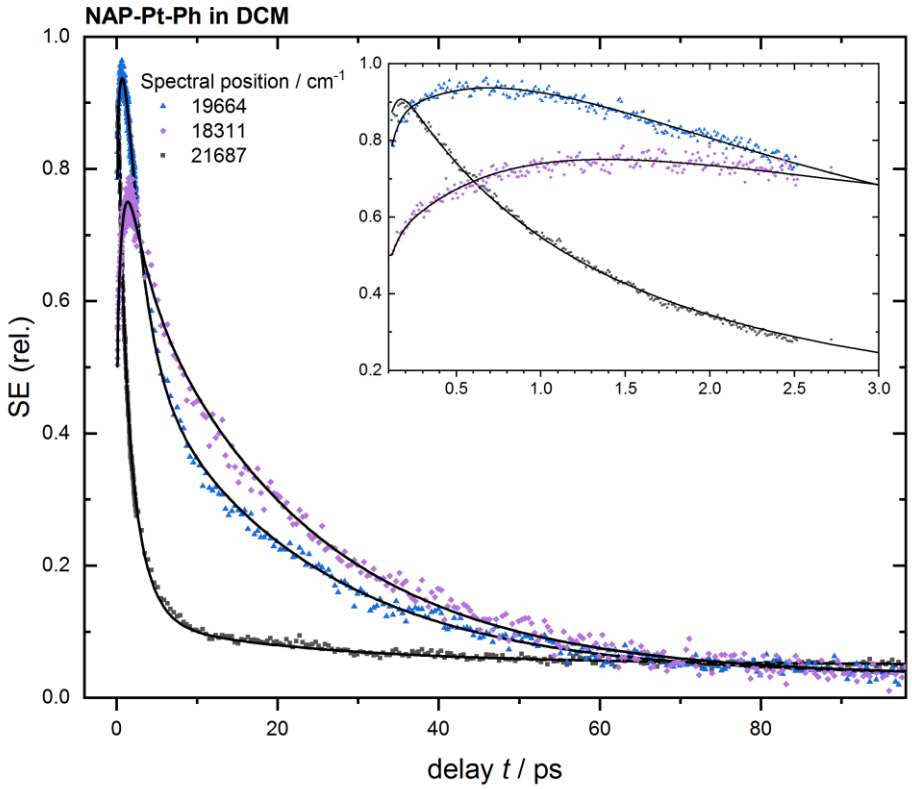

Figure 3.14 Kinetic traces showing the dynamics of the emission of NAP-Pt-Ph, at select spectral positions. Solid lines represent best fits obtained via global analysis using three exponential time functions. Inset shows an expansion of the first 3 ps.

Kinetic traces at select spectral positions, alongside the fits obtained with global analysis are shown in **Figure 3.14**. For NAP-Pt-Ph, a four-component function best describes the evolution of the data.

NAP-Pt-PTZ

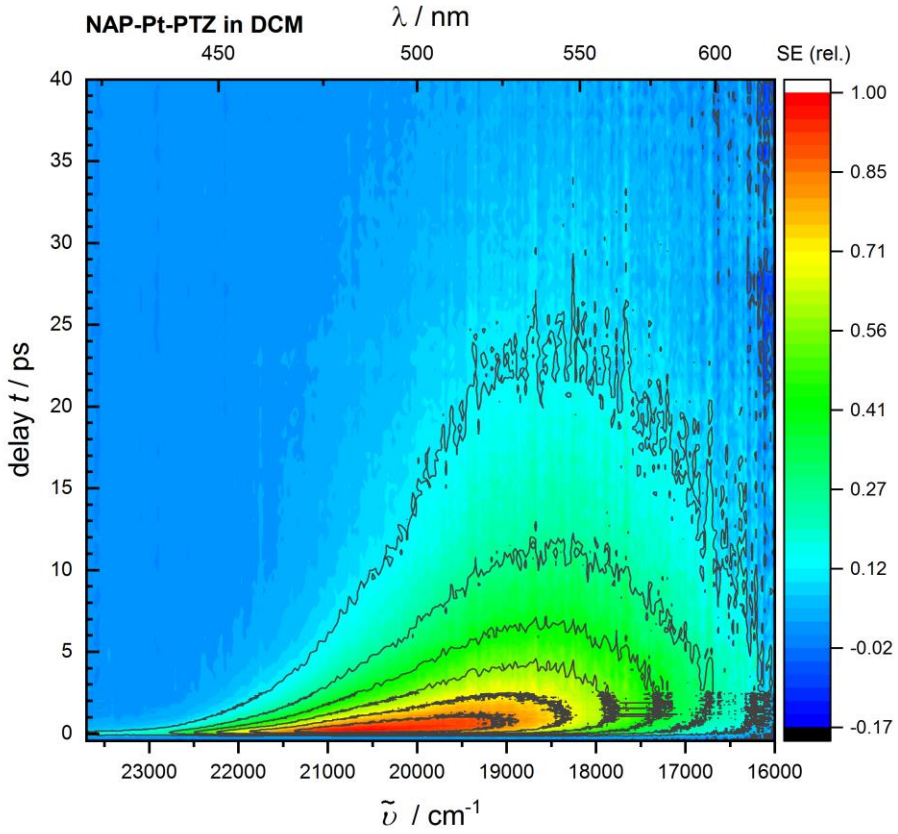

Figure 3.15 2D map of time-resolved emission spectra of NAP-Pt-PTZ in dichloromethane upon 400 nm excitation, obtained by fluorescence upconversion. The optical density at the pump wavelength was approximately 0.3. Photometric- and time-zero dispersion- corrections have been applied to the raw data.

Figure 3.15 and **Figure 3.16** show time-resolved emission spectra of NAP-Pt-PTZ, in a dichloromethane (CH_2Cl_2) solution, upon ~70 fs, 400 nm excitation. Spectrally and temporally the behaviour observed with this compound is very similar to that of NAP-Pt-Ph, with three distinct temporal regions identified as shown in panels **A**, **B** and **C** in **Figure 3.15**. As in the other NAP-Pt-X compounds, excitation with 400 nm light leads to population of a vibrationally hot (an excess vibrational energy of 1415 cm^{-1}), ^{1}MMLL'CT state (absorption maximum at 430 nm).

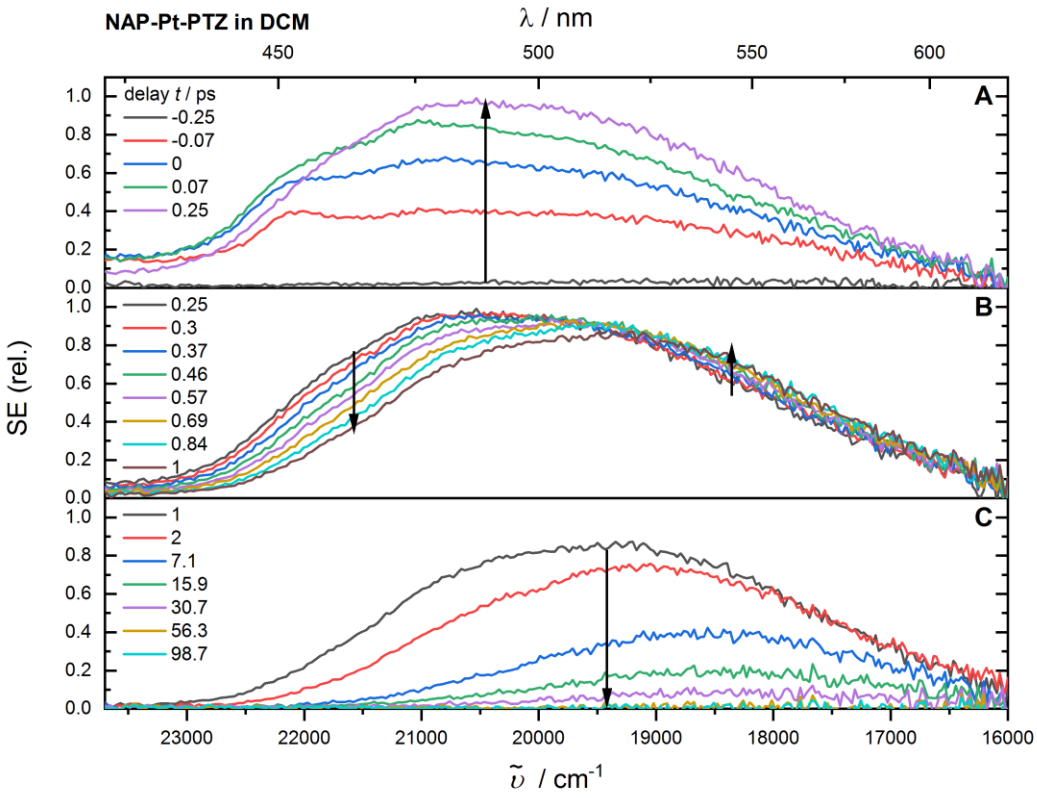

Figure 3.16 Time-resolved emission spectra of NAP-Pt-PTZ in dichloromethane upon 400 nm excitation, obtained by fluorescence upconversion. The optical density at the pump wavelength was approximately 0.3. Three distinct temporal ranges are shown in each of the panels, A, B and C. Arrows indicate the characteristic evolutionary feature within each range. Photometric- and time-zero dispersion- corrections have been applied to the raw data.

Panel **A** shows the rise of a broad emission band, growing in with the instrument response, with a maximum at about 20,750 cm^{-1}, rising uniformly across the region of 16,000 to 23,000 cm^{-1}. This immediate emission band is 4000 cm^{-1} lower in energy than the 25,000 cm^{-1} (400 nm) excitation, with the excess energy dissipated almost instantaneously with respect to the instrument response. Initially, as is evident in for example the spectrum at 0.25 ps, the emission appears to be composed of multiple bands, with a weak shoulder at about 19,000 cm^{-1}.

As with the NAP-Pt-Cl and NAP-Pt-Ph spectra (**Figure 3.5** and **Figure 3.11**), a relatively sharp band (FWHM ~800 cm^{-1}) at about 22,000 cm^{-1}, which rises and decays with the IRF is assigned to a Raman band of the solvent.

Within the first 10 picoseconds, considerable spectral change is observed. As illustrated in Panel **B**, the band shifts towards lower energy, from 20750 cm^{-1} to a maximum at about 18,500 cm^{-1} by around 7.1 ps, by which time the spectral shift is complete. Concomitantly

with the shift, a narrowing of the band and a significant change in spectral shape are observed. The spectrum at 7.1 ps, unlike that of 0.25 ps, has FWHM of 3982 cm^{-1}, can be fitted with a single Voight-function, and thus could be interpreted as an emission from one excited state. These 'early time' dynamics could be signatures of vibrational relaxation.

Once again, panel **C** shows the exponential decay of the quasi-stationary emission band on a ~20 ps time scale. By 98.7 ps, virtually no emission signal remains.

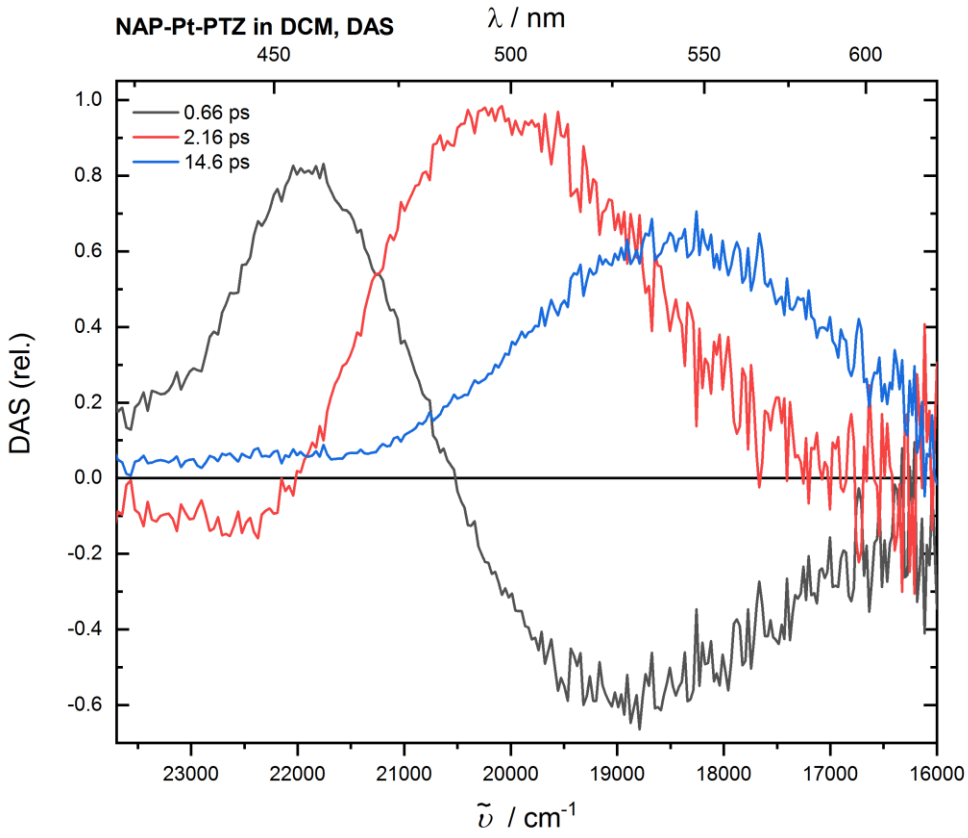

Figure 3.17 Decay-Associated Spectra (DAS) of the emission spectra of NAP-Pt-PTZ (shown in **Figure 3.16**), obtained via global analysis using three exponential time functions. The corresponding time constants are given as insets.

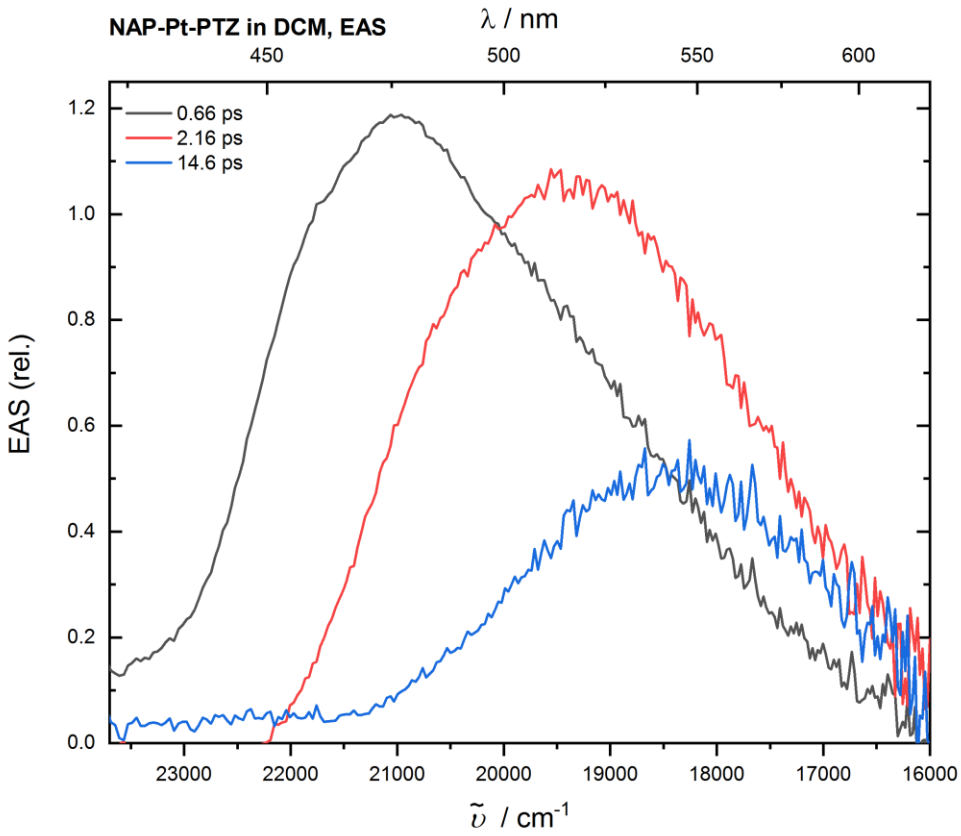

Figure 3.18 Evolution-Associated Spectra (EAS) of the emission spectra of NAP-Pt-PTZ (shown in **Figure 3.16**), obtained via global analysis using three exponential time functions. The corresponding time constants are given as insets.

A similar global analysis procedure, as above, was performed on this data set, in order to extract spectral and dynamic information. Initially a parallel model with three exponential time functions was used to fit the data. The resultant Decay-Associated Spectra (DAS) are shown in **Figure 3.17**, with the corresponding kinetic parameters shown in the legend. The 0.66 and 2.16 ps DAS components (black and red line, respectively) describe the initial red-shift and narrowing, illustrated in panel **B** and **C** of **Figure 3.16**. The 14.6 ps component describes the decay of band, illustrated in panel **C** of **Figure 3.16**. This component is a good match with the steady-state emission spectrum of the complex and is therefore assigned as emission from a charge transfer state. The DAS obtained suggest the emission observed arises from a single electronic state. The spectra of the 14.6 ps component can be considered as that of the thermally-equilibrated electronic state, with the 0.66 and 2.16 ps components describing the relaxation from the initially populated, hot, state. The temporal components needed to describe the evolution of the data are relatively distinct,

i.e. each of different orders of magnitude. As this is the case, with both parallel and sequential models, fits of the data reveal identical time constants. With these types of systems, a sequential model for the excited state decay is typically more applicable, excitation from 0 (ground-state) to A (EAS1), followed by transition to B (EAS2) then C (EAS3), and a return back to 0 (ground-state).

The Evolution-Associated Spectra obtained with a sequential model for the NAP-Pt-PTZ, alongside their time constants are shown in **Figure 3.18**.

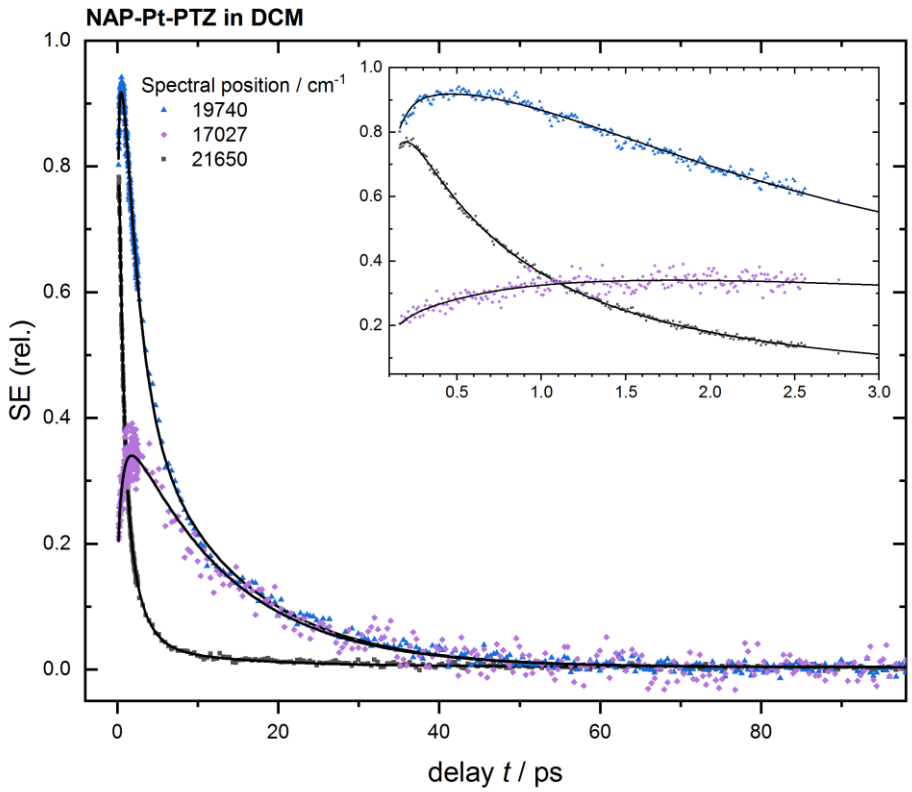

Figure 3.19 Kinetic traces showing the dynamics of the emission of NAP-Pt-PTZ, at select spectral positions. Solid lines represent best fits obtained via global analysis using three exponential time functions. Inset shows an expansion of the first 3 ps.

Kinetic traces at select spectral positions, alongside the fits obtained with global analysis are shown in **Figure 3.19**. For NAP-Pt-PTZ, a three-component function best describes the evolution of the data.

Concentration dependence of time-resolved emission

The stimulated emission (SE) of each complex, seen in the transient absorption spectra appears to undergo a spectral shift. This could be due to genuine dynamic processes (relaxation) of the state from which the emission arises. However, the SE is overlapped with excited-state absorption (ESA), the shifting of which would also result in the apparent shifting of the SE signal. If the shifting were to be due to such an 'inner filter' effect, the magnitude of the shifting would be dependent on the concentration of the sample, and hence concentration of the excited-state species responsible for the inner filter effect. In order to rule out this effect, time-resolved emission measurements were repeated at different concentrations. Preliminary experiments were performed with optical densities set to ca. 1 at excitation wavelength (400 nm). Global analysis was performed on the resultant data, where a shift of the emission band, responsible for the SE in TA, was observed. Experiments, for all complexes, were repeated at much lower concentration, with optical densities set to ca. 0.3 at the excitation wavelength. The spectral and dynamic components extracted in global analysis were identical for both sets of experiments for each of the complexes, this indicating any shifts observed in the emission are as a result of changes occurring in the emissive state and not as a consequence of the ESA shifting. Spectra and EAS obtained via global analysis for the three complexes, are presented in the Appendices (**A. Appendix to Chapter 3**).

Summary

Table 3.1 summarises the time constants, extracted with global analysis, for the three Donor-Bridge-Acceptor compounds studied here (the structures shown in **Figure 3.1 (top)**). Time constants, τ, describing different steps in the excited state dynamics of these compounds, obtained via TRIR and TA spectroscopy are also shown for comparison.

Table 3.1 Summary of the time constants obtained by method of FLUPS, TA and TRIR, for the three compounds, NAP-Pt-Cl, NAP-Pt-Ph and NAP-Pt-PTZ, all in solutions of dichloromethane.

Complex	Abs max	Emission max	τ (ps) / FLUPS	τ (ps) / TA	τ (ps) / TRIR
NAP-Pt-Cl	430	518	0.7 ± 0.1	0.9 ± 0.3	
			6.36 ± 0.8		
			198 ± 4.2	206 ± 5	212 ± 7
NAP-Pt-Ph	430	522	0.69 ± 0.1	0.6 ± 0.3	1 ± 0.2
			2.12 ± 0.4	2.2 ± 0.6	3.2 ± 0.3
			21.5 ± 1.3	19 ± 2	20 ± 1
NAP-Pt-PTZ	424	498	0.66 ± 0.1	0.5 ± 0.3	1.1 ± 0.3
			2.16 ± 0.3	1.8 ± 0.3	3.1 ± 1
			14.6 ± 1.1	13 ± 1	14 ± 1

3.3 Discussion

For all three of the complexes investigated, ultrafast (sub ps) emission was observed. This earliest emission, in all cases, is superseded by lower energy emission, and therefore must occur prior to other relaxation processes of some description, most likely vibrational relaxation and intersystem crossing. All complexes therefore display behaviour in direct contradiction to Kasha's rule. In all cases the earliest distinct emission band undergoes a redshift concomitant with loss in intensity, the initial emissive state is followed by a lower energy (red-shifted) emissive state. In the literature, there can be found numerous reports of ultrafast emission from transition metal complexes. In the vast majority of cases, an initial intense emission band, typically labelled as a singlet excited state, decays on a sub-picosecond timescale via intersystem crossing to a much more weakly emitting, lower energy excited state, typically labelled as a triplet excited state (for a more detailed discussion and all relevant references please see the introduction chapter at the beginning of this thesis). The complexes investigated here show quite different photophysical behaviour; there is no such distinct drop in emission intensity on the sub-picosecond timescale, instead there is a gradual reduction in intensity which occurs in parallel with a shift of the emission to lower energy.

Earliest observable emission

Figure 3.20 shows the steady-state absorption (dashed line) of NAP-Pt-Cl alongside the first EAS (EAS1) component (solid line) extracted from the global analysis of the time-resolved emission spectra. The data was fit using 3 exponential time functions convoluted with an IRF function (ca. 300 fs). EAS1 grows in with the instrument response, i.e. it's growth cannot be temporally resolved. EAS1 decays with a lifetime of 0.70 ps. The absorption band centred at 424 nm (23,585 cm^{-1}) is assigned as being ground-state to a manifold of ^{1}MLCT states. EAS1, centred at 457 nm (21,836 cm^{-1}), appears very mirror symmetric to the absorption band. The mirror symmetry suggests that the state responsible for the emission has dissipated excess vibrational energy, i.e. it is has reached equilibration with regards to the population of vibrational energy levels. The symmetry also indicates that on this timescale, little conformational change of the complex has taken place. This emission grows with the IRF, which is ca. 300 fs, and decays with a lifetime of 700 fs. No faster dynamics components were uncovered in the global analysis, this meaning any dynamics preceding the formation of the state responsible for this emission must have occurred in less than 100 fs (a third of the IRF). Three possible explanations for the origins of this earliest emission are presented below.

1. Optical excitation of the ^{1}MLCT manifold is followed by ISC, with lifetime <100 fs, populating a manifold of ^{3}MLCT states. These states would be very similar to the ^{1}MLCT states, with little conformational rearrangement. For numerous TM complexes, there are reports of ISC on timescales of sub-30 fs to around 150 fs,[10–16] so this appears plausible. However, in nearly all cases, SE is seen to decay on this timescale, here SE persists much longer; for 10s of picoseconds for the Ph- and PTZ- complexes, and even longer for the Cl complex (around 200 ps). With the majority of these reporting's, significant loss in emission intensity is also observed on this timescale, this is not the case here.
2. Optical excitation of the ^{1}MLCT manifold is followed by vibratioanal relaxation, resulting in a vibrationall relaxed pool of ^{1}MLCT states within 100 fs. The pool of ^{1}MLCT states are responible for this emission. It is however unlikely as 100 fs is too short a time for IVR, i.e. vibrational energy transfer typically occurs on timescales of 100s of femtoseconds to tens of picoseconds.[17–19]

3. Optical excitation of the ^{1}MLCT manifold is followed by vibrational relaxation concomitant with ISC, occurring in <100 fs. Populated ^{3}MLCT states also undergo back-ISC, a pool of ^{1}MLCT and ^{3}MLCT states are formed in equilibrium.

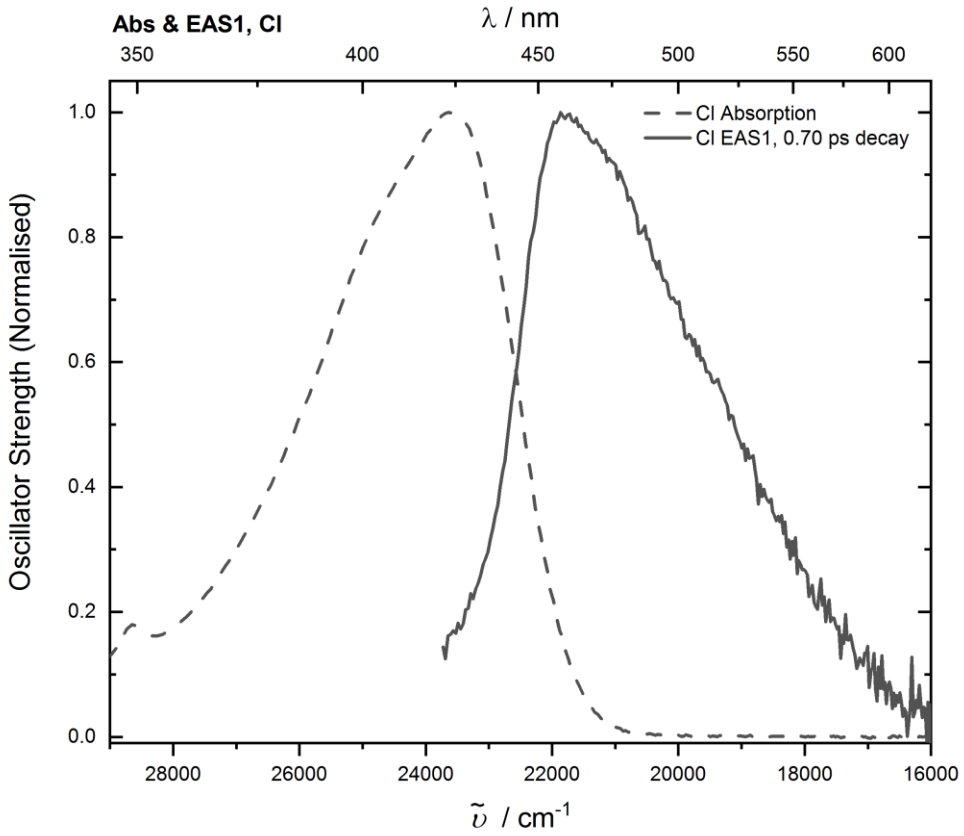

Figure 3.20 Normalised steady-state absorption of NAP-Pt-Cl, in dichloromethane, is shown alongside the first Evolution-Associated Spectra (EAS1), component extracted from global analysis of the time-resolved emission of NAP-Pt-Cl, in dichloromethane, upon 400 nm excitation. EAS1 grows in with IRF (ca. 300 fs) and decays with a lifetime of 0.70 ps. The steady-state absorption and EAS1 appear to be mirror symmetric.

In both NAP-Pt-Ph and NAP-Pt-PTZ the earliest observable emission appears very similar to that of NAP-Pt-Cl. The emission is mirror symmetric with absorption, growing in with the IRF and decaying with very similar lifetimes (0.69 and 0.66 ps for NAP-Pt-Ph and NAP-Pt-PTZ respectively, which are the same within experimental error). Absorption spectra alongside the first EAS component for NAP-Pt-Ph and NAP-Pt-PTZ are shown in **Figure 3.21** and **Figure 3.22** respectively.

For all three complexes, the early time emission appears very similar, both spectrally and dynamically. The structural differences between the complexes seems to make little difference to the earliest emission, i.e. the ligand trans to the acetylide-acceptor unit

seems to play very little part (if any) in the early time dynamics, further evidence the origin of the emission is a MLCT state(s).

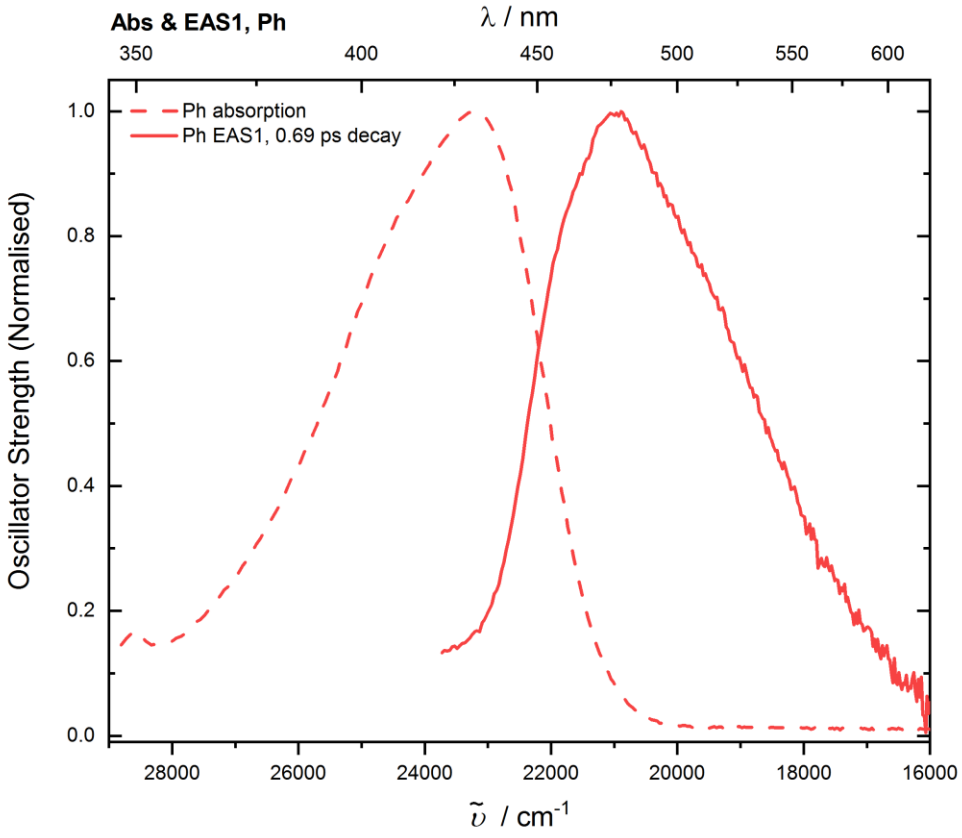

Figure 3.21 Normalised steady-state absorption of NAP-Pt-Ph, in dichloromethane, is shown alongside the first Evolution-Associated Spectra (EAS1), component extracted from global analysis of the time-resolved emission of NAP-Pt-Ph, in dichloromethane, upon 400 nm excitation. EAS1 grows in with IRF (ca. 300 fs) and decays with a lifetime of 0.69 ps. The steady-state absorption and EAS1 appear to be mirror symmetric.

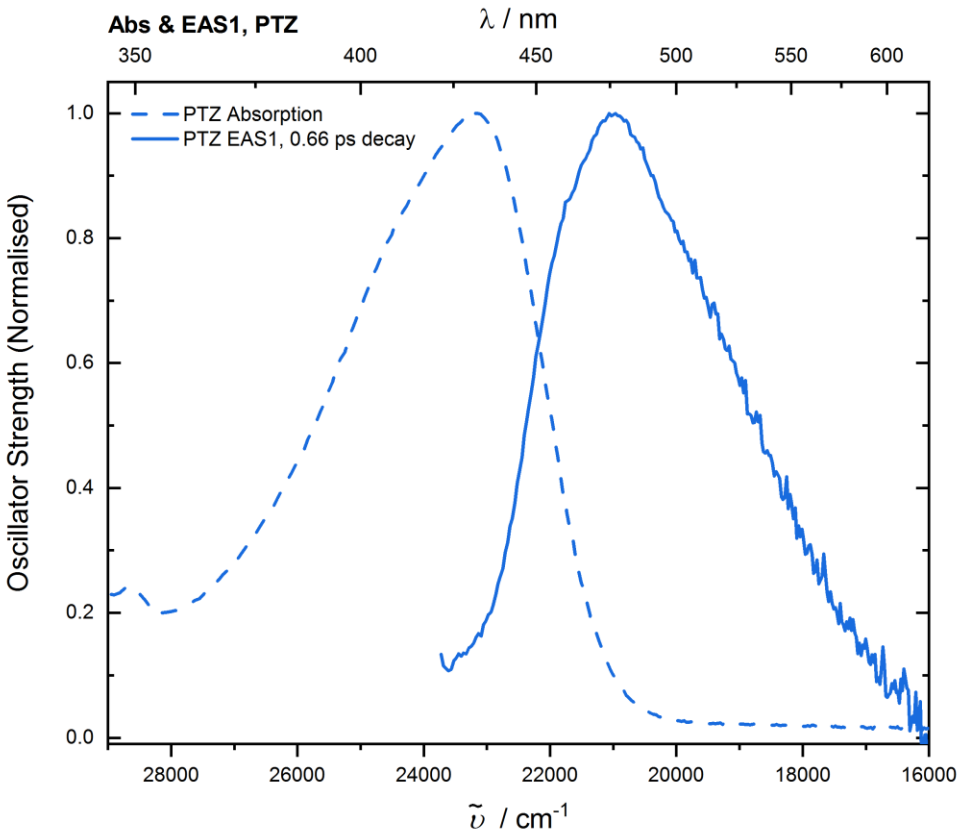

Figure 3.22 Normalised steady-state absorption of NAP-Pt-PTZ, in dichloromethane, is shown alongside the first Evolution-Associated Spectra (EAS1), component extracted from global analysis of the time-resolved emission of NAP-Pt-PTZ, in dichloromethane, upon 400 nm excitation. EAS1 grows in with IRF (ca. 300 fs) and decays with a lifetime of 0.66 ps. The steady-state absorption and EAS1 appear to be mirror symmetric.

Decay-Associated Spectra (DAS), along with the corresponding time-constants describe how the sum of the emission from all participating states, decay as a function of time. Positive amplitude within DAS represents decay of emission at that particular spectral position, while negative amplitude represents growth. Where bands are seen to shift, DAS show a characteristic differential shape. The first DAS component for the three complexes, extracted by global analysis using a parallel model for the decay of the emission, are shown in **Figure 3.23**. The time constants for the first DAS are essentially identical for all complexes (0.66 – 0.70 ps), and spectrally they are very similar, all sharing a differential type shape, describing the red-shift of the band at early times.

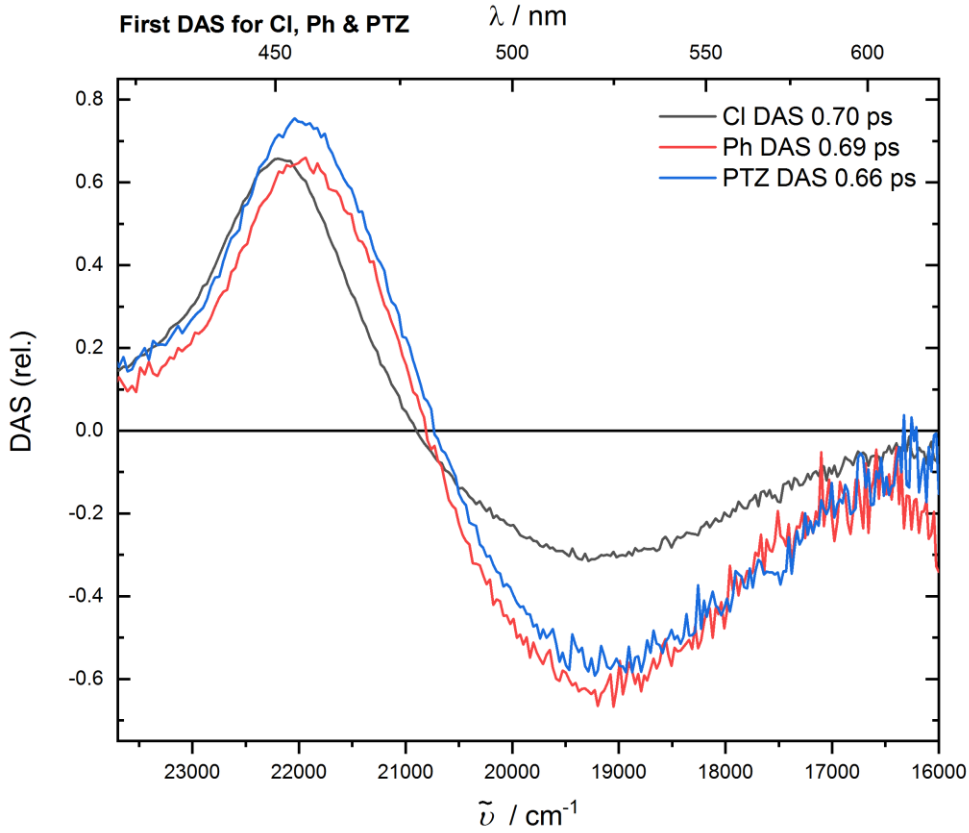

Figure 3.23 Graph shows the first Decay-Associated Spectra (DAS), component extracted from global analysis of the time-resolved emission of NAP-Pt-Cl, NAP-Pt-Ph and NAP-Pt-PTZ, in dichloromethane, upon 400 nm excitation. Lifetimes are essentially identical, 0.66 ps to 0.70 ps. And all DAS show very similar spectral shape.

Comparison of final EAS with steady-state emission spectra

For each complex, the 'final' EAS, that is the third EAS, EAS3, is a good match with the steady-state emission. (for NAP-Pt-Ph, an additional minor component, EAS4, is extracted). Steady-state emission along with 'late' flups emission, for NAP-Pt-Cl, are shown alongside one another in **Figure 3.6**. Conventionally with TM complexes, the dominant band in the steady state emission would be assigned as originating from a triplet state, with rapid ISC assumed. In the present case, that does not appear to be true. The late emission seen in the time-resolved emission experiments resembling that of the SE seen in TA, and also that of the steady-state emission.

Corroboration of transient absorption and time-resolved infrared results

For all complexes, the final form of the emission, recorded with time-resolved emission, resembles that of the SE observed in TA measurements, see NAP-Pt-Cl for example in **Figure 3.24**. The dynamics components extracted by global analysis for the time-resolved emission also match those obtained via TA and TRIR, see **Table 3.1** above.

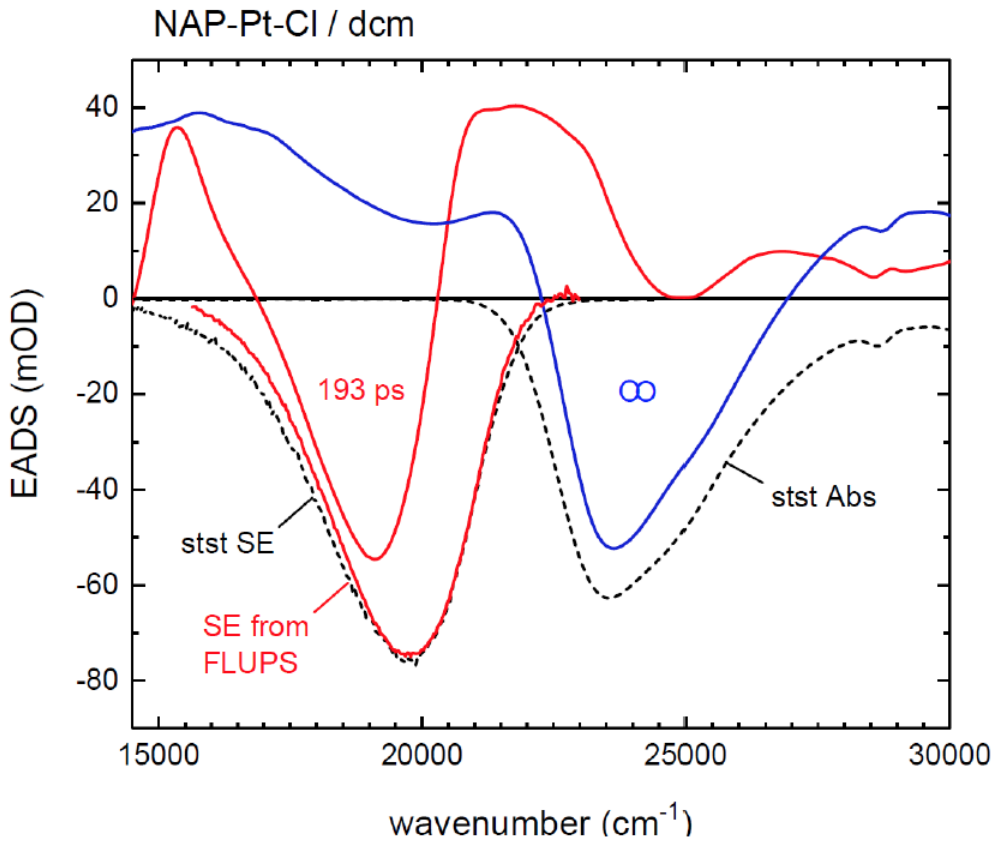

Figure 3.24 EAS from transient absorption spectra, with lifetime 193 ps (red), showing stimulated emission and final EAS (blue), from transient absorption spectra, with infinite lifetime, showing ground state bleach. The steady-state absorption (black dashed), steady-state emission (black dashed) and time-resolved emission, by flups, in the form of SE (red solid) are shown overlaid for comparison. All spectra for NAP-Pt-Cl, in solution of dichloromethane, with excitation at 400 nm.

Change in oscillator strength over time

The oscillator strength for emission, from a particular excited state will scale proportionally with emission intensity integrated over the entire band, i.e. the area under each EAS1 represents the oscillator strength of the corresponding electronic excited state. Scaling of the area under each EAS to that of the first EAS, 'EAS1' gives an idea of the change in oscillator strength as a function of time. **Figure 3.25** shows EAS for NAP-Pt-Cl, obtained by global analysis using a sequential model with 3 exponential time functions convoluted with an IRF function. Bars are shown, overlaid on the EAS, with their height representing the area under the corresponding EAS. For NAP-Pt-Cl very little change in area under the EAS and hence oscillator strength is seen.

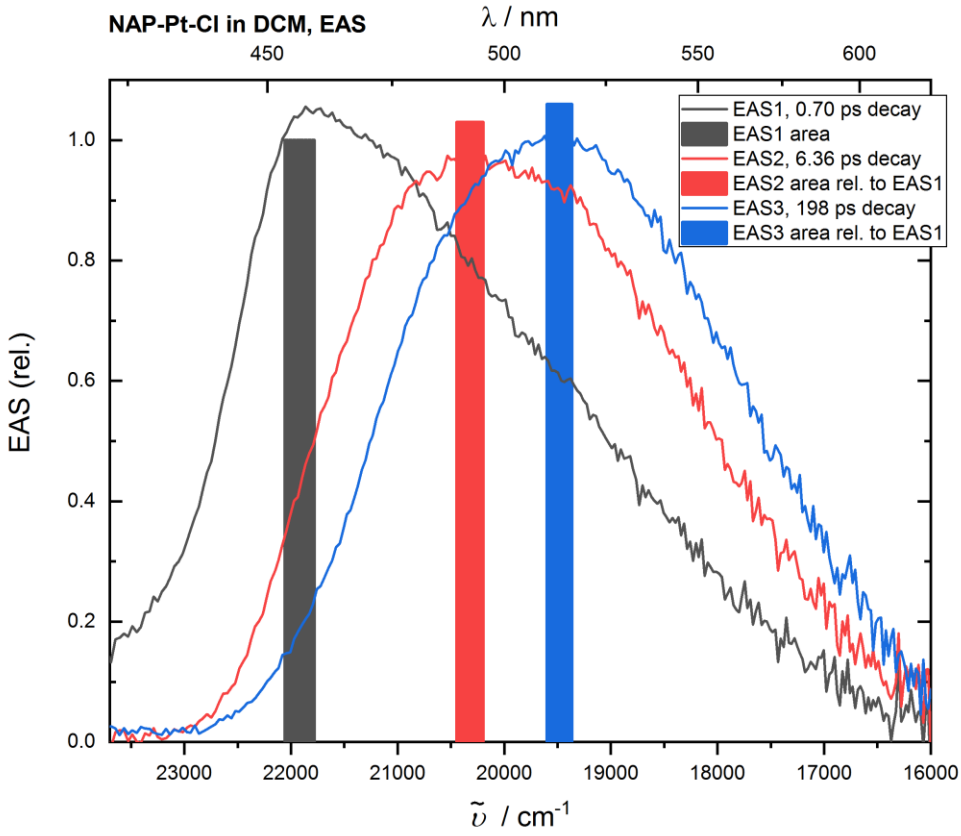

Figure 3.25 Evolution-Associated Spectra (EAS) for the time-resolved emission spectra of NAP-Pt-Cl, in dichloromethane, upon 400 nm excitation. EAS are extracted by global analysis using a sequential model with 3 exponential time functions convoluted with an IRF function. The height of the bars overlaid represent the area under each EAS, relative to that of EAS1 (normalised to 1).

A change in spin, singlet to triplet for instance, usually manifests itself in a significant change in oscillator strength and therefore a significant change in emission intensity. This is not observed, however, and therefore intersystem crossing on a timescale > 100 fs the IRF-limited value) can be ruled out for NAP-Pt-Cl in dichloromethane solution. Or more precisely, a large decrease in singlet character / a large increase in triplet character, can be ruled out on timescale of > 100 fs. One can't however exclude the possibility, on the basis of these time-resolved emission data alone, of an ISC being faster than the 100-fs IRF-limit, and that therefore all states that have been detected being of a triplet character. We note that however this interpretation contradicts the intense stimulated emission observed.

Figure 3.26 and **Figure 3.27** shows EAS for NAP-Pt-Ph and NAP-Pt-PTZ, obtained by global analysis using a sequential model with 3 and 4 exponential time functions, for NAP-Pt-Ph and NAP-Pt-PTZ respectively, convoluted with an IRF function. Bars are shown, overlaid on the EAS, with their height representing the area under the corresponding EAS.

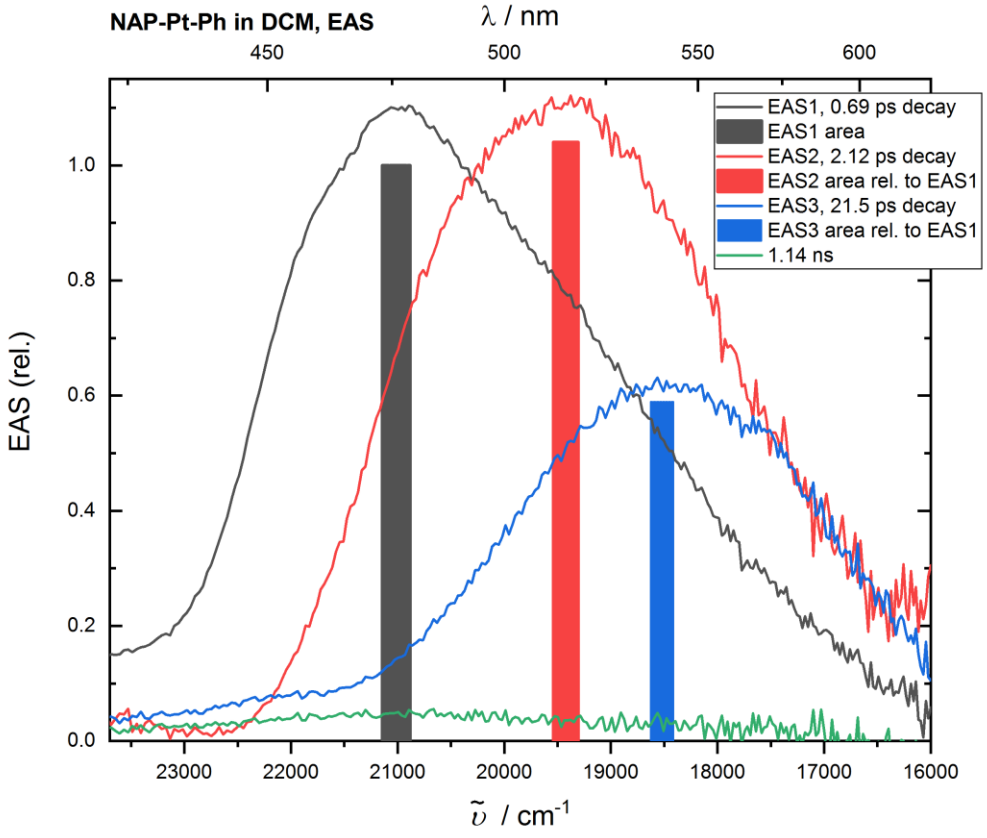

Figure 3.26 Evolution-Associated Spectra (EAS) for the time-resolved emission spectra of NAP-Pt-Ph, in dichloromethane, upon 400 nm excitation. EAS are extracted by global analysis using a sequential model with 4 exponential time functions convoluted with an IRF function. The height of the bars overlaid represent the area under each EAS, relative to that of EAS1 (normalised to 1).

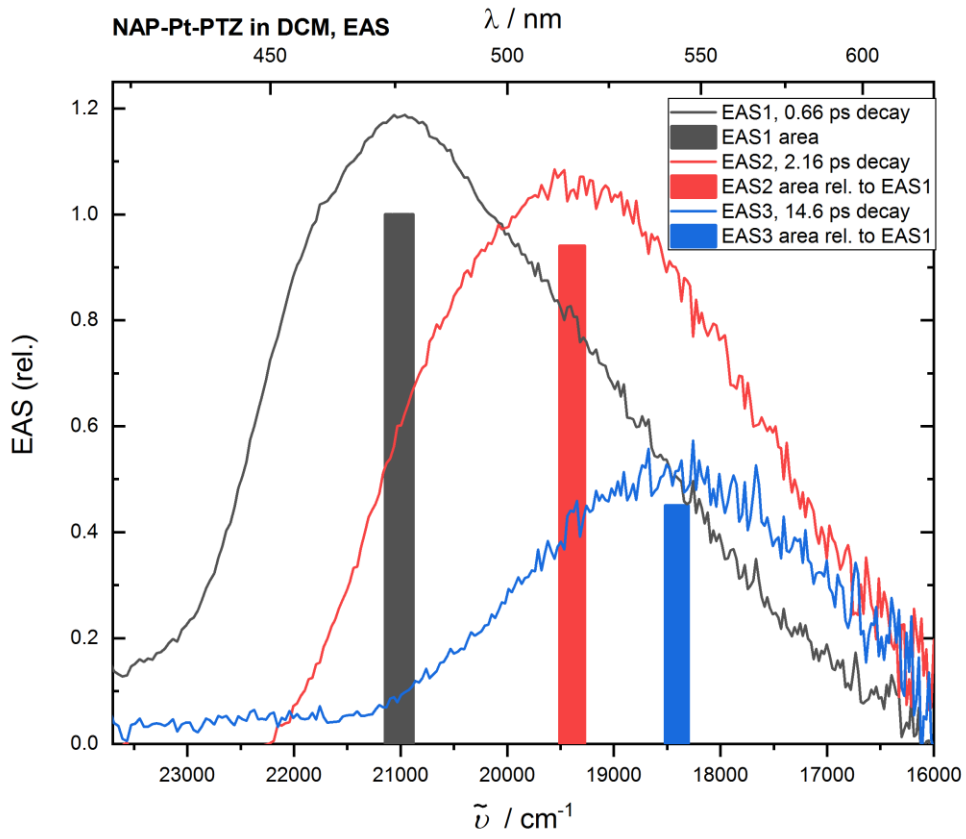

Figure 3.27 Evolution-Associated Spectra (EAS) for the time-resolved emission spectra of NAP-Pt-PTZ, in dichloromethane, upon 400 nm excitation. EAS are extracted by global analysis using a sequential model with 3 exponential time functions convoluted with an IRF function. The height of the bars overlaid represent the area under each EAS, relative to that of EAS1 (normalised to 1).

For NAP-Pt-Ph and NAP-Pt-PTZ very little change in area under the EAS and hence oscillator strength is seen between the first two EAS components, suggesting no sign of ISC on this early time scale.

EAS3 for both NAP-Pt-Ph and NAP-Pt-PTZ shows some decrease in area under the spectra relative to EAS1 and 2. In each case the relative area is around 40 – 50 % of that of EAS1.

3.4 Conclusion

Time-resolved emission spectra for three linear asymmetric Pt (II) donor-bridge-acceptor complexes, NAP-Pt-Cl, NAP-Pt-Ph and NAP-Pt-PTZ, have been measured. The IRF of the spectrometer was determined to be around 300 fs for this set of experiments. Samples were prepared as solutions in dichloromethane solvent. Photometric- and group velocity dispersion- corrections have been applied to all data. For the data presented here, optical densities at excitation wavelength were kept to around 0.3. Measurements were also performed at much higher concentration; spectra were found to be identical in both cases, with no apparent dependence on concentration.

In all cases, broad emission, assigned as originating from MLCT states, was seen to grow in with the instrument response. Earliest observable emission was mirror symmetric with respect to the absorption spectra.

All bands were seen to undergo biexponential red-shifting and narrowing on timescales of 0.5 to 6 ps. The earliest component in each case (for all 3 complexes) appeared almost identical, both spectrally and dynamically. This observation corroborates the assignment that the earliest excited-states populated feature no involvement of the 'donor' ligand and are comprised of metal-to-acceptor charge-transfer transitions.

With the IRF at around 300 fs, processes occurring on a timescale of 100 fs and upwards will be observable. On this timescale, there is no significant change in the overall emission intensity and therefore, it is deemed that there is also no significant change in oscillator strength in any of the three complexes.Therefore it is proposed that ISC, at least in a conventional sense, can be ruled out as occurring with lifetimes larger than 100 fs.

The 'final' emission, observable in the flups experiments, resembles that of both the steady-state MLCT emission and also that of the SE observed in the transient absorption experiments. This appears somewhat contradictory with SE assigned as arising from singlet states and the steady-state emission that of the triplet MLCT manifold.

It is concluded that for these types of platinum complexes, ISC does not give rise to the types of spectroscopic signatures typically seen in many other transition metal complexes, discussed in the introduction chapter. The behaviour seen with these complexes is somewhat unique, there appears to be 'duel' behaviour, with evidence pointing to there

being both strong singlet and triplet character throughout the entire relaxation process, we speculate that the population is equilibrium between the singlet and triplet states which lie very close in energy to one another. The resultant mixed-character of the ensemble allows the expression of both singlet and triplet-like behaviour, with the triplet component providing a decay pathway to the 3NAP states and the singlet component responsible for the SE signal observed in the TA. The rapid equilibration of states deems the individual states indistinguishable through time-resolved emission spectroscopy, at least on the with our instrument capabilities, which allow for access to timescales on the order of 100 fs and above. These results call for a revaluation of the photophysical assumptions typically employed in addressing the interpretation of the spectra of such systems.

3.5 References

1 S. Archer and J. A. Weinstein, *Coord. Chem. Rev.*, 2012, **256**, 2530–2561.

2 K. Kalyanasundaram, *Coord. Chem. Rev.*, 1998, **177**, 347–414.

3 C. Cebrián and M. Mauro, *Beilstein J. Org. Chem.*, 2018, **14**, 1459–1481.

4 J. N. Demas and B. A. DeGraff, *Coord. Chem. Rev.*, 2001, **211**, 317–351.

5 P. A. Scattergood, M. Delor, I. V. Sazanovich, O. V. Bouganov, S. A. Tikhomirov, A. S. Stasheuski, A. W. Parker, G. M. Greetham, M. Towrie, E. S. Davies, A. J. H. M. Meijer and J. A. Weinstein, *Dalt. Trans.*, 2014, **43**, 17677–17693.

6 M. Delor, P. A. Scattergood, I. V Sazanovich, A. W. Parker, G. M. Greetham, A. J. H. M. Meijer, M. Towrie and J. A. Weinstein, *Science*, 2014, **346**, 1492–5.

7 X.-X. Zhang, C. Würth, L. Zhao, U. Resch-Genger, N. P. Ernsting and M. Sajadi, *Rev. Sci. Instrum.*, 2011, **82**, 063108.

8 M. Gerecke, G. Bierhance, M. Gutmann, N. P. Ernsting and A. Rosspeintner, *Rev. Sci. Instrum.*, 2016, **87**, 053115.

9 P. A. Scattergood, M. Delor, I. V Sazanovich, O. V Bouganov, S. A. Tikhomirov, A. S. Stasheuski, A. W. Parker, G. M. Greetham, M. Towrie, E. S. Davies, A. J. H. M. Meijer and J. A. Weinstein, *Dalt. Trans.*, 2014, **43**, 17677–17693.

10 W. Gawelda, A. Cannizzo, V.-T. Pham, F. van Mourik, C. Bressler and M. Chergui, *J. Am. Chem. Soc.*, 2007, **129**, 8199–8206.

11 C. Bressler, C. Milne, V.-T. Pham, A. Elnahhas, R. M. van der Veen, W. Gawelda, S. Johnson, P. Beaud, D. Grolimund, M. Kaiser, C. N. Borca, G. Ingold, R. Abela and M. Chergui, *Science*, 2009, **323**, 489–92.

12 C. Consani, M. Prémont-Schwarz, A. Elnahhas, C. Bressler, F. van Mourik, A. Cannizzo and M. Chergui, *Angew. Chem. Int. Ed. Engl.*, 2009, **48**, 7184–7.

13 A. Cannizzo, F. van Mourik, W. Gawelda, G. Zgrablic, C. Bressler and M. Chergui, *Angew. Chem. Int. Ed. Engl.*, 2006, **45**, 3174–6.

14 O. Bräm, F. Messina, A. M. El-Zohry, A. Cannizzo and M. Chergui, *Chem. Phys.*, 2012, **393**, 51–57.

15 A. Cannizzo, A. M. Blanco-Rodríguez, A. El Nahhas, J. Šebera, S. Záliš, A. Vlček and M. Chergui, *J. Am. Chem. Soc.*, 2008, **130**, 8967–8974.

16 O. Bräm, F. Messina, E. Baranoff, A. Cannizzo, M. K. Nazeeruddin and M. Chergui, *J. Phys. Chem. C*, 2013, **117**, 15958–15966.

17 I. V Rubtsov, *Acc. Chem. Res.*, 2009, **42**, 1385–1394.

18 V. M. Kasyanenko, Z. Lin, G. I. Rubtsov, J. P. Donahue and I. V Rubtsov, *J. Chem. Phys*, 2009, **131**, 154508.

19 S. Kaziannis, J. A. Wright, M. Candelaresi, R. Kania, G. M. Greetham, A. W. Parker, C. J. Pickett and N. T. Hunt, *Phys. Chem. Chem. Phys*, 2011, **13**, 10295–10305.

4 Ultrafast Emission and Intersystem Crossing in Symmetric Platinum(II) 'Acceptor-Bridge-Acceptor' Complexes

4.1 Introduction

Transition metal (TM) complexes capable of undergoing charge-transfer upon photoexcitation are of great interest, due to their ability to perform in numerous applications including photocatalysis,[1–3] as phosphorescent light emitting diodes,[4] and in artificial photosynthesis.[3,5,6] In all applications, the formation of a triplet metal-to-ligand charge-transfer (^{3}MLCT) states is essential.

Of paramount importance to the formation of their long-lived charge-separated states, and therefore the employment of such molecules, is ultrafast intersystem crossing (ISC). The presence of the heavy-metal atom in these systems often leads to rapid ISC occurring on timescales as fast as 10's of femtoseconds to a few picoseconds.[1,7–25] Numerous investigations into the ISC rates of TM complexes suggest there to be a complex dependence of the rates on molecular structure, with the heavy-atom effect alone insufficient in the explanation of the trends. There are reports of ISC dependent upon metal-ligand bond stretch frequency,[21] ligand size,[23] and solvent.[24] A literature review of ISC in TM complexes can be found in Chapter 1 – Introduction.

The previous chapter discussed our attempts to determine the rates of ISC in a series of Donor-Bridge-Acceptor complexes, where the central unit is a Pt(II) trans-acetylide. On the other hand, many symmetrical Pt(II) trans-acetylide complexes find application in optoelectronics, and consequently have been subject to numerous photophysical studies.

However, perhaps largely due to instrument limitations, there have been only few investigations of this class of compounds on the timescale that could monitor directly the process of the ISC.

For example, for a series of symmetrical platinum(II) trans- acetylide complexes, 'PE1-Pt', 'PE2-Pt' and 'PE3-Pt' (molecular structures shown in **Figure 4.1**), ISC rates were determined using a combination of narrowband time-resolved emission (by fluorescence upconversion method) and transient absorption measurements. ISC rates were found to

decrease with increasing size of ligand, i.e. ISC was fastest in PE1-Pt followed by PE2-Pt and then PE3-Pt.

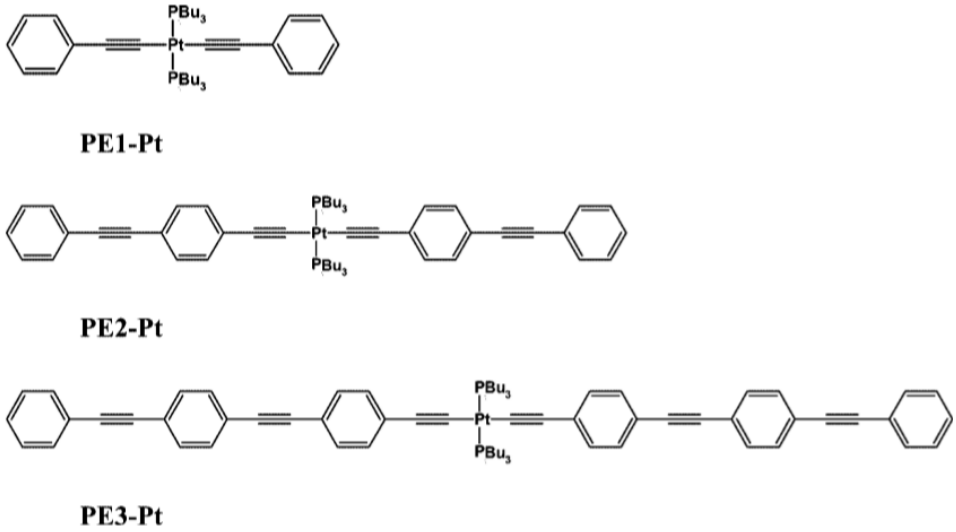

Figure 4.1 Molecular structures of the three symmetrical platinum acetylide complexes, PE1-Pt, PE2-Pt and PE3-Pt. Figure taken directly from source.[23]

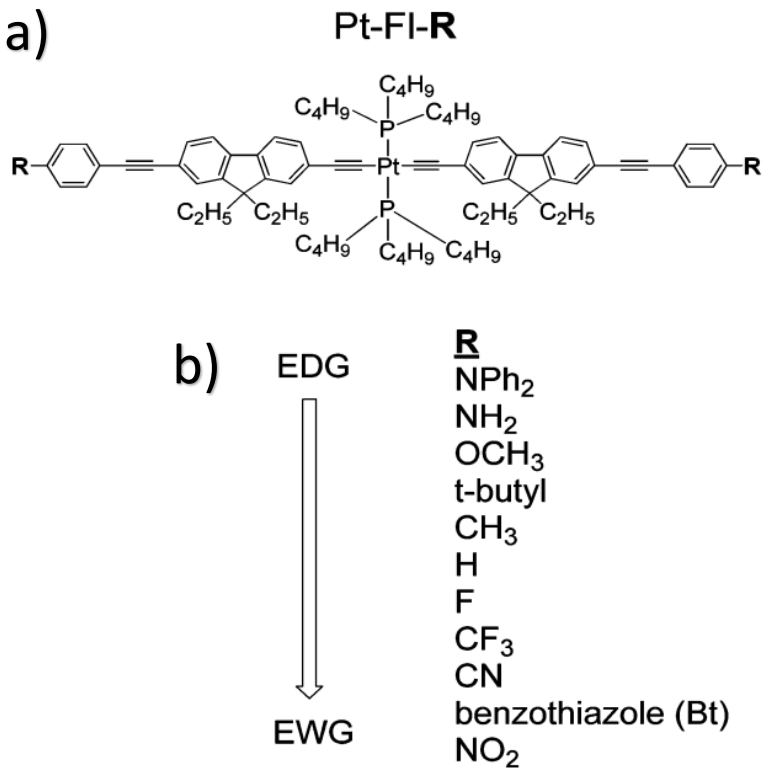

Figure 4.2 General molecular structure of the series of 'Pt-Fl-**R'** complexes (**a**). Substituents '**R**' are also listed (**b**). Where EDG is electron-donating group and EWG is electron-withdrawing group. Figure taken directly from source.[26]

The photophysics of a similar series of symmetric platinum(II) acetylide complexes, shown in **Figure 4.2**, was subject to spectroscopic investigation by Haley et al.[26] An array of different substituents, with a broad range of electron withdrawing / donating powers, were employed. For this series, ISC rates of between 12.1 (CF_3) and 109 ps (NO_2), were determined. Given the presence of the heavy platinum centre, these rates are remarkably slow compared with those stated in the literature, see **table 1.5** in Chapter 1.

In the work presented here, the photophysics of a very similar series of complexes, to the 'PEn-Pt' series, are explored. Molecular structures of the complexes are presented below in **Figure 4.3**. The series – 'Pt0', 'Pt1' and 'Pt2' are all of a general 'acceptor-bridge-acceptor' (A-B-A) design motif. All complexes are symmetrical about the central platinum atom, with two trans- 'NAP' acceptor ligands attached via varying lengths of conjugated acetylide / phenyl bridges. In all cases, two trans- phosphine ligands (cis to the NAP ligands) complete the square planar coordination sphere.

A combination of UV-Vis absorption, steady-state emission, time-resolved emission (by upconversion) and transient absorption spectroscopies are used in order to develop an understanding of the ultrafast dynamics following the photoexcitation into charge-transfer excited-states. This series is ideal for investigating the influence of the extension of ligands, and subsequent increase in delocalisation, the electron/hole "distance", and potentially of the extent of the central metal involvement in the excited states, on rates of ISC. Further, a comparison with the properties of an asymmetric, Cl-Pt-NAP compound described in Ch. 3, would provide an additional insight into the role of delocalisation of electron density on the rates, and mechanism, of the ISC in such complexes.

The compounds have been provided by the group of Professor Kirk Schanze, University of Texas at San Antonio, USA.

4.2 Results

4.2.1 Pt0, Pt1 and Pt2 Chemical Structures

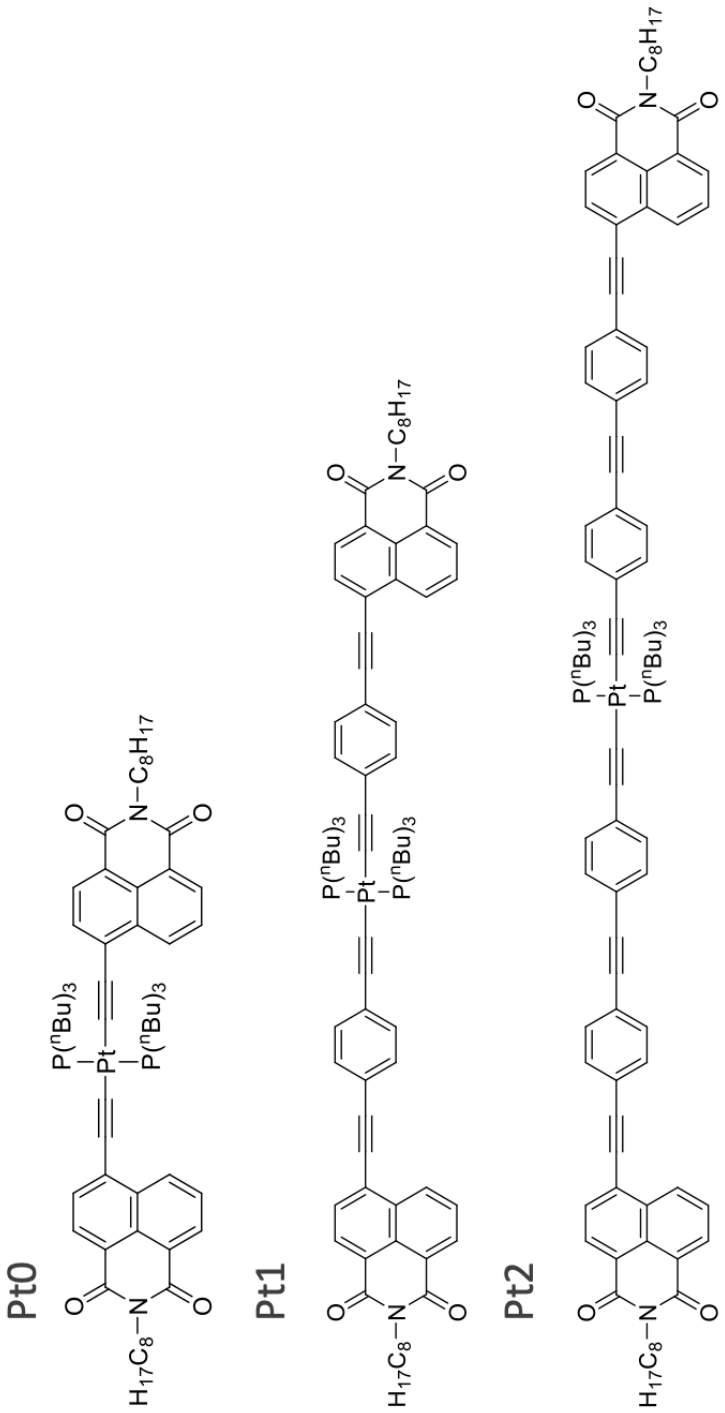

Figure 4.3 Molecular structures of the three symmetrical platinum acetylide complexes, 'Pt0', 'Pt1' and 'Pt2'.

The chemical structures of Pt0, Pt1 and Pt2 are shown in **Figure 4.3**. All complexes are symmetrical about the central metal atom, with an acceptor-bridge-acceptor type

structure. All of the complexes feature the same central unit, comprised of a square planar platinum centre and two trans 'PBu_3' (phosphine) groups. The neutral phosphine ligands lack low lying π^* orbitals,[27–35] hence do not engage in charge-transfer processes and are used as co-ligands in numerous Pt(II) trans-acetylide complexes. Attached to the Pt centre, via linkers of varying length, are two 'NAP' acceptor ligands. In Pt0 the NAP ligands are attached via acetylide linkers alone, whilst the linkers in Pt1 and Pt2 consist of alternating acetylide and phenyl units, Pt2 having one repeat unit longer than that of Pt1. Structurally, these complexes form an ideal chemical series for the investigation of rates of photophysical processes on extension of ligand conjugation. The Ph-CC-unit is considered to have excited states too high in energy to become engaged in excited state processes initiated by visible light (indeed, Ph-CCH only absorbs in the UV region). It has been noted previously, however, that as the number of (Ph-CC)- units increases, so does the conjugation, leading to an increase in the energy of the π, and a decrease in the energy of the π^* orbitals located on the (Ph-CC)n moiety. Consequently, the $\pi\pi^*$ state located on the (Ph-CC) moiety may become lowest in energy, and the "extended bridge" is no longer just a bridge but becomes engaged in electron/energy transfer.

4.2.2 UV-Vis Absorption and Steady-State Emission Spectroscopy

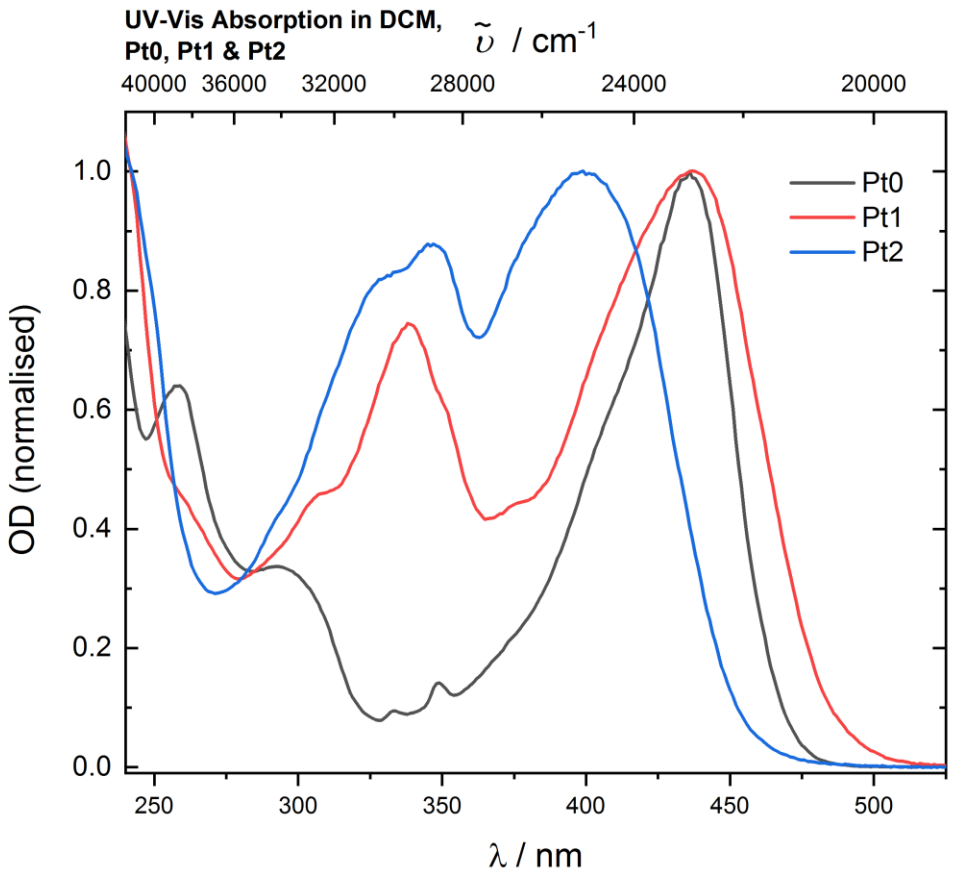

Figure 4.4 UV-Vis absorption spectra for Pt0 (solid black line), Pt1 (solid red line) and Pt2 (solid blue line) in dichloromethane (CH_2Cl_2) at room temperature.

The steady-state absorption spectra of the three complexes, in CH_2Cl_2 are shown in **Figure 4.4**. Both Pt1 (red line) and Pt2 (blue line) exhibit absorption bands in the region of 300 to 360 nm, with maxima at 338 and 347 nm respectively. These bands are assigned as arising from intraligand π-π^* transitions situated on the Ph units of the bridge; Pt0, which contains no Ph units, exhibits no such band in this region. For Pt0 and Pt1 the position of this band is almost identical, at 436 and 437 nm respectively. However, the band is significantly broader for Pt1 compared to Pt0. These bands show solvatochromic behaviour and are assigned as arising from metal-to-ligand charge-transfer transitions. The lowest-energy band for Pt2 is considerably blue-shifted relative to that of Pt0 and Pt1, with the band centred at 402 nm.

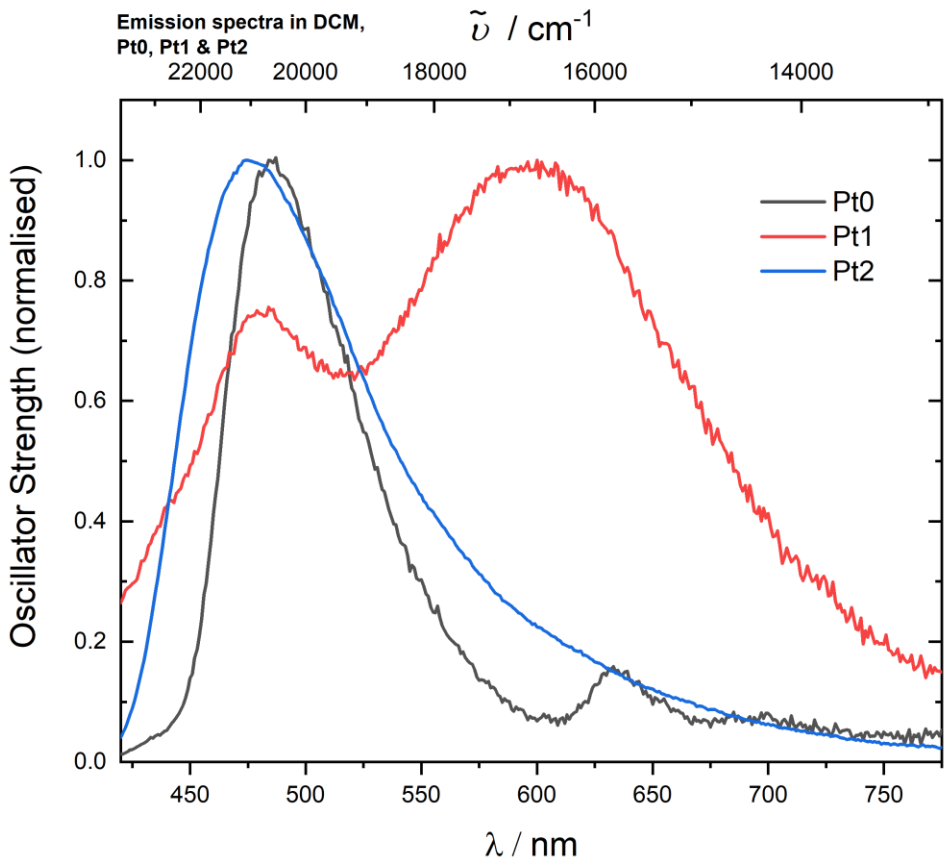

Figure 4.5 Steady-state emission spectra for Pt0 (solid black line), Pt1 (solid red line) and Pt2 (solid blue line) in dichloromethane (CH_2Cl_2) at room temperature, with excitation at 400 nm.

Steady-state emission spectra, in the region of 420 to 770 nm, of Pt0, Pt1 and Pt2, in DCM shown in **Figure 4.5**. All complexes exhibit a structureless, broad emission band centred in the region of 470 nm; with the maxima at 484 (Pt0), 479 (Pt1) and 474 nm (Pt2). The emission band of Pt2 is very broad, spanning the range of 420 to 750 nm. These bands are tentatively assigned as emission from MLCT states, due to lack of vibronic progression.

Rather interestingly, Pt1 displays an additional intense, broad band centred at around 600 nm. There is so trace of such a band with either Pt0 or Pt2. This band is assigned to an additional MLCT transition.

Pt0 displays additional, comparatively weak, two bands at around 633 and 699 nm. Almost identical bands are observed in the emission spectra of the closely related NAP-Pt-PTZ series discussed in the previous chapter and in the literature,[36] where they are

assigned to emission from a NAP-localised, $^3\pi\pi^*$* state. Emission spectra for Pt0 recorded in both oxygenated and de-oxygenated DCM are shown in **Figure 4.6**. The intensity of the low-energy bands at 633 and 699 nm, is enhanced with the de-oxygenation of the solvent, corroborating the assignment of these bands as being due to emission from a NAP-centred π-π^* transition.

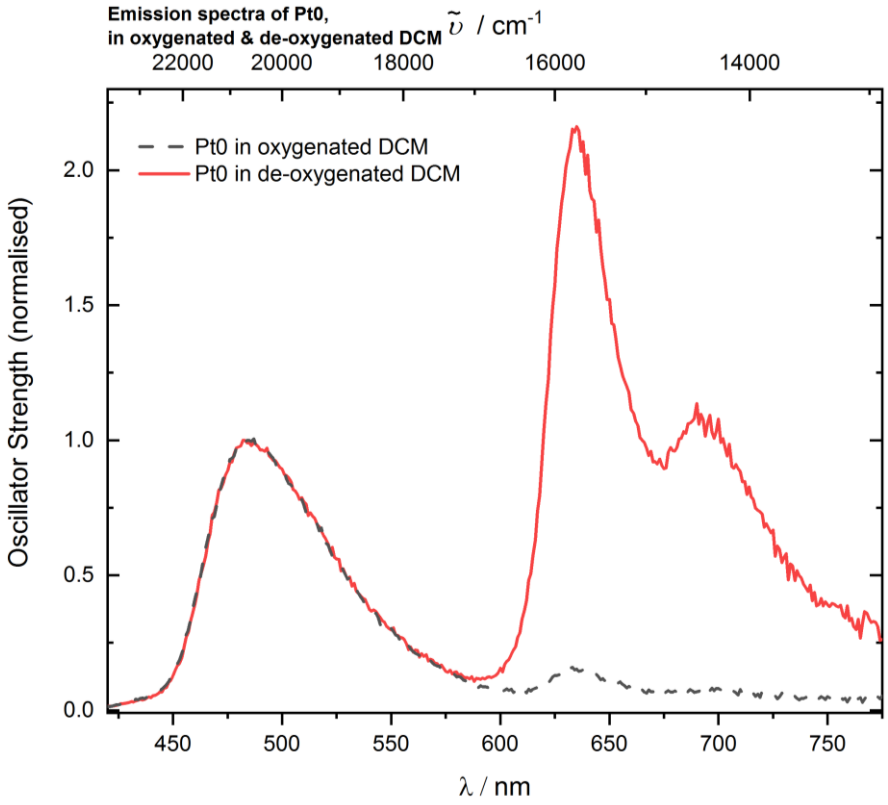

Figure 4.6 Steady-state emission spectra, upon 400 nm excitation, of Pt0 in oxygenated dichloromethane (CH_2Cl_2) (dashed black line) and Pt0 in de-oxygenated dichloromethane (solid red line), both recorded at room temperature.

4.2.3 Ultrafast Time-Resolved Fluorescence Spectroscopy

Time-resolved emission studies where performed using upconversion as the method of time-gating. Excitation of the sample with 400 nm, ca. 70 fs pulses, leads to emission across visible spectrum. This emission signal is upconverted (sum-frequency) with ~100 fs near-infrared “gate pulses” (1340 nm), and the resulting emission spectrum is recorded on a multiplex detector. Photometric correction for set-up sensitivity across the wavelength range of interest (300 – 430 nm) and time-zero dispersion (group-velocity dispersion) are performed, see Experimental Section and references for details.[37,38] In this way, a spectrum as distribution of emission photons over wavenumbers for a range of delay times between pump and gate pulses, are obtained. The details of the procedure are discussed in Chapter 2 – ‘Fluorescence Upconversion Spectroscopy (FLUPS)’.

Transient absorption spectra for the compounds discussed here have been recorded by our group. For ease of comparison between the time-resolved emission data presented here and the stimulated emission observed in the transient absorption spectra, the data here are presented in the form of stimulated emission distributions. Optical densities at excitation wavelengths, in the path lengths used, were approximately 0.3.

Pt0

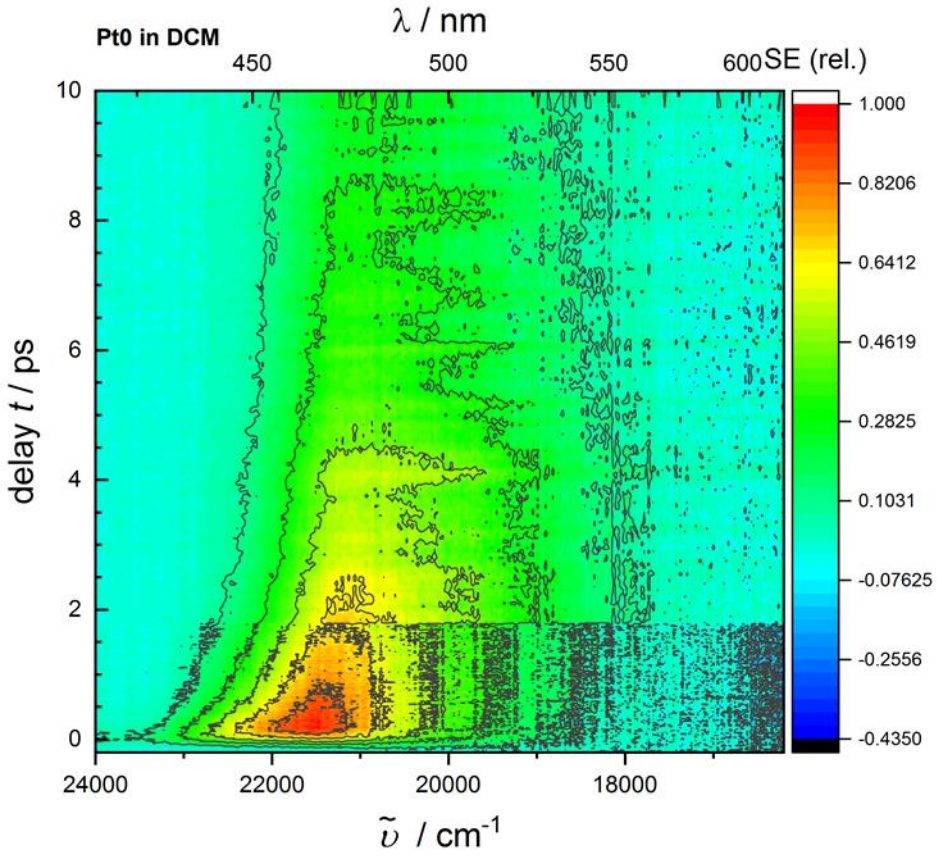

Figure 4.7 2D map of time-resolved emission spectra of Pt0 in dichloromethane upon 400 nm excitation, obtained by fluorescence upconversion. The optical density at the pump wavelength was approximately 0.3. Photometric- and time-zero dispersion- corrections have been applied to the raw data. Spectra are presented in the form of stimulated emission.

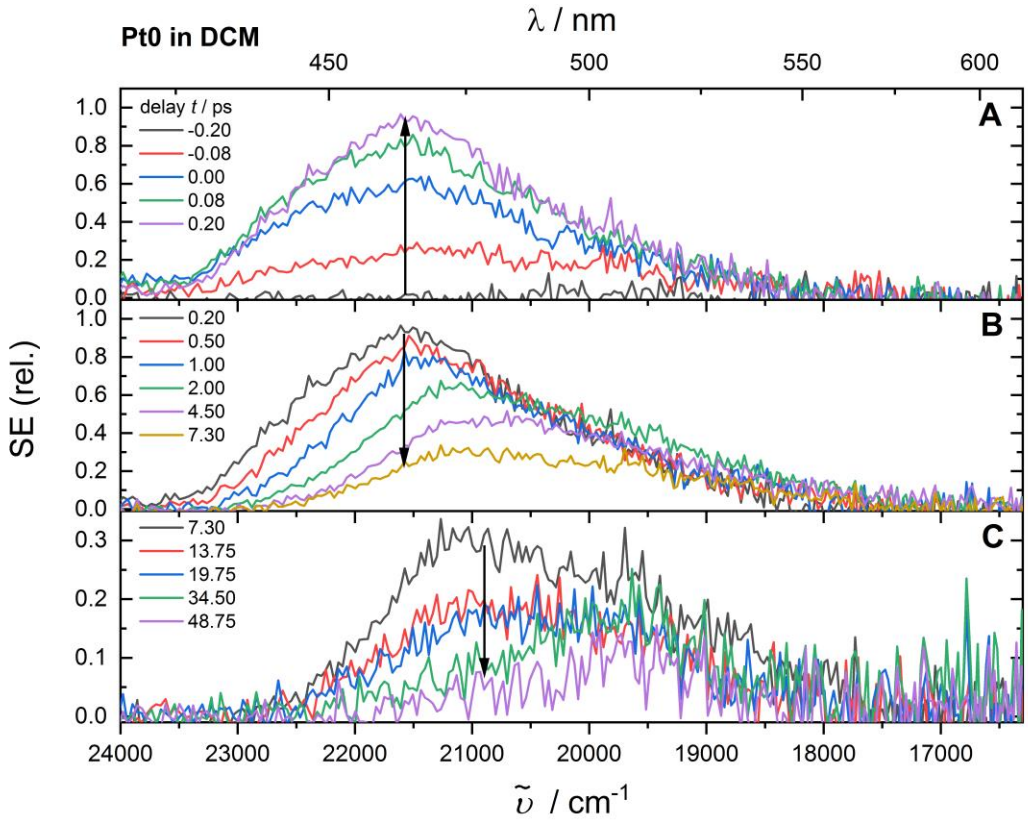

Figure 4.8 Time-resolved emission spectra of Pt0 in dichloromethane upon 400 nm excitation, obtained by fluorescence upconversion. The optical density at the pump wavelength was approximately 0.3. Three distinct temporal ranges are shown in each of the panels, A (-200 – 200 fs), B (200 fs – 7.30 ps) and C (7.30 ps – 48.75 ps). Arrows indicate the characteristic evolutionary feature within each range. Photometric- and time-zero dispersion-corrections have been applied to the raw data. Spectra are presented in the form of stimulated emission.

Figure 4.7 and **Figure 4.8** show the time-resolved emission spectra of Pt0, in a dichloromethane (CH_2Cl_2) solution, upon ~70 fs, 400 nm excitation. The spectra were obtained by fluorescence upconversion as outlined above. Three distinct temporal regions, each showing clear changes in the spectral shape were identified, and are shown in each of the panels **A**, **B** and **C**. Excitation with 400 nm (25,000 cm^{-1}) light leads to population of a singlet metal-to- to-ligand charge transfer state, ^{1}MLCT (absorption maximum at 436 nm or 22,936 cm^{-1}), with excess vibrational energy of 2064 cm^{-1} (0.256 eV). Panel **A** shows the rise of a broad emission band, covering the region of 18,000 to 23,500 cm^{-1}, with a maximum at about 21,500 cm^{-1}. Within experimental error the intensity rises uniformly across all wavenumbers, within the instrument response. This immediately detected emission band is 3500 cm^{-1} lower in energy than the 25,000 cm^{-1} (400 nm) excitation, with the excess energy dissipated within the instrument response.

Initially, as seen for example in the spectrum at 0.20 ps, the emission appears to be composed of multiple bands, with a weak shoulder at about 22,500 cm^{-1}.

Within the first 7 picoseconds, considerable spectral change is observed (**Figure 4.8**, Panel **B**). The emission spectrum shifts towards lower energy, to a maximum at about 21,000 cm^{-1} by ca. 7 ps. After 7.30 ps, the band shifts further to around 19,500 cm^{-1} by around 35 ps. Concomitantly with the spectral shift, the emission spectrum becomes narrower and undergoes significant change in spectral shape. The spectrum at 7.3 ps, unlike that of 0.20 ps, exhibits no obvious shoulder and displays a shape more typical of a single emission band. These 'early time' dynamics are characteristic signatures of vibrational relaxation. Within the first 7 ps, considerable loss in emission intensity is observed, the area under the spectra at 7.30 ps is approximately a quarter of that at 200 fs.

Panel **C** shows the decay of the emission band on a ~10 ps time scale. At 48.75 ps, the longest time delay measured, very weak emission signal persists.

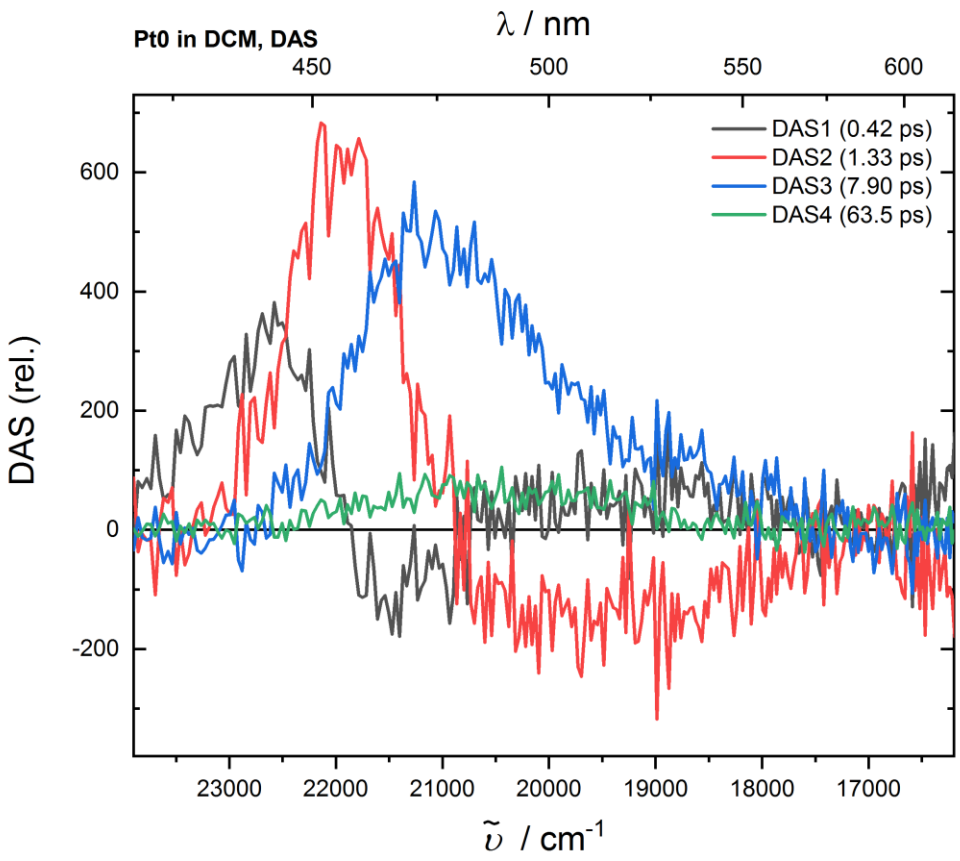

Figure 4.9 Decay-Associated Spectra (DAS) of the emission spectra of Pt0 (shown in ***Figure 4.8***), obtained via global analysis using four exponential time functions. The corresponding time constants are given as insets.

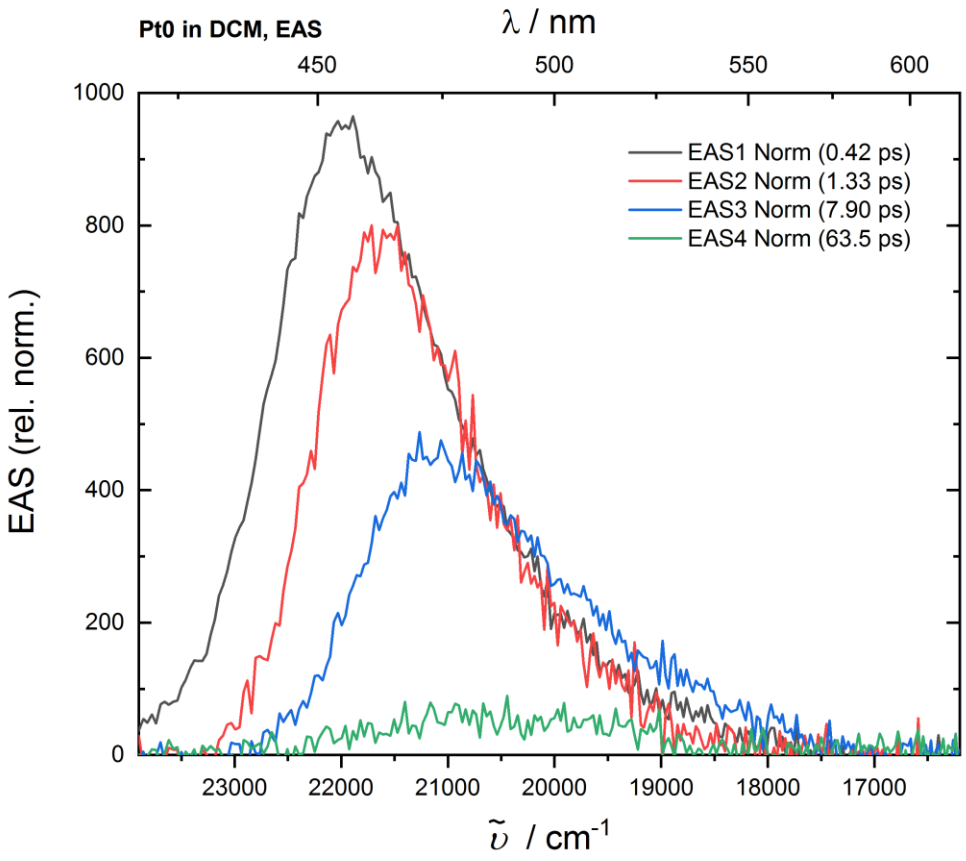

Figure 4.10 Evolution-Associated Spectra (EAS) of the emission spectra of Pt0 (shown in ***Figure 4.8***), obtained via global analysis using four exponential time functions. The corresponding time constants are given as insets.

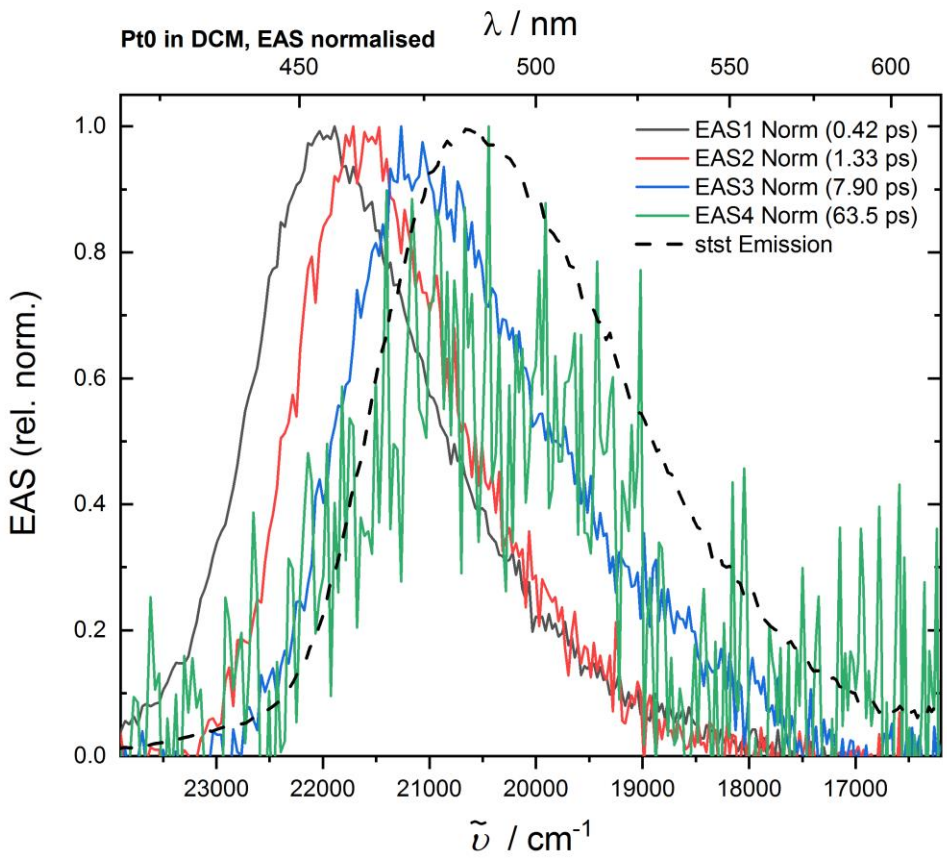

Figure 4.11 Normalised version of the Evolution-Associated Spectra (EAS), of Pt0, shown in ***Figure 4.10***. Obtained via global analysis using four exponential time functions, normalised to peak values. The corresponding time constants are given as insets. The steady-state (stst) emission spectrum of Pt0, converted to the form of stimulated-emission (SE), is also shown (black dashed trace, stst Emission). Spectra are shown as normalised here to allow for better comparison of spectral position between EAS and for comparison of steady-state emission with EAS4.

Global analysis has been performed in order to extract spectral and dynamic information. Initially a parallel kinetic model with four exponential time functions was used to analyse the data, i.e., it is assumed that the initial population of states decays along 4 parallel pathways to the ground state. The resultant Decay-Associated Spectra (DAS) are shown in **Figure 4.9**, with the corresponding kinetic parameters shown in the inset. The decomposition of the spectra into the DAS gives an estimate of the number of observable processes / states involved in the dynamics. The 0.42, 1.33 and 7.90 ps DAS components (black, red and blue line, respectively) describe the initial red-shift and narrowing, illustrated in panel **B** and **C** of **Figure 4.8**. The 7.90 ps component, along with the 63.5 ps component describes the decay of band, illustrated in panel **C** of **Figure 4.8**. The spectrum of this component matches the steady-state emission spectrum of the

complex (displayed in **Figure 4.11**, dashed grey line) and is therefore assigned as emission from a charge transfer state. The spectra of the 63.5 ps component can be considered as that of the thermally-equilibrated electronic state, with the 0.42, 1.33 and 7.90 ps components describing the relaxation from the initially populated, hot, state. The temporal components needed to describe the evolution are relatively distinct, i.e. each of different orders of magnitude. As this is the case, both parallel and sequential models yield identical time-constants. With these types of systems, a sequential model for the excited state decay is typically more applicable.

In summary, there is excitation from 0 (ground-state) to A (represented by EAS1), followed by transition to B (EAS2), then C(EAS3), then D(EAS4) and ultimately return back to 0 (ground-state), 0→A→B→C→D→0.

The Evolution-Associated Spectra (EAS), obtained with a sequential model represent emission from the various states populated after excitation are shown in **Figure 4.10**. Normalised EAS are shown in **Figure 4.11**. The normalised EAS allow for better comparison of the shift in spectral position as a function of time, as well for better comparison of the steady-state emission and the final EAS, EAS4.

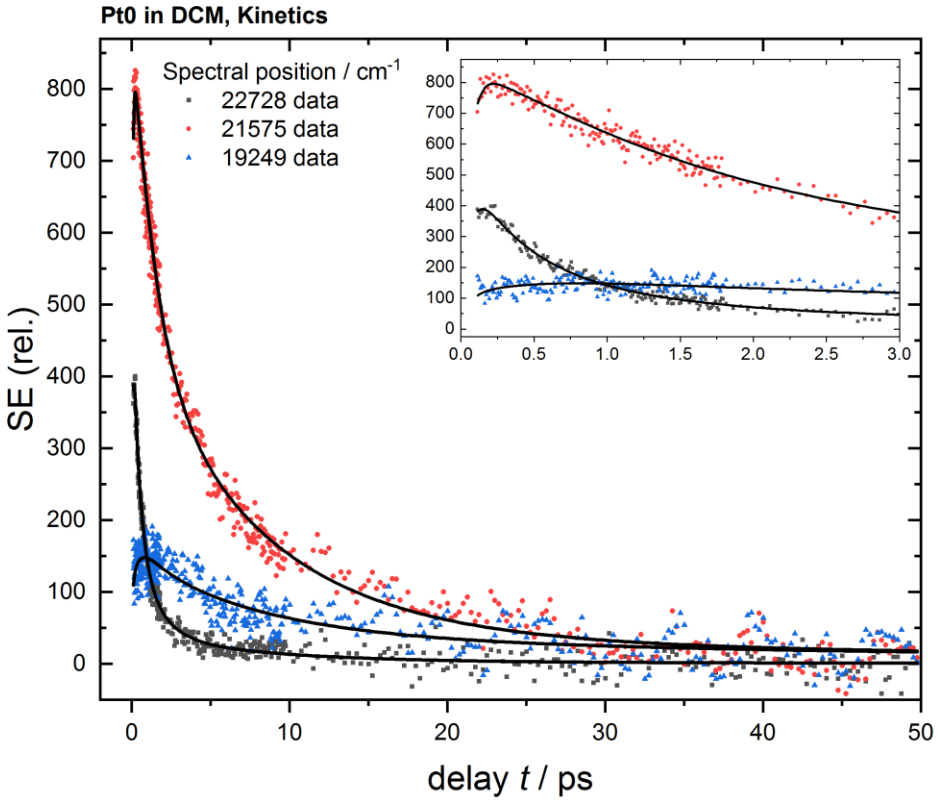

Figure 4.12 Kinetic traces showing the dynamics of the emission of Pt0, at select spectral positions. Solid lines represent best fits obtained via global analysis using four exponential time functions in a sequential model. The inset shows an expansion of the first 3 ps.

Kinetic traces at select spectral positions, alongside the fits obtained with global analysis are shown in **Figure 4.12**. For Pt0, four exponential time components were the minimum number required in order to achieve a satisfactory fit of the data, without a systematic deviation of the residual vs. signal.

Pt1

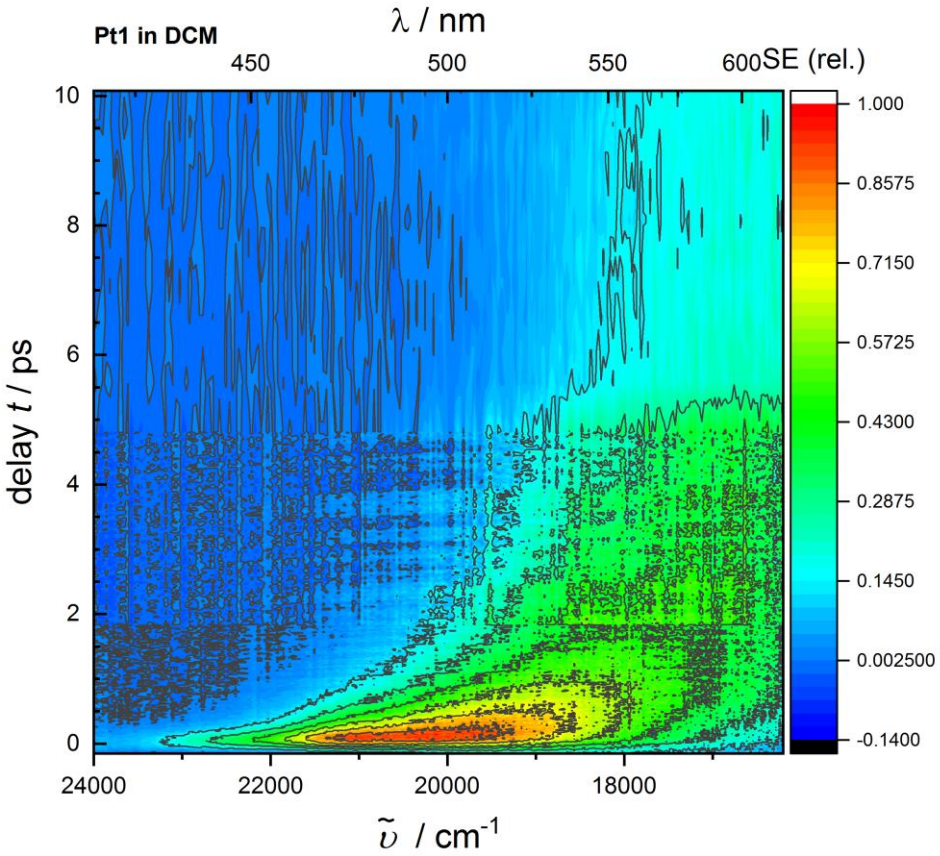

Figure 4.13 2D map of time-resolved emission spectra of Pt1 in dichloromethane upon 400 nm excitation, obtained by fluorescence upconversion. The optical density at the pump wavelength was approximately 0.3. Photometric- and time-zero dispersion- corrections have been applied to the raw data. Spectra are presented in the form of stimulated emission.

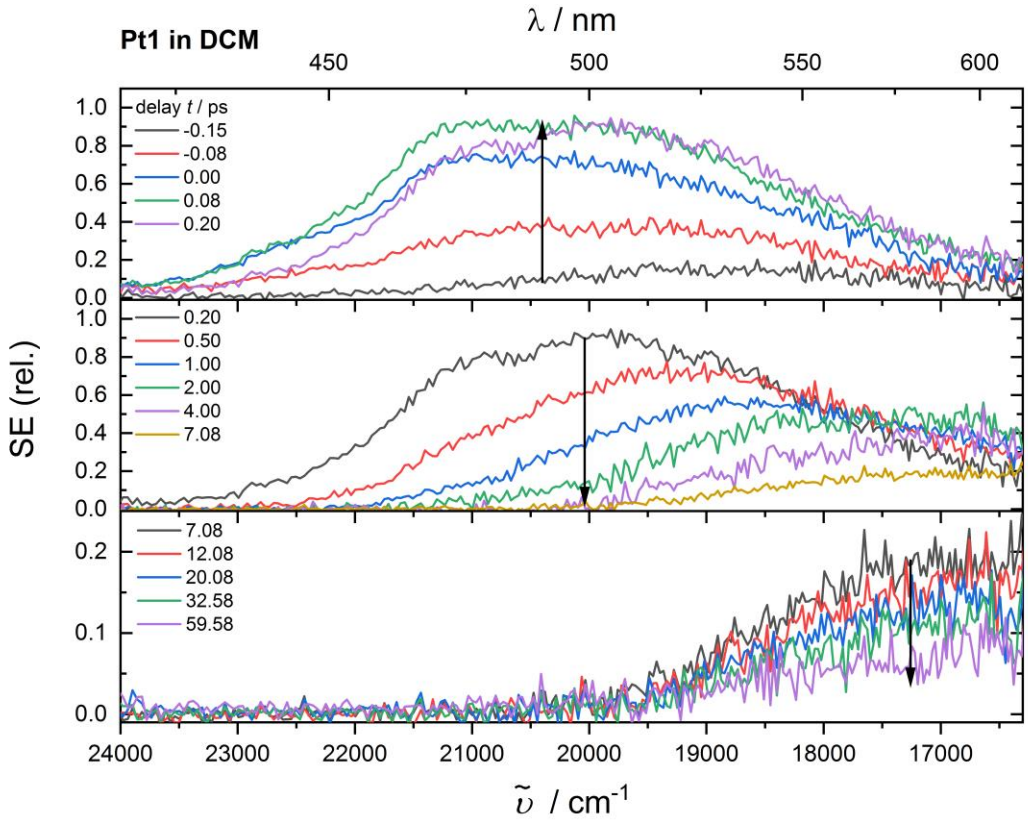

Figure 4.14 Time-resolved emission spectra of Pt1 in dichloromethane upon 400 nm excitation, obtained by fluorescence upconversion. The optical density at the pump wavelength was approximately 0.3. Three distinct temporal ranges are shown in each of the panels, A (-150 – 200 fs), B (200 fs – 7.08 ps) and C (7.08 ps – 59.58 ps). Arrows indicate the characteristic evolutionary feature within each range. Photometric- and time-zero dispersion-corrections have been applied to the raw data. Spectra are presented in the form of stimulated emission.

Figure 4.13 and **Figure 4.14** show the time-resolved emission spectra of Pt1, in a dichloromethane (CH_2Cl_2) solution, upon ~70 fs, 400 nm excitation. The spectra were obtained by fluorescence upconversion method as outlined above. Similarly to the Pt0 data described above, three distinct temporal regions associated with spectral changes are identified and are shown in each of the panels **A**, **B** and **C**. Excitation with 400 nm (25,000 cm^{-1}) light leads to population of a manifold of metal-to-ligand charge transfer state, ^{1}MLCT (absorption maximum at 436 nm or 22,936 cm^{-1}), with excess vibrational energy of 2064 cm^{-1} (0.256 eV). It is an assumption that a singlet state is populated (whilst it is possible that within the laser pulse a conversion into triplet and/or spin-orbit states is already taking place). We also note that whilst a ”metal to ligand state” is stated, it is likely to be a manifold of several states, of different degrees of MLCT nature. Hereafter, the manifold of spin-orbit states will be called “^{1}MLCT”, for simplicity. Panel **A** shows the rise of a broad emission band, covering the region of 16,400 to 24,000 cm^{-1}. with a maximum at about 21,250 cm^{-1}. Within the instrument response, the intensity

does not rise uniformly across all wavenumbers, the spectrum at 0.00 ps shows a relatively well-defined shoulder at around 19,750 cm^{-1}, unlike that at -0.15 or -0.08 ps. This immediate emission band is 3750 cm^{-1} lower in energy than the 25,000 cm^{-1} (400 nm) excitation, with the excess energy dissipated within the instrument response. Initially, as seen for example in the spectrum at 0.20 ps, the emission appears to be composed of multiple bands, the peak of the broad band at 20,000 cm^{-1}, with a weak shoulder at about 21,250 cm^{-1} as mentioned previously.

Within the first 7 picoseconds, considerable spectral change is observed (**Figure 4.14**, Panel **B**). The emission spectrum shifts towards lower energy, to a maximum at about 17,000 cm^{-1} by ca. 7 ps. After 7.08 ps, there is no further shifting of the band. Concomitantly with the spectral shift, the emission spectrum becomes narrower and undergoes significant change in spectral shape. The spectrum at 7.08 ps, unlike that of 0.20 ps, exhibits no obvious shoulder and displays a shape more typical of a single emission band. These 'early time' dynamics are characteristic signatures of vibrational relaxation. Within the first 7 ps, considerable loss in emission intensity is observed, the area under the spectra at 7.08 ps is approximately one tenth of that at 200 fs.

Panel **C** shows the decay of the emission band on a ~10 ps time scale. At 59.58 ps, the longest time delay measured, weak emission signal persists.

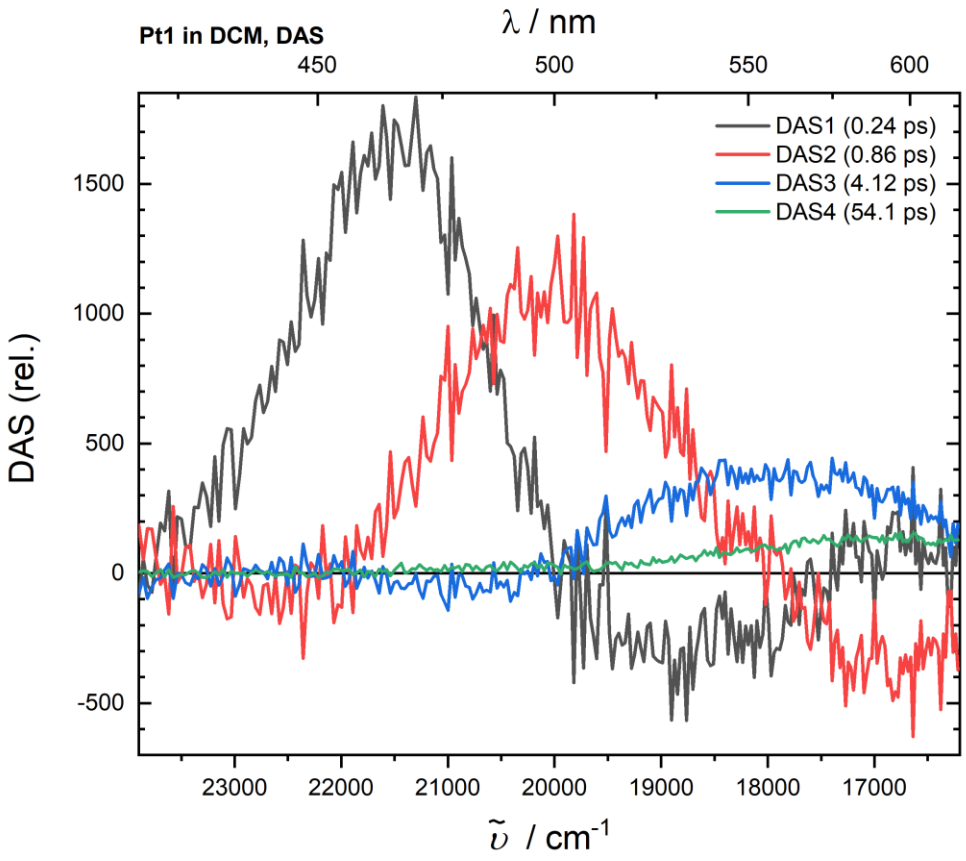

Figure 4.15 Decay-Associated Spectra (DAS) of the emission spectra of Pt1 (shown in ***Figure 4.14***), obtained via global analysis using four exponential time functions. The corresponding time constants are given as insets.

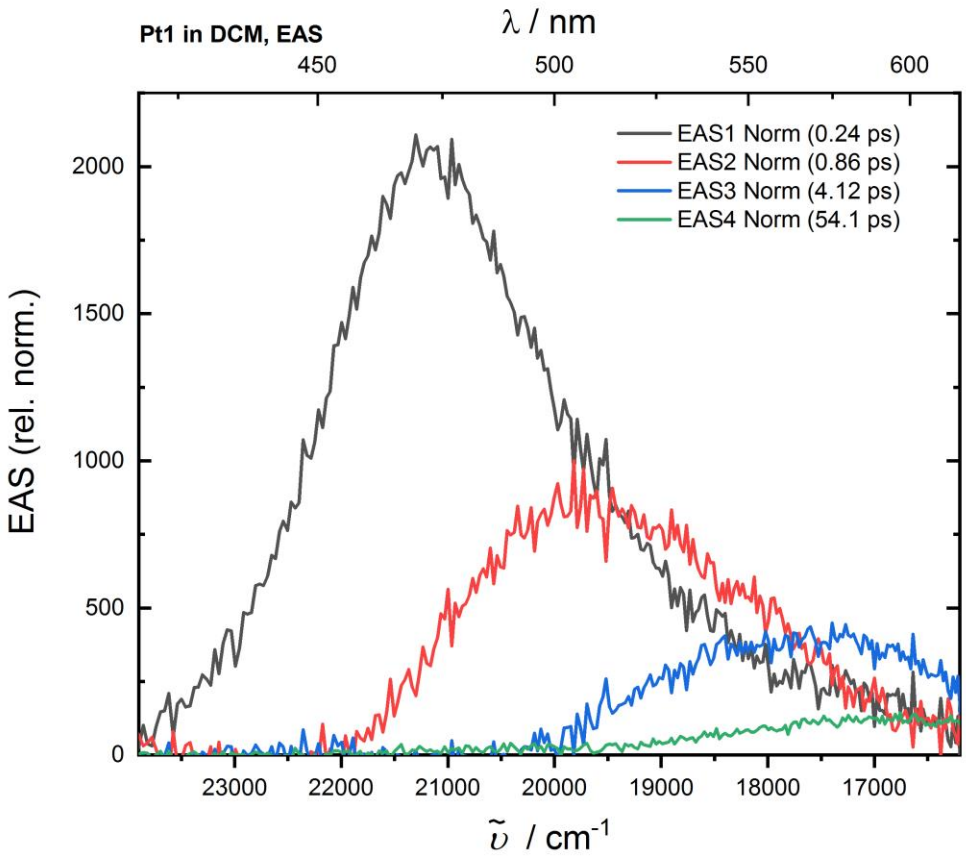

Figure 4.16 Evolution-Associated Spectra (EAS) of the emission spectra of Pt1 (shown in ***Figure 4.14***), obtained via global analysis using four exponential time functions. The corresponding time constants are given as insets.

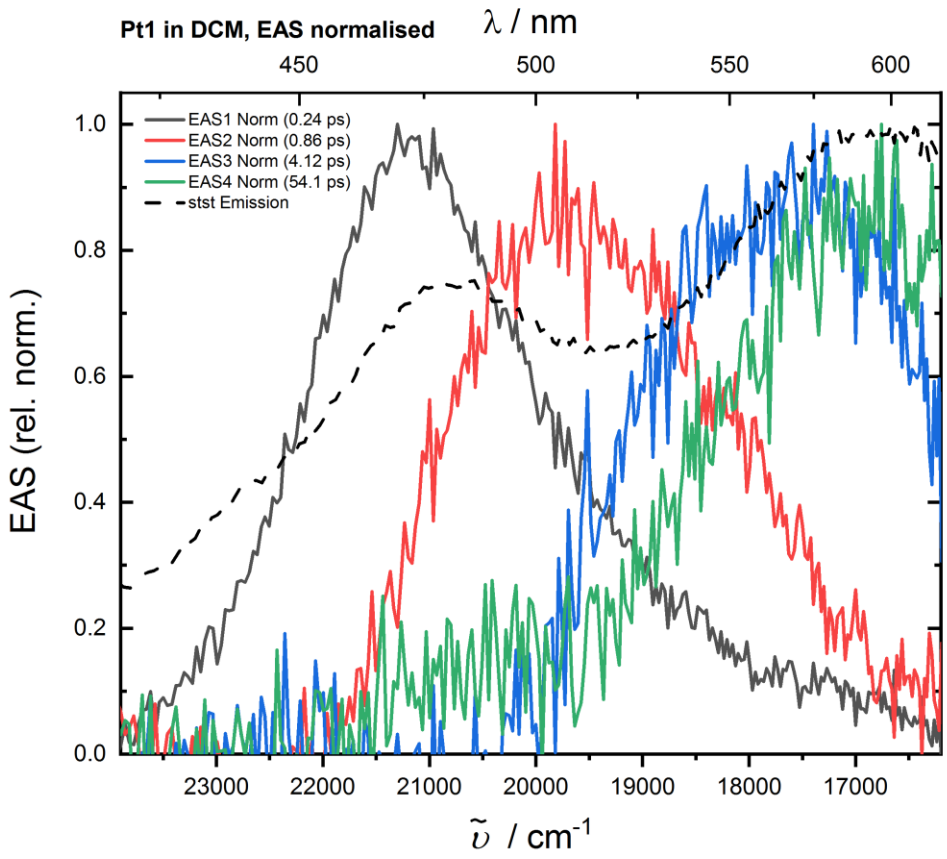

Figure 4.17 Normalised version of the Evolution-Associated Spectra (EAS), of Pt1, shown in ***Figure 4.16***. Obtained via global analysis using four exponential time functions, normalised to peak values. The corresponding time constants are given as insets. The steady-state (stst) emission spectrum of Pt0, converted to the form of stimulated-emission (SE), is also shown (black dashed trace, stst Emission). Spectra are shown as normalised here to allow for better comparison of spectral position between EAS and for comparison of steady-state emission with EAS4.

A similar global analysis procedure, as above, was performed on this data set, in order to extract spectral and dynamic information. Initially a parallel model with four exponential time functions was used to fit the data. The resultant Decay-Associated Spectra (DAS) are shown in **Figure 4.15**, with the corresponding kinetic parameters shown in the inset. The decomposition of the spectra into the DAS gives an estimate of the number of observable processes / states involved in the dynamics. The 0.24, 0.86 and 4.12 ps DAS components (black, red and blue line, respectively) describe the initial red-shift and narrowing, illustrated in panel **B** and **C** of **Figure 4.14**. The 4.12 ps component, along with the 54.1 ps component describes the decay of band, illustrated in panel **C** of **Figure 4.14**. The spectrum of this component matches the lowest energy band seen in the steady-state emission spectrum of the complex (displayed in, dashed grey line) and is therefore assigned as emission from a charge transfer state. The spectra of the 54.1 ps

component can be considered as that of the vibrationally equilibrated electronic state, with the 0.24, 0.86 and 4.12 ps components describing the relaxation from the initially populated, hot, state. The temporal components needed to describe the evolution of the data differ by at least an order of magnitude. As this is the case, both parallel and sequential models yield identical time-constants.

The model implies excitation from 0 (ground-state) to A (represented by EAS1), followed by transition to B (EAS2), then C(EAS3), then D(EAS4) and ultimately return back to 0 (ground-state), 0->A->B->C->D->0.

The Evolution-Associated Spectra (EAS) obtained with a sequential model represent emission from the various states populated after excitation are shown in **Figure 4.16**.

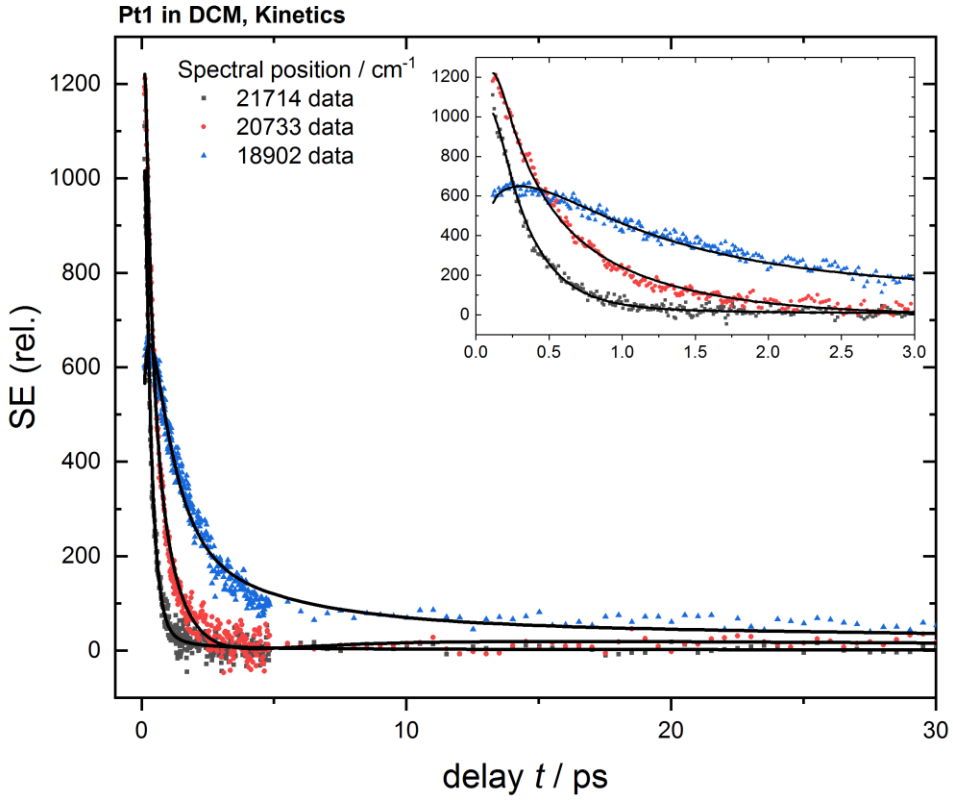

Figure 4.18 Kinetic traces showing the dynamics of the emission of Pt1, at select spectral positions. Solid lines represent best fits obtained via global analysis using four exponential time functions in a sequential model. Inset shows an expansion of the first 3 ps.

Kinetic traces at select spectral positions, alongside the fits obtained with global analysis are shown in **Figure 4.18**. For Pt1, four exponential time components were the minimum number required in order to achieve a satisfactory ft of the data, without a systematic deviation of the residual vs. signal.

Pt2

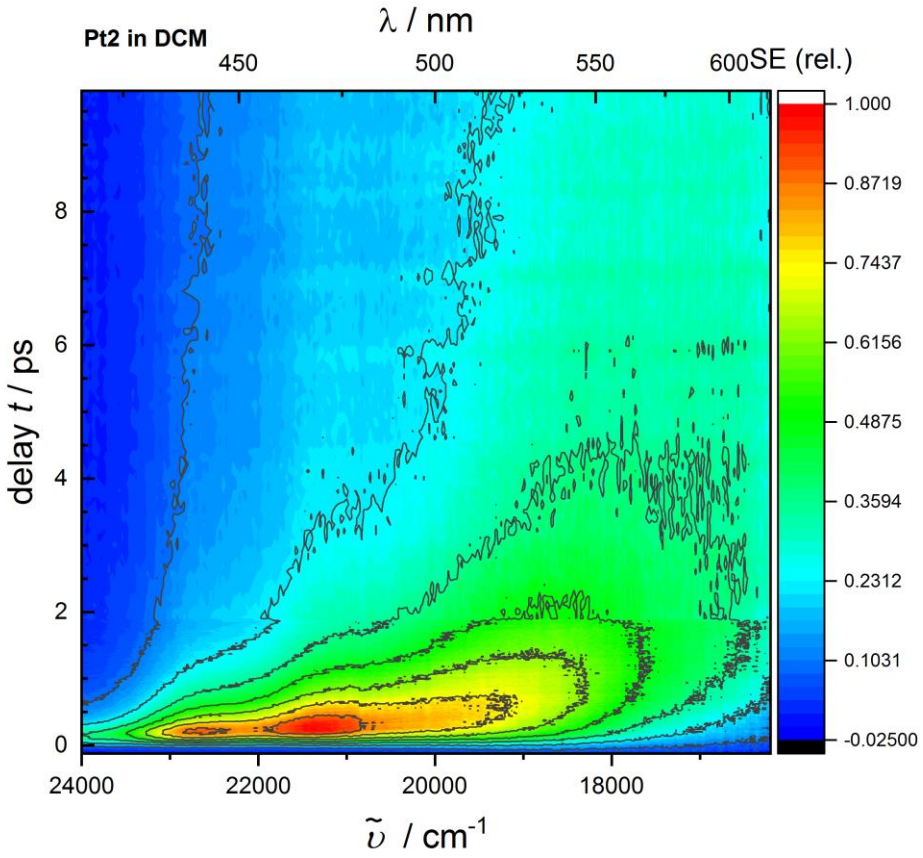

Figure 4.19 2D map of time-resolved emission spectra of Pt2 in dichloromethane upon 400 nm excitation, obtained by fluorescence upconversion. The optical density at the pump wavelength was approximately 0.3. Photometric- and time-zero dispersion- corrections have been applied to the raw data. Spectra are presented in the form of stimulated emission.

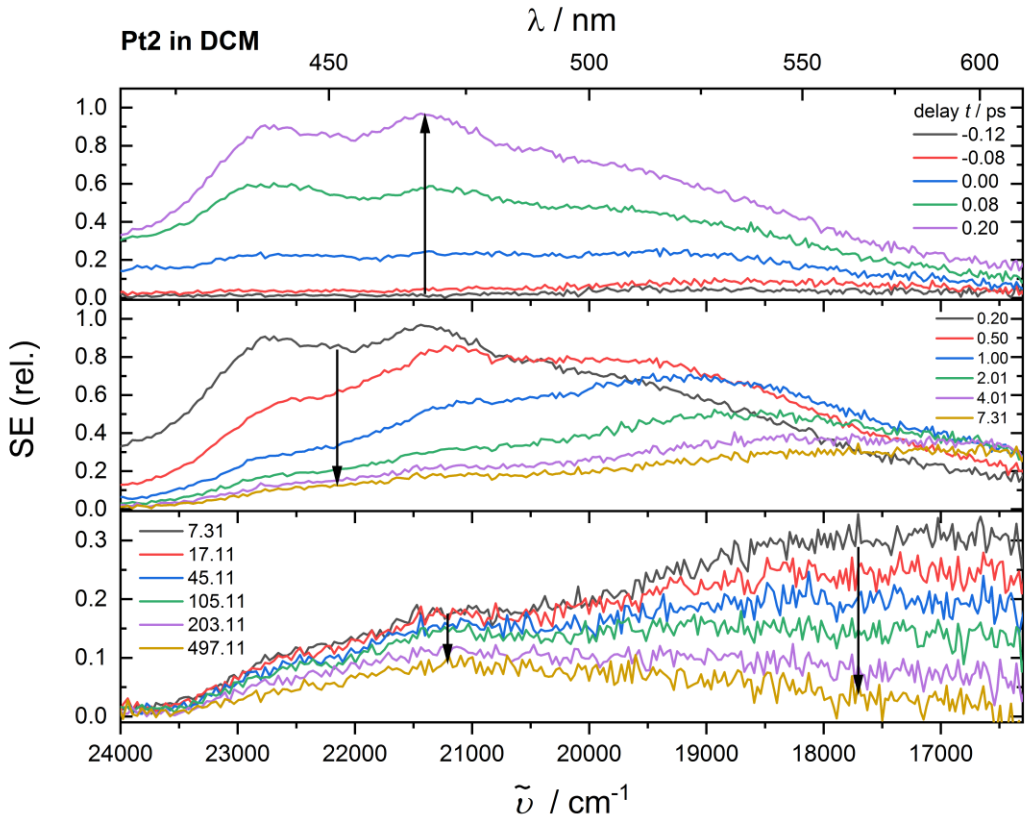

Figure 4.20 Time-resolved emission spectra of Pt2 in dichloromethane upon 400 nm excitation, obtained by fluorescence upconversion. The optical density at the pump wavelength was approximately 0.3. Three distinct temporal ranges are shown in each of the panels, A (-120 – 200 fs), B (200 fs – 7.31 ps) and C (7.31 ps – 497.11 ps). Arrows indicate the characteristic evolutionary feature within each range. Photometric- and time-zero dispersion-corrections have been applied to the raw data. Spectra are presented in the form of stimulated emission.

Figure 4.19 and **Figure 4.20** show the time-resolved emission spectra of Pt2, in a dichloromethane (CH_2Cl_2) solution, upon ~70 fs, 400 nm excitation. The spectra were obtained by fluorescence upconversion method as outlined above. Three distinct temporal regions each showing clear changes in the spectral shape were identified, and are shown in each of the panels **A**, **B** and **C**. Excitation with 400 nm (25,000 cm^{-1}) light leads to population of a singlet metal-to-ligand charge transfer state, ^{1}MLCT (absorption maximum at 402 nm or 24,876 cm^{-1}), with excess vibrational energy of only 124 cm^{-1} (0.0154 eV). Panel **A** shows the rise of a broad emission band, covering the region of 16,400 to 24,000 cm^{-1}. with a maximum at about 21,450 cm^{-1}. Within the instrument response, the intensity does not rise uniformly across all wavenumbers, the spectrum at 0.20 ps shows a well-defined second peak at around 22,900 cm^{-1}, unlike that at 0.00 ps. The higher in energy (22,900 cm^{-1}) of the two immediate emission bands is 2100 cm^{-1}

lower in energy than the 25,000 cm^{-1} (400 nm) excitation, with the excess energy dissipated within the instrument response.

Within the first 7 picoseconds, considerable spectral change is observed (Panel **B**). The emission spectrum shifts towards lower energy, to a maximum at about 17,500 cm^{-1} by ca. 7 ps. These 'early time' dynamics are characteristic signatures of vibrational relaxation. Within the first 7 ps, considerable loss in emission intensity is observed, the area under the spectra at 7.08 ps is approximately a quarter of that at 200 fs.

Illustrated in Panel **C** of **Figure 4.20**, the band undergoes a significant blue-shift on the time scale of 100s of picoseconds. The emission centred at about 17,500 cm^{-1} decays, revealing a longer-lived, higher energy emission band. The spectra of the longest recorded time-delay, 497.11 ps, shows a broad emission band centred at about 21,250 cm^{-1}. This behaviour is unique to this complex, and not observed in either Pt0 or Pt1.

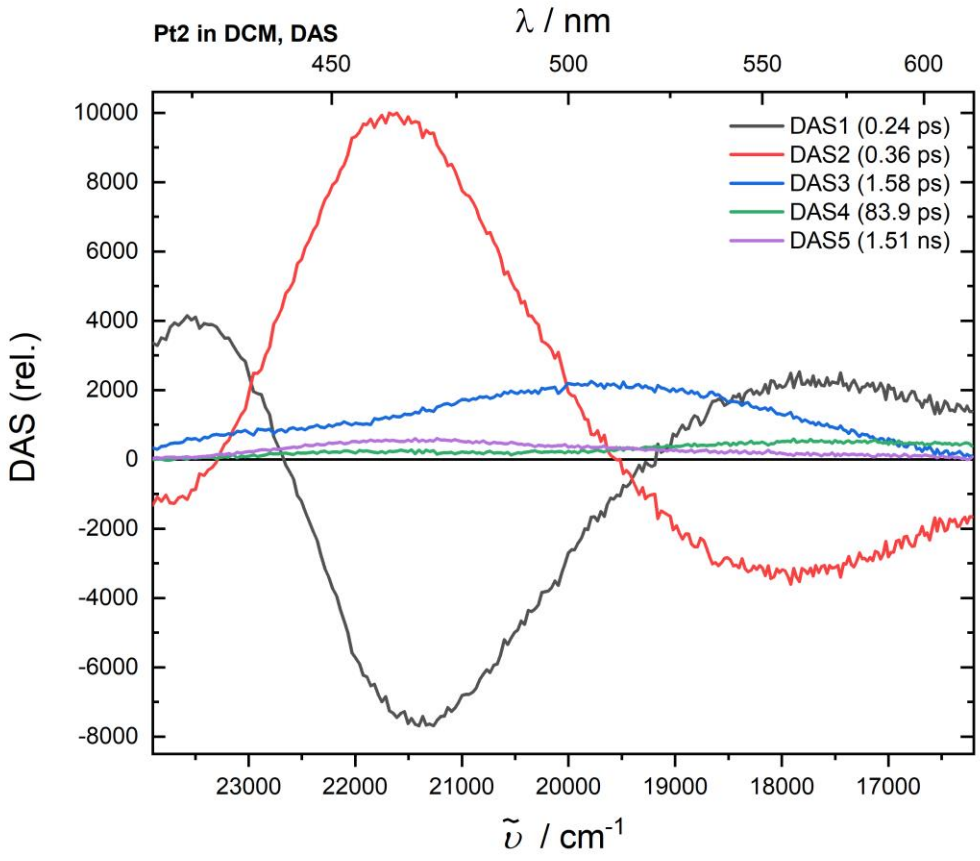

Figure 4.21 Decay-Associated Spectra (DAS) of the emission spectra of Pt2 (shown in ***Figure 4.20***), obtained via global analysis using four exponential time functions. The corresponding time constants are given as insets.

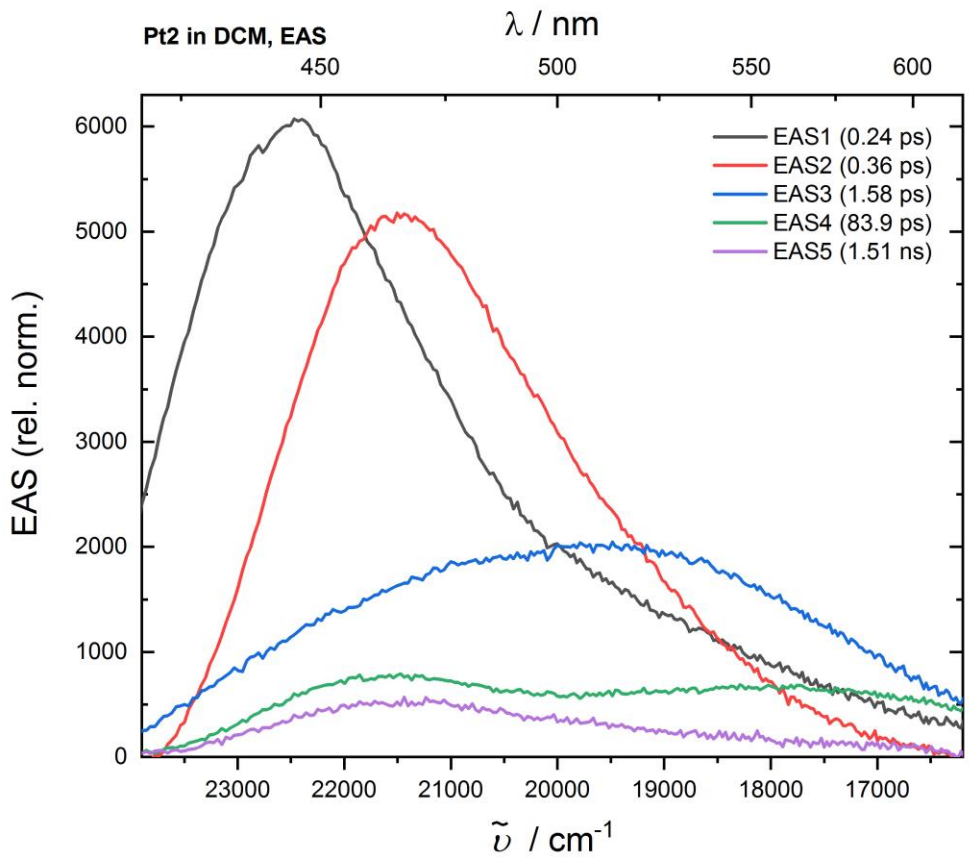

Figure 4.22 Evolution-Associated Spectra (EAS) of the emission spectra of Pt2 (shown in ***Figure 4.20***), obtained via global analysis using 5 exponential time functions. The corresponding time constants are given as insets.

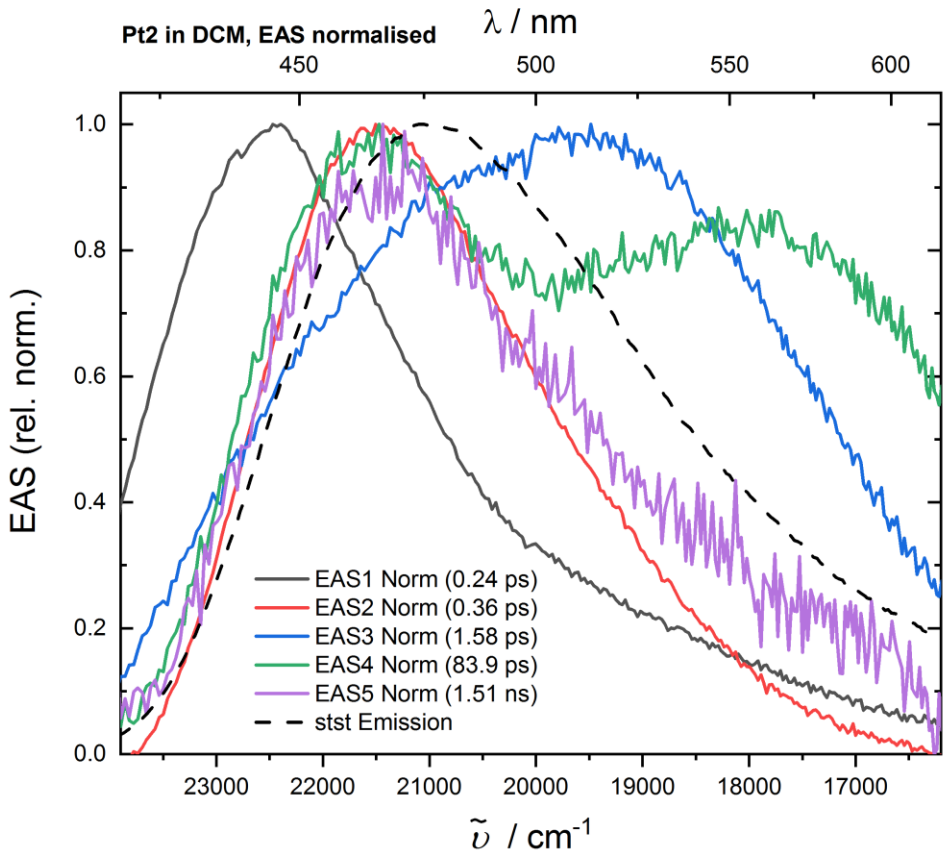

Figure 4.23 Normalised version of the Evolution-Associated Spectra (EAS), of Pt2, shown in ***Figure 4.22***. Obtained via global analysis using 5 exponential time functions, normalised to peak values. The corresponding time constants are given as insets. The steady-state (stst) emission spectrum of Pt0, converted to the form of stimulated-emission (SE), is also shown (black dashed trace, stst Emission). Spectra are shown as normalised here to allow for better comparison of spectral position between EAS and for comparison of steady-state emission with EAS5.

A similar global analysis procedure, as above, was performed on this data set, in order to extract spectral and dynamic information. Initially a parallel model with 5 exponential time functions was used to fit the data. The resultant Decay-Associated Spectra (DAS) are shown in **Figure 4.21**, with the corresponding kinetic parameters shown in the inset. The decomposition of the spectra into the DAS gives an estimate of the number of observable processes / states involved in the dynamics. The 0.24, 0.36 and 1.58 ps DAS components (black, red and blue line, respectively) describe the initial red-shift and narrowing, illustrated in panel **B** of **Figure 4.20**. The 83.9 ps component describes the blue shift of the band illustrated in panel **C** of **Figure 4.20**. The final DAS, DAS5, with an associated lifetime of 1.51 ns, describes the decay of the final emissive state, illustrated in panel **C** of **Figure 4.20**. Measurements were made up to a maximum delay-time of

497.11 ps, this temporal component (1.51 ns) is therefore unreliable, measurements should be repeated up to maximum possible delay time, currently around 3 ns.

The steady-state emission spectrum of Pt2 in DCM is shown alongside normalised EAS in **Figure 4.23**. The steady-state spectra (dashed black line) is similar to that of EAS2, the high-energy band of EAS4 and EAS. The 0.24, 0.36 and 1.58 ps components describe the relaxation from the initially populated, hot, state. The temporal components needed to describe the evolution of the data differ by at least an order of magnitude. As this is the case, both parallel and sequential models yield identical time-constants. With these types of systems, a sequential model for the excited state decay is typically more applicable.

The model implies excitation from 0 (ground-state) to A (represented by EAS1), followed by transition to B (EAS2), then C(EAS3), then D(EAS4), then E(EAS5), ultimately return back to 0 (ground-state), 0->A->B->C->D->E->0. This is however implausible as EAS5 lies much higher in energy than EAS3 and EAS4. There is most likely branching at early times, with some population left 'trapped' in a higher energy state, comparable to that of EAS2.

The Evolution-Associated Spectra (EAS) obtained with a sequential model represent emission from the various states populated after excitation are shown in **Figure 4.22** and **Figure 4.23**.

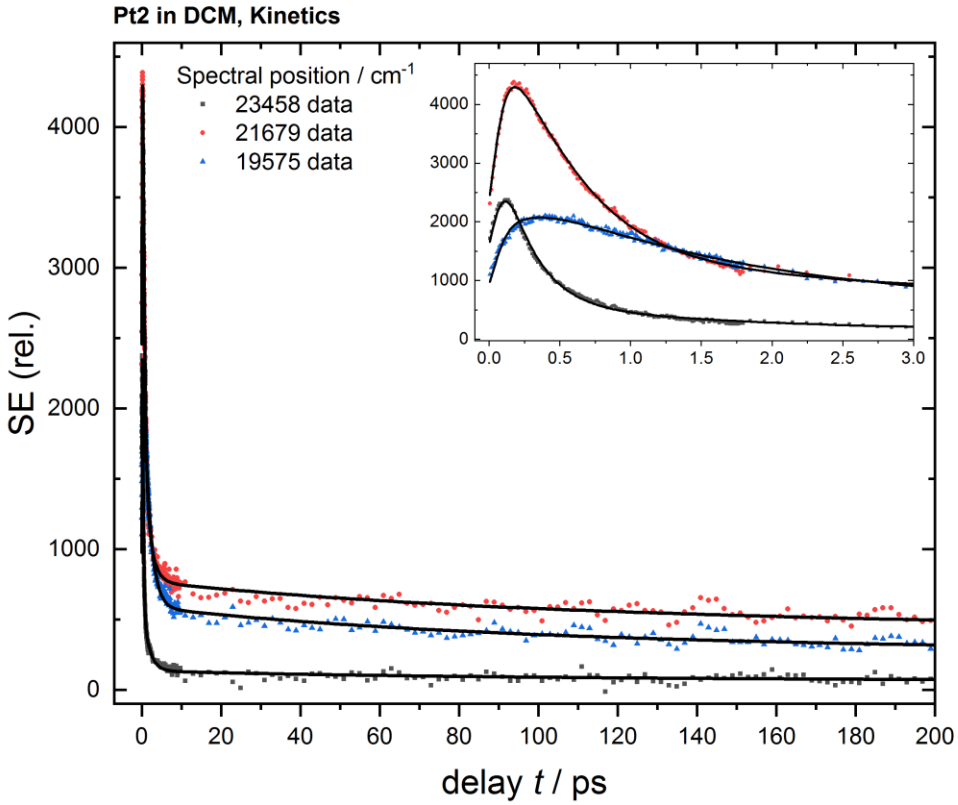

Figure 4.24 Kinetic traces showing the dynamics of the emission of Pt2, at select spectral positions. Solid lines represent best fits obtained via global analysis using 5 exponential time functions in a sequential model. Inset shows an expansion of the first 3 ps.

Kinetic traces at select spectral positions, alongside the fits obtained with global analysis are shown in **Figure 4.24**. For Pt1, a three-exponential function describes the evolution of the data best.

All time constants obtained via global analysis of the time-resolved emission spectra are presented below in

4.2.4 Ultrafast Transient Absorption Spectroscopy

In addition to the time-resolved emission measurements presented above, ultrafast transient absorption spectra (time-resolved UV-Vis absorption) were also recorded. Spectra were recorded on a commercial instrument, the Helios by Ultrafast Systems. Excitation of the sample was with 400 nm, ca. 70 fs pulses, with probing in the region of 420 to 670 nm. Optical densities at excitation wavelengths, in the path lengths used, were approximately 0.3. Time-zero dispersion (group-velocity dispersion) corrections are applied to all data before fitting.

Pt0

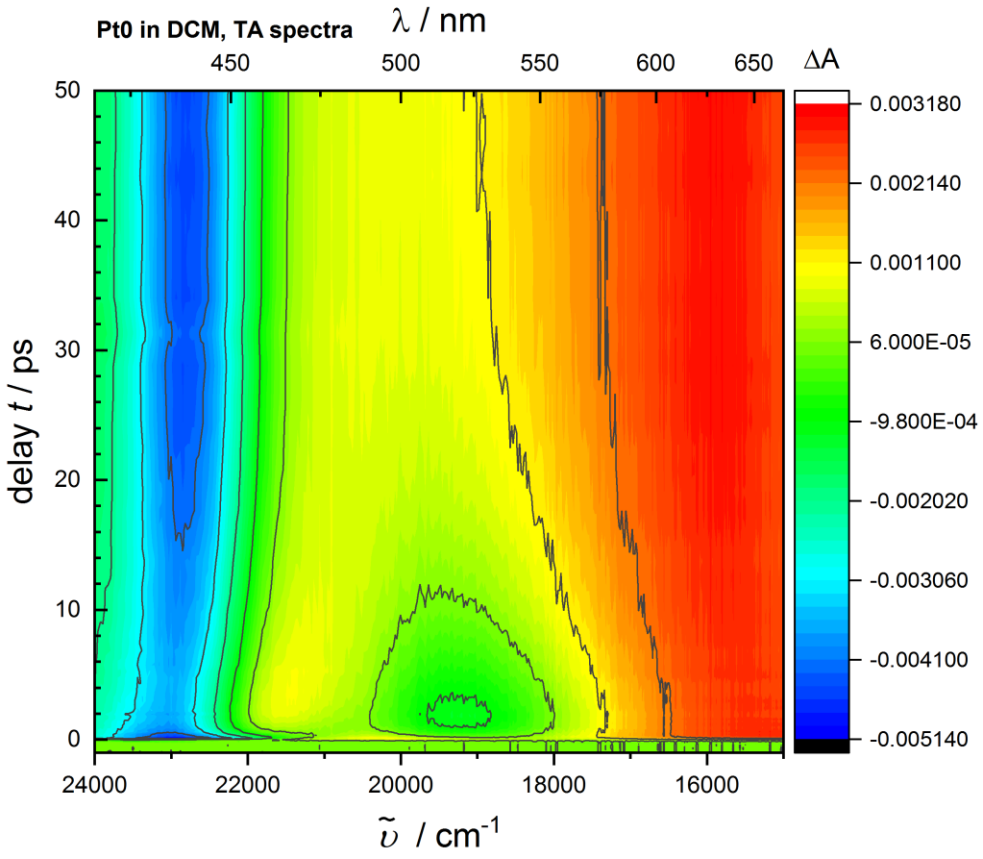

Figure 4.25 2D map of transient absorption spectra (time-resolved UV-Vis spectra) of Pt0 in dichloromethane upon 400 nm excitation. The optical density at the pump wavelength was approximately 0.3. Time-zero dispersion-corrections have been applied to the raw data.

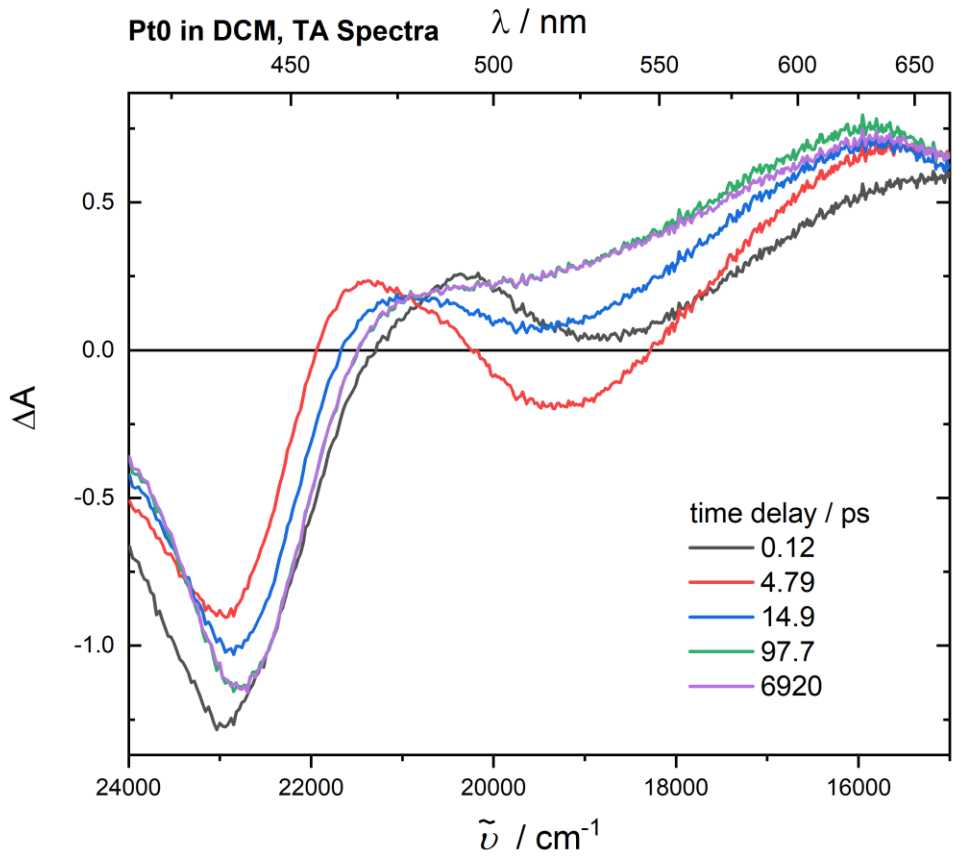

Figure 4.26 Transient absorption spectra of Pt0 in dichloromethane upon 400 nm excitation, with probing in the region of 420 to 670 nm. The optical density at the pump wavelength was approximately 0.3. Spectra at select time-delays between 0.12 and 6920 ps are shown. Time-zero dispersion corrections have been applied to the raw data.

Figure 4.25 and **Figure 4.26** show the transient absorption spectra of Pt0, in a dichloromethane (CH_2Cl_2) solution, upon ~70 fs, 400 nm excitation. Excitation with 400 nm light leads to population of a vibrationally hot (an excess vibrational energy of 2064 cm^{-1}), MLCT state (absorption maximum at 436 nm). A ground-state bleach (GSB) centred at 23,000 cm^{-1} (435 nm) is seen to grow in with the instrument response. The bleach shows dynamics on the timescale 10's of picoseconds. By 97.7 ps the bleach is static, with no change observed up until the latest time-delay recorded, 6.92 ns. An excited-state absorption (ESA) band centred around 16,000 cm^{-1} (625 nm) also grows in with the instrument response. This band shows dynamics on a similar timescale to the bleach, remaining relatively stationary by 97.7 ps and beyond. Heavily overlapped with both GSB and ESA bands, is a negative band, assigned as stimulated emission from a MLCT state. At 4.79 ps, where this shows highest effective intensity, the band is centred

around 19,400 cm^{-1} (515 nm). This band decays on a timescale of 10's of picoseconds, with no signal remaining at 97.7 ps.

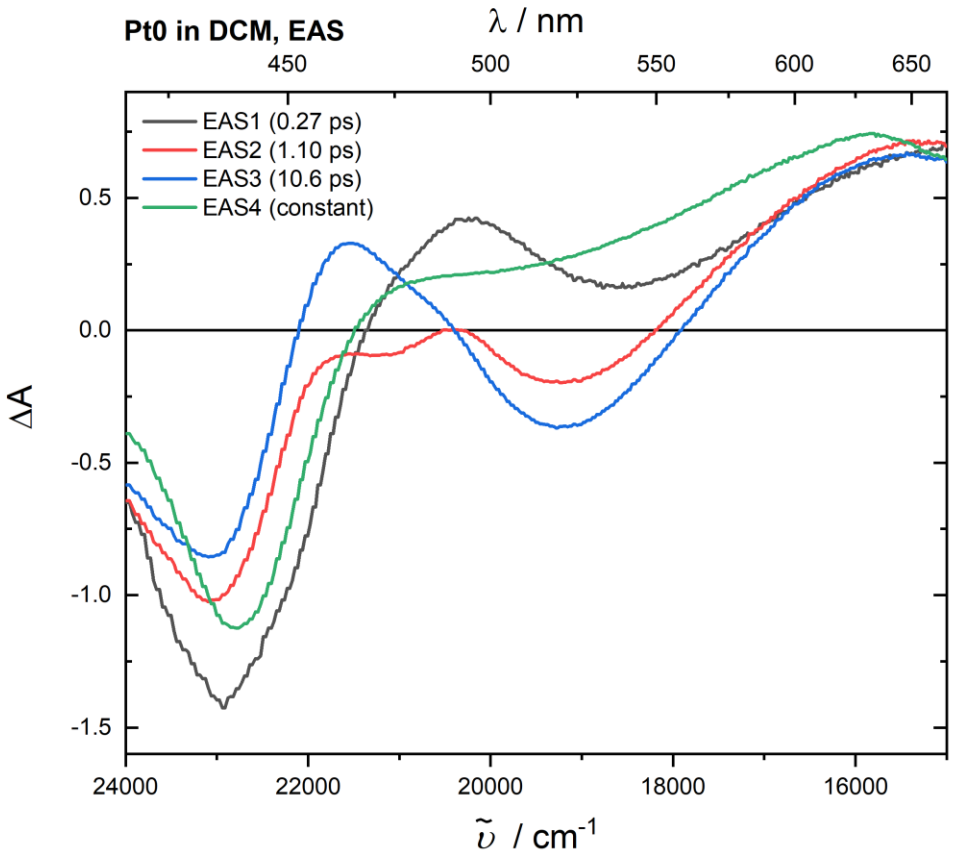

Figure 4.27 Evolution-Associated Spectra (EAS) of the transient absorption spectra of Pt0 (shown in ***Figure 4.25*** and ***Figure 4.26***), obtained via global analysis using 3 exponential time functions and a constant time constant. The corresponding time constants are given in the legend.

Global analysis has been performed in order to extract spectral and dynamic information. A sequential kinetic model with three exponential time functions, along with a constant time function, was used to analyse the data. The resultant Evolution-Associated Spectra (EAS) are shown in **Figure 4.27**, with the corresponding kinetic parameters shown in the inset. The decomposition of the spectra into the EAS gives an estimate of the number of observable processes / states involved in the dynamics. The 0.27, 1.10 and 10.6 ps EAS components (black, red and blue line, respectively) contain a band corresponding to SE, seen in **Figure 4.26**.

Pt1

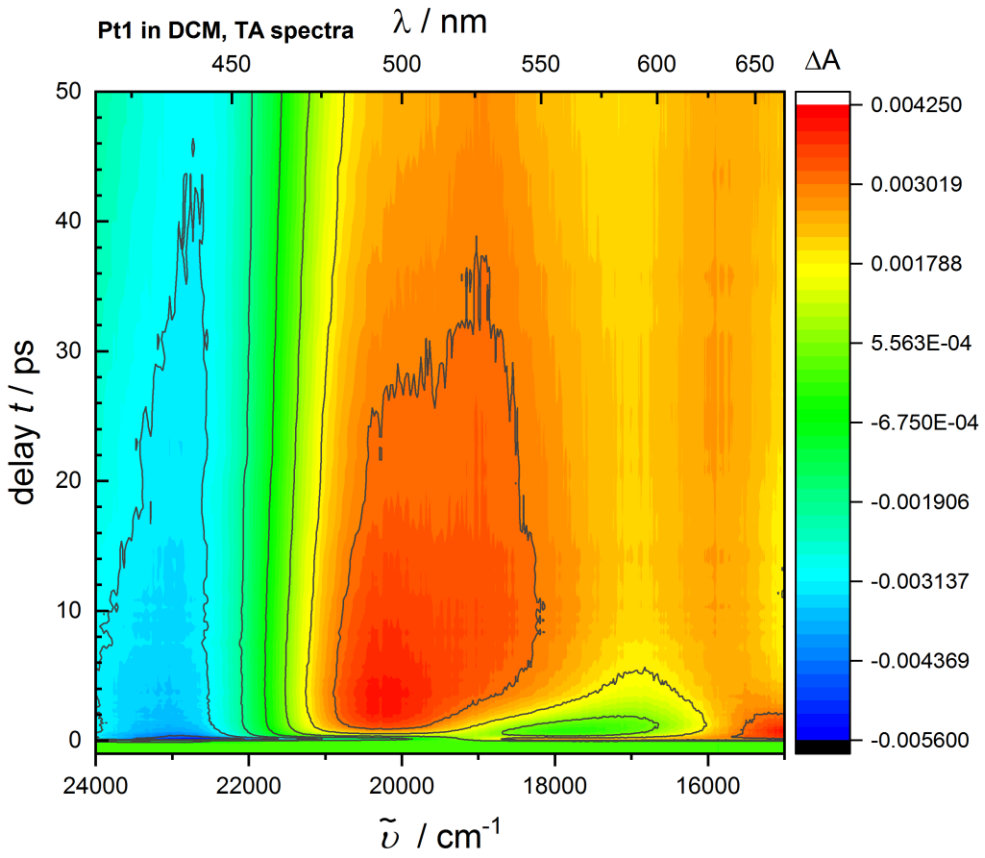

Figure 4.28 2D map of transient absorption spectra (time-resolved UV-Vis spectra) of Pt1 in dichloromethane upon 400 nm excitation. The optical density at the pump wavelength was approximately 0.3. Time-zero dispersion-corrections have been applied to the raw data.

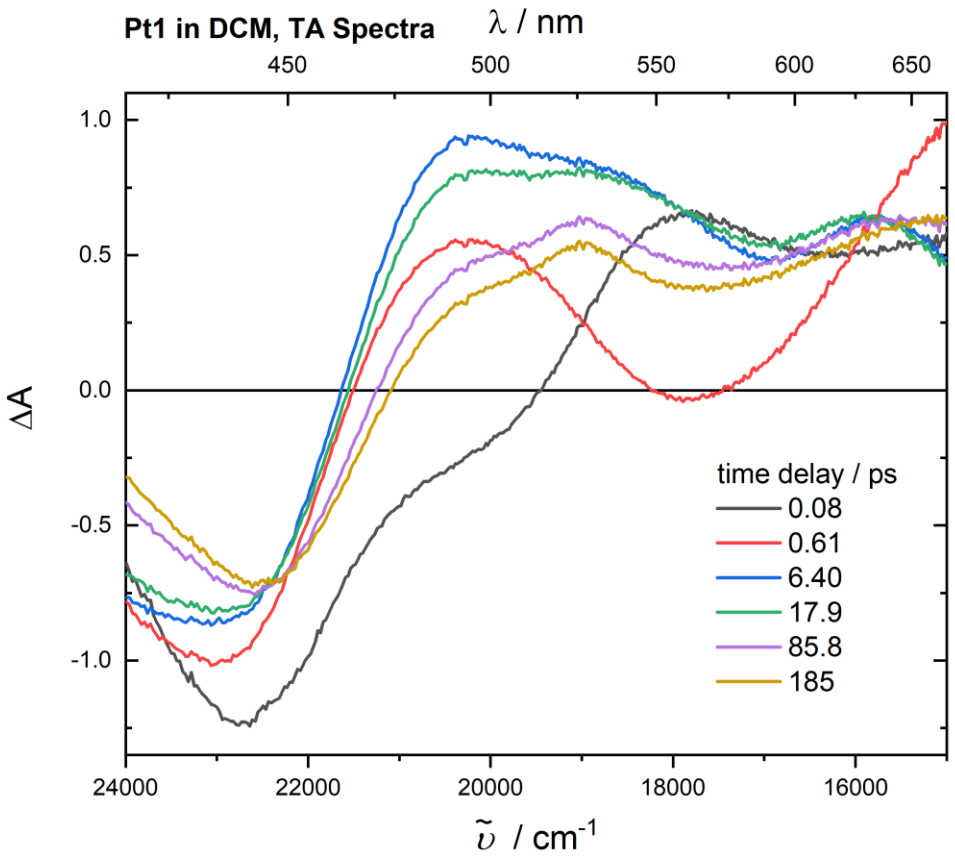

Figure 4.29 Transient absorption spectra of Pt1 in dichloromethane upon 400 nm excitation, with probing in the region of 420 to 670 nm. The optical density at the pump wavelength was approximately 0.3. Spectra at select time-delays between 0.08 and 185 ps are shown. Time-zero dispersion corrections have been applied to the raw data.

Figure 4.28 and **Figure 4.29** show the transient absorption spectra of Pt1, in a dichloromethane (CH_2Cl_2) solution, upon ~70 fs, 400 nm excitation. Excitation with 400 nm light leads to population of a vibrationally hot (an excess vibrational energy of 2117 cm^{-1}), MLCT state (absorption maximum at 437 nm). A ground-state bleach (GSB) centred at 22,800 cm^{-1} (438 nm) is seen to grow in with the instrument response. The bleach shows dynamics on the timescale 10's of picoseconds. By 85.8 ps the bleach is effectively static, with no further change observed up until the latest time-delay recorded, 185 ps. Excited-state absorption (ESA) is seen in the region of 460 to 670 nm, overlap with stimulated emission (SE), centred around 18,000 cm-1 (555 nm) gives apparent peaks of ESA at around 485 and 625 nm. The SE is most intense at 0.61 ps and is almost fully decayed by 6.40 ps.

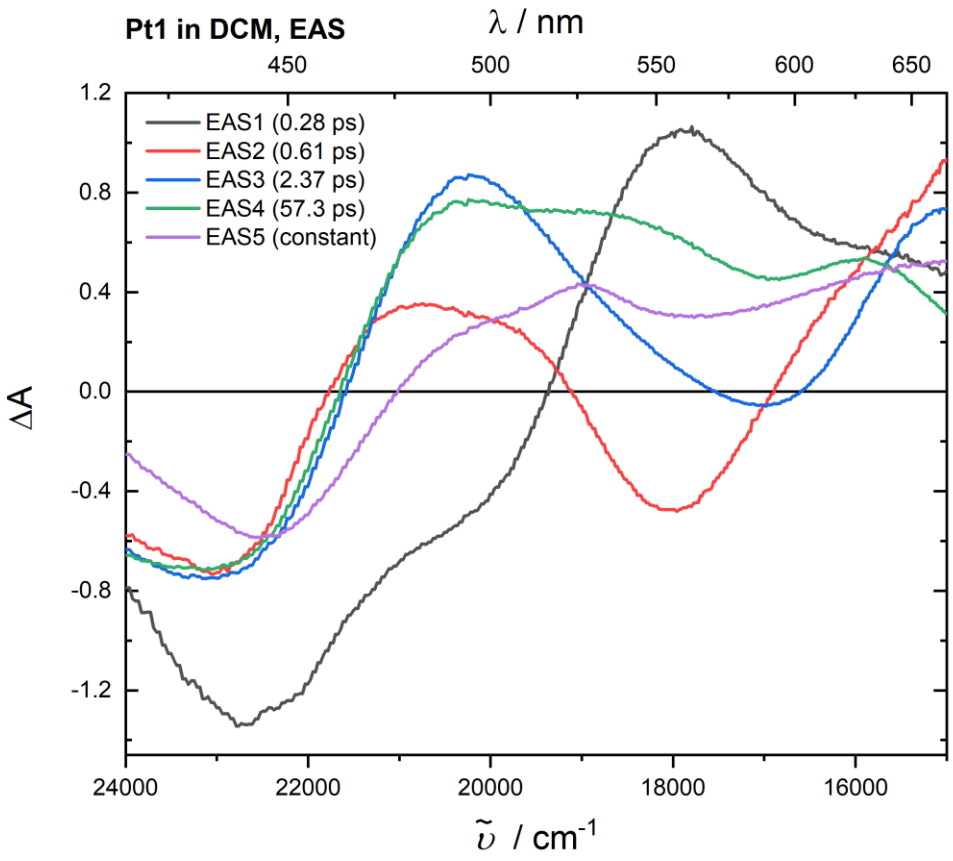

Figure 4.30 Evolution-Associated Spectra (EAS) of the transient absorption spectra of Pt1 (shown in ***Figure 4.28*** and ***Figure 4.29***), obtained via global analysis using 3 exponential time functions and a constant time constant. The corresponding time constants are given in the legend.

Global analysis has been performed in order to extract spectral and dynamic information. A sequential kinetic model with four exponential time functions, along with a constant time function, was used to analyse the data. The resultant Evolution-Associated Spectra (EAS) are shown in **Figure 4.30**, with the corresponding kinetic parameters shown in the inset. The decomposition of the spectra into the EAS gives an estimate of the number of observable processes / states involved in the dynamics. The 0.28, 0.61, 2.37 and 57.3 ps EAS components (black, red, blue and green line respectively) contain a band corresponding to SE, seen in **Figure 4.29**.

Pt2

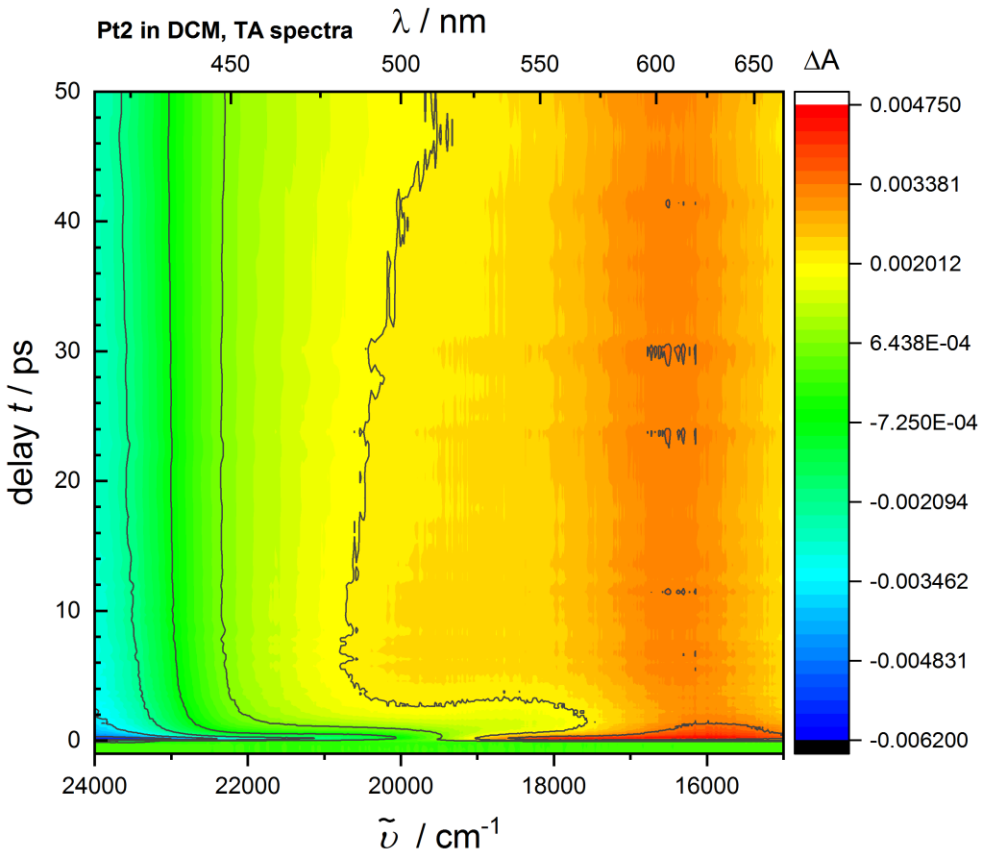

Figure 4.31 2D map of transient absorption spectra (time-resolved UV-Vis spectra) of Pt2 in dichloromethane upon 400 nm excitation. The optical density at the pump wavelength was approximately 0.3. Time-zero dispersion-corrections have been applied to the raw data.

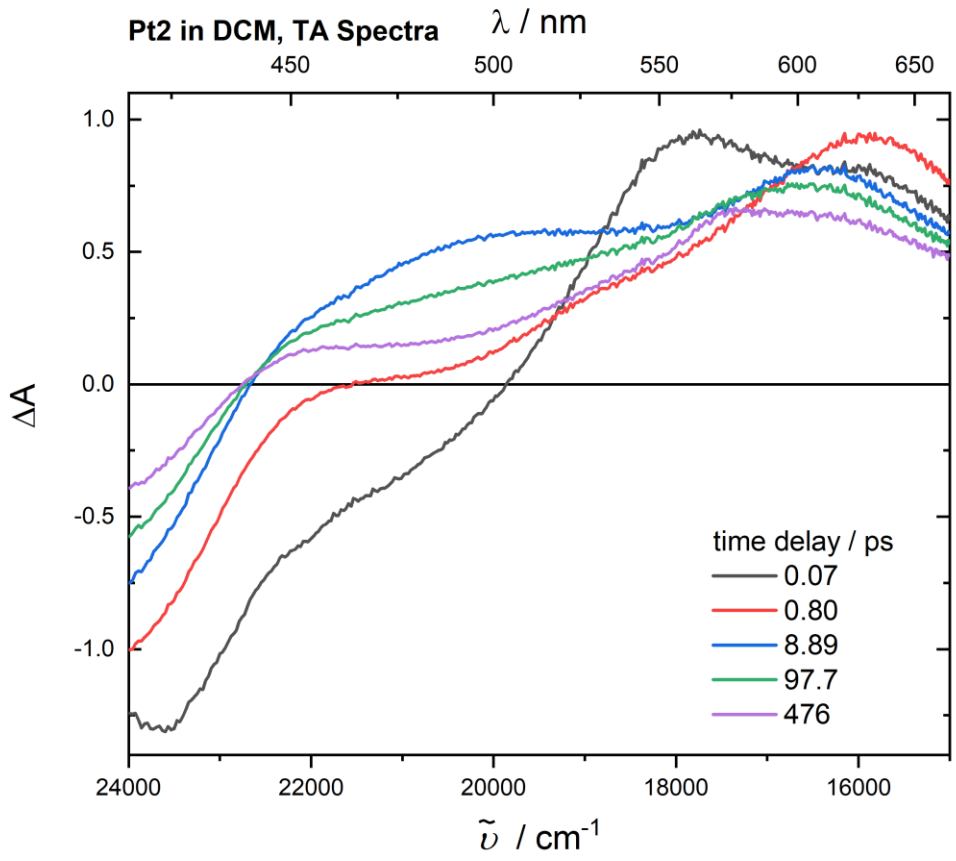

Figure 4.32 Transient absorption spectra of Pt2 in dichloromethane upon 400 nm excitation, with probing in the region of 420 to 670 nm. The optical density at the pump wavelength was approximately 0.3. Spectra at select time-delays between 0.07 and 476 ps are shown. Time-zero dispersion corrections have been applied to the raw data.

Figure 4.31 and **Figure 4.32** show the transient absorption spectra of Pt2, in a dichloromethane (CH_2Cl_2) solution, upon ~70 fs, 400 nm excitation. Excitation with 400 nm light leads to population of an MLCT state (absorption maximum at 402 nm). A ground-state bleach (GSB) centred at 23,500 cm^{-1} (426 nm) is seen to grow in with the instrument response. An excited-state absorption (ESA) band centred around 16,000 cm^{-1} (625 nm) also grows in with the instrument response. Heavily overlapped with both GSB and ESA bands is stimulated emission from a MLCT state, seen as a shoulder to the GSB, around 21,000 cm^{-1}, at 0.07 ps.

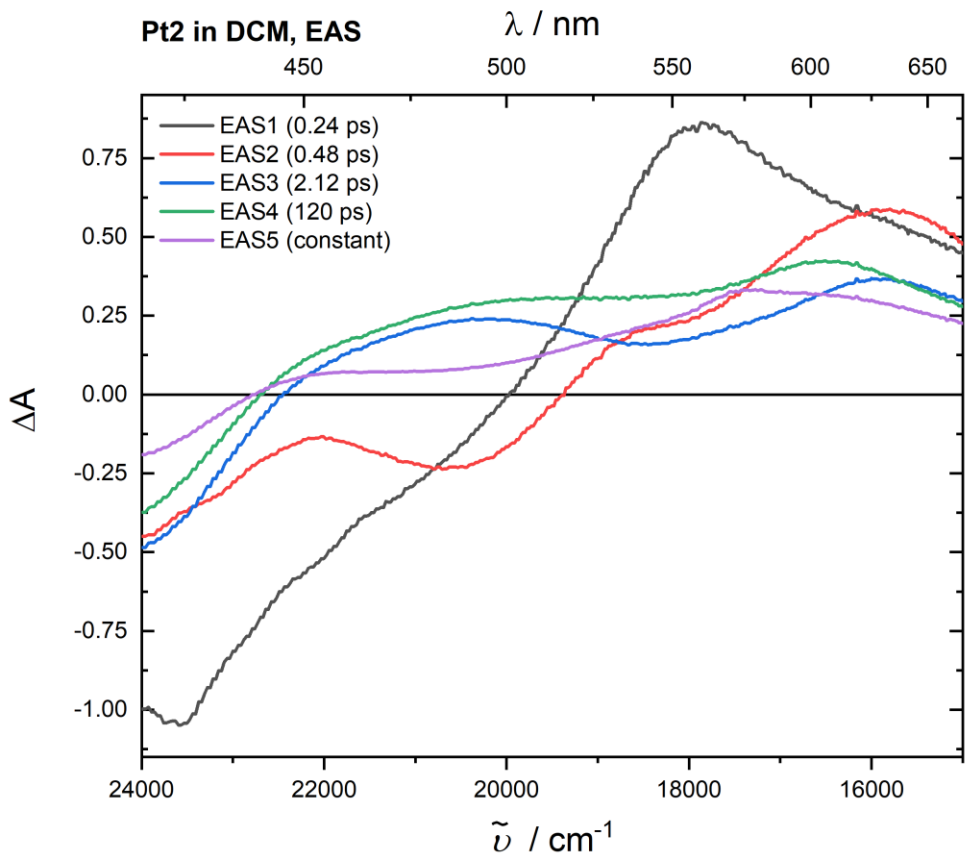

Figure 4.33 Evolution-Associated Spectra (EAS) of the transient absorption spectra of Pt2 (shown in ***Figure 4.28*** and ***Figure 4.29***), obtained via global analysis using 3 exponential time functions and a constant time constant. The corresponding time constants are given in the legend.

Global analysis has been performed in order to extract spectral and dynamic information. A sequential kinetic model with four exponential time functions, along with a constant time function, was used to analyse the data. The resultant Evolution-Associated Spectra (EAS) are shown in **Figure 4.33**, with the corresponding kinetic parameters shown in the inset. The decomposition of the spectra into the EAS gives an estimate of the number of observable processes / states involved in the dynamics. The 0.24, 0.48, 2.12 and 120 ps EAS components (black, red, blue and green line respectively) contain a band corresponding to SE, seen in **Figure 4.32**.

Summary

Table 4.1 summarises the time constants, extracted with global analysis, for the three Acceptor-Bridge-Acceptor compounds studied here (the structures shown in **Figure 4.3**). Time constants, τ, describing different steps in the excited state dynamics of these compounds, obtained via FLUPS and TA are presented, along with spectral peak positions of absorption and emission bands for the three complexes.

Table 4.1 Summary of the time constants obtained by method of FLUPS, TA and TRIR, for the three compounds, Pt0, Pt1 and Pt2, all in solutions of dichloromethane.

Complex	Abs max / nm (lowest energy band)	Emission max / nm	τ (ps) / FLUPS	τ (ps) / TA
Pt0	436	486	0.42 ± 0.06	0.27 ± 0.16
			1.33 ± 0.11	1.1 ± 0.25
			7.90 ± 0.42	10.6 ± 1.13
			63.5 ± 2.13	Constant
Pt1	437	479 & 600	0.24 ± 0.06	0.28 ± 0.12
			0.86 ± 0.06	0.61 ± 0.22
			4.12 ± 0.27	2.37 ± 0.47
			54.1 ± 3.78	57.3 ± 5.90
				Constant
Pt2	402	477	0.24 ± 0.04	0.24 ± 0.08
			0.36 ± 0.04	0.48 ± 0.30
			1.58 ± 0.09	2.12 ± 0.36
			83.9 ± 4.56	120 ± 8.44
			1510 ± 367	Constant

4.3 Discussion

Ultrafast transient absorption and emission spectra were obtained for the three complexes, Pt0, Pt1, and Pt2 in solutions of DCM upon 400 nm excitation. Global analysis was used in order to extract spectral and kinetic information. For all complexes, the time constants extracted from the two techniques, are in good agreement with one another (see **Table 4.1**). This series of complexes are subject to ongoing theoretical and spectroscopic investigation; a preliminary discussion is presented here.

Similarly, to in the previous chapter, for all three of the complexes investigated, ultrafast (sub ps) emission was observed, superseded by lower energy emission and therefore displaying behaviour in direct contradiction to Kasha's rule. Unlike the bulk of results reported in the literature the complexes investigated here show quite different photophysical behaviour; there is no distinct drop in emission intensity on the sub-picosecond timescale, instead there is a gradual reduction in intensity which occurs in parallel with a shift of the emission to lower energy

Transient Absorption and Stimulated Emission

The transient absorption spectra of each of the 3 complexes shows stimulated emission. In each case, this SE is much shorter lived than in the complexes discussed in the previous chapter (NAP-Pt-Cl, NAP-Pt-Ph and NAP-Pt-PTZ), seen to decay within 10's of ps, see **Table 4.1**. Global analysis was performed in order to extract kinetic and spectral information. For all complexes, multiple EAS describing the SE decay are extracted. The longest-lived EAS components, containing SE, are 10.6, 2.37 and 2.12 ps for Pt0, Pt1 and Pt2 respectively. This is suggestive that with these complexes, the excited state maintains strong singlet character considerably longer than the IRF. The time constants obtained from global analysis of the TA data show good agreement with the time constants obtained in the analysis of the time-resolved emission (FLUPS) data, indicative that the SE and spontaneous emission measured originate from the same electronic excited states.

Relative Emission Intensity

In the time-resolved emission measurements (FLUPS) all samples were prepared such that the optical density at 400 nm (excitation wavelength) was around 0.3. Additionally,

for all experiments, the pump power was held constant, at around 2 mW. Therefore, in all cases, similar excited-state populations will be formed upon excitation. The relative emission intensities for the three complexes, at 0 ps, was approximately 1 (Pt0), 2 (Pt1), and 6 (Pt2). This may be due to the reduction in rate of ISC as the systems are extended, and the effect of the heavy Pt(II) centre is diluted. This appears to contradict to the rates of decay of SE observed in the TA spectra. Additional experiments will be performed in order to enable a more qualitative assessment of the relative emission intensities.

Earliest observable emission

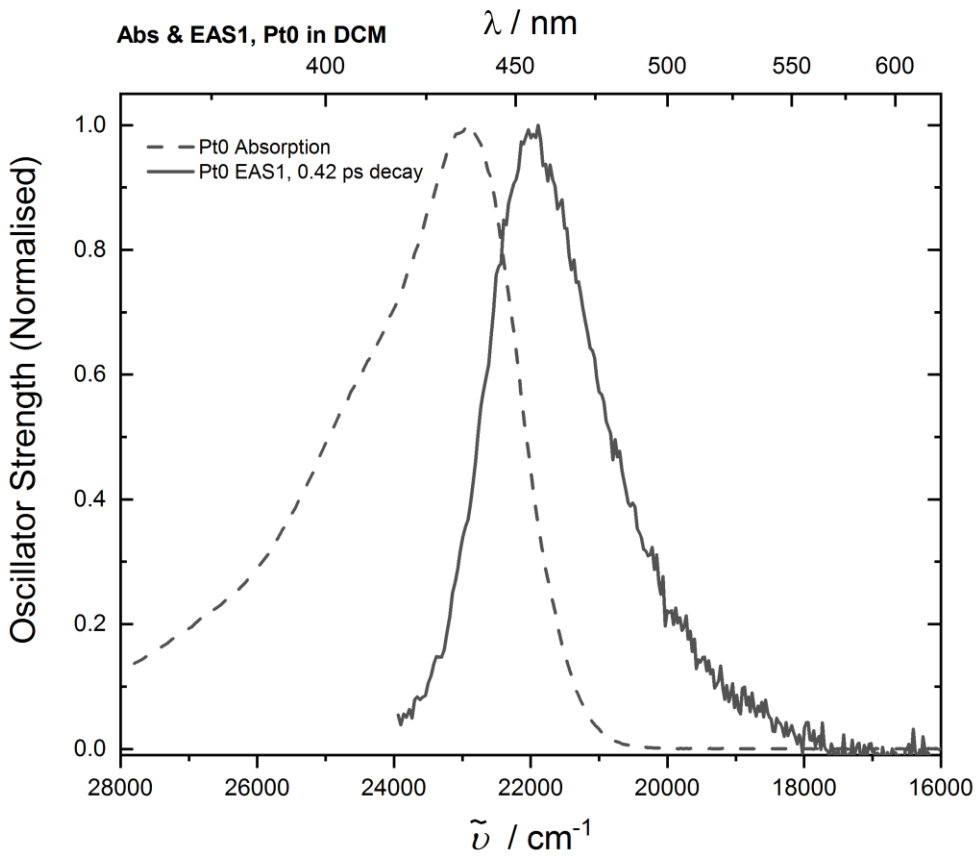

Figure 4.34 Normalised steady-state absorption of Pt0, in dichloromethane (dashed line), is shown alongside the first Evolution-Associated Spectra (EAS1) (solid line), component extracted from global analysis of the time-resolved emission of Pt0, in dichloromethane, upon 400 nm excitation. EAS1 grows in with IRF (ca. 300 fs) and decays with a lifetime of 0.42 ps.

Figure 4.34 shows the steady-state absorption (dashed line) of Pt0 alongside the first EAS (EAS1) component (solid line) extracted from the global analysis of the time-resolved emission spectra. The data was fit using 4 exponential time functions convoluted with an IRF function (ca. 300 fs). EAS1 grows in with the instrument response, i.e. it's growth cannot be temporally resolved. EAS1 decays with a lifetime of

0.42 ps. The absorption band centred at 436 nm (22,936 cm^{-1}) is assigned as being ground-state to a manifold of ^{1}MLCT states. The left-hand side of EAS1, centred at 455 nm (21,961 cm^{-1}), appears mirror symmetric to that of the absorption band (right-hand side). The emission band is much narrower than that of the absorption. Additionally, the emission band exhibits no obvious shoulder, unlike that of the absorption band. Excitation with 400 nm will likely populate multiple electronic transitions, the absence of a shoulder in the emission may indicate that there is rapid exchange between the states, with all molecules populating a single emissive state within the IRF. Alternatively, multiple states may be populated, but only one may be emissive. For Pt1 and Pt2, similar narrow emission bands are observed at early times, see **Figure 4.35** and **Figure 4.36**.

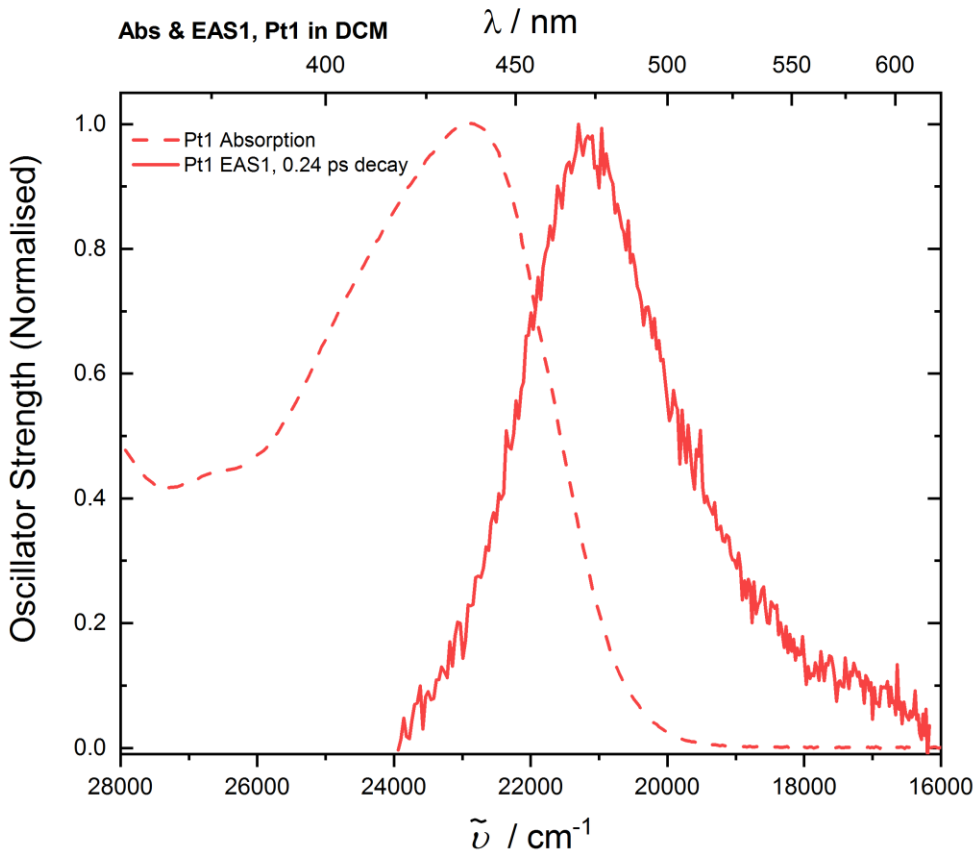

Figure 4.35 Normalised steady-state absorption of Pt1, in dichloromethane (dashed line), is shown alongside the first Evolution-Associated Spectra (EAS1) (solid line), component extracted from global analysis of the time-resolved emission of Pt1, in dichloromethane, upon 400 nm excitation. EAS1 grows in with IRF (ca. 300 fs) and decays with a lifetime of 0.24 ps.

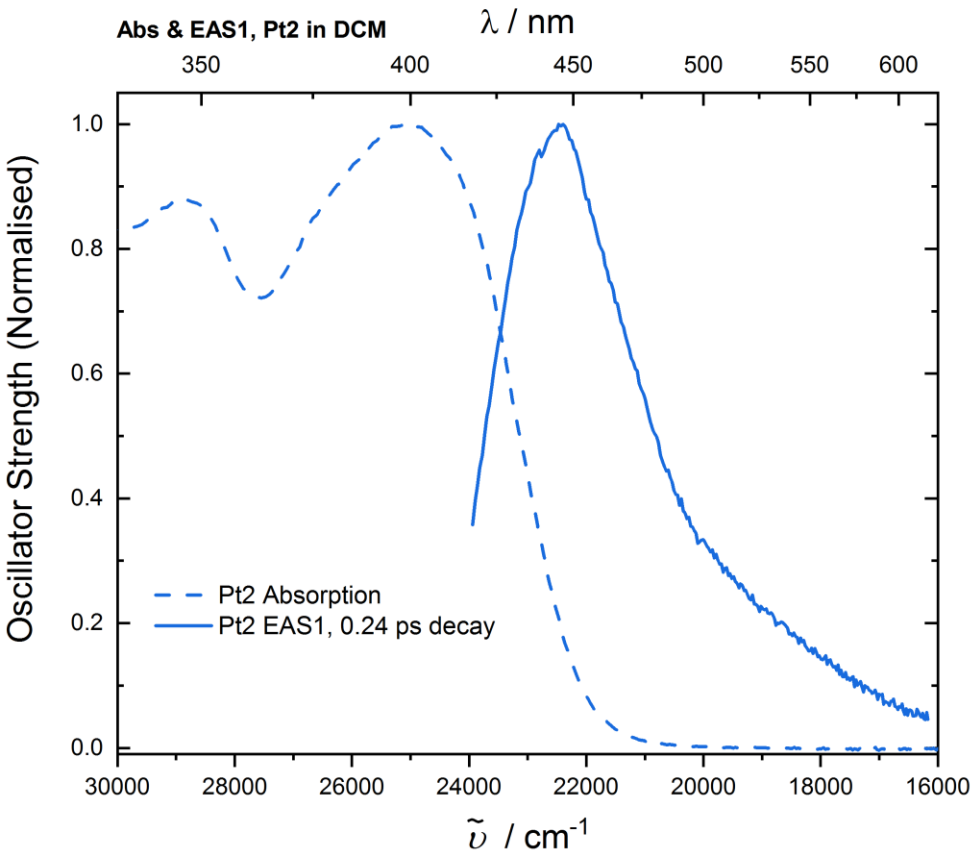

Figure 4.36 Normalised steady-state absorption of Pt2, in dichloromethane (dashed line), is shown alongside the first Evolution-Associated Spectra (EAS1) (solid line), component extracted from global analysis of the time-resolved emission of Pt2, in dichloromethane, upon 400 nm excitation. EAS1 grows in with IRF (ca. 300 fs) and decays with a lifetime of 0.24 ps.

Change in oscillator strength over time

The oscillator strength for emission, from a particular excited state will scale proportionally with emission intensity integrated over the entire band, i.e. the area under each EAS1 represents the oscillator strength of the corresponding electronic excited state. Scaling of the area under each EAS to that of the first EAS, 'EAS1' gives an idea of the change in oscillator strength as a function of time. **Figure 4.37** shows EAS for Pt0, obtained by global analysis using a sequential model with 4 exponential time functions convoluted with an IRF function. Bars are shown, overlaid on the EAS, with their height representing the area under the corresponding EAS. For Pt0, the first 3 EAS show moderate change in integrated area, with the 4th EAS having a considerably smaller area than the previous 3. The time constant for the decay of 3rd component, 7.90 ps, matches well with the decay of the SE seen in TA, which has a time constant for decay of 10.6 ps. EAS3 is preliminary assigned as that of the lowest-energy singlet excited state, and EAS4 as that of the corresponding triplet state. In this system, ISC occurs on a timescale of 7.90 to 10.6 ps.

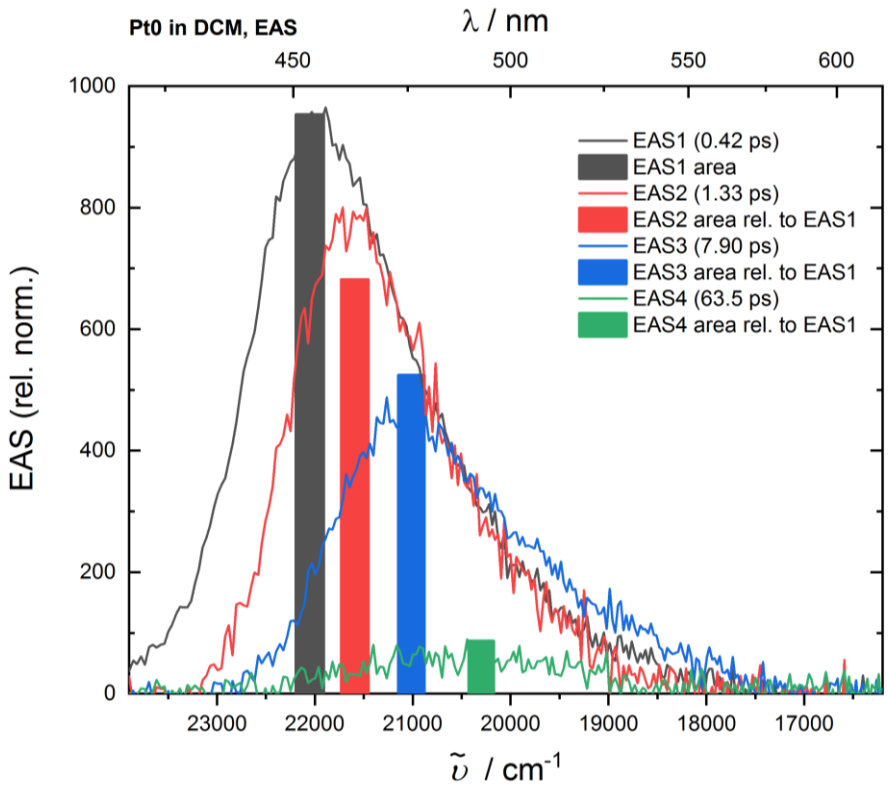

Figure 4.37 Evolution-Associated Spectra (EAS) for the time-resolved emission spectra of Pt0, in dichloromethane, upon 400 nm excitation. EAS are extracted by global analysis using a sequential model with 4 exponential time functions convoluted with an IRF function. The height of the bars overlaid represent the area under each EAS, relative to that of EAS1.

Figure 4.38 and **Figure 4.39** show equivalent figures for complexes Pt1 and Pt2 respectively. For Pt1, considerable reduction in the area under the spectra is observed between EAS1 and EAS2. With EAS2 having around 50% of the area of EAS1. There is also around a 50% reduction in area between EAS2 and EAS3. Additionally, unlike the EAS of Pt0, considerable spectral shift is observed between the EAS. With this complex, it is more difficult to assign ISC to a single time constant.

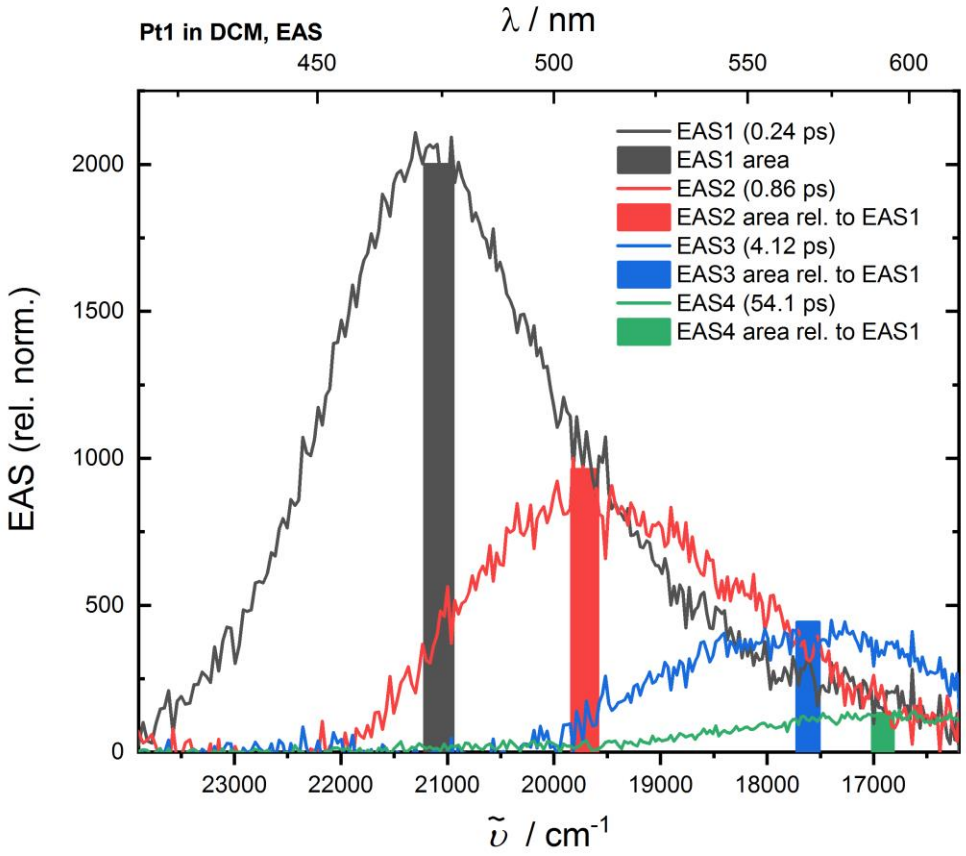

Figure 4.38 Evolution-Associated Spectra (EAS) for the time-resolved emission spectra of Pt1, in dichloromethane, upon 400 nm excitation. EAS are extracted by global analysis using a sequential model with 4 exponential time functions convoluted with an IRF function. The height of the bars overlaid represent the area under each EAS, relative to that of EAS1.

The global analysis of Pt2 reveals rather unusual behaviour, compared to that of Pt0 and Pt1. Initially there is the red shifting of emission, with time constants of 0.24, 0.36 and 1.58 ps. The lowest-energy band decays with a lifetime of 83.9 ps revealing a long-lived high energy emission band (EAS5), with lifetime of 1.51 ns. Spectrally, this long-lived band is very similar to that of EAS2 and the blue component of EAS4. The return to high-

energy emission indicates there is excited-state branching with a population being 'trapped' in the higher energy state.

The recording of pump wavelength-dependent time-resolved emission may provide additional information on this excited state branching. Sample excitation is likely to lead to the population of several electronic excited states. The 'branching' may be due to the different electronic states initially having different coupling strengths to the subsequently populated states. Pumping the system with a different wavelength will lead to the population of a different ratio of excited states and may lead to relative differences in the intensity of the long-lived high energy emission. Further experimentation is required.

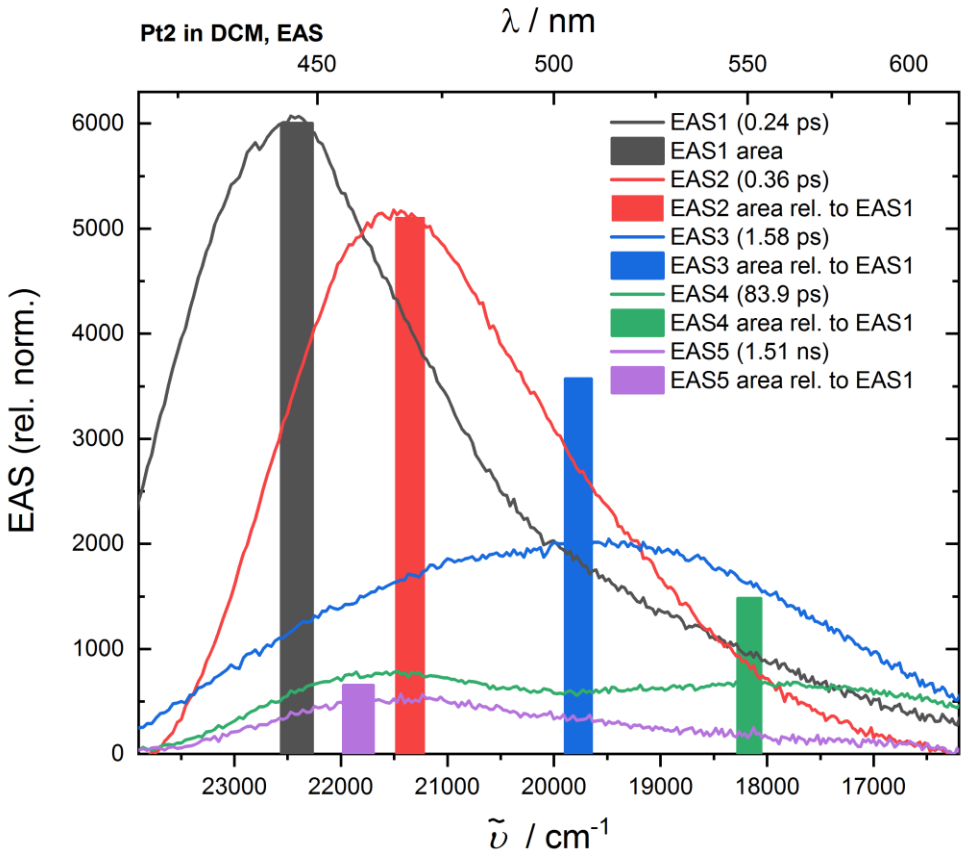

Figure 4.39 Evolution-Associated Spectra (EAS) for the time-resolved emission spectra of Pt0, in dichloromethane, upon 400 nm excitation. EAS are extracted by global analysis using a sequential model with 4 exponential time functions convoluted with an IRF function. The height of the bars overlaid represent the area under each EAS, relative to that of EAS1.

Energy Level Diagrams

Provisional energy-level diagrams, for the three complexes, Pt0, Pt1, and Pt2, in dichloromethane solutions, are presented here.

The approximate energies of each state are estimated using peak positions of absorption/emission bands as recorded with steady-state absorption, steady-state emission and ultrafast emission measurements. In all cases, the transient absorption spectra show a final excited-state which effectively has an infinite lifetime on the timescale of the time-resolved methods applied within, for this reason, the final emission decay time obtained in each case is shown to be that between this penultimate excited-state and the final excited-state (not return to the ground-state), in all cases, state F, represents the 'infinitely' long-lived final excited-state. **Figure 4.40**, **Figure 4.41**, and **Figure 4.42** show suggested energy level diagrams for Pt0, Pt1, and Pt2 respectively. The 'energy levels' shown are not intended to represent distinct electronic excited states, that act merely as a summarisation of the dynamics observed. For example, levels B and C of **Figure 4.40**, may be 'energy levels' of the same electronic state, pre- and post- vibrational relaxation perhaps.

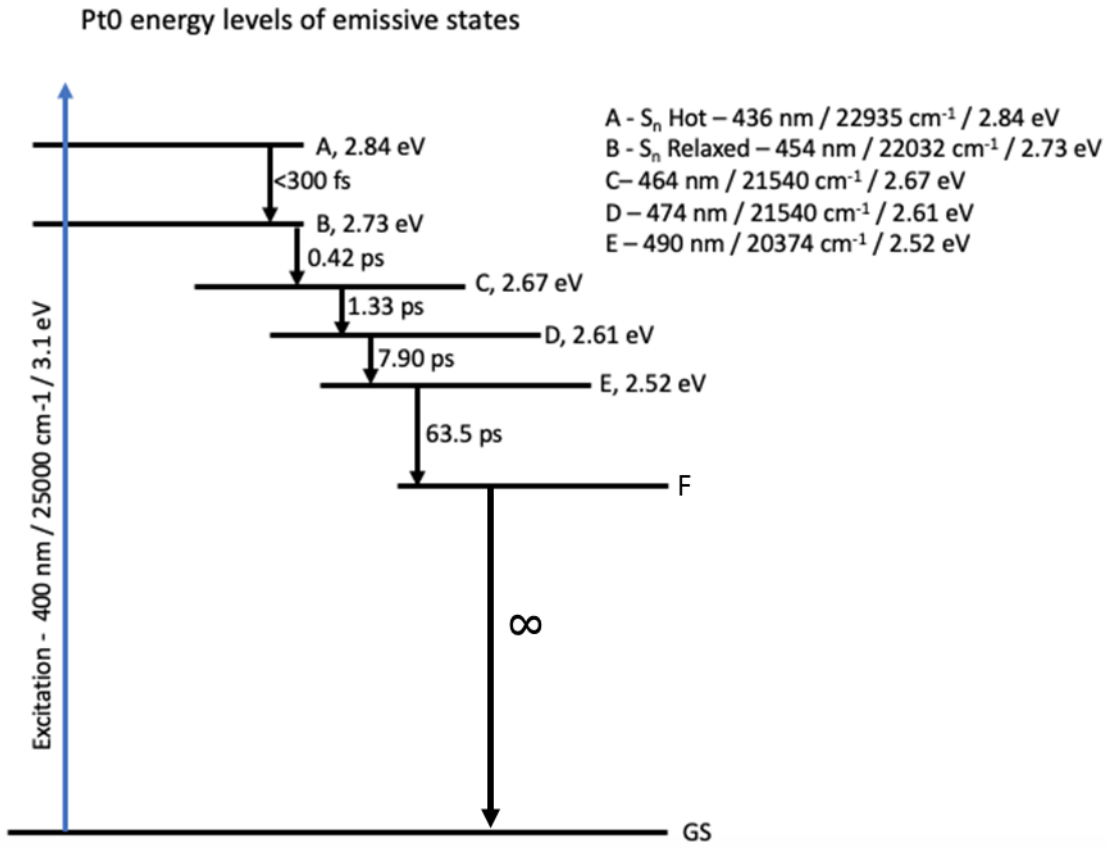

Figure 4.40 Schematic energy level diagram for Pt0, in dichloromethane solution, upon 400 nm excitation. The time-constants shown are obtained from global analysis of the time-resolved emission spectra. The scheme is not to scale.

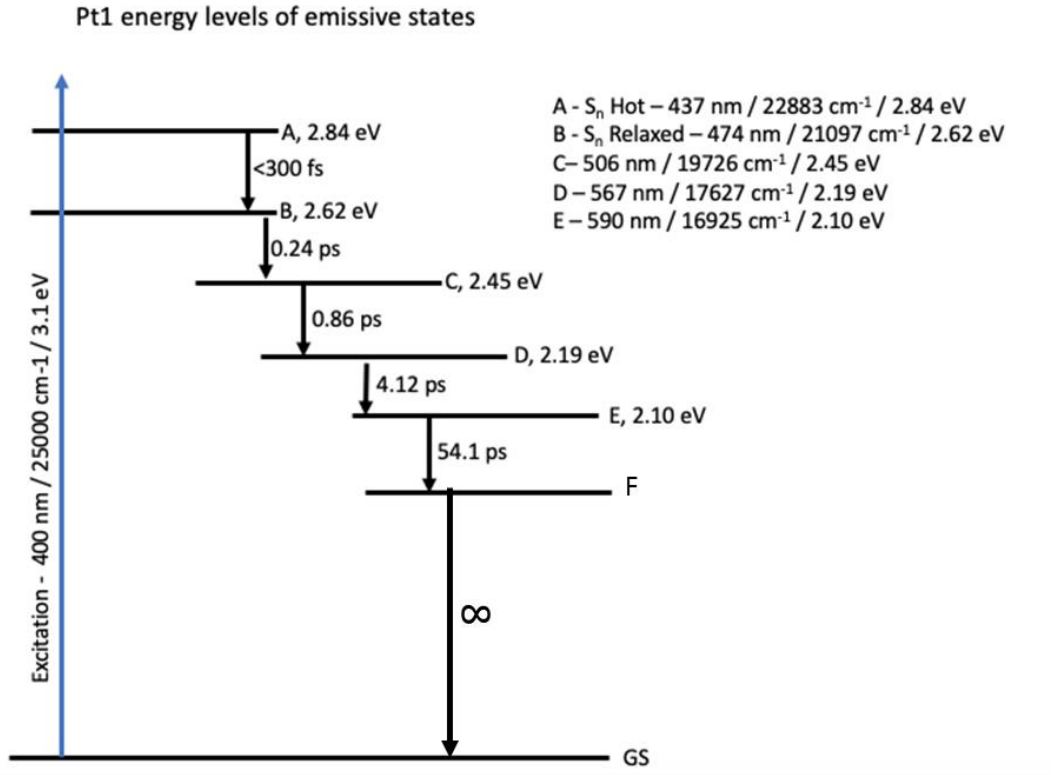

Figure 4.41 Schematic energy level diagram for Pt1, in dichloromethane solution, upon 400 nm excitation. The time-constants shown are obtained from global analysis of the time-resolved emission spectra. The scheme is not to scale.

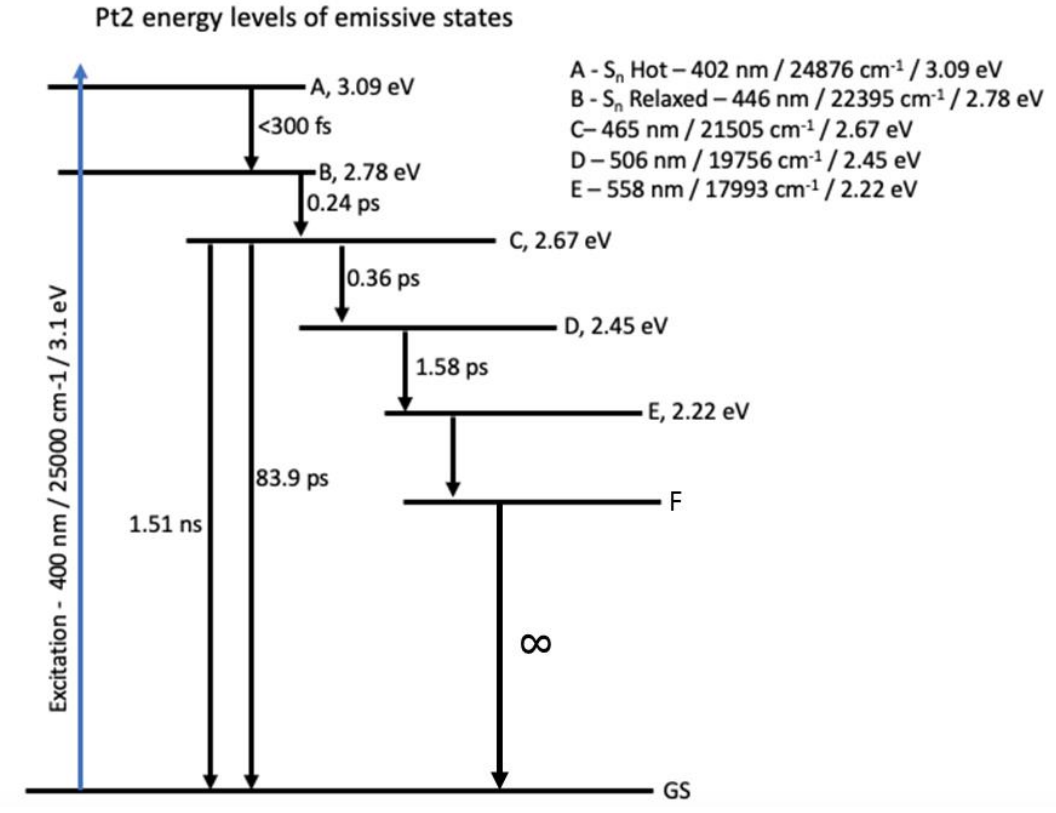

Figure 4.42 Schematic energy level diagram for Pt2, in dichloromethane solution, upon 400 nm excitation. The time-constants shown are obtained from global analysis of the time-resolved emission spectra. The scheme is not to scale.

4.4 Conclusion & Future Work

The work presented here is subject to ongoing investigation. Preliminary results indicate that ISC for this series of symmetrical complexes is slower than that of similar complexes reported in the literature.[23] The energy levels and decay lifetimes of all observable emissive states are summarised in **Figure 4.40**, **Figure 4.41**, and **Figure 4.42** for Pt0, Pt1 and Pt2 respectively.

There is no obvious trend between the rates of decay of emission and the extension of the ligands, however, there appears to be a systematic increase in emission intensity from Pt0, to Pt1, to Pt2, i.e. with the increase in ligand size. Potentially, this means that the degree of singlet character is increasing or, that the rate of the ISC is decreasing with an increase in distance between Pt-center and the NAP – which might imply smaller participation of Pt-orbitals in the frontier orbitals. This observation would be consistent with that reported in the literature.[23]

There appears to be a 'switch' in excited-state behaviour, for Pt2, compared with Pt0 and Pt1. Pt2, the complex featuring the longest 'bridge' between the metal centre and the acceptor substituents. We speculate that the extended bridge becomes involved in electron transfer processes. This complex also shows interesting 'dual emission', with a high-energy emissive state populated until the latest times recorded in the emission experiments.

Future work would include excitation wavelength dependence time-resolved emission measurements. It is hypothesised that the branching between the high-energy long-lived state and the faster decaying lower-energy excited-states will be dependent upon the energy at which the system is first excited.

All of the time-resolved emission experiments presented within this chapter should be performed in a range of different solvents, of varying polarity. The energy of the various charge-transfer states populated upon excitation will be dependent on the solvent.

The series of complexes was designed with the idea of studying the rate of ISC as a function of distance between the metal centre and the acceptor. It was however reliant on the assumption that the "bridge" remains innocent, not involved in the electronic processes. This does not seem to be the case as extending the conjugated system of the

–CC-Ph-bridge leads to a decrease in the π^* orbitals of the bridge, making it potentially an additional acceptor on the way to the NAP-acceptor. Therefore, the change in the photophysical properties observed manifests the change in the role of the bridge from simply “spectator” to a participant. This also means that in order to study distance-dependence of ISC, one would need to use rigid but not so conjugated bridge – for example, such as adamantane.

4.5 References

1 R. Monni, G. Capano, G. Auböck, H. B. Gray, A. Vl Cek, I. Tavernelli and M. Chergui, *Proc. Natl. Acad. Sci. U. S. A.*, 2018, **115**, E6396–E6403.

2 M. Falkenström, O. Johansson and L. Hammarström, *Inorganica Chim. Acta*, 2007, **360**, 741–750.

3 J. H. Alstrum-Acevedo, M. K. Brennaman and T. J. Meyer, *Inorg. Chem.*, 2005, **44**, 6802–27.

4 C. Cebrián and M. Mauro, *Beilstein J. Org. Chem.*, 2018, **14**, 1459–1481.

5 S. Archer and J. A. Weinstein, *Coord. Chem. Rev.*, 2012, **256**, 2530–2561.

6 J. Barber, *Chem. Soc. Rev.*, 2009, **38**, 185–196.

7 J. N. Schrauben, K. L. Dillman, W. F. Beck and J. K. Mccusker, *Chem. Sci.*, 2010, **1**, 405–410.

8 E. A. Juban, A. L. Smeigh, J. E. Monat and J. K. Mccusker, *Coord. Chem. Rev.*, 2006, **250**, 1783–1791.

9 W. Gawelda, A. Cannizzo, V.-T. Pham, F. van Mourik, C. Bressler and M. Chergui, *J. Am. Chem. Soc.*, 2007, **129**, 8199–8206.

10 C. Consani, M. Prémont-Schwarz, A. ElNahhas, C. Bressler, F. van Mourik, A. Cannizzo and M. Chergui, *Angew. Chemie Int. Ed.*, 2009, **48**, 7184–7187.

11 C. Bressler, C. Milne, V.-T. Pham, A. Elnahhas, R. M. van der Veen, W. Gawelda, S. Johnson, P. Beaud, D. Grolimund, M. Kaiser, C. N. Borca, G. Ingold, R. Abela and M. Chergui, *Science*, 2009, **323**, 489–92.

12 A. L. Smeigh, M. Creelman, R. A. Mathies and J. K. McCusker, *J. Am. Chem. Soc.*, 2008, **130**, 14105–14107.

13 O. S. Wenger, *Coord. Chem. Rev.*, 2009, **253**, 1439–1457.

14 J. Tribollet, G. Galle, G. Jonusauskas, D. Deldicque, M. Tondusson, J. F. Letard and E. Freysz, *Chem. Phys. Lett.*, 2011, **513**, 42–47.

15 A. Lapini, P. Foggi, L. Bussotti, R. Righini and A. Dei, *Inorganica Chim. Acta*, 2008, **361**, 3937–3943.

16 M. Iwamura, H. Watanabe, K. Ishii, S. Takeuchi and T. Tahara, *J. Am. Chem. Soc.*, 2011, **133**, 7728–7736.

17 M. T. Colvin, A. L. Smeigh, E. M. Giacobbe, S. M. M. Conron, A. B. Ricks and M. R. Wasielewski, *J. Phys. Chem. A*, 2011, **115**, 7538–7549.

18 F. Frei, A. Rondi, D. Espa, M. L. Mercuri, L. Pilia, A. Serpe, A. Odeh, F. Van Mourik, M. Chergui, T. Feurer, P. Deplano, A. Vlček and A. Cannizzo, *Dalton Trans.*, 2014, **43**, 17666–17676.

19 A. Cannizzo, F. van Mourik, W. Gawelda, G. Zgrablic, C. Bressler and M. Chergui, *Angew. Chemie Int. Ed.*, 2006, **45**, 3174–3176.

20 O. Bräm, F. Messina, A. M. El-Zohry, A. Cannizzo and M. Chergui, *Chem. Phys.*, 2012, **393**, 51–57.

21 A. Cannizzo, A. M. Blanco-Rodríguez, A. El Nahhas, J. Šebera, S. Záliš, A. Vlček and M. Chergui, *J. Am. Chem. Soc.*, 2008, **130**, 8967–8974.

22 O. Bräm, F. Messina, E. Baranoff, A. Cannizzo, M. K. Nazeeruddin and M. Chergui, *J. Phys. Chem. C*, 2013, **117**, 15958–15966.

23 G. Ramakrishna, T. Goodson, J. E. Rogers-Haley, T. M. Cooper, D. G. McLean and A. Urbas, *J. Phys. Chem. C*, 2009, **113**, 1060–1066.

24 R. M. van der Veen, A. Cannizzo, F. van Mourik, A. Vlček and M. Chergui, *J. Am. Chem. Soc.*, 2011, **133**, 305–315.

25 I. L. Zheldakov, M. N. Ryazantsev and A. N. Tarnovsky, *J. Phys. Chem. Lett.*, 2011, **2**, 1540–1545.

26 J. E. Haley, D. M. Krein, J. L. Monahan, A. R. Burke, D. G. McLean, J. E. Slagle, A. Fratini and T. M. Cooper, *J. Phys. Chem. A*, 2011, **115**, 265–273.

27 G. Zhou, W.-Y. Wong, S.-Y. Poon, C. Ye and Z. Lin, *Adv. Funct. Mater.*, 2009, **19**, 531–544.

28 P. Nguyen, G. Lesley, T. B. Marder, I. Ledoux and J. Zyss, *Chem. Mater.*, 1991, **455**, 406–408.

29 T. M. Cooper, D. M. Krein, A. R. Burke, D. G. McLean, J. E. Rogers and J. E. Slagle, *J. Phys. Chem. A*, 2006, **110**, 13370–13378.

30 L. Kondrachova, K. E. Paris, P. C. Sanchez, A. M. Vega, R. Pyati and C. D. Rithner, *J.*

Electroanal. Chem., 2005, **576**, 287–294.

31 E. Glimsdal, M. Carlsson, T. Kindahl, M. Lindgren, C. Lopes and B. Eliasson, *J. Phys. Chem. A*, 2010, **114**, 3431–3442.

32 T. M. Cooper, B. C. Hall, A. R. Burke, J. E. Rogers, D. G. McLean, J. E. Slagle and P. A. Fleitz, *Chem. Mater.*, 2004, **16**, 3215–3217.

33 A. Mohammed, B. Minaev, H. Ågren, M. Lindgren and P. Norman, *Chem. Phys. Lett.*, 2009, **481**, 209–213.

34 S. C. Jones, V. Coropceanu, S. Barlow, T. Kinnibrugh, T. Timofeeva, J.-L. Brédas and S. R. Marder, *J. Am. Chem. Soc.*, 2004, **126**, 11782–11783.

35 L. Liu, D. Huang, S. M. Draper, X. Yi, W. Wu and J. Zhao, *Dalt. Trans.*, 2013, **42**, 10694–10706.

36 P. A. Scattergood, M. Delor, I. V Sazanovich, O. V Bouganov, S. A. Tikhomirov, A. S. Stasheuski, A. W. Parker, G. M. Greetham, M. Towrie, E. S. Davies, A. J. H. M. Meijer and J. A. Weinstein, *Dalt. Trans.*, 2014, **43**, 17677–17693.

37 X.-X. Zhang, C. Würth, L. Zhao, U. Resch-Genger, N. P. Ernsting and M. Sajadi, *Rev. Sci. Instrum.*, 2011, **82**, 063108.

38 M. Gerecke, G. Bierhance, M. Gutmann, N. P. Ernsting and A. Rosspeintner, *Rev. Sci. Instrum.*, 2016, **87**, 053115.

5 Vibrational Energy Transport in Platinum(II) Diimine Complexes – Utilising Ultrafast Two-Dimensional Infrared Spectroscopy

5.1 Introduction

In the previous two chapters, the dynamics of the electronic excited-states of Pt(II) acetylide complexes, were explored. Here interplay between the ground state vibrational modes of a Pt(II)(diimine)(thiolate) complex and two related complexes, featuring O- and CC- in place of the S- respectively, is investigated. Such complexes, capable of generating charge-transfer states, are of great interest in many applications including as chromophores in artificial photosynthetic systems.[1–7] Square planar complexes of Pt(II) are much less studied than the archetypal $[Ru(bpy)_3]^{2+}$, and derivatives, but offer numerous advantages. These complexes typically feature a lowest-energy excited state of mixed metal-ligand-to-ligand charge transfer character.[8–10] There is a lack of chirality with square planar complexes, simplifying synthesis. There is also often more, a clear directionality to electron transfer, absent in octahedral complexes.

The interplay of electronic states within such systems, is strongly dependent on the vibrational modes, specifically vibrational relaxation (VR) and the redistribution of vibrational energy within the molecules - 'vibrational energy transfer' (VET). VR and VET typically take place on the timescale of femtoseconds to hundreds of picoseconds.[11–14] Previous work in the group revealed a remarkable dependence of excited-state dynamics on the excitation of specific vibrational modes following electronic excitation. The pumping of acetylide groups within an asymmetrical Pt(II) acetylide complex, led to drastic changes in the branching ratio between electronic excited-states with route to population of a full charge-separated state completely 'switched off'.

With the goal of improving the properties of metal complexes, the development of an understanding of the relationship between structure and molecular dynamics, the ground-state vibrational modes, and their couplings is of great importance.[7,12,15,16] Ultrafast two-dimensional infrared (2DIR) spectroscopy is used to study the population of vibrational modes within molecules, and the subsequent decay in population and redistribution of vibrational energy. The information obtained can provide enlightenment on the couplings between modes and the timescales over which VR and VET take place.[12,15,17–20] The are multiple possible mechanisms for the interaction of one vibrational

mode with another, introduced in chapter 1. The rates of redistribution, the magnitude of the signals, and the anharmonicity between bleach and transients may provide information on the types of mechanism at play.

Here, ultrafast 2DIR spectroscopy is used in the investigation of intermode coupling in a series of three Pt(II) diimine complexes, see **Figure 5.1**. The complexes all feature strong IR-reporter groups on either on end of the molecule. With two amide (CO) groups attached to the bipyridine ligand and ester groups attached, via the para- position of the phenyl group, on the opposite side of the molecule.

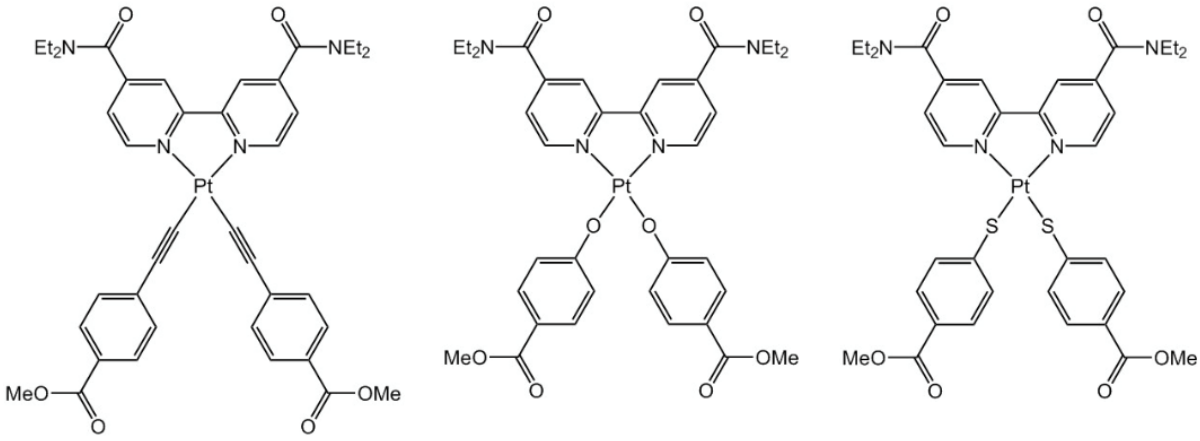

Figure 5.1 From left to right, chemical structures of; Pt(bpy-amide)(S-Ph-ester)$_2$, Pt(bpy-amide)(O-Ph-ester)$_2$ and Pt(bpy-amide)(CC-Ph-ester)$_2$.

5.2 Experimental

2DIR experiments were initially performed utilising a frequency-domain, pump-probe method.[21] With this method a narrowband IR pump is tuned to the wavenumber of the IR modes of interest. In theory, an individual vibrational mode is pumped in isolation, this is followed by a broad band IR probe pulse which will interrogate the system at various time delays after excitation, by means of a computer-controlled delay stage. The IR pump will then be tuned as to pump another IR mode, with subsequent probing. This procedure is repeated for all modes of interest, generating a '2D' map. Analysis of the 2DIR spectra obtained with this method revealed that the IR pump was insufficiently narrow to pump the IR bands in isolation, as a result, the spectra obtained are effectively uninterpretable.

2DIR experiments were repeated utilising a time-domain method, where the IR pump is effectively much narrower than that used in the frequency-domain method.

Time-domain 2DIR spectra were obtained using the pseudo-pump-probe geometry method,[22] with the LIFEtime spectrometer at the STFC Rutherford Appleton Laboratory.[23]

In brief, mid-infrared laser pulses were generated by three optical parametric amplifiers (OPA) pumped by two 100 kHz Yb:KGW amplified laser systems, (6 W, 180 fs, and 15 W, 300 fs) pumping one pump OPA (OPA_1) and two probe OPAs (OPA_2 and OPA_3, respectively). OPA_1 provided the 2DIR excitation pulses centred near 1640 cm^{-1}, resonant with the amide stretching modes and 1710cm^{-1}, resonant with ester stretching modes. OPA_2 provided probe pulses also centred on these modes (~1580 – 1780 cm^{-1}. OPA_3 provided probe pulses centred on the lower frequency modes (~1450 – 1650 cm^{-1}). The probe pulse durations produced by the OPAs were ~200 fs. Two collinear pump pulses, separated by a variable time delay, τ, were created by directing the output of OPA_1 into a mid-IR pulse shaper (Phasetech), and the waiting (pump-probe delay) time was set using an optical delay line situated after the pulse shaper. The pump pulse duration was ∼300 fs, providing the lower limit for the temporal resolution of the system. The two probe beams were dispersed in separate spectrometers, each equipped with a 128-element MCT array detector. 2DIR signals were measured using phase cycling, and 2DIR data sets were obtained by scanning τ for a fixed waiting time. Spectra were obtained by Fourier transform along τ.

5.3 Results

5.3.1 Chemical Structures and FTIR

The three complexes, (**Figure 5.1**) feature two strong infrared reporter groups, attached to either end of the molecule; the ester group attached to the phenyl ring and the amide group attached to the bi-pyridine ligand. The complexes all differ in the attachment of the phenyl ring to the platinum metal centre. By pumping both the ester/amide groups in isolation and probing the response at various vibrational modes in the molecules, at multiple time delays, the vibrational coupling and rates of vibrational relaxation can be assessed.

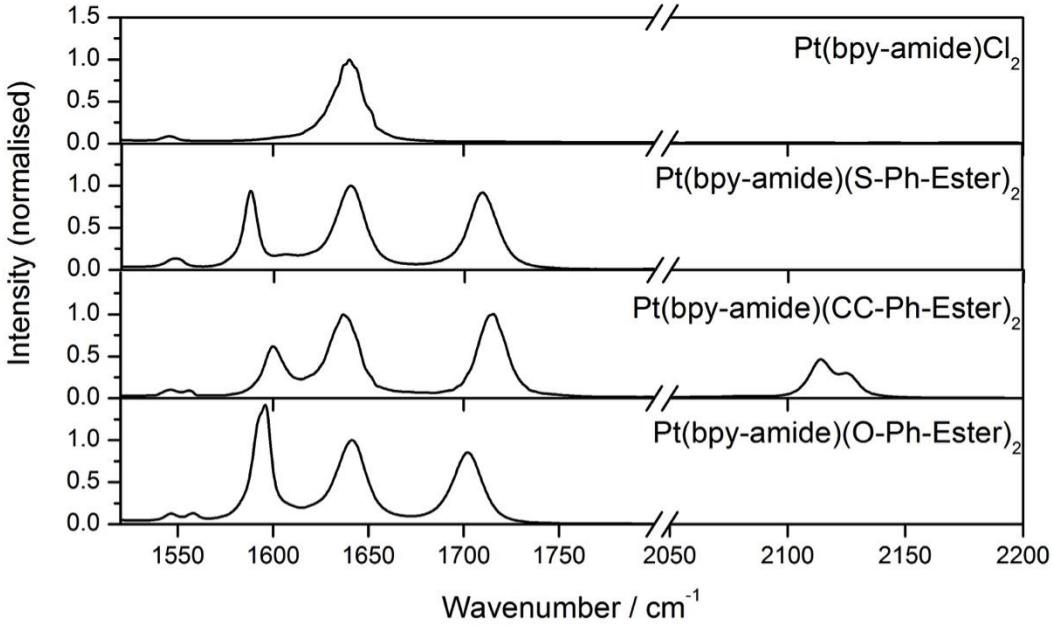

Figure 5.2 FTIR spectra of the complexes, Pt(bpy-amide)(S-Ph-ester)$_2$, Pt(bpy-amide)(O-Ph-ester)$_2$ and Pt(bpy-amide)(CC-Ph-ester)$_2$, as well as that of the pre-cursor molecule Pt(bpy-amide)Cl$_2$, in solutions of dichloromethane at room temperature.

Prior to undertaking the 2DIR experiments it is essential to have an understanding of the steady-state FTIR spectrum of each complex, i.e. what vibrational modes are responsible for each of the absorption bands observed. **Figure 5.2** shows the FTIR spectrum for each of the three molecules introduced above, as well as the di-chloride pre-cursor, Pt(bpy-amide)Cl$_2$. The pre-cursor complex aids in the assignment of absorption bands. The band(s) at around 1550 cm^{-1}, present in all four complexes, are assigned as the bi-pyridine, ring-breathing modes. The band at around 1640 cm^{-1}, present in all four complexes, is assigned as the amide, CO, stretching mode. The band at around 1590 cm^{-1} in each of the

three Pt(bpy-amide)(R-Ph-ester)$_2$ type complexes, is assigned as a phenyl mode. The band at around 1705 cm^{-1} in each of the three Pt(bpy-amide)(R-Ph-ester)$_2$ type complexes, is assigned as the ester, CO, stretching mode. The Pt(bpy-amide)(CC-Ph-ester)$_2$ complex also exhibits two bands at ~2110 and 2115 cm^{-1}, these are assigned as the asymmetric and symmetric acetylide stretching modes respectively. Theoretical calculations agree with these assignments.

In order to investigate the vibrational mode couplings and energy transport in these molecules 2DIR experiments have been performed, with the pumping of both the amide and ester with the bands in the region of 1550 to 1720 being probed in all experiments.

5.3.2 Pt(bpy-amide)(S-Ph-ester)$_2$ - ground-state vibrational dynamics

Amide pump: Figure 5.3 shows the GS-2DIR spectrum of Pt(bpy-amide)(S-Ph-ester)$_2$, in DCM, upon excitation of the amide stretching mode (CO) centred at 1640 cm^{-1}. **Figure 5.3 A** shows the crosspeaks in the region of 1450 to 1740 cm^{-1}, and **Figure 5.3 B** shows the self-response. Kinetic traces at select band positions are shown in **Figure 5.3 C.**

Self-response: Immediately upon excitation a bleach of the $v = 1 \leftarrow 0$ amide transition is present, i.e. a loss of population in the ground vibrational state, $v = 0$, causes an increase in transmission of probe light at ~1640 cm^{-1}. Accompanying the formation of this bleach is the associated transient ($v = 2 \leftarrow 1$ transition) signal, appearing at ~1622.5 cm^{-1}. Due to the overlap of the negative bleach and positive transient signals, the peaks of each appear shifted away from their true position, i.e. the bleach has a peak maximum at 1642 cm^{-1}, whereas the corresponding band in the FTIR appears at 1640 cm^{-1}. The peak position of the transient signal shifts appears to shift towards higher energy with time (0 ps peak position: 1622.5 cm^{-1}, 1.6 ps peak position: 1626.5 cm^{-1}), however, due to the spectral resolution achieved (~2 cm^{-1}) in this region it is difficult to draw conclusions from this spectral shift. The transient signal has completely decayed within 7.5 ps. The bleach signal doesn't fully return to the baseline, there is a fixed offset. This offset is most likely scattered pump light, kinetic traces at the bleach position show that this offset has no apparent decay on the timescale of this experiment. The amide self-response decays bi-exponentially with lifetimes of 0.39 and 1.22 ps.

Crosspeaks: At the '0 ps' time delay crosspeaks can be seen at: ~1550, ~1587 and 1712.5 cm^{-1}, corresponding to responses of the bi-pyridine, phenyl and ester modes respectively. Due to poor signal-to-noise and overlap of the crosspeaks with the amide self-response, quantitative kinetic information cannot be extracted for the signals corresponding to the response of the phenyl and the ester. The crosspeak at ~1543 cm^{-1}, rises with instrument response and decays bi-exponentially with lifetimes of 0.25 and 4.35 ps. The ester crosspeak signal at 17 ps is suggestive that there is vibrational energy transport across the entire molecule within this timescale.

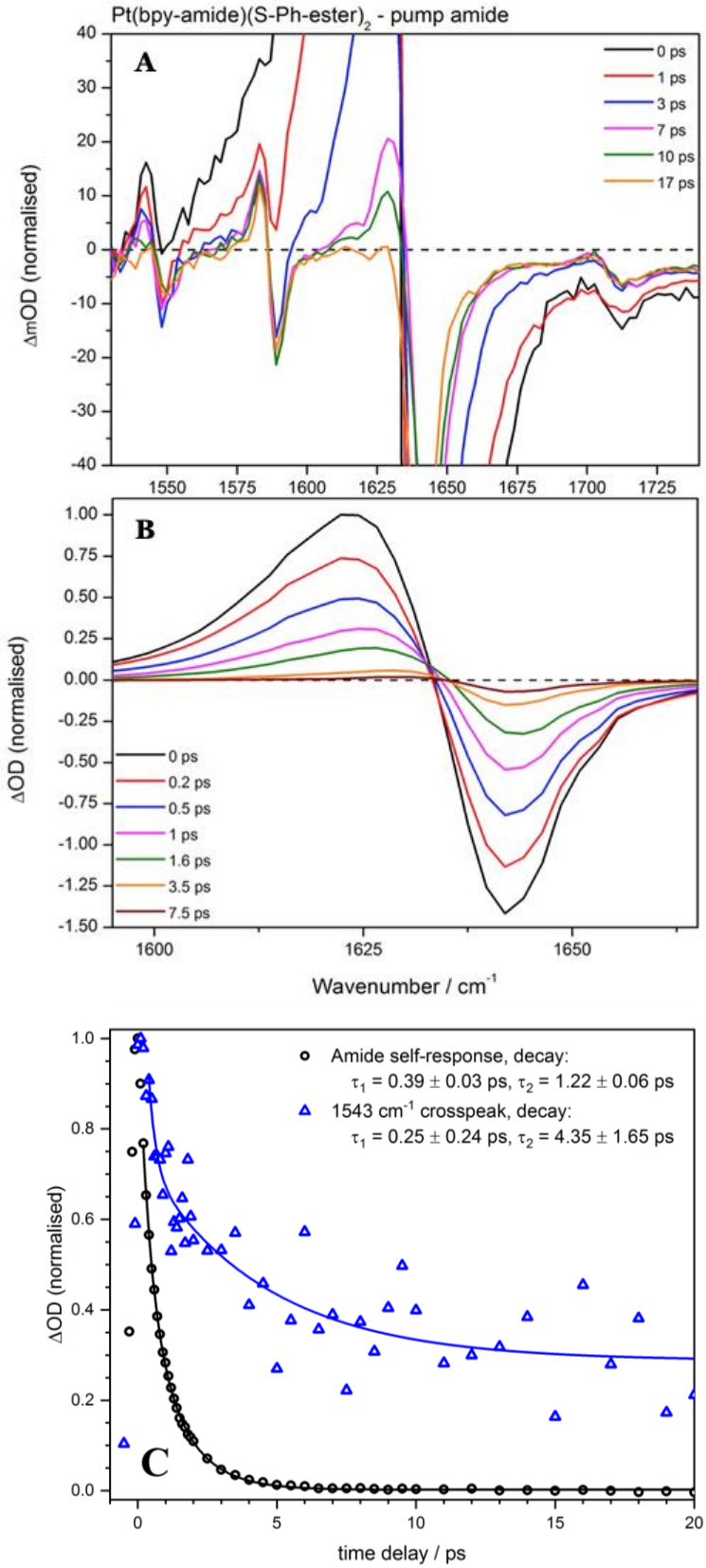

Figure 5.3 **A:** GS-2DIR spectra of Pt(bpy-amide)(S-Ph-ester)$_2$ in DCM solution, with pump at 1640 cm^{-1}, at various pump-probe time delays, showing the 1520 – 1740 cm^{-1} probe region. Spectra scaled to show close up of the crosspeaks. **B:** The same 2DIR spectra shown in **A** but centred on/scaled to the self-response of the ester. **C:** Kinetic traces at specific spectral positions, of the data shown in the panels **A** and **B**.

Ester pump: Figure 5.4 shows the GS-2DIR spectrum of Pt(bpy-amide)(S-Ph-ester)$_2$, in DCM, upon excitation of the ester stretching mode (CO) centred at 1709 cm^{-1}. **Figure 5.4 A** shows the crosspeaks in the region of 1450 to 1740 cm^{-1}, and **Figure 5.4 B** shows the self-response. Kinetic traces at select band positions are shown in **Figure 5.4 C**. **For select kinetic traces it was not possible to fit both the growth and decay of the signal with a single multi-exponential function convoluted with an IRF.Separate multi-exponential fits of the both the growth and then decay of the singal were deemed sufficient to make comparisons between the dynamics of the different complexes.**

Self-response: Immediately upon excitation a bleach of the $v = 1 \leftarrow 0$ ester transition is present, i.e. a loss of population in the ground vibrational state, $v = 0$, causes an increase in transmission of probe light at ~1713 cm^{-1}. Accompanying the formation of this bleach is the associated transient ($v = 2 \leftarrow 1$ transition) signal, appearing at ~1695 cm^{-1}. Due to the overlap of the negative bleach and positive transient signals, the peaks of each appear shifted away from their true position, i.e. the bleach has a peak maximum at 1712.5 cm^{-1}, whereas the corresponding band in the FTIR appears at 1709 cm^{-1}. There is no apparent shift in peak position of the transient signal with time, however, due to the spectral resolution achieved (~2 cm^{-1}) in this region it is difficult to draw conclusions from this lack of spectral shift. The transient signal has completely decayed within 7.5 ps. The bleach signal doesn't fully return to the baseline, there is a fixed offset. This offset is most likely scattered pump light, kinetic traces at the bleach position show that this offset has no apparent decay on the timescale of this experiment. The ester self-response decays bi-exponntially with lifetimes of 0.20 and 2.58 ps. **Crosspeaks**: At the '0 ps' time delay crosspeaks can be seen at: ~1550 and ~1587 cm^{-1}, corresponding to responses of the bi-pyridine and phenyl modes respectively. Due to poor signal-to-noise and overlap of the crosspeaks with the ester self-response, quantitative kinetic information cannot be extracted for the bi-pyridine crosspeak. The phenyl mode transient (~1573 cm^{-1}), shows delayed growth, i.e. growth longer than IRF, with a lifetime of 0.95 ps. The phenyl signal reaches maximum amplitude by around 4 ps and decays mono-exponentially with a lifetime of 12.12 ps. The lifetime of 12.12 ps is likely to be associated with vibrational cooling, energy dissipation to solvent. The lack of response at the amide position suggests that vibrational energy redistribution is more favourable in the amide to ester direction.

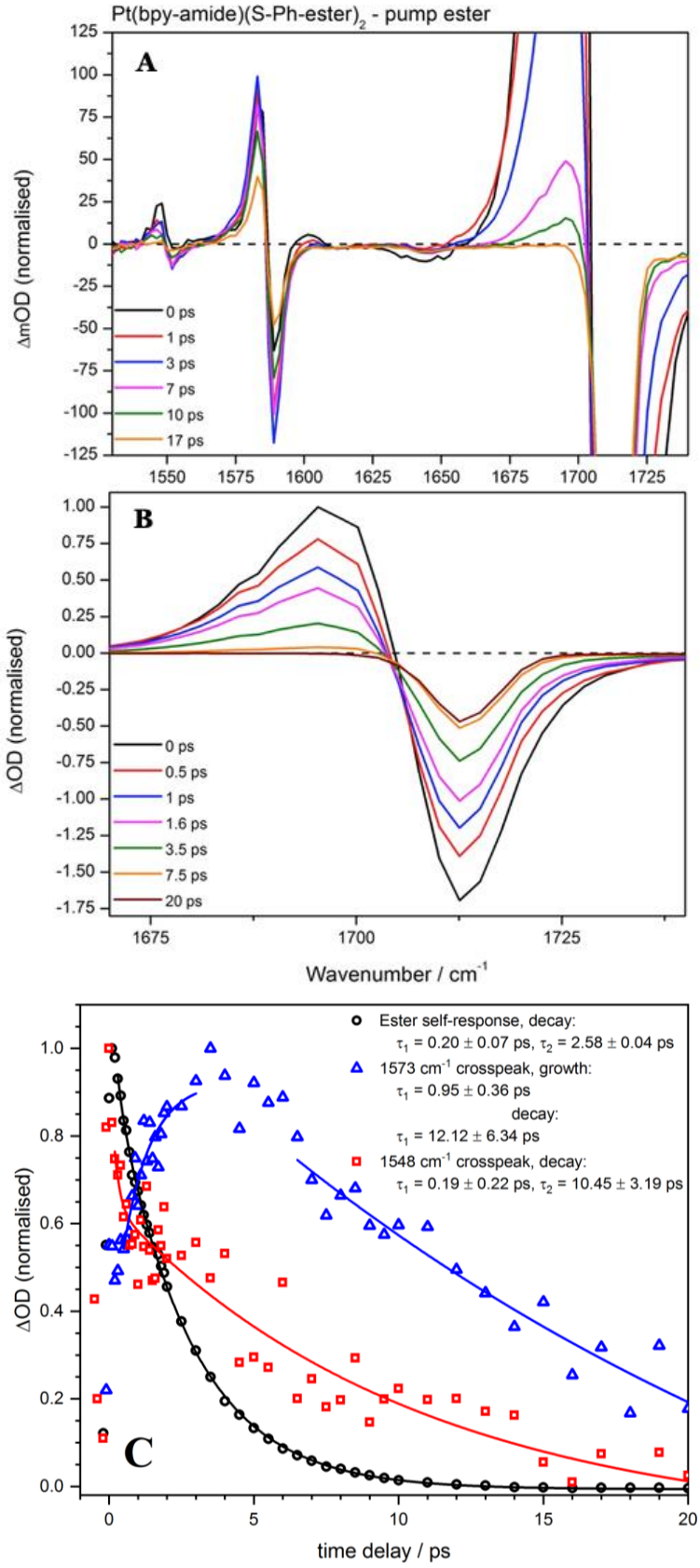

Figure 5.4 **A:** GS-2DIR spectra of Pt(bpy-amide)(S-Ph-ester)$_2$ in DCM solution, with pump at 1710 cm^{-1}, at various pump-probe time delays, showing the 1520 – 1740 cm^{-1} probe region. Spectra scaled to show close up of the crosspeaks. **B:** The same 2DIR spectra shown as in **A** but centred on/scaled to the self-response of the ester. **C:** Kinetic traces at specific spectral positions, of the data shown in the panels **A** and **B**.

5.3.3 Pt(bpy-amide)(O-Ph-ester)$_2$ - ground-state vibrational dynamics

Amide pump: Figure 5.5 shows the GS-2DIR spectrum of Pt(bpy-amide)(O-Ph-ester)$_2$, in DCM, upon excitation of the amide stretching mode (CO) centred at 1641.5 cm^{-1}. **Figure 5.5 A** shows the crosspeaks in the region of 1450 to 1740 cm^{-1}, and **Figure 5.5 B** shows the self-response. Kinetic traces at select band positions are shown in **Figure 5.5 C**.

Self-response: Immediately upon excitation a bleach of the $v = 1 \leftarrow 0$ amide transition is present, i.e. a loss of population in the ground vibrational state, $v = 0$, causes an increase in transmission of probe light at ~1644 cm^{-1}. Accompanying the formation of this bleach is the associated transient ($v = 2 \leftarrow 1$ transition) signal, appearing at ~1626 cm^{-1}. Due to the overlap of the negative bleach and positive transient signals, the peaks of each appear shifted away from their true position, i.e. the bleach has a peak maximum at 1644 cm^{-1}, whereas the corresponding band in the FTIR appears at 1641.5 cm^{-1}. There is no apparent shift in peak position of the transient signal with time, however, due to the spectral resolution achieved (~2 cm^{-1}) in this region it is difficult to draw conclusions from this spectral shift. The transient signal has completely decayed within 7.5 ps. The bleach signal doesn't fully return to the baseline, there is a fixed offset. This offset is most likely scattered pump light, kinetic traces at the bleach position show that this offset has no apparent decay on the timescale of this experiment. The ester self-response decays bi-exponentially with lifetimes of 0.34 and 1.24 ps. **Crosspeaks**: At the '0 ps' time delay crosspeaks can be seen at: ~1550, ~1595 and ~1705 cm^{-1}, corresponding to responses of the bi-pyridine, phenyl and ester modes respectively. Due to poor signal-to-noise and overlap of the crosspeaks with the amide self-response, quantitative kinetic information cannot be extracted for the crosspeaks at ~1595 and ~1705 cm^{-1}. The crosspeak at ~1544 cm^{-1}, rises with instrument response and decays bi-exponentially with lifetimes of 0.63 and 4.11 ps. The ester crosspeak signal at 17 ps is suggestive that there is vibrational energy transport across the entire molecule within this timescale.

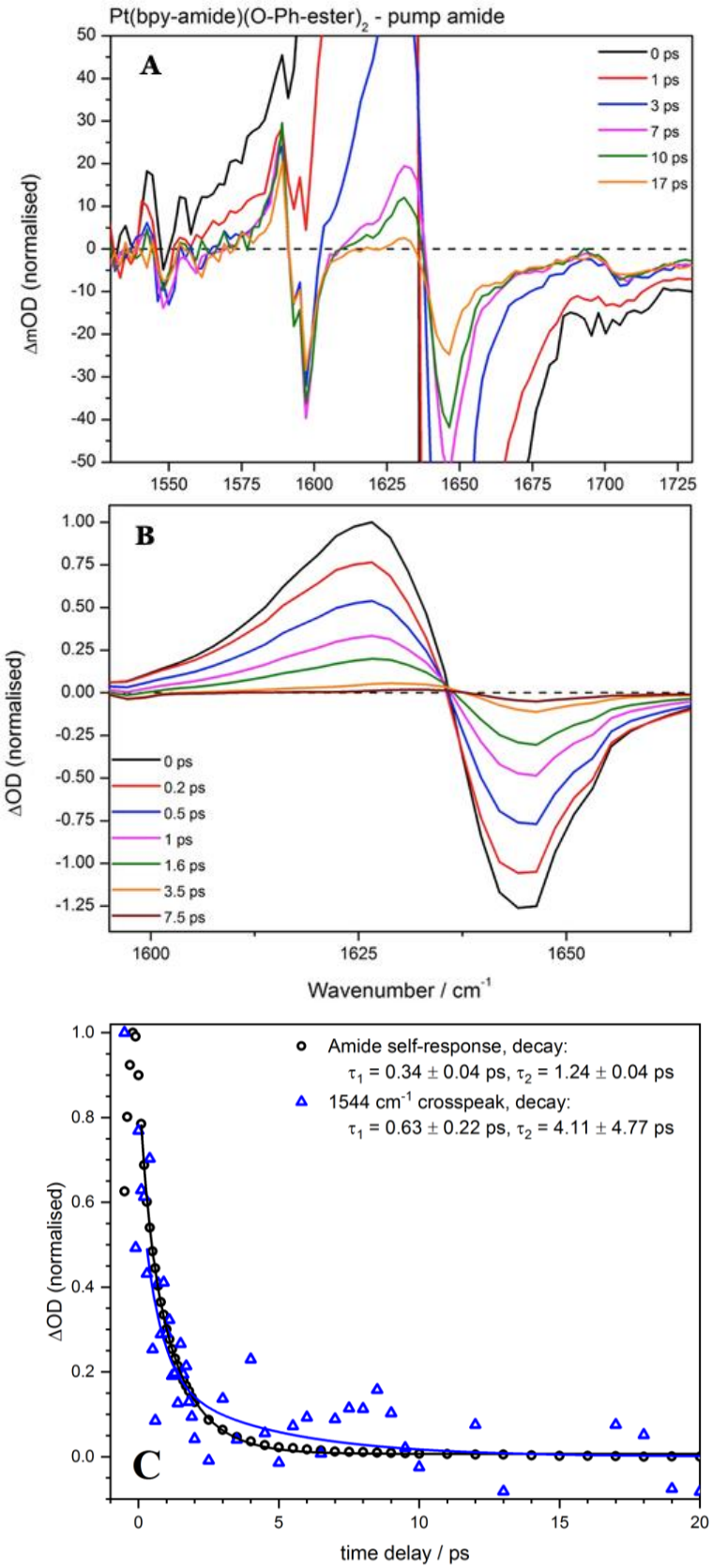

Figure 5.5 **A:** GS-2DIR spectra of Pt(bpy-amide)(O-Ph-ester)$_2$ in DCM solution, with pump at 1645 cm^{-1}, at various pump-probe time delays, showing the 1520 – 1740 cm^{-1} probe region. Spectra scaled to show close up of the crosspeaks. **B:** The same 2DIR spectra shown as in **A** but centred on/scaled to the self-response of the ester. **C:** Kinetic traces at specific spectral positions, of the data shown in the panels **A** and **B**.

Ester pump: Figure 5.6 shows the GS-2DIR spectrum of Pt(bpy-amide)(O-Ph-ester)$_2$, in DCM, upon excitation of the ester stretching mode (CO) centred at 1702 cm^{-1}. **Figure 5.6 A** shows the crosspeaks in the region of 1450 to 1740 cm^{-1}, and **Figure 5.6** B shows the self-response. Kinetic traces at select band positions are shown in **Figure 5.6 C**. **For select kinetic traces it was not possible to fit both the growth and decay of the signal with a single multi-exponential function convoluted with an IRF.Separate multi-exponential fits of the both the growth and then decay of the singal were deemed sufficient to make comparisons between the dynamics of the different complexes.**

Self-response: Immediately upon excitation a bleach of the $v = 1 \leftarrow 0$ ester transition is present, i.e. a loss of population in the ground vibrational state, $v = 0$, causes an increase in transmission of probe light at ~1708 cm^{-1}. Accompanying the formation of this bleach is the associated transient ($v = 2 \leftarrow 1$ transition) signal, appearing at ~1690 cm^{-1}. Due to the overlap of the negative bleach and positive transient signals, the peaks of each appear shifted away from their true position, i.e. the bleach has a peak maximum at 1708 cm^{-1}, whereas the corresponding band in the FTIR appears at 1702 cm^{-1}. There is no apparent shift in peak position of the transient signal with time, however, due to the spectral resolution achieved (~2 cm^{-1}) in this region it is difficult to draw conclusions from this spectral shift. The transient signal has completely decayed within 7.5 ps. The bleach signal doesn't fully return to the baseline, there is a fixed offset. This offset is most likely scattered pump light, kinetic traces at the bleach position show that this offset has no apparent decay on the timescale of this experiment. The ester self-response decays bi-exponentially with a lifetime of 0.59 and 2.42 ps. **Crosspeaks**: At the '0 ps' time delay crosspeaks can be seen at: ~1555 and ~1595 cm^{-1}, corresponding to responses of the bi-pyridine and phenyl modes respectively. Due to poor signal-to-noise and overlap of the crosspeaks with the ester self-response, quantitative kinetic information cannot be extracted for the bi-pyridine crosspeak. The phenyl mode transient appears to rise with the IRF and decays mono-exponentially with a lifetime of 17.50 ps. The lifetime of 17.50 ps is likely to be associated with vibrational cooling, energy dissipation to solvent. The lack of response at the amide position suggests that vibrational energy redistribution is more favourable in the amide to ester direction.

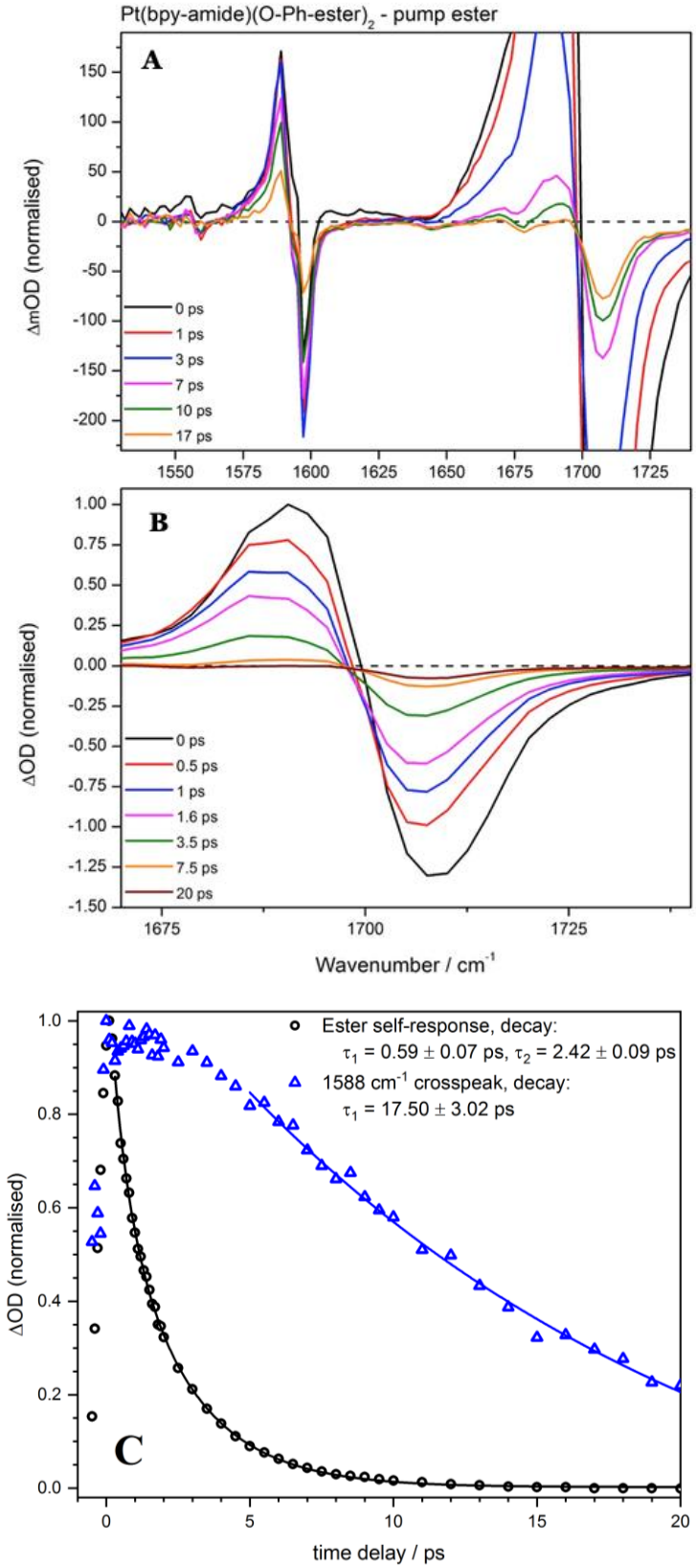

Figure 5.6 **A:** GS-2DIR spectra of Pt(bpy-amide)(O-Ph-ester)$_2$ in DCM solution, with pump at 1710 cm^{-1}, at various pump-probe time delays, showing the 1520 – 1740 cm^{-1} probe region. Spectra scaled to show close up of the crosspeaks. **B:** The same 2DIR spectra shown as in **A** but centred on/scaled to the self-response of the ester. **C:** Kinetic traces at specific spectral positions, of the data shown in the panels **A** and **B**.

5.3.4 Pt(bpy-amide)(CC-Ph-ester)$_2$ - ground-state vibrational dynamics

Amide pump: Figure 5.7 shows the GS-2DIR spectrum of Pt(bpy-amide)(CC-Ph-ester)$_2$, in DCM, upon excitation of the amide stretching mode (CO) centred at 1637 cm^{-1}. **Figure 5.7 A** shows the crosspeaks in the region of 1450 to 1740 cm^{-1}, and **Figure 5.7 B** shows the self-response. Kinetic traces at select band positions are shown in **Figure 5.7 C**.

Self-response: Immediately upon excitation a bleach of the $v = 1 \leftarrow 0$ amide transition is present, i.e. a loss of population in the ground vibrational state, $v = 0$, causes an increase in transmission of probe light at ~1642 cm^{-1}. Accompanying the formation of this bleach is the associated transient ($v = 2 \leftarrow 1$ transition) signal, appearing at ~1625 cm^{-1}. Due to the overlap of the negative bleach and positive transient signals, the peaks of each appear shifted away from their true position, i.e. the bleach has a peak maximum at 1642 cm^{-1}, whereas the corresponding band in the FTIR appears at 1637 cm^{-1}. The peak position of the transient signal shifts appears to shift towards higher energy with time (0 ps peak position: 1622.5 cm^{-1}, 1.6 ps peak position: 1626.5 cm^{-1}), however, due to the spectral resolution achieved (~2 cm^{-1}) in this region it is difficult to draw conclusions from this spectral shift. The transient signal has completely decayed within 7.5 ps. The bleach signal doesn't fully return to the baseline, there is a fixed offset. This offset is most likely scattered pump light, kinetic traces at the bleach position show that this offset has no apparent decay on the timescale of this experiment. The amide self-response decays bi-exponentially with lifetimes of 0.37 and 1.25 ps.

Crosspeaks: At the '0 ps' time delay crosspeaks can be seen at: ~1550, ~1600 and ~1725cm^{-1}, corresponding to responses of the bi-pyridine, phenyl and ester modes respectively. Due to poor signal-to-noise and overlap of the crosspeaks with the amide self-response, quantitative kinetic information cannot be extracted for the phenyl and ester mode crosspeaks. The signal at ~1546 cm^{-1} grows with the IRF and decays mono-exponentially with a lifetime of 2.84 ps. The ester crosspeak signal at 17 ps is suggestive that there is vibrational energy transport across the entire molecule within this timescale. The ester crosspeak signal appears larger in this complex than in the other two complexes, this suggests more efficient vibrational energy transport. This could perhaps be due to the more rigid framework, imposed by the conjugated acetylide linker.

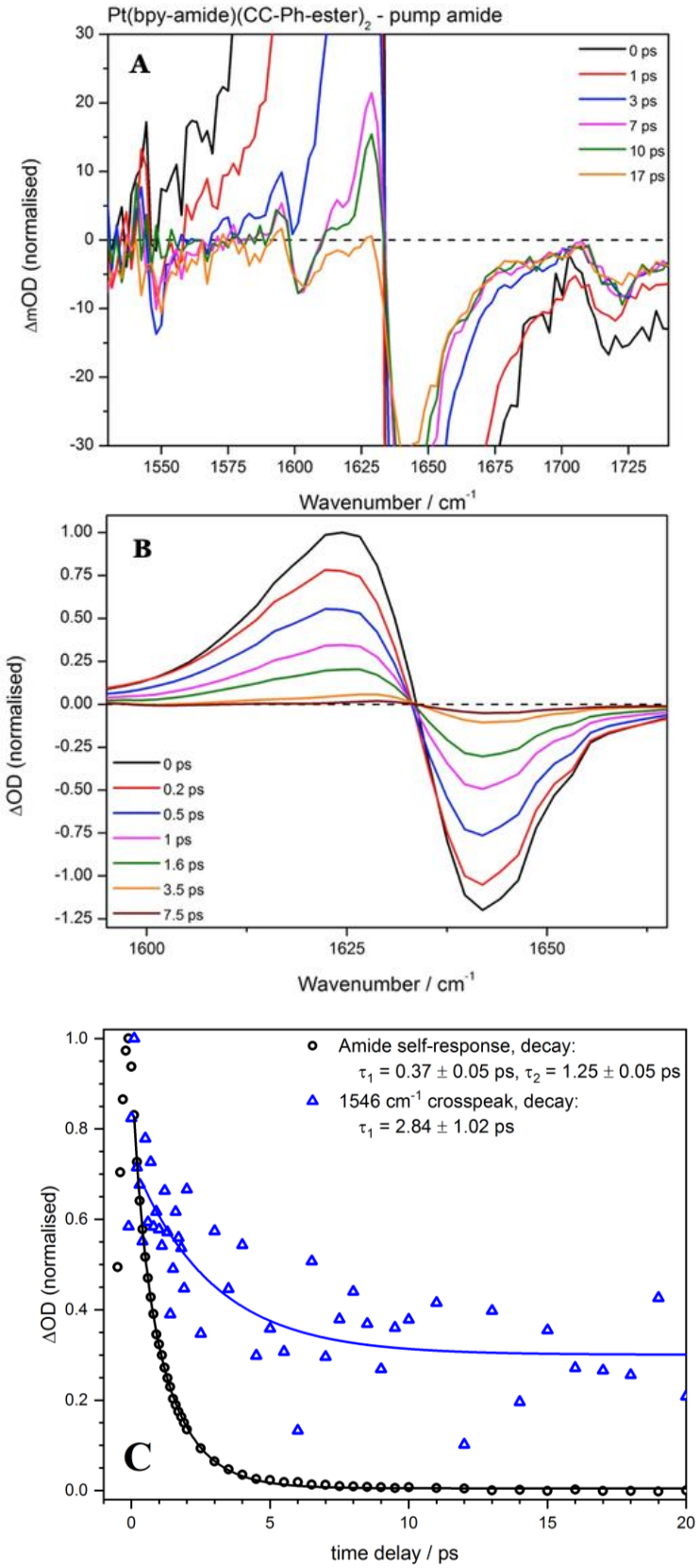

Figure 5.7 **A:** GS-2DIR spectra of Pt(bpy-amide)(CC-Ph-ester)$_2$ in DCM solution, with pump at 1640 cm^{-1}, at various pump-probe time delays, showing the 1520 – 1740 cm^{-1} probe region. Spectra scaled to show close up of the crosspeaks. **B:** The same 2DIR spectra shown as in **A** but centred on/scaled to the self-response of the ester. **C:** Kinetic traces at specific spectral positions, of the data shown in the panels **A** and **B**.

Ester pump: Figure 5.8 shows the GS-2DIR spectrum of Pt(bpy-amide)(CC-Ph-ester)$_2$, in DCM, upon excitation of the ester stretching mode (CO) centred at 1714.5 cm^{-1}. **Figure 5.8 A** shows the crosspeaks in the region of 1450 to 1740 cm^{-1}, and **Figure 5.8 B** shows the self-response. Kinetic traces at select band positions are shown in **Figure 5.8 C**. **For select kinetic traces it was not possible to fit both the growth and decay of the signal with a single multi-exponential function convoluted with an IRF.Separate multi-exponential fits of the both the growth and then decay of the singal were deemed sufficient to make comparisons between the dynamics of the different complexes.**

Self-response: Immediately upon excitation a bleach of the $v = 1 \leftarrow 0$ ester transition is present, i.e. a loss of population in the ground vibrational state, $v = 0$, causes an increase in transmission of probe light at ~1720 cm^{-1}. Accompanying the formation of this bleach is the associated transient ($v = 2 \leftarrow 1$ transition) signal, appearing at ~1700 cm^{-1}. Due to the overlap of the negative bleach and positive transient signals, the peaks of each appear shifted away from their true position, i.e. the bleach has a peak maximum at 1720 cm^{-1}, whereas the corresponding band in the FTIR appears at 1714.5 cm^{-1}. There is no apparent shift in peak position of the transient signal with time, however, due to the spectral resolution achieved (~2 cm^{-1}) in this region it is difficult to draw conclusions from this spectral shift. The transient signal has completely decayed within 7.5 ps. The bleach signal doesn't fully return to the baseline, there is a fixed offset. This offset is most likely scattered pump light, kinetic traces at the bleach position show that this offset has no apparent decay on the timescale of this experiment. The ester self-response decays bi-exponentially with a lifetime of 0.52 and 2.22 ps.

Crosspeaks: At the '0 ps' time delay crosspeaks can be seen at: ~1550, ~1587 cm^{-1} and ~1640 cm^{-1} corresponding to responses of the bi-pyridine, phenyl and amide modes respectively. Due to poor signal-to-noise and overlap of the crosspeaks with the ester self-response, quantitative kinetic information cannot be extracted for the amide crosspeak at ~1640 cm^{-1}. The phenyl mode transient appears to grow bi-exponentially, with approx. 90% of the amplitude growing within the IRF with minor growth continuing until approx. 4 ps. The phenyl crosspeak decays mono-exponentially with a lifetime of 18.35 ps. The lifetime of 18.35 ps is likely to be associated with vibrational cooling, energy dissipation to solvent. As with the amide pumping in this molecule, larger crosspeaks at the amide

and bi-pyridine modes are seen relative to the other two compounds, this suggests vibrational energy transport is more efficient with the acetylide linker in the ester to amide direction as well.

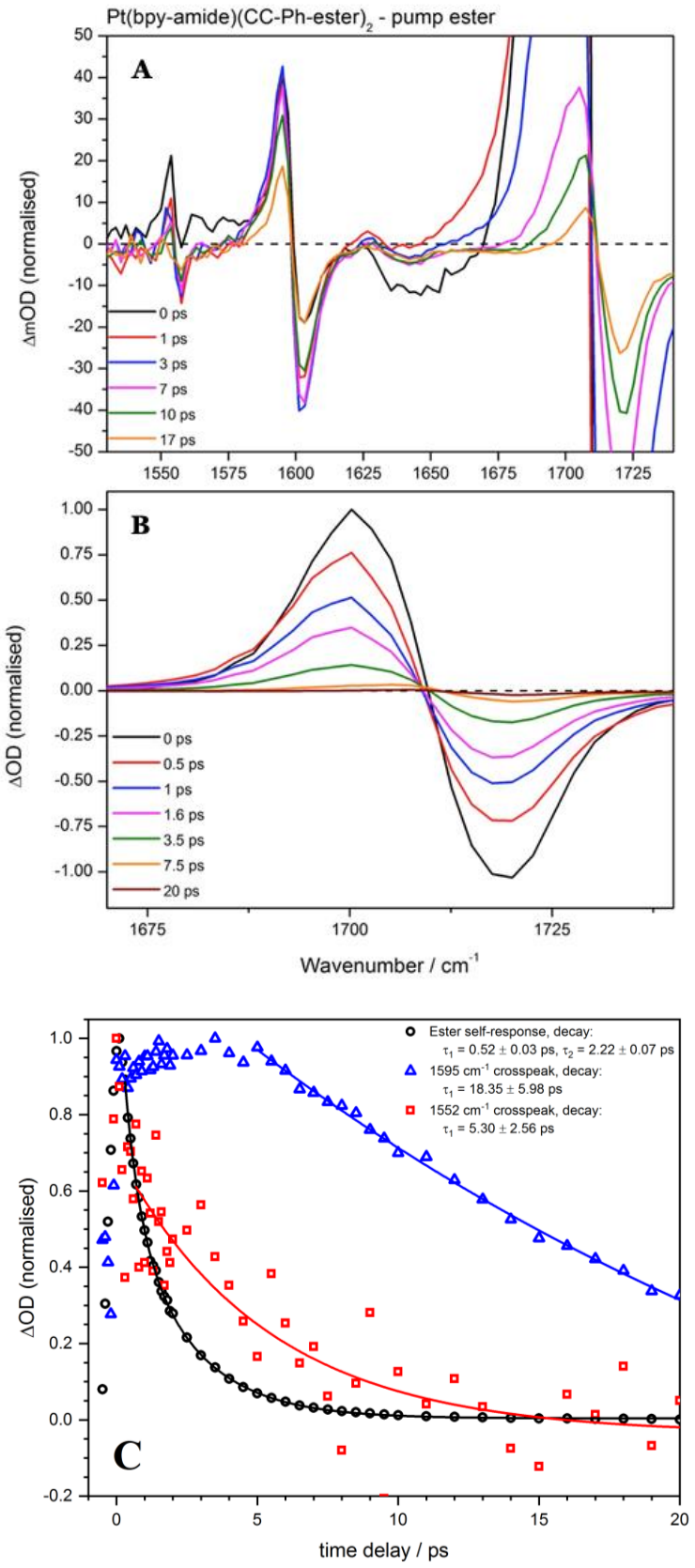

Figure 5.8 **A:** GS-2DIR spectra of Pt(bpy-amide)(CC-Ph-ester)$_2$ in DCM solution, with pump at 1715 cm^{-1}, at various pump-probe time delays, showing the 1520 – 1740 cm^{-1} probe region. Spectra scaled to show close up of the crosspeaks. **B:** The same 2DIR spectra shown as in **A** but centred on/scaled to the self-response of the ester. **C:** Kinetic traces at specific spectral positions, of the data shown in the panels **A** and **B**.

5.3.5 Summary of the Dynamics of the Signals

The lifetimes and anharmonicity values for Pt(bpy-amide)(S-Ph-ester)$_2$, Pt(bpy-amide)(O-Ph-ester)$_2$, and Pt(bpy-amide)(CC-Ph-ester)$_2$, are summarised in**Table 5.1**, **Table 5.2**, and **Table 5.3**, respectively. The anharmonicity values were obtained by taking the difference in spectral position (wavenumber) of the peak of the positive, and corresponding negative band, respectively. Anharmonicity values quoted are for the spectra at 3 ps, where crosspeaks are near maximum amplitude.

Table 5.1 Summary of the time constants obtained in the analysis of the 2DIR spectra of Pt(bpy-amide)(**S**-Ph-ester)$_2$, in dichloromethane solution. Anharmonicity values, the difference in spectral position of the positive and negative signal, are also presented.

Pt(bpy-amide)(S-Ph-ester)$_2$

		Probe Position			
		Ester	Amide	approx. 1543 cm^{-1}	approx. 1573 cm^{-1}
Pump Position	Ester	Decay τ_1 = 0.20 ± 0.07 ps τ_2 = 2.58 ± 0.04 ps		Decay τ_1 = 0.19 ± 0.22 ps τ_2 = 10.45 ± 3.19 ps	Growth τ_1 = 0.95 ± 0.36 ps Decay τ_2 = 12.12 ± 6.34 ps
		Anharmonicity 18 cm^{-1}		Anharmonicity 5 cm^{-1}	Anharmonicity 7 cm^{-1}
	Amide		Decay τ_1 = 0.39 ± 0.03 ps τ_2 = 1.22 ± 0.06 ps	Decay τ_1 = 0.25 ± 0.24 ps τ_2 = 4.35 ± 1.65 ps	
			Anharmonicity 17 cm^{-1}	Anharmonicity 5 cm^{-1}	Anharmonicity 6 cm^{-1}

Table 5.2 Summary of the time constants obtained in the analysis of the 2DIR spectra of Pt(bpy-amide)(**O**-Ph-ester)$_2$, in dichloromethane solution. Anharmonicity values, the difference in spectral position of the positive and negative signal, are also presented.

Pt(bpy-amide)(O-Ph-ester)$_2$

		Probe Position			
		Ester	Amide	approx. 1543 cm^{-1}	approx. 1573 cm^{-1}
Pump Position	Ester	Decay $\tau_1 = 0.59 \pm 0.07$ ps $\tau_2 = 2.42 \pm 0.09$ ps		Decay $\tau_1 = 0.19 \pm 0.22$ ps $\tau_2 = 10.45 \pm 3.19$ ps	Decay $\tau_2 = 17.50 \pm 3.02$ ps
		Anharmonicity 18 cm^{-1}		Anharmonicity 5 cm^{-1}	Anharmonicity 7 cm^{-1}
	Amide		Decay $\tau_1 = 0.34 \pm 0.04$ ps $\tau_2 = 1.24 \pm 0.04$ ps	Decay $\tau_1 = 0.63 \pm 0.22$ ps $\tau_2 = 4.11 \pm 4.77$ ps	
			Anharmonicity 17 cm^{-1}	Anharmonicity 5 cm^{-1}	Anharmonicity 6 cm^{-1}

Table 5.3 Summary of the time constants obtained in the analysis of the 2DIR spectra of Pt(bpy-amide)(**CC**-Ph-ester)$_2$, in dichloromethane solution. Anharmonicity values, the difference in spectral position of the positive and negative signal, are also presented.

Pt(bpy-amide)(CC-Ph-ester)$_2$

		Probe Position			
		Ester	Amide	approx. 1543 cm^{-1}	approx. 1573 cm^{-1}
Pump Position	Ester	Decay $\tau_1 = 0.52 \pm 0.03$ ps $\tau_2 = 2.22 \pm 0.07$ ps		Decay $\tau_1 = 5.30 \pm 2.56$ ps	Decay $\tau_2 = 18.35 \pm 5.98$ ps
		Anharmonicity 18 cm^{-1}		Anharmonicity 5 cm^{-1}	Anharmonicity 7 cm^{-1}
	Amide		Decay $\tau_1 = 0.37 \pm 0.05$ ps $\tau_2 = 1.25 \pm 0.05$ ps	Decay $\tau_1 = 2.84 \pm 1.02$ ps	
			Anharmonicity 17 cm^{-1}	Anharmonicity 5 cm^{-1}	Anharmonicity 6 cm^{-1}

5.4 Discussion

For each of the complexes investigated vibrational energy transport across the entire molecular framework is observed. The temporal response of cross peaks appears to be multi-exponential in all cases suggesting multiple routes for the transport of energy are taken.

For all three complexes, the self-response of both amide (C=O) and ester (C=O) modes, rises within the IRF. In all cases, the self-response of the amide (C=O) decays bi-exponentially with time constants in the region of 0.34 – 0.39 and 1.22 – 1.25 ps, and the self-response of the ester (C=O) decays bi-exponentially with time constants in the region of 0.22 – 0.59 and 2.22 – 2.58 ps. Within experimental error, the rate of decay of self-response of both the amide and ester is effectively the same for all three complexes. The fast decay component is attributed to intramolecular vibrational-energy redistribution (IVR). The slow component is attributed to vibrational cooling, that is, the transfer of vibrational energy from the molecule to the solvent.

In all complexes, the anharmonicity of the self-response of the ester and amide, is 18 and 17 cm^{-1} respectively. Crosspeak anharmonicity values were all in the range of 5 – 7 cm^{-1}, and with the achievable spectral resolution of the spectrometer, were identical for all complexes. The magnitude of the anharmonic splitting observed for all crosspeaks, is much smaller than that of the self-responses, this suggests that no population transfer occurred between the pumped amide / ester group and any other vibrational mode. The observed effect is most likely due to the high-frequency modes, populated upon excitation, transfer energy to low-frequency modes along the entirety of the molecule, which in turn perturb the environment of the other high-frequency modes, i.e. the probed modes. These relatively small anharmonicity values are comparable to those reported in the literature.[12,15,24,25]

All spectra are normalised to the transient signal, of the self-response of the pumped mode, i.e. normalised to either the amide or ester transient. The oscillator strengths of the various vibrational modes, are essentially the same for each of the 3 complexes, that is, the area under the absorption bands is effectively identical. The normalisation means that the amplitude of the crosspeaks observed are comparable from one complex to

another. With Pt(bpy-amide)(S-Ph-ester)$_2$ and Pt(bpy-amide)(O-Ph-ester)$_2$, crosspeaks corresponding to response of the amide (C=O) mode are observed, but are only just resolvable above the noise level. However, with Pt(bpy-amide)(CC-Ph-ester)$_2$ the amide (C=O) mode crosspeak has a considerably larger amplitude. The complex featuring the CC-linker will be significantly more rigid than the complexes featuring the -S- and -O- linkers, it is hypothesised that the increased rigidity within this part of the molecule increases the efficiency of vibrational energy transport, in the direction of the ester group to the amide.

Kinetic analysis of the crosspeaks reveals interesting behaviour in all cases. This behaviour can be described by two different contributing processes. The first process, is the rise of the crosspeak signal with the same lifetime as the self-response of the pumped mode, this is within the IRF. The 'instantaneous' rise may have two possible origins, firstly, this 'rise' may in fact be a background of the much-larger signal of the self-response. This is unlikely however, because of the large spectral separation (> 100 cm^{-1}) between the pumped and the probed modes. Additionally, there is a lack of detectable background offset, see **Figure 5.6 A** for example. The second possible explanation for this fast-growing component to the crosspeaks is a contribution of a dipole-dipole interaction, which will also appear as an 'instantaneous' signal. Occurrences of these types of interactions are reported in the literature.[20,26–28] The second component contributing to the crosspeak signals grows in slower than the IRF, this 'slow' growth is most pronounced with the response of the phenyl mode (~1587 cm^{-1}) upon the pumping of the ester (C=O) mode (~1710 cm^{-1}), see **Figure 5.4 C**, **Figure 5.6 C**, and **Figure 5.8 C**. This slower component of the growth of the crosspeak signals is attributed to energy transfer, from the pumped modes, to low-frequency modes along the entirety of the molecule, resulting in the perturbation of the environment of the other high-frequency modes, this mechanism is effectively a summation of numerous population transfers between vibrational modes and is hence 'delayed' with respect to the faster direct population transfer or dipole-dipole interactions. These types of 'relaxation-assisted' crosspeaks are well documented in similar molecular systems in the literature.[28–32]

5.5 Conclusion and Future Work

Utilizing 2DIR spectroscopy, vibrational energy transport was observed in three Pt(bpy-amide)(R-Ph-ester)$_2$. Due to relatively weak signal of the amide-ester and ester-amide crosspeaks, minimal quantitative kinetic analysis was possible, for these longest distant couplings. However, through-bond couplings between amide and ester were present in all three complexes. Relative signal strength suggested preferential energy transport in the amide to ester direction in each case. Crosspeaks were most intense in the Pt(bpy-amide)(CC-Ph-ester)$_2$, this is perhaps due to increased rigidity in this complex, imposed by the acetylide linker. Decay of the amide self-response had a decay lifetime of ~1 ps in each complex, while the ester self-response had a decay lifetime of ~2 ps. Vibrational cooling of the phenyl ring, in each complex, occurred with a lifetime of ~10-15 ps.

In order to get quantitative kinetic information on these types of complexes, larger signals are required; this could be achieved by using more strongly absorbing IR reporters.

In order to overcome low signal-to-noise and to remove the influence of any baseline, peak-to-peak analysis of the crosspeaks should be performed. Additionally, more information may be extracted by analysis of the peak area / width as a function of time. Crosspeaks should be fit with Voigt functions, with the resultant FWHM plotted against time delay.

These types of, metal-centred, Donor-Acceptor systems are frequently used for solar energy harvesting and photocatalysis. This preliminary investigation paves the way to more detailed studies of energy transport in the charge-separated excited states of such molecules in the future.

5.6 References

1 S. D. Cummings and R. Eisenberg, *J. Am. Chem. Soc.*, 1996, **118**, 1949–1960.

2 M. Hissler, J. E. McGarrah, W. B. Connick, D. K. Geiger, S. D. Cummings and R. Eisenberg, *Coord. Chem. Rev.*, 2000, **208**, 115–137.

3 E. O. Danilov, I. E. Pomestchenko, S. Kinayyigit, P. L. Gentili, M. Hissler, R. Ziessel and F. N. Castellano, *J. Phys. Chem. A*, 2005, **109**, 2465–2471.

4 J. Moussa, L.-M. Chamoreau, A. Degli Esposti, M. P. Gullo, A. Barbieri and H. Amouri, *Inorg. Chem.*, 2014, **53**, 6624–33.

5 W. A. Tarran, G. R. Freeman, L. Murphy, A. M. Benham, R. Kataky and J. A. G. Williams, *Inorg. Chem.*, 2014, **53**, 5738–49.

6 M. Delor, P. A. Scattergood, I. V Sazanovich, A. W. Parker, G. M. Greetham, A. J. H. M. Meijer, M. Towrie and J. A. Weinstein, *Science*, 2014, **346**, 1492–1495.

7 S. Archer and J. A. Weinstein, *Coord. Chem. Rev.*, 2012, **256**, 2530–2561.

8 J. M. Bevilacqua, J. A. Zuleta and R. Eisenberg, *Inorg. Chem.*, 1994, **33**, 258–266.

9 J. A. Weinstein, M. T. Tierney, E. S. Davies, K. Base, A. A. Robeiro and M. W. Grinstaff, *Inorg. Chem.* , 2006, **45**, 4544–4555.

10 M. Hissler, W. B. Connick, D. K. Geiger, J. E. Mcgarrah, D. Lipa, R. J. Lachicotte and R. Eisenberg, *Inorg. Chem.*, 2000, **39**, 447–457.

11 T. Elsaesser and W. Kaiser, *Annu. Rev. Phys. Chem.*, 1991, **42**, 83–107.

12 I. V Rubtsov, *Acc. Chem. Res.*, 2009, **42**, 1385–1394.

13 R. M. van der Veen, A. Cannizzo, F. van Mourik, A. Vlček and M. Chergui, *J. Am. Chem. Soc.*, 2011, **133**, 305–315.

14 P. A. Scattergood, M. Delor, I. V. Sazanovich, O. V. Bouganov, S. A. Tikhomirov, A. S. Stasheuski, A. W. Parker, G. M. Greetham, M. Towrie, E. S. Davies, A. J. H. M. Meijer and J. A. Weinstein, *Dalt. Trans.*, 2014, **43**, 17677–17693.

15 I. V Rubtsov and R. M. Hochstrasser, *J. Phys. Chem. B*, 2002, **106**, 9165–9171.

16 J. Bredenbeck, J. Helbing, C. Kolano and P. Hamm, *ChemPhysChem*, 2007, **8**, 1747–1756.

17 P. Hamm and M. Zanni, *Concepts and Methods of 2D Infrared Spectroscopy*, Cambridge University Press, 2011.

18 P. Hamm, M. Lim and R. M. Hochstrasser, *J. Phys. Chem. B.*, 1998, **102**, 6123–6138.

19 R. M. Hochstrasser, *Proc. Natl. Acad. Sci. U. S. A.*, 2007, **104**, 14190–14196.

20 D. V. Kurochkin, S. R. G. Naraharisetty and I. V. Rubtsov, *Proc. Natl. Acad. Sci.*, 2007, **104**, 14209–14214.

21 G. M. Greetham, P. M. Donaldson, C. Nation, I. V. Sazanovich, I. P. Clark, D. J. Shaw, A. W. Parker and M. Towrie, *Appl. Spectrosc.*, 2016, **70**, 645–653.

22 L. P. DeFlores, R. A. Nicodemus and A. Tokmakoff, *Opt. Lett.*, 2007, **32**, 2966.

23 P. M. Donaldson, G. M. Greetham, D. J. Shaw, A. W. Parker and M. Towrie, *J. Phys. Chem. A*, 2018, **122**, 780–787.

24 N. T. Hunt, *Chem. Soc. Rev.*, 2009, **38**, 1837–1848.

25 S. Kaziannis, J. A. Wright, M. Candelaresi, R. Kania, G. M. Greetham, A. W. Parker, C. J. Pickett and N. T. Hunt, *Phys. Chem. Chem. Phys*, 2011, **13**, 10295–10305.

26 M. Fedoseeva, M. Delor, S. C. Parker, I. V. Sazanovich, M. Towrie, A. W. Parker and J. A. Weinstein, *Phys. Chem. Chem. Phys.*, 2015, **17**, 1688–1696.

27 C. S. Keating, B. A. McClure, J. J. Rack and I. V. Rubtsov, *J. Chem. Phys.*, 2010, **133**, 144513.

28 V. M. Kasyanenko, Z. Lin, G. I. Rubtsov, J. P. Donahue and I. V Rubtsov, *J. Chem. Phys.*, 2009, **131**, 154508.

29 J. M. Anna, J. T. King and K. J. Kubarych, *Inorg. Chem.*, 2011, **50**, 9273–9283.

30 C. R. Baiz, P. L. McRobbie, J. M. Anna, E. Geva and K. J. Kubarych, *Acc. Chem. Res.*, 2009, **42**, 1395–1404.

31 J. Bredenbeck, J. Helbing and P. Hamm, *J. Am. Chem. Soc.*, 2004, **126**, 990–991.

32 M. Delor, I. V. Sazanovich, M. Towrie, S. J. Spall, T. Keane, A. J. Blake, C. Wilson, A. J. H. M. Meijer and J. A. Weinstein, *J. Phys. Chem. B*, 2014, **118**, 11781–11791.

6 Summary and Conclusions

The primary aim of the work presented in this thesis was to investigate ISC in TM complexes using an array of ultrafast spectroscopic techniques. In all work presented, measurements' of the ultrafast emission of a series of asymmetrical platinum(II) 'donor-bridge-acceptor' complexes (**Chapter 3**) demonstrated the ability of fluorescence upconversion spectroscopy to resolve ultrafast dynamics of such complexes on the time scale of 100's of femtoseconds. The work illustrated the complex nature of the dependence of ISC rates on molecular structure, with singlet emission persistent for 10's of picoseconds, with ISC evidently occurring on timescales much slower than that of complexes featuring much lighter metal centres of Ru and Re, contrary to the 'heavy atom effect'.

In **Chapter 4** the ultrafast emission of a series of symmetrical platinum(II) 'donor-bridge-donor' complexes were presented. Unlike with closely related systems presented in the literature, no clear decrease in the rate of ISC upon extension of ligand size was observed. However, there appeared to be a correlation between the extension of the linker and the intensity of emission, perhaps indicating a 'dilution' of the SOC effect of the metal and subsequent reduction in ISC efficiency.

Perhaps the most striking findings presented here are found within Chapters 3 and 4, where photophysical behaviour in direct contradiction with Kasha's rule are observed.

The investigation of vibrational couplings within the ground-state vibrational modes of three closely related platinum(II) diimine complexes (**Chapter 5**) demonstrated the ability of 2DIR spectroscopy in the resolution of competing vibrational coupling mechanisms. Long-range (> 10 Å) coupling between strong IR reporter groups (amide and ester (C=O) modes) was observed in all cases, with the amplitude of observed crosspeaks suggesting enhanced vibrational energy transport the complex featuring the 'rigid' acetylide linker.

The complexes studied within this thesis display interesting excited-state behaviour, often in contradiction to the 'rules' of photophysical processes. These findings pave the way for further investigation of such systems, with the aim of developing a 'handle' on the relationship between molecular structure and excited-state properties, essential for the tailoring of systems for use in solar energy harvesting applications. The utilisation of

different solvent systems may be a particularly interesting method for shedding more light on the early time dynamics, via the altering of relative energies of excited states.

7 Experimental

7.1 Ultrafast Time-Resolved Fluorescence, UV-Vis, TRIR and 2DIR Spectroscopy

All spectroscopic measurements were performed in the solution phase. In order to minimise photodecomposition, the samples were flown in specifically designed cells to continuously refresh the sample in the path of excitation. Ground-state UV-Vis absorption and infrared absorption measurements were taken periodically throughout experimentation in order to assess the extent to which photodecomposition had occurred, where necessary, new solutions were prepared with fresh, pure samples.

7.1.1 Ultrafast Time-Resolved Fluorescence - Broadband Fluorescence Upconversion Spectroscopy (FLUPS)

Broadband femtosecond fluorescence spectroscopy experiments were performed in the Lord Porter Ultrafast Laser Spectroscopy Laboratory at the University of Sheffield. Experiments were performed on a spectrometer developed by Niko P. Ernsting and co-workers at Humboldt University, Berlin and supplied by LIOP-TEC GmbH. The experimental setup is described in detail in reference 1[1] and in Chapter 2.

Laser System

A Ti:Sapphire regenerative amplifier (Spitfire ACE PA-40, Spectra-Physics) provided $800\ \mathrm{nm}$ pulses ($40\ \mathrm{fs}$ fwhm, $10\ \mathrm{kHz}$, $1.2\ \mathrm{mJ}$). $800\ \mathrm{nm}$ seed pulses ($25\ \mathrm{fs}$ fwhm, $84\ \mathrm{MHz}$) for the amplifier were provided by a Ti:Sapphire oscillator (Mai Tai, Spectra-Physics). Two Nd:YLF lasers (Empower, Spectra-Physics) were used to pump the two amplification stages of the Spitfire ACE PA-40.

Sample Excitation

Frequency doubling of the $800\ \mathrm{nm}$ output of the amplifier, in a β-barium borate crystal within a commercially available doubler/tripler (TimePlate, Photop Technologies), was used to generate the $400\ \mathrm{nm}$ pump pulses ($40\ \mathrm{fs}$ fwhm, $10\ \mathrm{kHz}$, ~$0.3\ \mu\mathrm{J}$). The pump pulses were passed through a computer-controlled optical delay line (M-IMS400LM, Newport), translation of which gave control of time delay between pump and gate pulses, within a $4\ \mathrm{ns}$ window with a temporal resolution of $1.67\ \mathrm{fs}$. The power of the pump pulses was controlled using a variable attenuation neutral-density filter wheel. Pump pulses were compressed in a double-pass two-prism compressor (AFS-FS Fused Silica Prism Pair,

Thorlabs) to achieve minimal fwhm of a cross-correlation between the gate and pump pulses. Polarization was set to magic angle, with respect to vertical, with a $\lambda/2$ plate. Pump pulses were then focused by a lens ($f = 200\ mm$, fused silica) onto the sample cell, to a spot diameter of $\leq 0.1\ mm$. The cell consisted of a fused silica cuvette with an internal path length of $1.0\ mm$. The sample solution was stirred with a magnetic stirrer.

Fluorescence Gating

The $1320\ nm$ gate pulses (80 fs fwhm, $10\ kHz$, $80\ \mu J$) were the signal pulses generated by a traveling-wave optical parametric amplifier of superfluorescence (TOPAS prime, Light Conversion) pumped by the $800\ nm$ (40 fs fwhm, $10\ kHz$, $0.5\ mJ$) output of Ti:Sapphire regenerative amplifier. The polarization of the gate pulses was set to horizontal using a wire-grid polariser in conjunction with a $\lambda/2$ plate. The wire-grid polarizer and $\lambda/2$ plate pair were also used to attenuate the power of the gate pulses.

Fluorescence Collection and Sum-Frequency Generation

Fluorescence from the sample was collected in a forward-scattering geometry. A small beam-stop was used to block any transmitted pump light. The fluorescence was directed onto a $100\ \mu m$ thick β-barium borate crystal (BBO crystal, EKSMA OPTICS) where it was upconverted by sum-frequency generation with the $1320\ nm$ gate pulses. The fluorescence and gate beams met at an angle of ~$21°$ at the crystal. Type II phasematching was used in order to provide broadest spectral window for upconversion.

Upconverted Fluorescence Signal Detection

The upconverted fluorescence was spatially filtered and then focused the entrance of a fiber bundle (Ceram Optek) with a concave mirror. A homebuilt spectrograph was used to disperse the upconverted fluorescence onto a CCD detector (iDus 420 DU440A-BU2, Andor). The detectable spectral range was ~$286 - 500\ nm$, this corresponding to original fluorescence of ~$360 - 780\ nm$.

7.1.2 Ultrafast Time-Resolved UV-Vis Absorption Spectroscopy ('Transient Absorption')

Transient Absorption (TA) experiments were performed in the Lord Porter Ultrafast Laser Spectroscopy Laboratory at the University of Sheffield. Experiments were performed on a Helios spectrometer (HE-VIS-NIR-3200) provided by Ultrafast Systems.

Laser system

A Ti:Sapphire regenerative amplifier (Spitfire ACE PA-40, Spectra-Physics) provided 800 nm pulses (40 fs FWHM, 10 KHz, 1.2 mJ). The amplifier was seeded by a Ti:Sapphire oscillator (Mai Tai, Spectra-Physics), providing 800 nm pulses (25 fs FWHM, 84 MHz). Both amplification stages of the Spitfire ACE were pumped by two Nd:YLF lasers (Empower, Spectra-Physics).

Sample excitation

500 nm pump pulses (80 fs FWHM, 2.5 KHz, 0.4 μJ) were generated by a travelling-wave optical parametric amplifier of superfluorescence (TOPAS prime, Light Conversion), which was pumped by the 800 nm (40 fs, 10 KHz, 0.5 mJ) output of the spitfire ACE. The pump pulse was passed through a mechanical chopper with a frequency of 2.5 KHz, to allow for the probing of both pumped and unpumped sample. The pump pulse was depolarised prior to sample excitation. The pump pulses were focussed onto the sample cell (fused silica with an internal path length of 2 mm), to a spot diameter of ≤ 0.3 mm. The pump pulse energy was controlled using a variable attenuation neutral-density filter wheel. The sample solution was stirred using a magnetic stirrer bar.

Sample probing

A broadband white light pulse (340 – 750 nm) was generated in situ, using a portion of the 800 nm output of the spitfire ACE. The 800 nm pulse was focussed, using a protected gold concave mirror (f = 100 mm), onto a 3 mm Calcium Fluoride crystal. The white light generated was focused onto the sample cell using a protected silver concave mirror (f = 50 mm). Prior to generation of the white light, the 800 nm pulses were passed through a computer controlled optical delay line (DDS300, Thorlabs), which provides 8 ns of delay, with a temporal resolution of 1.67 fs.

Detection

The probe light transmitted through the sample was filtered to remove excess 800 nm light, then focussed using two lenses (f = 250 mm, f = 50 mm) onto the entrance of a fibre

bundle. A CMOS detector with an intrinsic resolution of 1.5 nm was used to measure the intensity of the transmitted light through the pumped and unpumped sample.

7.1.3 Ultrafast Time-Resolved Infrared Absorption Spectroscopy (TRIR)

TRIR experiments were performed using the ULTRA instrument at the STFC Rutherford Appleton Laboratory. The experimental set-up is described in detail in the literature.[2]

In brief, a Ti:Sapphire regenerative amplifier (Thales) provides 800 nm pulses (40 fs FWHM, 10 KHz, 1 mJ), a portion of which was used to generate tuneable, 400 cm^{-1}, broad mid-IR probe pulses. Additionally, a fraction of the amplifier output was used to pump a fs-NOPA TOPAS which was used to provide 520 nm excitation pulses. The probe and pump beams were focussed onto a Harrick cell (CaF_2 windows, 630 μm internal path) to yield spot sizes of 70 μm and 120 μm at the sample, respectively. The sample solution was flowed through the cell using a peristaltic pump, while the cell was simultaneously raster-scanned to avoid decomposition. The relative polarisation between the pump and probe was set to magic angle. The IR light transmitted through the sample was recorded using two, linear, 128 array HgCdTe detectors (Infrared Associates).

7.1.4 Ultrafast Time-Domain Two-Dimensional Infrared Spectroscopy (2DIR)

Time-domain 2DIR spectra were obtained using the pseudo-pump-probe geometry method,[3] with the LIFEtime spectrometer at the STFC Rutherford Appleton Laboratory.[4]

In brief, mid-infrared laser pulses were generated by three optical parametric amplifiers (OPA) pumped by two 100 kHz Yb:KGW amplified laser systems, (6 W, 180 fs, and 15 W, 300 fs) pumping one pump OPA (OPA_1) and two probe OPAs (OPA_2 and OPA_3, respectively). OPA_1 provided the 2DIR excitation pulses centred near 1640 cm^{-1}, resonant with the amide stretching modes and 1710cm^{-1}, resonant with ester stretching modes. OPA_2 provided probe pulses also centred on these modes (~1580 – 1780 cm^{-1}. OPA_3 provided probe pulses centred on the lower frequency modes (~1450 – 1650 cm^{-1}). The probe pulse durations produced by the OPAs were ~200 fs. Two collinear pump pulses, separated by a variable time delay, τ, were created by directing the output of OPA_1 into a mid-IR pulse shaper (Phasetech), and the waiting (pump-probe delay) time was set using an optical delay line situated after the pulse shaper. The pump pulse duration was ∼300 fs, providing the lower limit for the temporal resolution of the system. The two probe

beams were dispersed in separate spectrometers, each equipped with a 128-element MCT array detector. 2DIR signals were measured using phase cycling, and 2DIR data sets were obtained by scanning τ for a fixed waiting time. Spectra were obtained by Fourier transform along τ. The data were collected by Dr M. Fedoseeva.

7.2 Steady-State Measurements, DFT and Data Analysis

7.2.1 UV-Vis Absorption Spectroscopy

UV-Vis absorption spectra were recorded in quartz cuvettes (1 / 10 mm path length) using a Cary 60 UV-Vis spectrometer (Agilent). Optical densities in region of interest were kept to below 1 by manipulation of sample concentration. Samples were prepared as solutions in dichloromethane unless otherwise stated.

7.2.2 Steady-State FTIR Spectroscopy

Steady-state FTIR spectra were recorded in Harrick cells, with CaF_2 windows, on a Nicolet iS20 FTIR spectrometer (Thermo Scientific). Optical densities in region of interest were kept to below 1 by manipulation of sample concentration. Samples were prepared as solutions in dichloromethane unless otherwise stated.

7.2.3 Steady-State Emission Spectroscopy

Emission spectra were recorded in quartz cuvettes of 10 mm path length using a Fluoromax-4 spectrofluorometer (Horiba). Samples were prepared as solutions in dichloromethane unless otherwise stated.

7.2.4 Data Analysis

Several software packages were used in the analysis and presentation of spectroscopic data. Plotting and basic analysis (single point kinetic fitting and peak fitting) were performed using OriginPro 2019. Global analysis of time-resolved data was performed using Glotaran v1.3. Singular Value Decomposition (SVD), global and target analysis were used to extract kinetic and spectral components. An in-depth description of these methods of analysis can be found in the literature.

7.3 References

1 X.-X. Zhang, C. Würth, L. Zhao, U. Resch-Genger, N. P. Ernsting and M. Sajadi, *Rev. Sci. Instrum.*, 2011, **82**, 063108.

2 G. M. Greetham, P. M. Donaldson, C. Nation, I. V. Sazanovich, I. P. Clark, D. J. Shaw, A. W. Parker and M. Towrie, *Appl. Spectrosc.*, 2016, **70**, 645–653.

3 L. P. DeFlores, R. A. Nicodemus and A. Tokmakoff, *Opt. Lett.*, 2007, **32**, 2966.

4 P. M. Donaldson, G. M. Greetham, D. J. Shaw, A. W. Parker and M. Towrie, *J. Phys. Chem. A*, 2018, **122**, 780–787.

A Appendix to Chapter 4

A.1 NAP-Pt-Cl

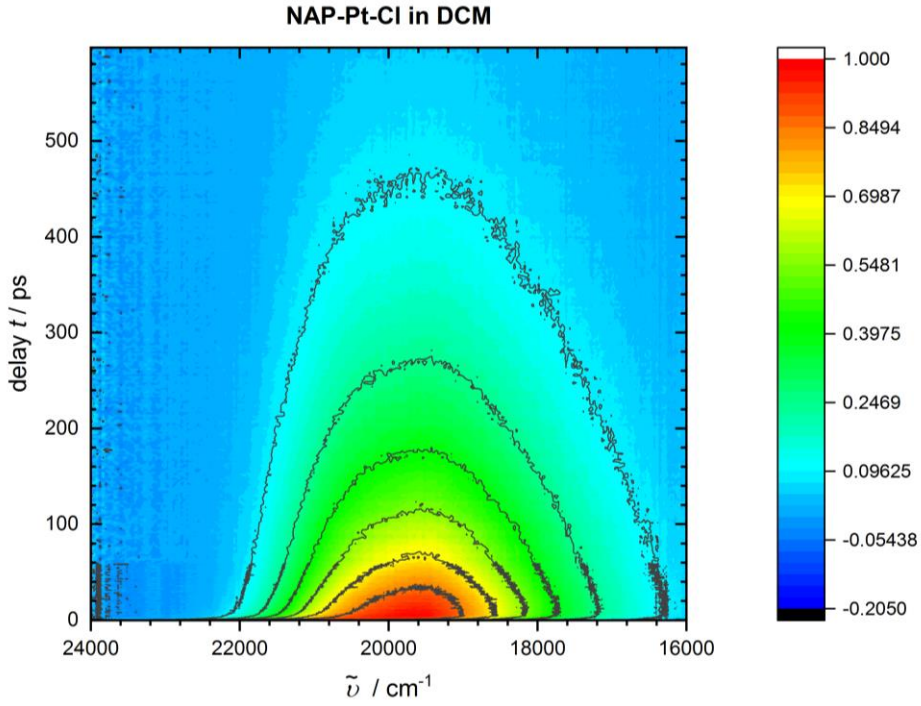

Figure A.1 A 2D map of time-resolved emission spectra of NAP-Pt-Cl in dichloromethane upon 400 nm excitation, obtained by fluorescence upconversion. The optical density at the pump wavelength was approximately 1. Photometric- and time-zero dispersion- corrections have been applied to the raw data.

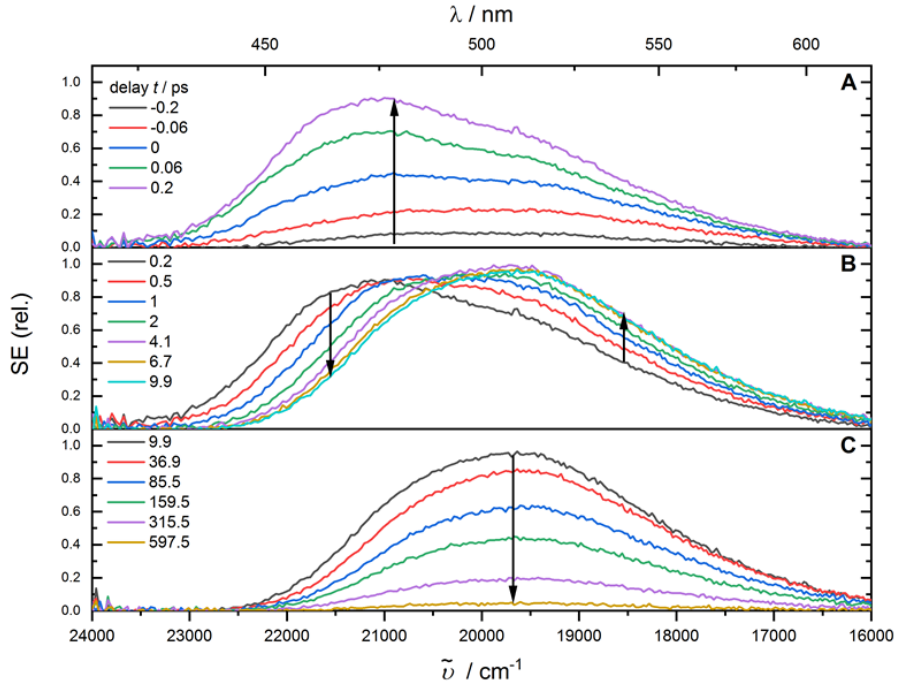

Figure A.2 Time-resolved emission spectra of NAP-Pt-Cl in dichloromethane upon 400 nm excitation, obtained by fluorescence upconversion. The optical density at the pump wavelength was approximately 1. Three distinct temporal ranges are shown in each of the panels, A (-200 – 200 fs), B (200 fs – 9.9 ps) and C (9.9 ps – 597.5 ps). Arrows indicate the characteristic evolutionary feature within each range. Photometric- and time-zero dispersion- corrections have been applied to the raw data.

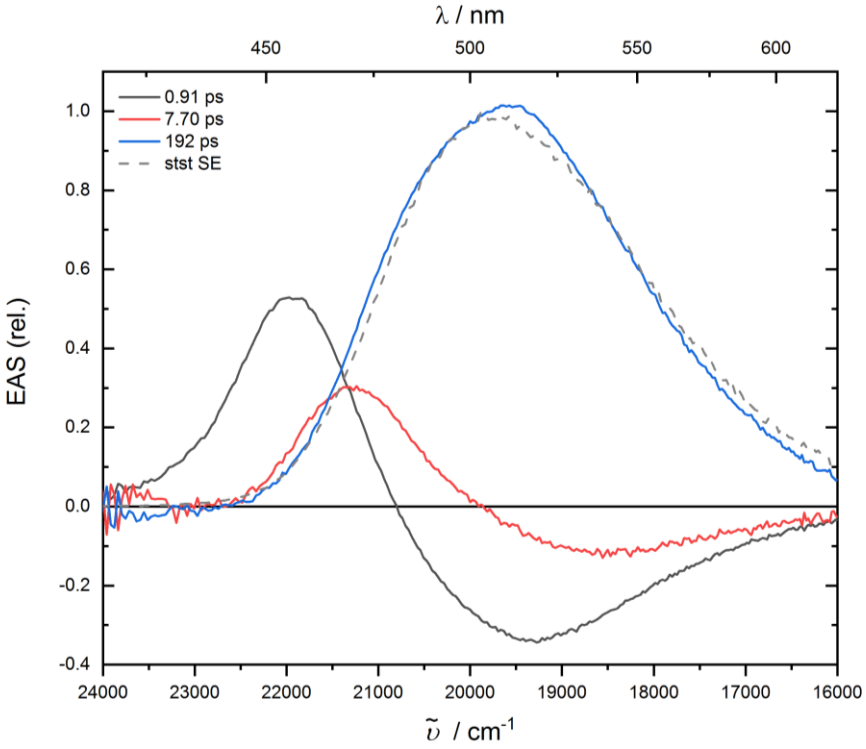

Figure A.3 Decay-Associated Spectra (DAS) of the emission spectra of NAP-Pt-Cl (shown in ***Figure A.2***), obtained via global analysis using three exponential time functions. The corresponding time constants are given as insets. The steady-state (stst) emission spectrum of NAP-Pt-Cl, converted to the form of stimulated-emission (SE), is also shown (grey dashed trace, stst SE).

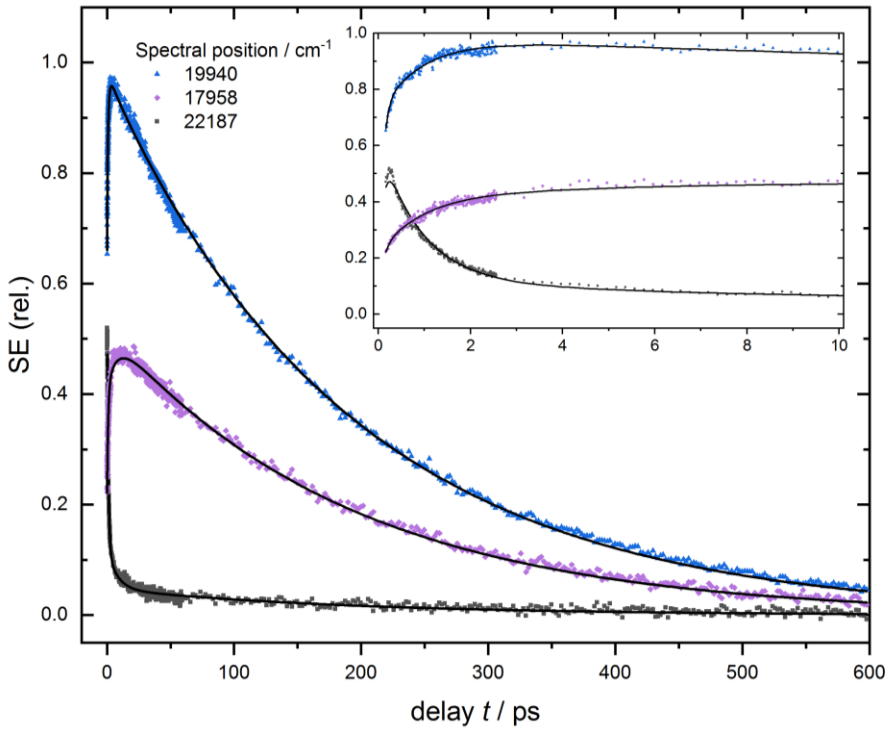

Figure A.4 Kinetic traces showing the dynamics of the emission of NAP-Pt-Cl, at select spectral positions. Solid lines represent best fits obtained via global analysis using three exponential time functions in a sequential model. Inset shows an expansion of the first 3 ps.

A.2 NAP-Pt-Ph

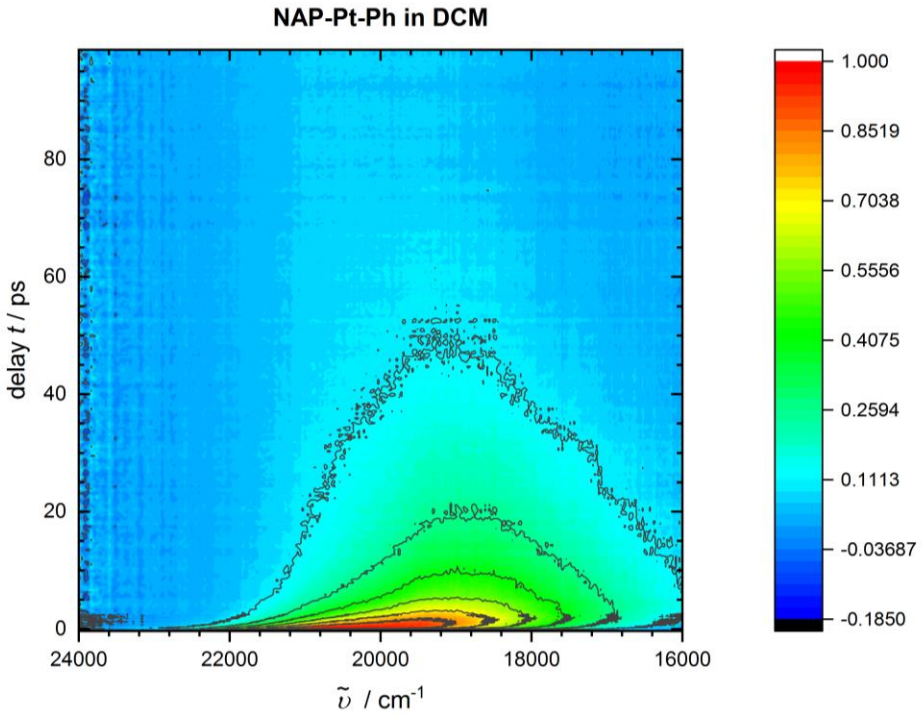

Figure A.5 A 2D map of time-resolved emission spectra of NAP-Pt-Ph in dichloromethane upon 400 nm excitation, obtained by fluorescence upconversion. The optical density at the pump wavelength was approximately 1. Photometric- and time-zero dispersion- corrections have been applied to the raw data.

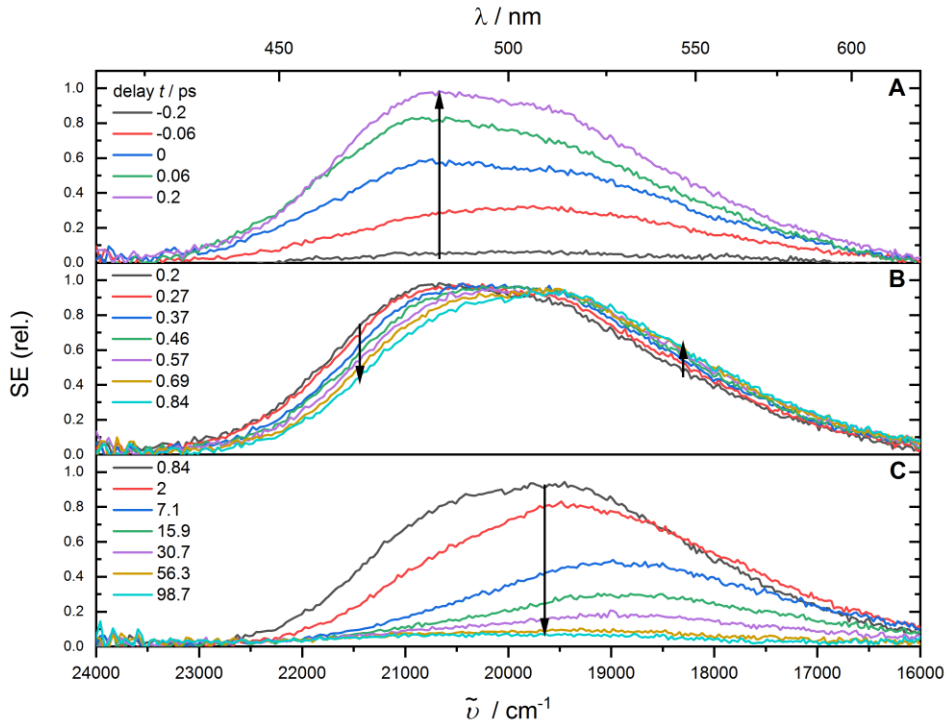

Figure A.6 Time-resolved emission spectra of NAP-Pt-Ph in dichloromethane upon 400 nm excitation, obtained by fluorescence upconversion. The optical density at the pump wavelength was approximately 1. Three distinct temporal ranges are shown in each of the panels, A, B and C. Arrows indicate the characteristic evolutionary feature within each range. Photometric- and time-zero dispersion- corrections have been applied to the raw data.

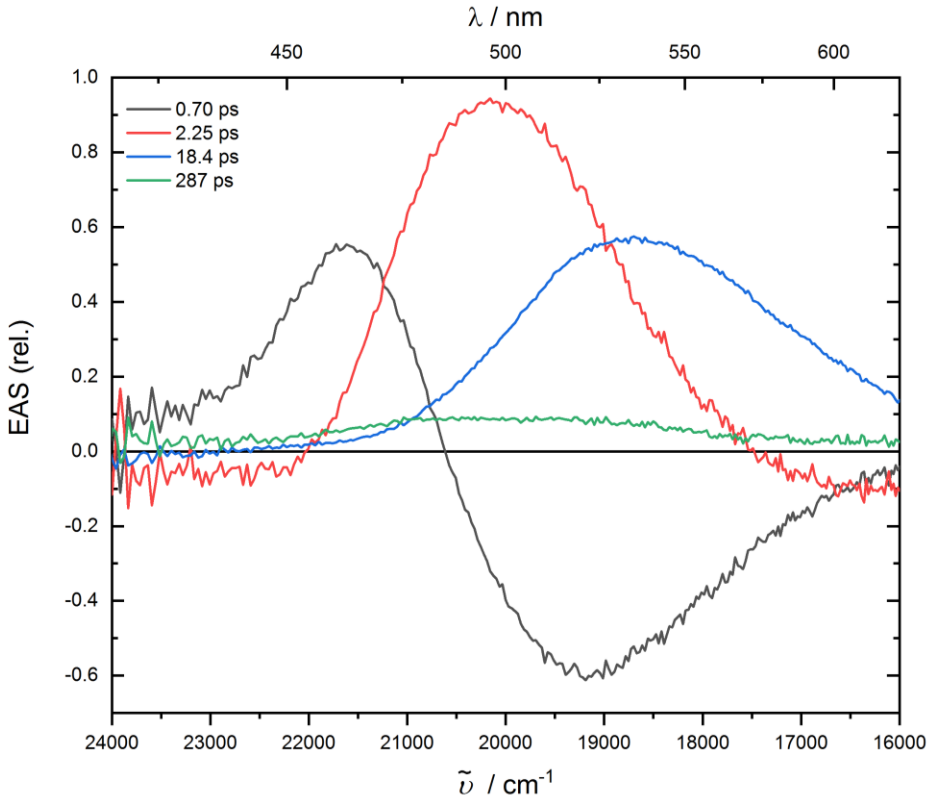

Figure A.7 Decay-Associated Spectra (DAS) of the emission spectra of NAP-Pt-Ph (shown in ***Figure A.6***), obtained via global analysis using three exponential time functions. The corresponding time constants are given as insets.

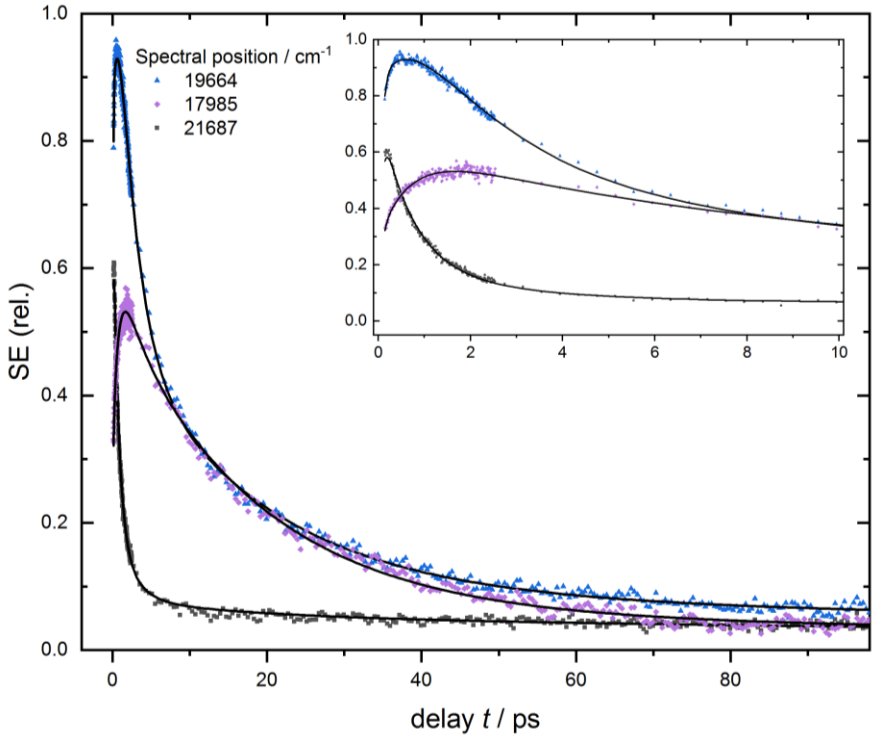

Figure A.8 Kinetic traces showing the dynamics of the emission of NAP-Pt-Ph, at select spectral positions. Solid lines represent best fits obtained via global analysis using three exponential time functions in a sequential model. Inset shows an expansion of the first 3 ps.

A.3 NAP-Pt-PTZ

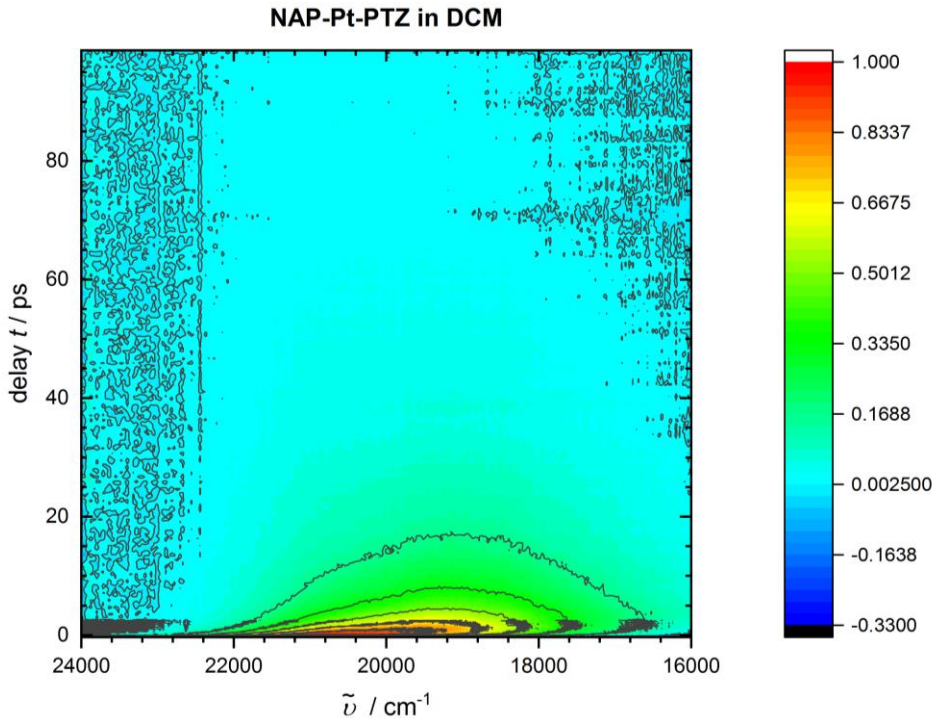

Figure A.9 2D map of time-resolved emission spectra of NAP-Pt-PTZ in dichloromethane upon 400 nm excitation, obtained by fluorescence upconversion. The optical density at the pump wavelength was approximately 1. Photometric- and time-zero dispersion- corrections have been applied to the raw data.

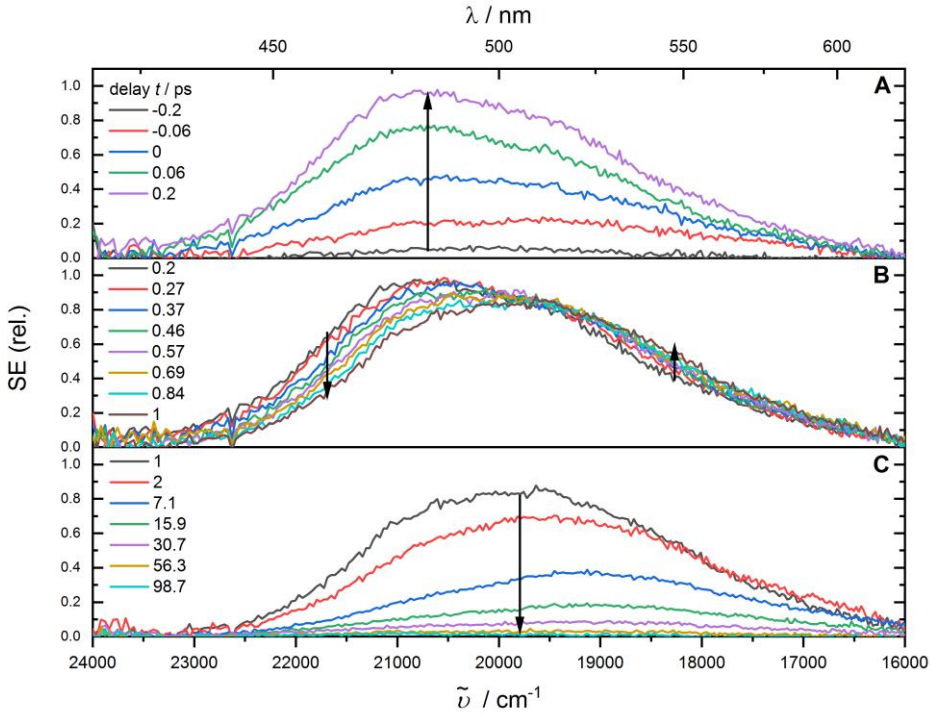

Figure A.10 Time-resolved emission spectra of NAP-Pt-PTZ in dichloromethane upon 400 nm excitation, obtained by fluorescence upconversion. The optical density at the pump wavelength was approximately 1. Three distinct temporal ranges are shown in each of the panels, A, B and C. Arrows indicate the characteristic evolutionary feature within each range. Photometric- and time-zero dispersion- corrections have been applied to the raw data.

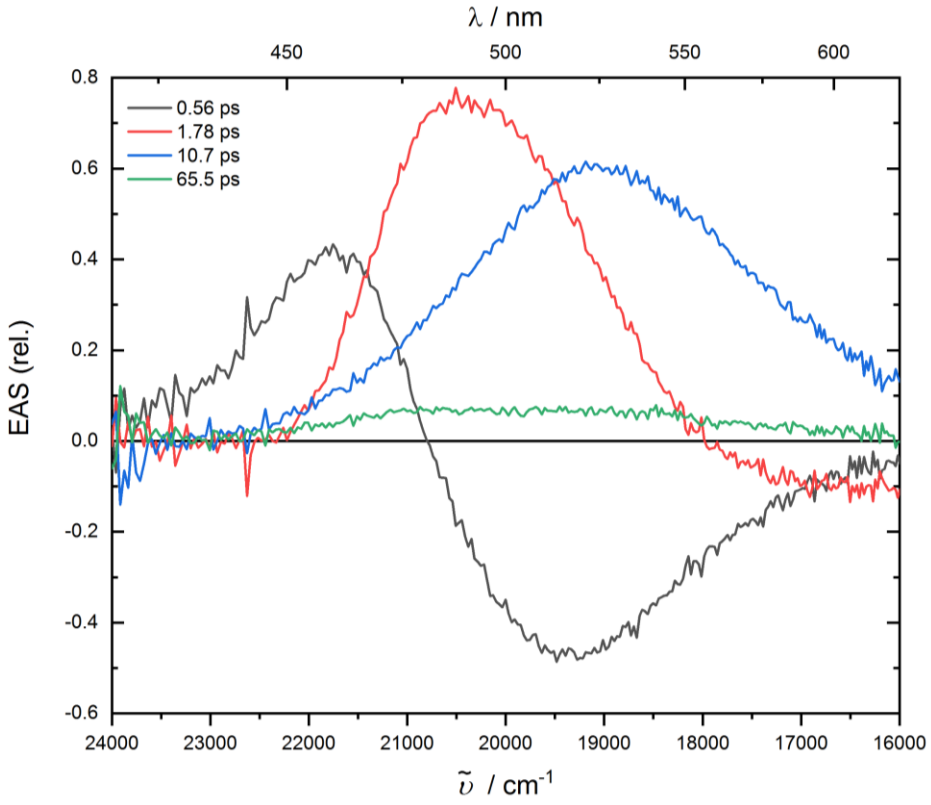

Figure A.11 Decay-Associated Spectra (DAS) of the emission spectra of NAP-Pt-PTZ (shown in ***Figure A.10***), obtained via global analysis using three exponential time functions. The corresponding time constants are given as insets.

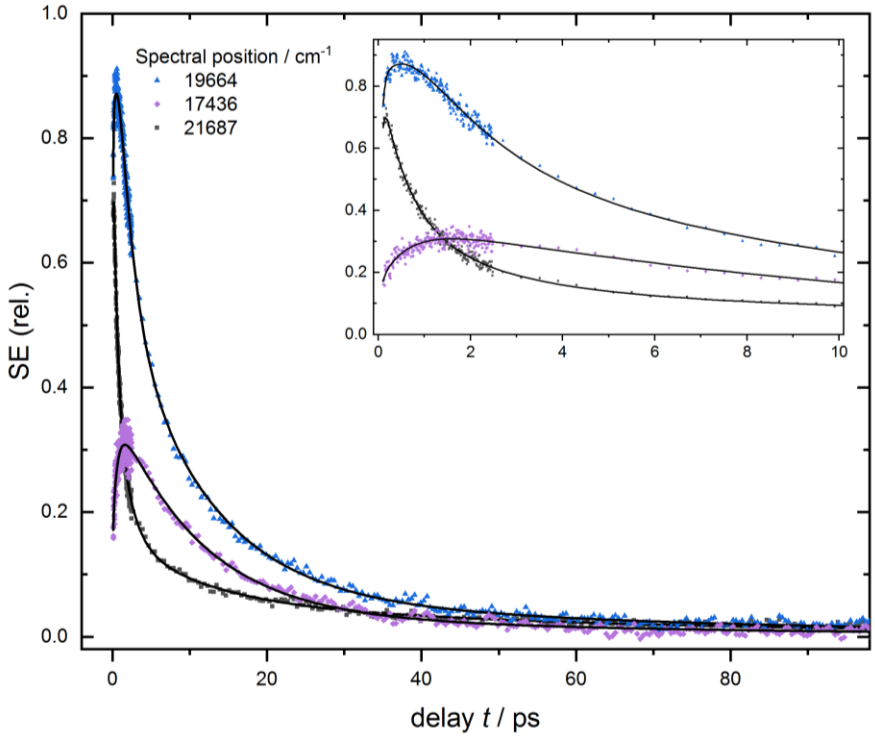

Figure A.12 Kinetic traces showing the dynamics of the emission of NAP-Pt-PTZ, at select spectral positions. Solid lines represent best fits obtained via global analysis using three exponential time functions in a sequential model. Inset shows an expansion of the first 3 ps.

B Anion-Mediated Photophysical Behaviour in a C_{60} Fullerene [3]Rotaxane Shuttle

Time-resolved infrared spectroscopy measurements were made of C_{60} Fullerene [3]Rotaxane Shuttle as part of a collaborative effort. The results form part of a published journal article, shown overleaf.

C Solvent-Mediated Activation/Deactivation of Photoinduced Electron-Transfer in a Molecular Dyad

Time-resolved UV-Vis absorption (TA) measurements were made of a molecular dyad, comprised of a [Ru(bpy)3]2+ photosensiter and an anthraquinone (AQ) acceptor coupled by an ethynyl linker ([Ru(bpy)2(bpy-CC-AQ)]2+). Research was performed as part of a collaborative effort. The results form part of a journal article, in preparation for publication, shown overleaf.